

University of Warsaw



DISSERTATION

The spin-orbit interaction of light in tunable
liquid crystal microcavities

Oddziaływanie spinowo-orbitalne światła w strojonych
mikrownękach ciekłokrystalicznych

Katarzyna Rechcińska

Faculty of Physics
Institute of Experimental Physics

**FACULTY OF
PHYSICS**

Supervised by:
dr hab. Jacek Szczytko, prof. UW

Warsaw, 2023

Streszczenie

Optoelektronika to dziedzina nauki zajmująca się interakcjami między światłem a materią, w tym generowaniem, przetwarzaniem i detekcją światła. Konstrukcja nowatorskich urządzeń fotonicznych jest ważnym elementem rozwoju optoelektroniki, ponieważ pozwala na stworzenie nowych rozwiązań technologicznych, które mogą mieć zastosowanie w różnych dziedzinach, takich jak telekomunikacja, medycyna, przemysł czy nauka. Nowe urządzenia fotoniczne mogą pozwolić na poprawę parametrów istniejących rozwiązań lub na stworzenie nowych funkcjonalności.

Jednym z szeroko stosowanych układów są wnęki optyczne, które pozwalają na zlokalizowanie fali elektromagnetycznej w strukturze i wzmacnianie efektów opartych na stymulacji optycznej, zwłaszcza przy efektach nieliniowych pojawiających się w związku z lokalizacją przestrzenną światła. Korzystają one zarówno ze wzrostu natężenia rezonansowego pola optycznego wprowadzanego przez wnękę, jak również selektywności długości fali, co pozwala m.in. na miniaturyzację urządzeń optoelektronicznych.

Niniejsza praca poświęcona jest badaniom nad oddziaływaniem spinowo-orbitalnym światła w mikrownękach wypełnionych materiałem dwójłomnym. Opisane badania przedstawiają zalety nowej konstrukcji wnęki optycznej, polegającej na wypełnieniu wnęki materiałem ciekłokrystalicznym, jako potencjalnej nowej platformy dla urządzeń optoelektronicznych, w których możliwe będzie badanie wpływu efektywnego pola magnetycznego i symulacja hamiltonianów opisujących zjawiska znane m.in. z fizyki ciała stałego. W przedstawionej pracy rozpatrywane są wnęki ciekłokrystaliczne, w których kontrolując parametry takie jak: dwójłomność, grubość warstwy ciekłokrystalicznej, czy początkowa orientacja średniego kierunku ułożenia molekuł, możliwe jest dostrojenie energetyczne rezonansów modów optycznych do różnych reżimów. Każdy z reżimów przedstawia inny efekt związany z oddziaływaniem spinowo-orbitalnym światła we wnękach.

Celem pracy jest eksperymentalna demonstracja i teoretyczna analiza efektów obserwowanych we wnękach ciekłokrystalicznych:

- przestrajalności modów fotonowych napięciem,
- strojonego spinowego optycznego efektu Halla,
- optycznego efektu Rashby-Dresselhausa,

- stanu optycznej trwałej helisy spinowej oraz fonicznego analogu eksperymentu Sterna-Gerlacha,
- przetestowanie integracji różnego rodzaju emiterów światła z wnękami ciekłokrystalicznymi.

W rozdziale 1 tej rozprawy przedstawione zostały podstawy fizyki światła spolaryzowanego, oddziaływania spinowo-orbitalnego światła oraz opis budowy i właściwości (w szczególności właściwości optycznych) ciekłych kryształów i wnęk optycznych.

W rozdziale 2 zostały opisane wykorzystane w trakcie badań metody eksperymentalne. Przedstawione zostały pomiary widm odbicia, transmisji i fotoluminescencji w przestrzeni rzeczywistej i odwrotnej, a także techniki przygotowania próbek.

W rozdziale 3 omówiona została możliwość dostrojenia wnęki do kolejnych rezonansów modów optycznych na podstawie wyników eksperymentalnych. Jednocześnie wprowadzona została klasyfikacja (nazewnictwo) kolejnych reżimów pracy wnęki.

Rozdział 4 zawiera opis teoretyczny badanych reżimów. Został przedstawiony opis symetrii w układzie w zależności od ułożenia molekuł we wnęce, jak również propozycja opisu za pomocą efektywnych hamiltonianów, która pozwoliła na powiązanie konkretnych obserwacji doświadczalnych z efektami znanymi z innych działów fizyki.

W rozdziale 5 opisano strojony optyczny spinowy efekt Halla. Pokazano, że dzięki wykorzystaniu wnęki ciekłokrystalicznej możliwe jest zaobserwowanie nowych wzorów polaryzacji spinowej.

W rozdziale 6 zaprezentowane zostały wyniki eksperymentalne pokazujące optyczny odpowiednik efektu Rashby-Dresselhausa. Wyniki otrzymane zostały dla wielomodowej strojonej wnęki optycznej.

Rozdział 7 przedstawia optyczną trwałą helisę spinową oraz optyczny odpowiednik eksperymentu Sterna-Gerlacha. Rozdział ten zawiera zarówno opis teoretyczny jak również wyniki eksperymentalne otrzymane dla różnych warunków pobudzenia.

Przedstawione w rozdziałach 5, 6 i 7 wyniki eksperymentalne zostały omówione w kontekście efektywnych hamiltonianów wprowadzonych w rozdziale 4.

Rozdział 8 zawiera opis struktur hybrydowych zawierających emiter umieszczony na powierzchni jednego z lusterek (monowarstwy MoSe_2) oraz zawierają-

cych emiter wewnątrz wnęki (białko fluorescencyjne mCherry lub barwnik laserowy Prromethene 580).

W ostatnim rozdziale 9 zebrane w pracy wyniki zostały podsumowane. Omówione zostały również możliwe kierunki rozwoju przedstawionych w rozprawie badań.

Abstract

The construction of novel optoelectronic devices is nowadays the subject of worldwide attention. Interesting effects that can be observed in photonic systems open new avenues in the constantly evolving field of optoelectronics. Resonant optical cavities are widely used in many fields of physics for localization of electromagnetic waves in structures and enhancing effects based on optical stimulation, especially with non-linear effects appearing due to the strong confinement of light.

This thesis is devoted to the spin-orbit interaction of light in microcavities filled with a birefringent material. Within this work we would like to present the advantages of the newly developed liquid crystal cavity as a possible new platform for optoelectronic devices, which will allow us to study the influence of the effective magnetic field and simulate Hamiltonians describing phenomena known, i.a., in solid-state physics. The aim of the study is to investigate and describe the spin-orbit interaction of light in an optical microcavity filled with a liquid crystal. The liquid crystal cavities have adjustable parameters such as birefringence, thickness of the liquid crystal layer, or initial orientation of the average orientation of molecules. This allows us to tune the energy of the modes into resonances belonging to different regimes. Each regime presents a different effect related to the spin-orbit interaction of light in the cavities.

The objectives of this work are experimental demonstration and theoretical analysis of spin-orbit effects observed in liquid crystal cavities:

- tunability of the photonic modes with external voltage,
- tunable optical spin Hall effect,
- optical Rashba-Dresselhaus effect,
- optical persistent spin helix state and photonic Stern-Gerlach experiment,
- testing the integration of various types of light emitters with liquid crystal cavities.

Chapter 1 of this dissertation presents the basics of the physics of polarized light, the spin-orbit interaction of light, and a description of the structure and properties (in particular optical ones) of liquid crystals and optical cavities.

Chapter 2 describes the experimental methods used during the research. Measurements of reflectivity, transmission, and photoluminescence spectra

in real and reciprocal space, as well as sample preparation techniques, are described.

Chapter 3 discusses the possibility of tuning the cavity modes to successive optical mode resonances based on experimental results. At the same time, the classification (nomenclature) of successive cavity work regimes is introduced.

Chapter 4 contains a theoretical description of the studied regimes. A description of symmetry in the system depending on the arrangement of the molecules in the cavity is presented, as well as a proposal for a description in terms of effective Hamiltonians, which makes it possible to link particular experimental observations with effects known from other fields of physics.

In chapter 5 the tunable optical spin Hall effect is described. It is shown that, thanks to the use of the tunable cavity, it is possible to observe new spin polarization patterns.

Chapter 6 presents experimental results on the optical Rashba–Dresselhaus effect that can be observed in the multimode liquid crystal cavity.

Chapter 7 shows the optical persistent spin helix as well as the photonic Stern–Gerlach experiment. This chapter contains both theory and experimental results of the spatial distribution of light polarization in the cavity for different excitation conditions.

In the chapters 5, 6 and 7 the experimental results are presented in the context of the effective Hamiltonians introduced in the chapter 4.

The following chapter - chapter 8 - contains a description of hybrid structures with emitters placed on top of a distributed Bragg reflector (MoSe₂ monolayers) and with an emitter inside the cavity (mCherry fluorescent protein or Pyrromethene 580 laser dye).

In the last chapter 9 the results are summarized. Possible directions of development of the research presented in the dissertation are discussed.

Acknowledgments

While it is not possible to mention everyone, I am grateful to so many people who contributed to this work and supported me over the last years.

First of all, I would like to thank my supervisor Prof. Jacek Szczytko for scientific guidance, all comments and encouragement on the way to the creation of this thesis. For understanding, patience, kindness, and unwavering support.

I would also like to thank Prof. Barbara Piętka for giving me so much knowledge about experimental setups and conducting measurements, and also for all the support over the years since my undergraduate studies.

I would like to extend my sincere thanks to researchers from Military University of Technology: Prof. Wiktor Piecek, Dr. Przemysław Morawiak, Dr. Rafał Mazur, and Prof. Przemysław Kula, for extremely valuable collaboration and for many fruitful discussions and sharing knowledge in the field of liquid crystal cell technology. The beginning of all presented research was the development of liquid crystal cavities.

I am deeply grateful to Prof. Pavlos Lagoudakis for the opportunity to take advantage of the knowledge and experience of such a great scientist.

I would like to offer my special thanks to Prof. Witold Bardyszewski for developing a theoretical model describing the cavities I studied, and to Dr. Helgi Sigurdsson for discussions and ideas, including the idea of the optical Stern-Gerlach experiment.

This work would not have been possible without the friendly and helpful colleagues from the Department of Solid State Physics of the University of Warsaw and, above all, the exciton-polariton group. Especially Mateusz, thank you for your time and for patiently explaining all my doubts. Mateusz and Rafał, thank you for the fascinating beginnings of this adventure in the optical laboratory.

Above all, I have to thank for the invaluable help to my Family and Friends who have constantly supported me on my way. Most of all, to my Brother, thank you for everything.

I could not have undertaken this journey without my Husband. Thank you for your love, for giving me motivation to complete my goals and for all substantive help while writing this thesis. Thank you for being there for me.

Pracę dedykuję moim córeczkom
Katarzyna Rechcińska

Contents

Chapter 1. Introduction	17
1.1. Polarization of light	17
1.2. Light propagation through dielectric layers	22
1.2.1. Transfer matrix method for isotropic materials	24
1.2.2. Berreman method	25
1.3. Optical cavities	28
1.3.1. Construction of the optical cavity	28
Distributed Bragg reflectors	28
Microcavity	30
1.3.2. Optical properties	32
Dispersion of the cavity modes – massive photons	32
TE–TM splitting	32
1.3.3. Light-matter coupling	35
1.4. Nematic liquid crystals	36
1.4.1. Optical properties	38
1.4.2. Liquid crystal in electric field	39
1.4.3. Liquid crystal cells	41
1.5. Spin-orbit interaction of light	44
1.5.1. Origin of spin-orbit interaction	44
Rashba and Dresselhaus effects	46
Persistent spin helix state	49
1.5.2. Spin-orbit interaction of light	53
Optical spin Hall effect	55
Chapter 2. Experimental methods and sample preparation	59
2.1. Experimental setup	59
2.1.1. Real and reciprocal space measurements	63
2.2. Design and preparation of the samples	65
2.2.1. Dielectric mirrors	65
2.2.2. Liquid crystals	66
2.2.3. Emitters	66
Thin layers of dichalcogenides	66
Fluorescent proteins	68

2.2.4. Liquid crystal cavities	68
Chapter 3. Tunable liquid crystal cavities	71
3.1. Liquid crystal microcavities – tuning ranges	71
3.2. Photonic modes resonances in LCMC	79
Chapter 4. Synthetic Hamiltonians of liquid crystal cavity	81
4.1. General information	81
4.2. Approximate model for an anisotropic cavity	82
4.3. Symmetry of the liquid crystal cavity	86
4.3.1. $(N + 1, N)$ regime	89
4.3.2. $(N + 2, N)$ regime	91
4.3.3. (N, N) regime	92
4.4. Synthetic Hamiltonians	95
Chapter 5. Tunable optical spin Hall effect	101
5.1. Sample	101
5.2. Dispersion relation: Tunability and H–V splitting	103
5.3. Polarization patterns	104
5.4. Summary	114
Chapter 6. Rashba-Dresselhaus interaction	115
6.1. Sample	115
6.2. $(N + 1, N)$ regime – the Rashba-Dresselhaus dispersion relation	116
6.2.1. (N, N) and $(N + 2, N)$ regimes	120
6.3. Tomography	122
6.4. Rashba-Dresselhaus parameter	126
6.5. Summary and discussion	128
Chapter 7. Persistent spin helix	133
7.1. Theory	133
7.2. All-optical persistent spin helix	136
7.2.1. Persistent spin helix for different incidence linear polarizations	142
7.3. Photonic Stern-Gerlach experiment	143
7.4. Summary	146
Chapter 8. Cavities with an emitter	149
8.1. Exciton types and emitter selection criteria	149
8.2. Emitter on top of the DBR	152
8.3. Emitter inside the liquid crystal	157
8.3.1. Fluorescent proteins	157
8.3.2. Pyrromethene 580	165

8.4. Summary	172
Chapter 9. Conclusions	175
List of publications	179
Publications directly related to this thesis	179
Publications related to this thesis	179
Publications not directly related to this thesis	180
Other achievements	181
Bibliography	183

Chapter 1

Introduction

In this chapter, the concepts of optics regarding the polarization of light in various types of media are presented. Afterwards, the spin-orbit interaction for light is discussed and an introduction to the subjects detailed in the experimental part, such as optical cavities or liquid crystals, is given.

In subsection 1.5 the selected aspects of the spin-orbit coupling physics are presented. Starting with a brief overview of the spin-orbit interactions in various areas of physics, through a description of the effects associated with a specific spin-orbit interaction, to which this work is devoted. The Rashba-Dresselhaus effect and the resulting formation of a persistent spin-helix are discussed. Particular emphasis is placed on the spin-orbit interaction of light, which is investigated in this work, including the optical spin Hall effect.

1.1. Polarization of light

Light is a transverse electromagnetic wave, that is, a wave in which electric (\mathbf{E}) and magnetic fields (\mathbf{B}) oscillate in directions perpendicular to the direction of the propagation of light. The classical laws of the electromagnetic field are described by Maxwell's equations:

$$\begin{aligned}\nabla \cdot \mathbf{D} &= \rho, \\ \nabla \cdot \mathbf{B} &= 0, \\ \nabla \times \mathbf{E} &= -\frac{\partial \mathbf{B}}{\partial t}, \\ \nabla \times \mathbf{H} &= \mathbf{j} + \frac{\partial \mathbf{D}}{\partial t},\end{aligned}\tag{1.1}$$

where the displacement field $\mathbf{D} = \varepsilon_0 \varepsilon_r \mathbf{E}$, and the magnetic field $\mathbf{B} = \mu_0 \mu_r \mathbf{H}$, where \mathbf{H} is the magnetizing field, μ_0 is the magnetic permeability in vacuum and ε_0 is the vacuum permittivity. ε_r (relative permittivity) and μ_r (relative permeability) characterize the medium permeated by the field, ρ is the total

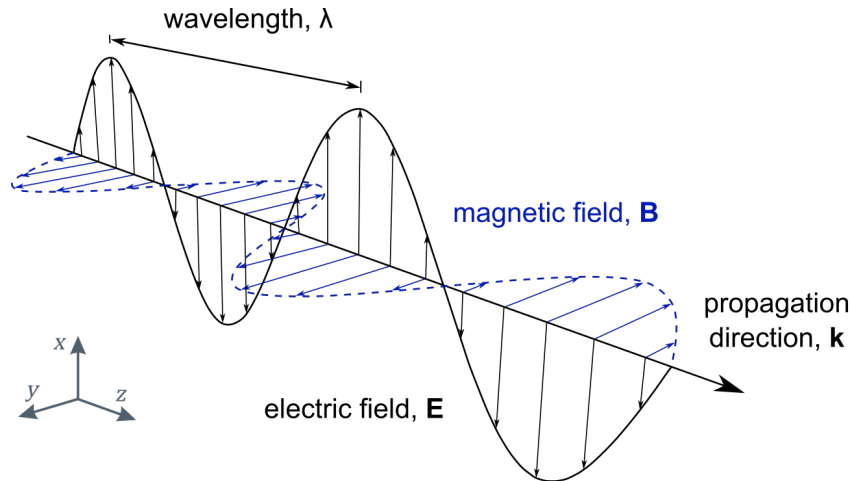


Figure 1.1: Scheme of the electromagnetic wave.

electric charge density, and \mathbf{j} is the total electric current density. According to Maxwell's equations, in the absence of electric charges, a spatially fluctuating electric field always corresponds to a magnetic field changing over time, while a spatially varying magnetic field is associated with changes in the electric field over time. An important consequence of Maxwell's equations is that they show that these synchronized oscillations of electric and magnetic fields propagate at a constant speed ($c = \frac{1}{\sqrt{\mu_0 \epsilon_0}}$) in a vacuum.

The electromagnetic wave equation derived from Maxwell's equations in a uniform isotropic medium gives rise to an electric field in the form of a plane wave:

$$\mathbf{E} = \mathbf{E}_0 e^{i(\mathbf{k}\mathbf{r} - \omega t)}, \quad (1.2)$$

where \mathbf{k} is the wave vector that determines the direction of propagation, ω is the angular frequency and \mathbf{E}_0 encodes the wave's amplitude and polarization with the condition $\mathbf{E}_0 \perp \mathbf{k}$. Only the real part of equation 1.2 is of physical importance. In a homogeneous medium $\omega = \frac{c}{n}|\mathbf{k}|$, where $n = \sqrt{\epsilon_r \mu_r}$ is the refractive index.

The polarization of light is defined to be the orientation of the oscillation of the electric field in the transverse plane. There are many types of polarization, depending on the direction of the oscillation and the state of polarization, that can be controlled by certain optical devices. Figure 1.1 presents a sketch of the linearly polarized electromagnetic wave propagating along the z axis. The electric field of light has components x and y which are in phase; both

components go to zero simultaneously, twice a period. In this case, the electric field is

$$\mathbf{E} = \begin{pmatrix} E_{x,0} \\ E_{y,0} \\ 0 \end{pmatrix} e^{i(k_z z - \omega t)}, \quad \text{Re } \mathbf{E} = \begin{pmatrix} E_{x,0} \cos(k_z z - \omega t) \\ E_{y,0} \cos(k_z z - \omega t) \\ 0 \end{pmatrix}, \quad (1.3)$$

where $E_{x,0}, E_{y,0}$ are real-valued amplitudes. The formula above explicitly expresses that the x and y components of the electric field oscillate in phase in a plane perpendicular to the direction of propagation.

More generally, polarization can be represented using the complex-valued Jones vector $\mathbf{J} = (J_1, J_2)$. The electric field in a plane wave is

$$\mathbf{E} = E_0 \begin{pmatrix} J_1 \\ J_2 \\ 0 \end{pmatrix} e^{i(k_z z - \omega t)}, \quad (1.4)$$

where E_0 is the field amplitude. The components J_i represent the relative amplitudes and phases of the electric field in the x and y directions. Their values for special cases of polarization are listed in Table 1.1. For instance, for right-handed circular polarization, the electric field is

$$\mathbf{E} = \frac{E_0}{\sqrt{2}} \begin{pmatrix} 1 \\ -i \\ 0 \end{pmatrix} e^{i(k_z z - \omega t)}, \quad \text{Re } \mathbf{E} = \frac{E_0}{\sqrt{2}} \begin{pmatrix} \cos(k_z z - \omega t) \\ \sin(k_z z - \omega t) \\ 0 \end{pmatrix}, \quad (1.5)$$

which shows that the components x and y are of equal amplitude but shifted in phase by $\pi/2$.

Although the Jones vector is convenient for describing pure states of polarization of monochromatic plane waves, it is not applicable eg. for mixtures of different pure polarization states. A more general tool for describing the state of light polarization are the Stokes parameters (degree of polarization) defined as:

$$S_1 = \frac{I_H - I_V}{I_H + I_V}, \quad (1.6)$$

$$S_2 = \frac{I_D - I_A}{I_D + I_A}, \quad (1.7)$$

$$S_3 = \frac{I_{\sigma_+} - I_{\sigma_-}}{I_{\sigma_+} + I_{\sigma_-}}, \quad (1.8)$$

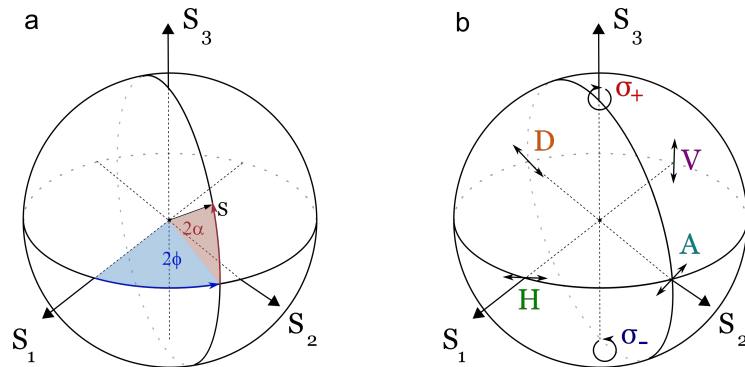


Figure 1.2: **a** Scheme showing a Poincaré sphere with Stokes vectors S_1 , S_2 and S_3 marked. **b** Poincaré sphere with six basis polarizations marked.

where the intensities I_p :

$$I_p = \langle E_p^2 \rangle = \left\langle \left| \begin{pmatrix} E_x^* \\ E_y^* \end{pmatrix} \cdot \mathbf{J}_p \right|^2 \right\rangle. \quad (1.9)$$

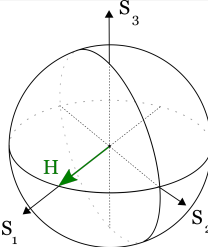
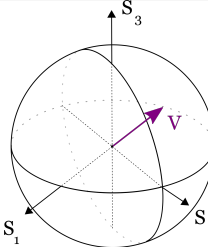
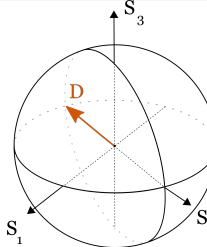
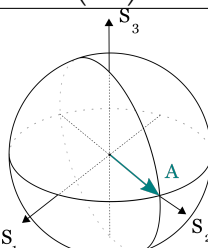
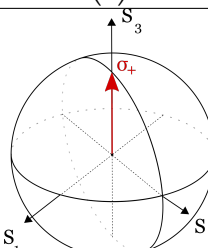
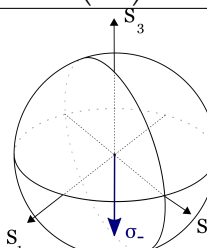
\mathbf{J}_p is the Jones vector for a polarization state p , as listed in Table 1.1, and the angle brackets denote the average over the measurement time. Stokes parameters allow one to describe the polarization properties of light beams, fully-, partially- or un-polarized. Stokes parameters can be used to describe coherent or incoherent beams. In general, the Stokes parameters are functions of the real space and reciprocal space coordinates. Parameter S_3 is often referred to as the degree of circular polarization (DOCP).

Stokes parameters can be represented on the so-called *Poincaré sphere* (Fig. 1.2). Each point on the surface of the sphere corresponds to a pure polarization state and is described by the Stokes vector (vector \mathbf{S} in the figure 1.2). This vector can be written using angles 2α i 2ϕ (Fig. 1.2 **a**) or components S_1 , S_2 and S_3 (Fig. 1.2 **b**) defined in equation (1.10).

$$\mathbf{S} = \begin{pmatrix} S_1 \\ S_2 \\ S_3 \end{pmatrix}. \quad (1.10)$$

Each component corresponds to a different basis of polarization, according to Eqs. (1.6)–(1.8). Partially polarized or unpolarized states of light are represented by points inside the sphere.

Table 1.1: Basis polarization states.

Polarization state	Horizontal, 0°	Vertical, 90°	Diagonal, 45°
Symbol	H	V	D
Jones vector	$\begin{pmatrix} 1 \\ 0 \end{pmatrix}$	$\begin{pmatrix} 0 \\ 1 \end{pmatrix}$	$\frac{1}{\sqrt{2}} \begin{pmatrix} 1 \\ 1 \end{pmatrix}$
Stokes parameter	$\begin{pmatrix} 1 \\ 0 \\ 0 \end{pmatrix}$	$\begin{pmatrix} -1 \\ 0 \\ 0 \end{pmatrix}$	$\begin{pmatrix} 0 \\ 1 \\ 0 \end{pmatrix}$
Poincaré sphere			
Polarization state	Antidiagonal, 135°	Right circular	Left circular
Symbol	A	σ_+	σ_-
Jones vector	$\frac{1}{\sqrt{2}} \begin{pmatrix} 1 \\ -1 \end{pmatrix}$	$\frac{1}{\sqrt{2}} \begin{pmatrix} 1 \\ -i \end{pmatrix}$	$\frac{1}{\sqrt{2}} \begin{pmatrix} 1 \\ i \end{pmatrix}$
Stokes parameter	$\begin{pmatrix} 0 \\ -1 \\ 0 \end{pmatrix}$	$\begin{pmatrix} 0 \\ 0 \\ 1 \end{pmatrix}$	$\begin{pmatrix} 0 \\ 0 \\ -1 \end{pmatrix}$
Poincaré sphere			

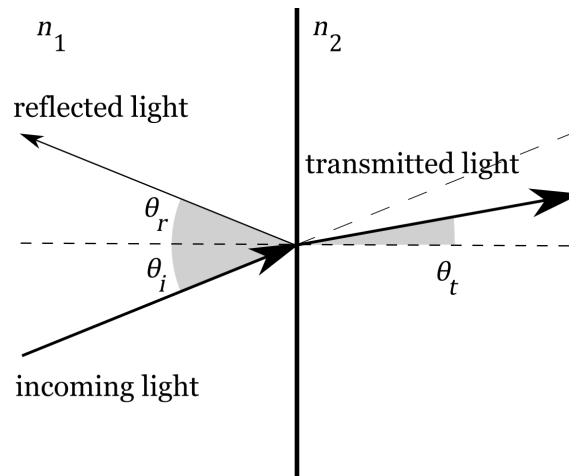


Figure 1.3: Refraction of the light at an interface between two media.

There is an analogy between the Poincaré sphere as established in optics and the Bloch sphere, a concept in quantum mechanics. The Bloch sphere is a geometric representation of two-level quantum mechanical system states as points on the surface of a unit sphere. One natural application is to represent states of a single spin $1/2$. This analogy is a motivation to interpret certain states of light as simulated electronic states, even though photons, unlike electrons, carry spin 1.

1.2. Light propagation through dielectric layers

When light reaches the interface between two different isotropic media, it is partially reflected back into the original medium and partially transmitted, as shown schematically in Figure 1.3.

Complete transmission of the wave can take place if the impedances¹ of the media are the same. In fact, dielectric optical materials (except, for example, photonic metamaterials) have magnetic permeability $\mu \approx 1$, which means that the impedance depends only on the refractive index. In the simplest case of normal incidence at the interface of the medium and no absorption, the reflectance R can be calculated using the following equation:

$$R = \left| \frac{n_1 - n_2}{n_1 + n_2} \right|^2 \quad (1.11)$$

¹ In case of dielectric material, the impedance is given by $\eta = \sqrt{\frac{\mu}{\epsilon}}$

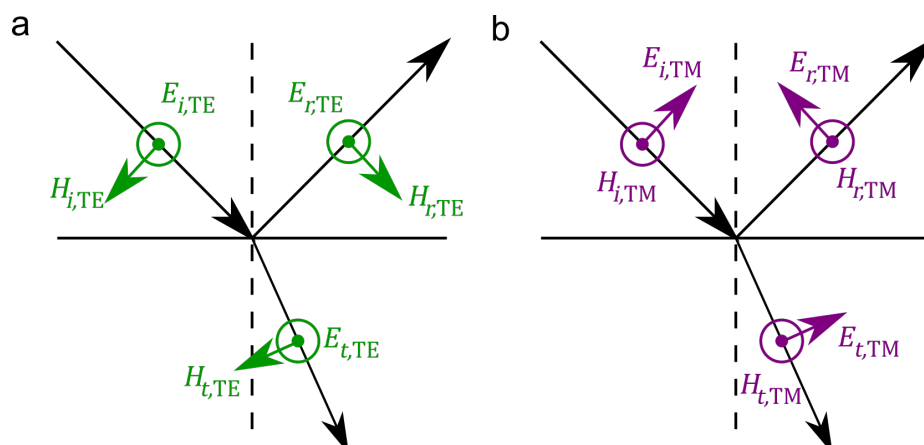


Figure 1.4: Representation of TE and TM polarization.

Thus, the optical reflectivity at such an interface depends on the refractive indices (n_1 and n_2) of the materials and vanishes if both are identical.

In general, the propagation of light at the interface is described by the Fresnel equations, which define the (Fresnel) amplitude coefficients for transmission and reflection at the boundary between two homogeneous media for an arbitrary angle of incidence.

It should be noted at this point that these coefficients depend on the polarization. The two orthogonal linear polarizations commonly used in this context are called TE, transverse electric (s, \perp) and TM, transverse magnetic (p, \parallel)². These polarizations are defined with respect to the plane of incidence of the electromagnetic wave (Fig. 1.4). The TE-polarized wave is perpendicular to this plane, and the TM-polarized wave is parallel.

These amplitude coefficients are expressed as follows:

$$\begin{aligned}
 r_{\text{TE}} &= \frac{n_1 \cos \theta_i - n_2 \cos \theta_t}{n_1 \cos \theta_i + n_2 \cos \theta_t} \\
 r_{\text{TM}} &= \frac{n_2 \cos \theta_i - n_1 \cos \theta_t}{n_1 \cos \theta_t + n_2 \cos \theta_i} \\
 t_{\text{TE}} &= \frac{2n_1 \cos \theta_i}{n_1 \cos \theta_i + n_2 \cos \theta_t} \\
 t_{\text{TM}} &= \frac{2n_1 \cos \theta_i}{n_1 \cos \theta_t + n_2 \cos \theta_i},
 \end{aligned} \tag{1.12}$$

² Note that this is not the same as the transverse modes of the waveguide.

where $\theta_i = \theta_r$ and θ_t are the propagation angles of the incoming, reflected, and transmitted light, respectively. Then we have the equations for the reflectance intensities R :

$$\begin{aligned} R_{\text{TE}} &= \left| \frac{n_1 \cos \theta_i - n_2 \cos \theta_t}{n_1 \cos \theta_i + n_2 \cos \theta_t} \right|^2 \\ R_{\text{TM}} &= \left| \frac{n_1 \cos \theta_t - n_2 \cos \theta_i}{n_1 \cos \theta_t + n_2 \cos \theta_i} \right|^2 \end{aligned} \quad (1.13)$$

In the simplest case, if we assume that there is no absorption, scattering, etc., reflection R and transmission T satisfy the following condition: $R_{\text{TE/TM}} + T_{\text{TE/TM}} = 1$ resulting from the conservation of energy. The Fresnel equations are strictly valid only if n_i are real values. For complex n_i (due to absorption or conductivity) Eqs. 1.11-1.13 are different, and they depend also on the imaginary component of refractive indices. In the following chapters we will assume negligible absorption.

1.2.1. Transfer matrix method for isotropic materials

The standard method used in optics to describe the propagation of light through isotropic (i.e., not birefringent) layers is *transfer matrix method*. This allows an accurate description of the behavior of light at the interface between layers. This method is based on the matrix notation of wave propagation, which is useful in the case of layered structures, where the quantitative description of light propagation in such a complex system leads to matrix multiplication.

$$\begin{bmatrix} U_2^+ \\ U_2^- \end{bmatrix} = \mathbf{M} \begin{bmatrix} U_1^+ \\ U_1^- \end{bmatrix}, \quad (1.14)$$

where:

$$\mathbf{M} = \begin{bmatrix} A & B \\ C & D \end{bmatrix}$$

is matrix called wave-transfer matrix and it depends on the optical properties of the medium, while U_1^+ , U_1^- , U_2^+ , and U_2^- are electric field amplitudes of the incident wave, the reflected wave, the transmitted wave, and the wave incident from the back, respectively, as shown in Figure 1.5.

For the multilayer structure (Fig. 1.6) the final result (the result matrix \mathbf{M} of the whole system) is given by the product of the successive matrices

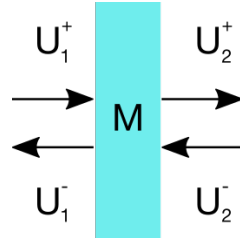
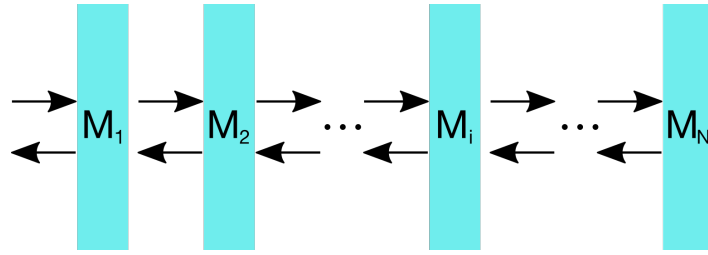


Figure 1.5: Scheme of transfer matrix method for one-layer material.

Figure 1.6: Propagation of light in multilayer structure with corresponding M matrices.

$M_1, M_2 \dots M_N$:

$$\mathbf{M} = M_N \cdot \dots \cdot M_2 \cdot M_1$$

1.2.2. Berreman method

The formalism proposed by Berreman [1, 2] is particularly useful for the description of anisotropic systems. It uses the full dielectric tensor $\hat{\epsilon}$, which allows us to consider birefringent media:

$$\hat{\epsilon} = \begin{bmatrix} \epsilon_{11} & \epsilon_{12} & \epsilon_{13} \\ \epsilon_{21} & \epsilon_{22} & \epsilon_{23} \\ \epsilon_{31} & \epsilon_{32} & \epsilon_{33} \end{bmatrix} \quad (1.15)$$

into the calculations. It is based on the TE/TM formalism and is presented schematically in Figure 1.7. In the following paragraphs we present the most important formulas from Refs. [1, 2].

The electric-field amplitudes for the TE and TM polarizations are, respectively: A – incident wave; B – reflected wave; C – transmitted wave; D – wave incident from the back. These amplitudes are related to the transfer matrix \mathbf{T} , as shown below:

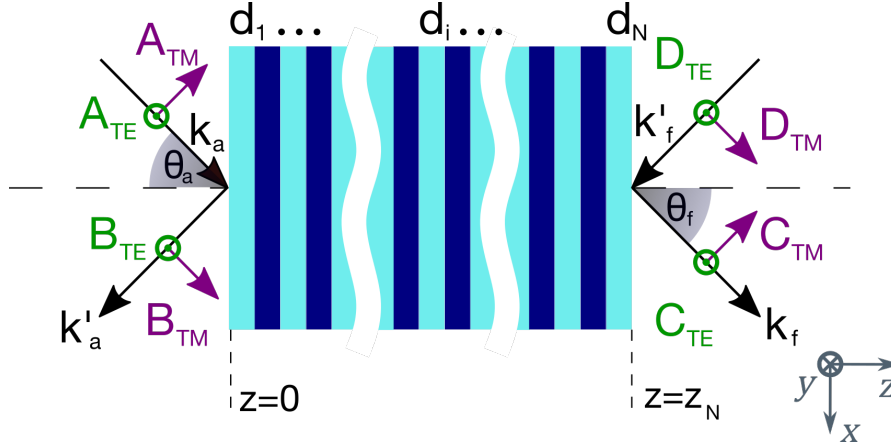


Figure 1.7: **Scheme of the Berreman method.** The waves are expressed using the TE/TM formalism. On the left-hand side of the layered structure, we have the incidence wave with the A_{TE} and A_{TM} amplitudes at the angle θ_a and the reflection of the wave with the B_{TE} and B_{TM} amplitudes. On the right, a wave with C_{TE} and C_{TM} amplitudes at angle θ_f is transmitted and a wave with D_{TE} and D_{TM} amplitudes backward propagating (in the presented considerations, they are equal to zero).

$$\begin{bmatrix} A_{TE} \\ B_{TE} \\ A_{TM} \\ B_{TM} \end{bmatrix} = \mathbf{T} \begin{bmatrix} C_{TE} \\ D_{TE} \\ C_{TM} \\ D_{TM} \end{bmatrix} = \begin{bmatrix} T_{11} & T_{12} & T_{13} & T_{14} \\ T_{21} & T_{22} & T_{23} & T_{24} \\ T_{31} & T_{32} & T_{33} & T_{34} \\ T_{41} & T_{42} & T_{43} & T_{44} \end{bmatrix} \begin{bmatrix} C_{TE} \\ D_{TE} \\ C_{TM} \\ D_{TM} \end{bmatrix}. \quad (1.16)$$

In the approach discussed, $D_{TE} = D_{TM} = 0$ is assumed.

For the \mathbf{T} matrix, the transmission coefficients are given by:

$$\begin{aligned} t_{TE/TM} &= \left(\frac{C_{TE}}{A_{TE}} \right)_{A_{TM}=0} = \frac{T_{33}}{T_{11}T_{33} - T_{13}T_{31}}, \\ t_{TM/TM} &= \left(\frac{C_{TM}}{A_{TM}} \right)_{A_{TE}=0} = \frac{T_{11}}{T_{11}T_{33} - T_{13}T_{31}}, \\ t_{TE/TE} &= \left(\frac{C_{TM}}{A_{TE}} \right)_{A_{TM}=0} = \frac{T_{31}}{T_{11}T_{33} - T_{13}T_{31}}, \\ t_{TM/TE} &= \left(\frac{C_{TE}}{A_{TM}} \right)_{A_{TE}=0} = \frac{T_{13}}{T_{11}T_{33} - T_{13}T_{31}}. \end{aligned} \quad (1.17)$$

For a single layer of a given material, the transfer matrix \mathbf{T}_i has the form

$$\mathbf{T}_i = \exp\left(i\frac{\omega}{c}\Delta d_i\right), \quad (1.18)$$

where d_i is the thickness of a given layer and Δ is

$$\Delta = \begin{bmatrix} -k_x \frac{\varepsilon_{31}}{\varepsilon_{33}} & -k_x \frac{\varepsilon_{32}}{\varepsilon_{33}} & 0 & 1 - \frac{k_x^2}{\varepsilon_{33}} \\ 0 & 0 & -1 & 0 \\ \varepsilon_{23} \frac{\varepsilon_{31}}{\varepsilon_{33}} - \varepsilon_{21} & k_x^2 - \varepsilon_{22} - \varepsilon_{23} \frac{\varepsilon_{32}}{\varepsilon_{33}} & 0 & k_x \frac{\varepsilon_{23}}{\varepsilon_{33}} \\ \varepsilon_{11} - \varepsilon_{13} \frac{\varepsilon_{31}}{\varepsilon_{33}} & \varepsilon_{12} - \varepsilon_{13} \frac{\varepsilon_{32}}{\varepsilon_{33}} & 0 & -k_x \frac{\varepsilon_{13}}{\varepsilon_{33}} \end{bmatrix}, \quad (1.19)$$

where $k_x = n_a \sin \theta_a$ with n_a – refractive index of the isotropic layer before the first layer of the structure and θ_a – incident angle of the incoming electromagnetic wave (as shown in Fig. 1.7). The dielectric tensor is defined as

$$\hat{\varepsilon} = \hat{R} \begin{bmatrix} \varepsilon_{0x} & 0 & 0 \\ 0 & \varepsilon_{0y} & 0 \\ 0 & 0 & \varepsilon_{0z} \end{bmatrix} \hat{R}^{-1}, \quad (1.20)$$

where \hat{R} is the standard orthogonal rotation matrix in a three-dimensional space around a chosen axis, and $\varepsilon_{0x}, \varepsilon_{0y}, \varepsilon_{0z}$ are the permittivity coefficients along the principal axes of the medium. The matrix \hat{R} is included to define the orientation of the principal axes of the layer independently of the definition of external TE/TM planes.

It is noted that in liquid crystals, which are made of anisotropic molecules, such rotation R of the dielectric function, and thus refractive indices, is caused by the tilt of the mean direction of the molecules with respect to the plane of the layer, and the angle of rotation can be modified by external parameters (e.g. voltage). This ability to control the optical path, i.e. the product of the refractive index and width of the medium in the direction of propagation of light, leads to all optical phenomena described in this thesis.

For a complete multilayer structure, we obtain the matrix \mathbf{T} :

$$\mathbf{T} = \mathbf{L}_a^{-1} \left(\prod_{i=1}^N \mathbf{T}_i \right) \mathbf{L}_f \quad (1.21)$$

where \mathbf{L}_a^{-1} is the matrix that transforms the incident and reflected wave from the TE/TM formalism (that is, in the laboratory frame of reference) into the

x/y formalism (that is, the frame of reference related to the main axes of an optical tensor $\hat{\epsilon}$).

$$\mathbf{L}_a^{-1} = \frac{1}{2} \begin{bmatrix} 0 & 1 & -1/n_a \cos \theta_a & 0 \\ 0 & 1 & 1/n_a \cos \theta_a & 0 \\ 1/\cos \theta_a & 0 & 0 & 1/n_a \\ -1/\cos \theta_a & 0 & 0 & 1/n_a \end{bmatrix}. \quad (1.22)$$

The matrix \mathbf{L}_f transforms from the TE/TM formalism into the x/y formalism the transmitted wave.

$$\mathbf{L}_f = \frac{1}{2} \begin{bmatrix} 0 & 1 & -n_f \cos \theta_f & 0 \\ 0 & 0 & 0 & 0 \\ \cos \theta_f & 0 & 0 & n_f \\ 0 & 0 & 0 & 0 \end{bmatrix}. \quad (1.23)$$

1.3. Optical cavities

A microcavity is a two-dimensional optical system composed of two parallel mirrors separated at some distance. The electromagnetic waves are confined in one dimension, whereas in in-plane directions they can propagate freely. The distance between the mirrors is of the order of the wavelength of light. It is a type of resonator in which wavelengths are selectively reflected or transmitted, depending on parameters defined by the structure. The historical prototype for optical microcavities is the Fabry–Perot resonator, consisting of two parallel plates, each with a sputtered silver layer. In modern systems distributed Bragg reflectors (DBR) are used as mirrors.

1.3.1. Construction of the optical cavity

Distributed Bragg reflectors

The Fresnel equation Eq. 1.11 shows that to obtain a high reflectance, R , from a layer we must use a medium with a high refractive index, n . However, in this case, based on the classical refractive index model (also known as *Lorentz dispersion model*), we know that by increasing the value of n , we simultaneously increase the absorption. The method used to solve this problem is the design of Bragg mirrors [3]. Their structure is based on two low-absorption materials with different refractive indices. By alternating

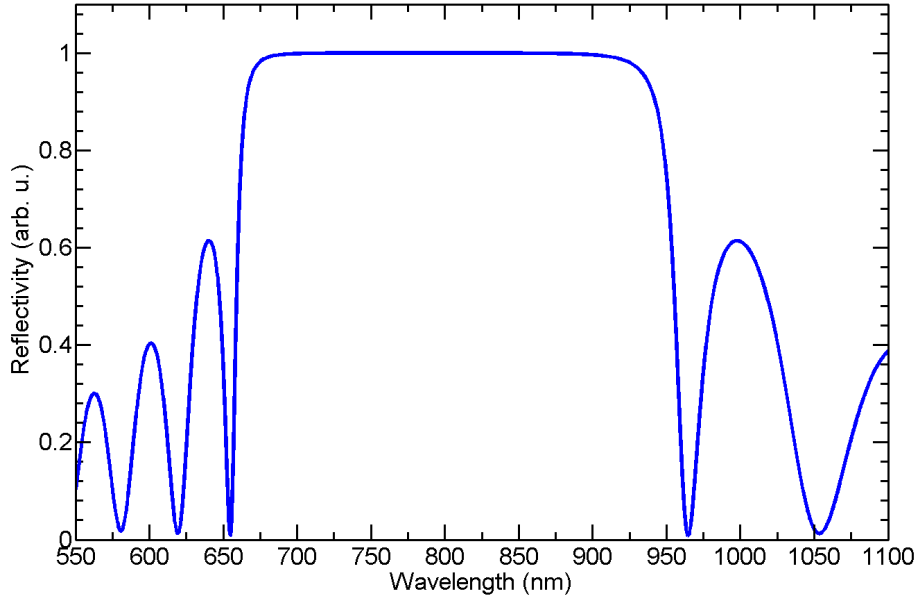


Figure 1.8: Reflectivity spectrum for an exemplary $\text{SiO}_2/\text{TiO}_2$ DBR structure consisting of 10 pairs of $\text{SiO}_2/\text{TiO}_2$ ($n_{\text{SiO}_2} = 1.456$, $n_{\text{TiO}_2} = 2.436$). Mirror stop-band centered at 780 nm. Spectrum calculated using transfer matrix method.

many thin layers of these materials, a constructive interference of all reflected waves is achieved, which results in high reflectance. The thickness of the alternating layers is selected in such a way that

$$n_1 d_1 = n_2 d_2 = \frac{\lambda_0}{4}, \quad (1.24)$$

where d_1 and d_2 are the thicknesses of successive layers with refractive indices n_1 and n_2 , respectively, and λ_0 is the central reflected wavelength. This condition means that, for incident light with a wavelength of λ_0 , a quarter of a wavelength is located in each layer. This results in destructive interference of the transmitted light. The light beam does not propagate through such a periodic structure and is almost completely reflected at each interface. We see this as high reflectance around the central wavelength λ_0 . This area is called the *photonic bandgap* or *stop-band*. An example of the reflectivity spectrum is shown in Figure 1.8. The reflectance value can be maximized by increasing the number of pairs of layers or by increasing the so-called optical contrast, i.e., using materials with a greater difference in refractive indices.

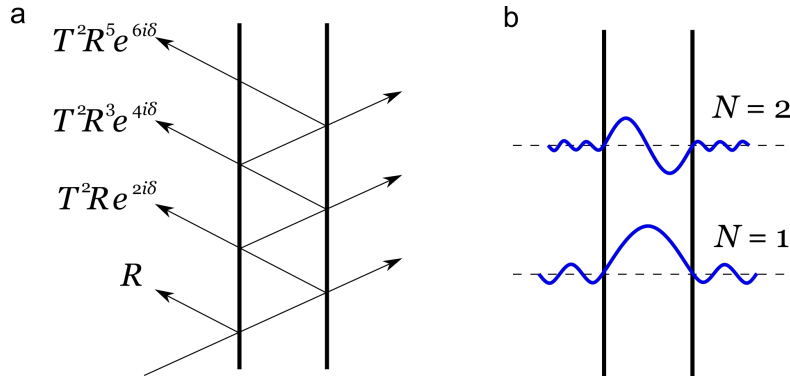


Figure 1.9: **a** Light reflection of a simple double-mirror structure (each mirror has reflectance R and transmittance T). **b** The formation of standing wave modes between mirrors with electric field profiles for the first two resonant frequencies.

Microcavity

A slightly more complex structure is the microcavity. It consists of two mirrors separated by an additional layer of material. This additional layer acts as a resonance cavity if the thickness of such a layer, d_C (characterized with a refractive index n_C)³, for normal incidence fulfills the condition:

$$d_C = \frac{N\lambda_0}{2n_C} \quad (1.25)$$

for an integer N . At resonant frequencies, light is transmitted through the structure (Fig. 1.9 a). This effect arises because of the presence of localized standing-wave modes of the electromagnetic field. Depending on the thickness of the cavity, several modes with different N indices may occur. The energetically lowest mode with $N = 1$ corresponds to a standing wave with wavelength $\lambda_0/2$, as presented in Fig. 1.9 b.

The reflectance in this case for λ_0 will be low even in the photonic bandgap region of the Bragg mirrors (Fig. 1.10). This decrease in reflectance within the *stopband* is called a *photonic mode* or *cavity mode*.

³ The product $d_C n_C$ is called optical cavity thickness.

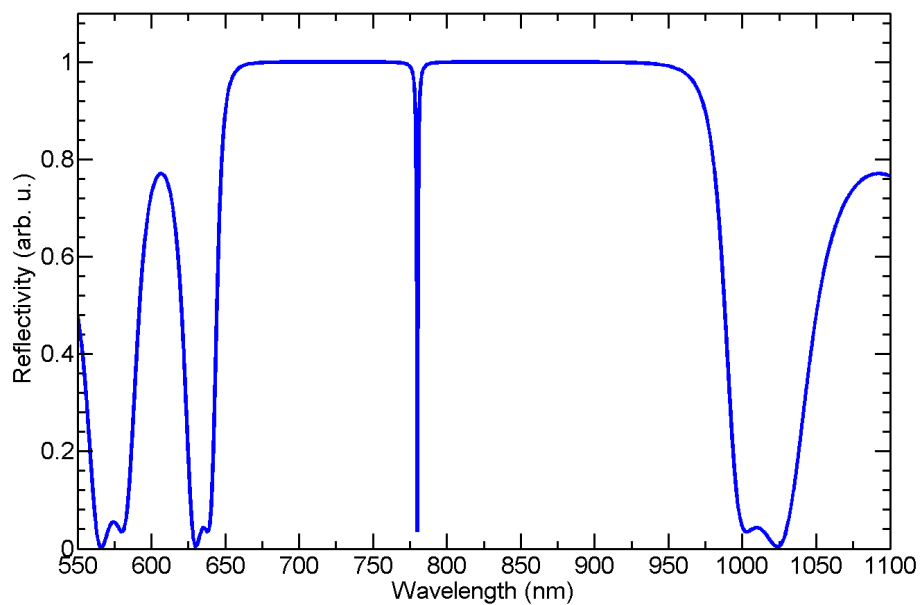


Figure 1.10: Reflectivity spectrum for an example of SiO₂/TiO₂ microcavity structure consisting of two mirrors composed of five pairs of SiO₂/TiO₂ layers ($n_{\text{SiO}_2} = 1.456$, $n_{\text{TiO}_2} = 2.436$) with cavity width $d_C = \frac{\lambda_0}{2n_C}$, where $\lambda_0 = 780$ nm and $n_C = 1.456$. Spectrum calculated using transfer matrix method.

1.3.2. Optical properties

Dispersion of the cavity modes – massive photons

To discuss the dispersion of the cavity modes, let us define the component of the wave vector $\mathbf{k} = (k_x, k_y, k_z)$. k_z is the wave vector in the confinement direction z and $\mathbf{k}_{\parallel} = (k_x, k_y)$ is the in-plane component of the wave vector, where (x, y) are the directions in the plane of the cavity. The photonic modes allowed in the resonator are given by:

$$N\pi = k_z d_C, \quad (1.26)$$

where N is an integer, $k_z = \frac{2\pi n_C}{\lambda_0}$ and d_C is the width of the cavity. The dependence of energy on the in-plane wave vector for small wave vectors (where we can use the series expansion) can be written as:

$$\begin{aligned} E(\mathbf{k}) &= \frac{\hbar c}{n_C} |\mathbf{k}| = \frac{\hbar c}{n_C} \sqrt{k_z^2 + k_{\parallel}^2} \cong \frac{\hbar c}{n_C} \left(k_z + \frac{k_{\parallel}^2}{2k_z} \right) = \frac{\hbar c}{n_C} \left(\frac{N\pi}{d_C} + \frac{k_{\parallel}^2 d_C}{2N\pi} \right) \\ &= \frac{\hbar c N\pi}{n_C d_C} + \frac{\hbar c d_C}{2n_C N\pi} k_{\parallel}^2, \end{aligned} \quad (1.27)$$

In this approximation, the dispersion for a cavity photon is not linear, as in the case of a photon in a vacuum. This is because in microcavities, one direction is confined (z). In this direction, the photon cannot propagate freely and a standing wave is formed. The dependence of energy on the in-plane wave vector takes a parabolic form. We can also define the quantity, the so-called effective mass

$$m_C^* = \frac{\hbar n_C k_z}{c} = \frac{\hbar n_C^2 N\pi}{c d_C}, \quad (1.28)$$

such that the dispersion (1.27) takes the form $E(\mathbf{k}_{\parallel}) = E_0 + \frac{\hbar^2 \mathbf{k}_{\parallel}^2}{2m_C^*}$, which is standard for a massive particle.

TE–TM splitting

There are several polarization effects observed in microcavities arising from differences between reflectances, transmittances, and phase shifts of the TE and TM states of polarization. Here, we will briefly introduce the TE-TM splitting, which allows the observation of phenomena that include the opti-

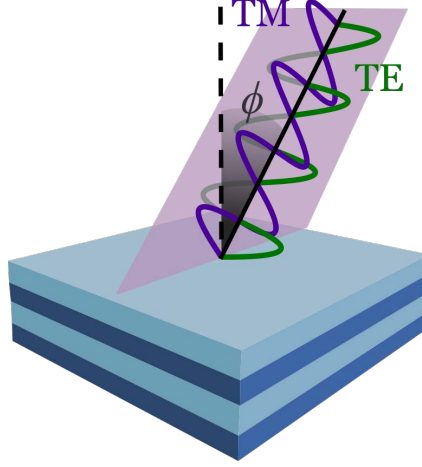


Figure 1.11: Scheme of the TE and TM polarized light incident at DBR surface.

cal spin Hall effect (more detailed in Section 1.5.2), or other interesting effects such as magnetic-monopole-like half-solitons [4], spinor condensate with half-quantum circulation [5], or possibly topological insulators [6].

The TE and TM polarizations are defined by the plane of incidence of the electromagnetic wave, and the Fresnel coefficients are written separately for both polarizations as shown in equations 1.13. For the DBR structure, the TE polarization is always in the plane of the mirror, whereas the TM polarization projects with an angle ϕ on the plane of the mirror (Fig. 1.11).

In order to consider the influence of polarization on the dispersion of the cavity modes, we must take into account the angular dependence of the reflection coefficients, r_{DBR}^{α} (where $\alpha = \text{TE}$ or $\alpha = \text{TM}$), of Bragg mirrors [7]⁴:

$$r_{\text{DBR}}^{\alpha}(\omega, \phi) = \pm \sqrt{R_{\alpha}(\phi)} \exp \left\{ i \frac{n_C}{c} d_{\text{DBR}}^{\alpha} [\omega - \omega_s^{\alpha}(\phi)] \cos \phi_C \right\}. \quad (1.29)$$

For the TE polarization, we have the following relations:

$$R_{\text{TE}}(\phi) = 1 - 4 \frac{n}{n_C} \frac{\cos \phi}{\cos \phi_C} \left(\frac{n_1 \cos \phi_1}{n_2 \cos \phi_2} \right)^{2N}, \quad (1.30)$$

$$\omega_s^{\text{TE}}(\phi) = \frac{\pi c}{2(d_1 + d_2)} \frac{n_1 \cos \phi_1 + n_2 \cos \phi_2}{n_1 n_2 \cos \phi_1 \cos \phi_2}, \quad (1.31)$$

⁴ The formulas are presented for $n_2 > n_1$

$$d_{\text{DBR}}^{\text{TE}} = \frac{2n_1^2 n_2^2 (d_1 + d_2) \cos^2 \phi_1 \cos^2 \phi_2}{n_C^2 (n_2^2 - n_1^2) \cos^2 \phi_C}. \quad (1.32)$$

For TM polarization:

$$R_{\text{TM}}(\phi) = 1 - 4 \frac{n \cos \phi_C}{n_C \cos \phi} \left(\frac{n_1 \cos \phi_2}{n_2 \cos \phi_1} \right)^{2\mathcal{N}}, \quad (1.33)$$

$$\omega_s^{\text{TM}}(\phi) = \frac{\pi c}{2} \frac{n_1 \cos \phi_2 + n_2 \cos \phi_1}{n_1 n_2 (d_1 \cos^2 \phi_1 + d_2 \cos^2 \phi_2)}, \quad (1.34)$$

$$d_{\text{DBR}}^{\text{TM}} = \frac{2n_1^2 n_2^2}{n_C^2} \frac{d_1 \cos^2 \phi_1 + d_2 \cos^2 \phi_2}{n_2^2 \cos^2 \phi_1 - n_1^2 \cos^2 \phi_2}, \quad (1.35)$$

where d_1, d_2 are the thicknesses of the DBR layers, ϕ_1, ϕ_2 are the propagation angles in the DBR layers with refractive indices n_1 and n_2 that fulfill Snell's law, respectively, and \mathcal{N} is the number of periods (i.e., pairs of dielectric layers) in the mirror. $\phi_C = \arcsin(n_{\text{ext}}/n_C \sin \phi)$ is the propagation angle in the cavity region with the refractive index n_C , while n_{ext} is the refractive index in the medium surrounding the device (e.g., air).

The TE-TM splitting results from the difference in the penetration depth of the electromagnetic wave into the mirrors for the TE and TM polarization. It can be seen that ω_s^{TM} increases faster than ω_s^{TE} with increasing angle of incidence and depth of penetration into mirrors d_{DBR}^α increases with ϕ in the case of polarization TM and decreases in the case of polarization TE. As shown by Pazarini *et al.* [7], the polarization splitting can be obtained by solving the equation

$$\left[r_{\text{DBR}}^\alpha(r_C + t_C)e^{ik_z d_C} - 1 \right] \left[r_{\text{DBR}}^\alpha(r_C - t_C)e^{ik_z d_C} - 1 \right] = 0, \quad (1.36)$$

for ω , separately for $\alpha = \text{TE}$ and $\alpha = \text{TM}$, where r_C, t_C are reflection and transmission coefficients of the cavity medium, and $k_z = (n_C \omega / c) \cos \phi_C$. The difference of solutions, for the case of empty cavity $r_C = 0, t_C = 1$, written in approximate form:

$$\omega_m^{\text{TM}}(\phi) - \omega_m^{\text{TE}}(\phi) \simeq \frac{d_c d_{\text{DBR}}(0)}{d_{\text{eff}}(0)^2} \frac{2 \cos \phi_{\text{eff}} \sin^2 \phi_{\text{eff}}}{1 - 2 \sin^2 \phi_{\text{eff}}} (\omega_s(0) - \omega_c(0)), \quad (1.37)$$

where ω_m is the cavity mode frequency, ω_C is the Fabry-Perot frequency ⁵, $d_{\text{eff}} = d_C + d_{\text{DBR}}$ is effective length (with d_C the length of the cavity region).

⁵ $\omega_C = (N\pi c/n_C)d_C \cos \phi_C$

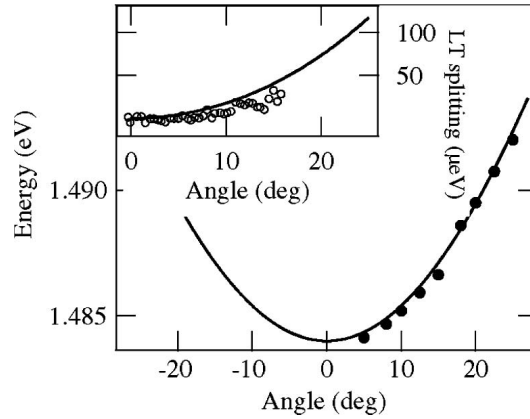


Figure 1.12: Angle-resolved bare photonic mode dispersion (solid line) with experimental points. Inset: longitudinal-transverse (LT) splitting of polaritons. Image after [8].

We note that TE/TM splitting is an angle- or k -dependent polarization splitting and it's vanishing at normal incidence $k_{\parallel} = 0$ ⁶. Effectively, it means that with increasing ϕ the difference between the refractive indices of the optical cavity for the TE mode and the TM mode also increases. This difference leads to the difference of effective masses due to Eq. 1.28 and thus to the presence of the splitting of linearly polarized modes.

1.3.3. Light-matter coupling

Microcavities are predominantly studied in the context of phenomena related to strong light-matter coupling, that lead to the emergence of quasiparticles called *exciton polaritons*. Although the phenomena investigated in this thesis do not show properties that can be attributed to strong coupling, their eventual observation was the driving force behind the investigations of our main subject, i.e., the liquid-crystal microcavity. Therefore, we will briefly introduce the concept of light-matter coupling.

The subject of light-matter coupling has been of great interest to the scientific community for many years. Microcavity exciton polaritons, the first experimental observation of which dates to 1992 [9], still arouse curiosity, and work on new realizations of structures in which it is possible to study this type of phenomena is constantly developing [10–15]. Microcavity exciton polari-

⁶ Note that $k_{\parallel} = (\omega/c) \sin \phi$. More information on the equivalence between the angle of incidence and the in-plane wavevector is shown in Section 2.1.1.

tons are quasiparticles formed by a strong coupling between a cavity photon and an exciton. Semiconductor heterostructures in the form of Bragg mirrors grown by molecular beam epitaxy (MBE) were the most frequently studied. However, in recent years, research on systems that show strong coupling at room temperature, for example, with organic materials [16–19], has been developed. To observe the light–matter coupling, a physical system (called an *emitter*) with energy transitions corresponding to the resonant wavelength of the microcavity must be placed between the two DBRs. In the case of the systems described above, the emitters are quantum wells, or a layer of organic material, placed in the spot of the maximum amplitude of the electromagnetic field. Excitons are created in the emitter, which can then strongly couple with the cavity photons. Research on exciton polaritons has shown that in such structures it is possible to observe phenomena known from the physics of atomic systems, such as Bose–Einstein condensate, superfluidity, or other nonlinear effects [20, 21].

1.4. Nematic liquid crystals

Liquid crystal compounds are materials that form an intermediate phase between a crystal and an isotropic liquid. Isotropic liquids are fluid and do not present long-range positional or orientational order, unlike crystals, which form structures with a high degree of both types of order. Liquid crystal materials are characterized by their ability to flow with the simultaneous orientation of molecules, leading to anisotropy of physical properties, such as the refractive index or viscosity.

On the basis of the method of generating liquid crystalline phases, we can distinguish thermotropic and lyotropic phases. In the first case, phase transitions are observed with a change of temperature. Typically, at high temperatures⁷ an isotropic liquid phase is observed. As the temperature of the system decreases, successive phase transitions are registered from the least ordered to the most ordered liquid crystal phases. In the case of lyotropic compounds, phase transitions are observed along with the change in solvent concentration.

The second criterion for the classification of liquid crystal compounds is based on the type of mesogenic substances. The liquid crystal phases are

⁷ The specific value of which depends on the type of compound.

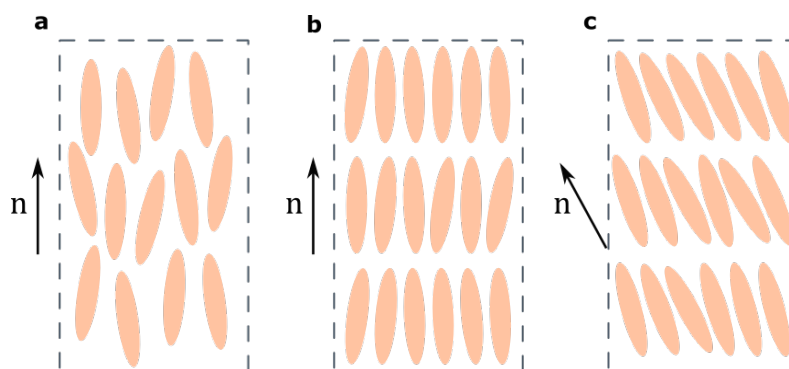


Figure 1.13: Liquid crystal types. **a** Nematic, where the molecules are elongated and create a structure with a distinguished orientation of the long axes of the molecules. The mean direction of the long axes of the molecules is determined by the unit ordering vector \mathbf{n} , the so-called *director*. In smectics the crystals are additionally confined to the parallel planes. In smectic A phase **b** the director \mathbf{n} is perpendicular to these planes, while in smectic C phase **c** \mathbf{n} is at some other angle to the planes.

formed by *mesogens*, that is, chemical compounds whose molecules have shape anisotropy and are composed of rigid and flexible parts. They can be either rod-like particles (classical liquid crystals) or flat disk-like particles. There are also other kinds like brick- and banana-shaped particles and others.

The classification of rod-like liquid crystals was made by Georges Friedel in 1931. He divided the liquid crystals into two basic groups: nematics (Figure 1.13 **a**) and smectics (examples of smectic phases are presented in Figure 1.13 **b,c**). Nematic liquid crystals also include cholesteric liquid crystals (chiral nematics), which are not discussed in this work. Liquid crystals belonging to different groups differ in physical properties (in particular, optical properties), resulting from differences in their structure.

In this work, we will focus on the nematic phase shown in Figure 1.13 **a**, which is the basic liquid crystal phase with the lowest degree of order. In this phase, there is no positional order, but molecules self-align nearly parallel to the orientation of the long axes of the molecules (orientational order). The mean direction of the long axes of the molecules, averaged over volume and time, is determined by the unit ordering vector \mathbf{n} , the so-called *director*. In nematics, a fluctuation of the director's arrangement is observed because of thermal vibrations, which means that the molecules can be deviated from the

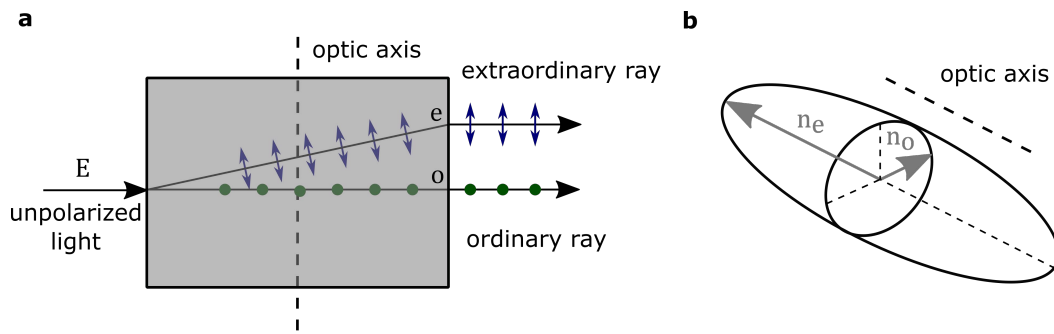


Figure 1.14: **a** Double refraction in birefringent material. The dots and arrows describe the direction of electromagnetic wave polarization. The dots are the perpendicular polarization to the surface of the figure and the arrows the parallel polarization. **b** Scheme of a liquid crystal molecule with ordinary (n_e) and extraordinary (n_o) refractive indices.

director by a certain small angle. Layer formation is not observed here, as is the case for phases with a higher degree of ordering.

In the present work, two different nematic liquid crystals were used as a material that fills the optical microcavity.

The subsections below summarize certain facts concerning the properties of nematic LCs, which are relevant to our applications. For a comprehensive introduction to the subject we refer the reader to the book by Yang and Wu [22].

1.4.1. Optical properties

The shape of a liquid crystal molecule determines the physical properties that have different values in a direction parallel and perpendicular to the long axis of the molecule. This leads, among other things, to dielectric and optical anisotropy.

The liquid crystal medium is described by a dielectric tensor (ϵ), that is, the permittivity has different values in different directions.

Optical anisotropy is manifested by the occurrence of birefringence. This phenomenon leads to the separation of incident light into two rays: ordinary o and extraordinary e (see Figure 1.14 **a**). As a result of the difference in the value of the electric permittivity of the material in different directions, the speed of light wave propagation differs depending on the polarization of the incident light. The special direction for which the speed of light is inde-

pendent of its polarization is called the optic axis. Depending on the number of these axes, one can distinguish between uniaxial and biaxial materials. In most cases, the molecules of liquid crystals are uniaxial and center-symmetric, making it possible to determine the optical axis and, consequently, define ordinary and extraordinary rays. We will therefore focus on the uniaxial liquid crystals. For an ordinary ray, the vector \mathbf{E} of the electromagnetic wave oscillates perpendicular to the plane defined by the direction of propagation of the wave and the optic axis. For the extraordinary ray, the direction of the \mathbf{E} field oscillations lies in this plane (see Figure 1.14 **a**). As discussed, the birefringence phenomenon is caused by differences in the interaction of the electromagnetic wave (the electric field vector \mathbf{E} of this wave) with the anisotropic medium with different relative orientations of the vector \mathbf{E} and the optical axis of the medium.

The anisotropy of the optical properties of birefringent substances is characterized by two refractive indices: ordinary n_o and extraordinary n_e , which are long and short semi-axes of the optical indicatrix (also known as an index ellipsoid) as shown in Figure 1.14 **b**. The magnitude of birefringence is described by the difference between the ordinary and extraordinary refractive indices:

$$\Delta n = n_e - n_o. \quad (1.38)$$

The nematic and smectic liquid crystals are typically optically positive ($\Delta n > 0$), and the direction of the long axes of the molecules in these compounds coincides with the direction of the optical axis.

1.4.2. Liquid crystal in electric field

The interaction of a liquid crystal with the electric field can in general be quite complex and, for dielectric liquid crystals, includes reorientation of the molecules, field-induced ordering, and the flexoelectric effect. In addition, certain liquid crystals are ferroelectrics, i.e., they have a spontaneous electric polarization at no external field. Here we confine our introduction to the phenomenon of reorientation of the molecular director under dielectric interaction, as it is the only effect relevant for the operation of the microcavities discussed in this work.

The dielectric effect in liquid crystals depends mostly on three factors:

- molecule polarizability anisotropy,
- the permanent electric dipole moment of the molecule,

— the angle between the permanent dipole moment and the direction of the director \mathbf{n} .

Electric field applied to a nematic liquid crystal induces polarization \mathbf{P} , which consists of the electronic polarization, resulting from the deformation of molecular electron clouds, the ionic polarization, which comes from the relative displacement of atoms in the molecule, and the dipolar polarization, which is due to reorientation of the molecule's permanent dipole (if present). The total polarization is given by

$$\mathbf{P} = \varepsilon_0(\chi_{\parallel}\mathbf{E}_{\parallel} + \chi_{\perp}\mathbf{E}_{\perp}), \quad (1.39)$$

where $\mathbf{E}_{\parallel(\perp)}$ is the electric field component parallel (perpendicular) to the molecular director \mathbf{n} , and $\chi_{\parallel(\perp)} = \varepsilon_{\parallel(\perp)} - 1$ is the appropriate permittivity element, which is in general a function of frequency. The electric field components can be expressed as

$$\mathbf{E}_{\parallel} = (\mathbf{E} \cdot \mathbf{n})\mathbf{n}, \quad \mathbf{E}_{\perp} = \mathbf{E} - \mathbf{E}_{\parallel}, \quad (1.40)$$

which yields

$$\mathbf{P} = \varepsilon_0[\chi_{\perp}\mathbf{E} + \Delta\varepsilon(\mathbf{E} \cdot \mathbf{n})\mathbf{n}]. \quad (1.41)$$

We have used the fact that the dielectric anisotropy is $\Delta\varepsilon = \varepsilon_{\parallel} - \varepsilon_{\perp} = \chi_{\parallel} - \chi_{\perp}$. Therefore, the electric energy density in the nematic liquid crystal is

$$u = -\frac{1}{2}\mathbf{P} \cdot \mathbf{E} = -\frac{1}{2}\varepsilon_0\chi_{\perp}|\mathbf{E}|^2 - \frac{1}{2}\varepsilon_0\Delta\varepsilon(\mathbf{E} \cdot \mathbf{n})^2. \quad (1.42)$$

Clearly, for $\Delta\varepsilon > 0$ the energy is lowest when $\mathbf{E} \parallel \pm\mathbf{n}$, and for $\Delta\varepsilon < 0$ it is lowest when $\mathbf{E} \perp \mathbf{n}$. Therefore, in the first case, the liquid crystal molecules subjected to the external electric field experience a torque which tends to align the molecular director with the electric field. This effect is counteracted by the viscosity of the medium and the anchoring of the molecules to the substrate surface. Therefore, at a given voltage across the liquid crystal layer, the molecules align with an orientation in which the competing torques are equilibrated. In analogy, for $\Delta\varepsilon < 0$, the molecular director tends to align perpendicular to the electric field.

$\Delta\varepsilon$ has contributions from all polarizability types, and depends primarily on ordering of the liquid crystal, electric field frequency, temperature, and the angle β between the LC molecule's permanent dipole and its long axis. At

low field frequencies, when β is close to zero, $\Delta\varepsilon > 0$, while when $\beta \approx 90^\circ$ and the permanent dipole moment is large, then $\Delta\varepsilon < 0$. For intermediate angles β and large permanent dipole moment, the LC may undergo a transition from $\Delta\varepsilon > 0$ at lower frequencies to $\Delta\varepsilon < 0$ at higher frequencies. The crossover frequency is typically of the order of a few or a few tens of kHz. At infrared frequencies (hundreds of GHz) and higher, $\Delta\varepsilon$ is always positive, since the contribution of the dipolar polarizability becomes negligible.

It is important that the effect of the liquid crystal reorientation occurs both for a constant and an alternating electric field, because the energy density u depends on the term $(\mathbf{E} \cdot \mathbf{n})^2$ independent of the sign of \mathbf{E} . The magnitude of the response is proportional to the frequency-dependent dielectric anisotropy $\Delta\varepsilon$.

In conclusion, the long-range ordering of elongated molecules of liquid crystals causes a strong directional anisotropy of many physical properties, in particular optical ones. Furthermore, the liquid nature of these materials and the relatively high ability to reorient molecules allow easy control of these properties with relatively weak external fields (a voltage of a few volts suffices to control the orientation in a few micron thick LC layer).

1.4.3. Liquid crystal cells

Typically, to change the tilt of the LC director with an electric field, an LC cell (transducer) is used. It consists of two transparent glass plates covered with a transparent conductive layer (e.g. indium tin oxide, ITO) and a *rubbing layer* (orientation layer). The rubbing layer is created by unidirectional rubbing of the polyimide film with a velvet cloth. In practice this is done by a rubbing machine, where a polymer-coated substrate moves under a rotating drum covered with a special velvet rubbing cloth. The rubbing layer forces the specific arrangement of the molecules to be homeotropic (HT) or homogeneous (HG) in the case where no voltage is applied by proper anchoring of the liquid crystals in the orientation layer. The homogeneous (planar) orientation is characterized by the long axes of the molecules lying in a plane parallel to the surface of the LC cell. A sketch of the arrangement of the molecules is presented in Figure 1.15 a. In homeotropic orientation, the long axes of the molecules are positioned perpendicular to the LC cell plane, as shown in Figure 1.15 b. It should be noted that the distribution of molecules presented in Figure 1.15 is a model system, in fact, disturbed by the thermal movements of the molecules.

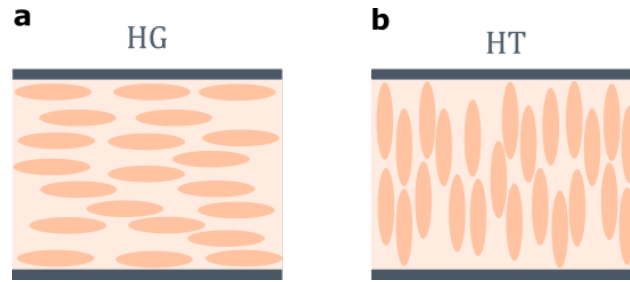


Figure 1.15: Orientation of the nematic phase of a liquid crystal: **a** homogeneous or planar (HG), **b** homeotropic (HT).

The liquid crystal is in contact with the conductive layers that cover the glass plates. To ensure constant thickness of the liquid crystal layer, the plates are glued with spacers. Electrical leads are connected to the conductive layer, allowing the application of an external electric field.

When constant- or low-frequency variable-alternating fields are applied (typically in square-wave form), the primary reaction of the liquid crystal will be the reorientation of the molecules inside the volume with respect to the direction of the applied field. The relatively high viscosity of the liquid crystals counteracts these changes. However, reorientation is usually fast because the molecules are located in the middle layers of the liquid crystal away from the surfaces that impose anchoring conditions. These molecules reorient very quickly when the voltage exceeds the threshold voltage U_c . This effect was first observed by Freederick in a magnetic field. The behavior in an electric field is analogous. Applying a voltage above the threshold voltage perpendicular to the liquid crystal cell with positive dielectric anisotropy ($\Delta\epsilon > 0$) of planar orientation causes a slow tilting of the molecular director of LC toward the direction of the controlling electric field (Fig. 1.16 **a**, **b**). On the other hand, a sufficiently high voltage reorients the molecules homeotropically (Fig. 1.16 **c**). The value of the threshold voltage is determined, among other things, by the thickness of the liquid crystal cell: the narrower the cell, the higher the anchoring energy, thus the higher the threshold.

The threshold value of the voltage causing Freederick's deformation (planar orientation) is given by the formula:

$$U_c = \pi \sqrt{\frac{k_{11}}{\Delta\epsilon}}. \quad (1.43)$$

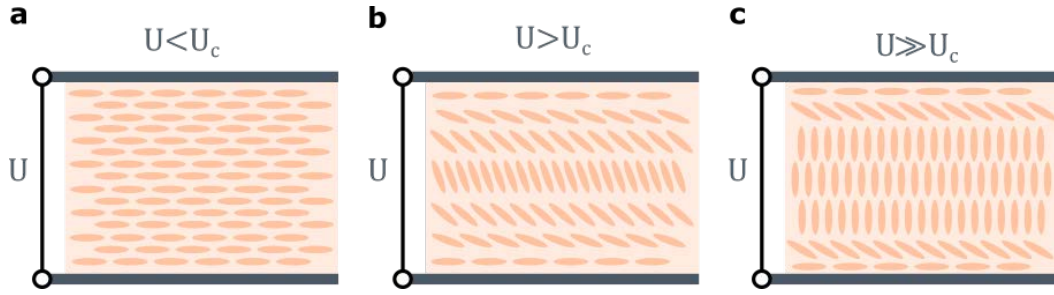


Figure 1.16: A scheme of deformation of nematic with positive dielectric anisotropy and homogeneous orientation: **a** when no voltage is applied. **b,c** Electrical Fredericik's effect: **b** when a voltage greater than the threshold voltage is applied, **c** when high voltage is applied.

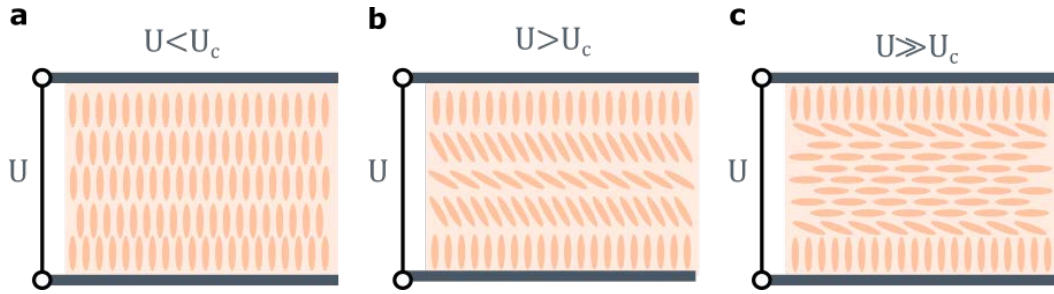


Figure 1.17: A scheme of deformation of nematic with negative dielectric anisotropy and homeotropic orientation: **a** when no voltage is applied. **b,c** electrical Fredericik's effect: **b** when a voltage greater than the threshold voltage is applied, **c** when high voltage is applied.

k_{ii} are the elastic coefficients describing the main deformations in the nematic liquid crystal ($i = 1$ – splay, $i = 2$ – twist, $i = 3$ – bend).

A similar effect is observed for nematics with negative dielectric anisotropy, $\Delta\epsilon < 0$, homeotropically oriented (Figure 1.17).

The threshold value of the voltage causing Fredericik's deformation for homeotropic orientation of the LC in the cell is given by the formula:

$$U_c = \pi \sqrt{\frac{k_{33}}{\Delta\epsilon}}. \quad (1.44)$$

While the idea of liquid crystal optical cavities has been established prior to this work, the research has focused mainly on the bistability of liquid crystals. Among the investigated systems were a planar-spherical cell and a spherical droplet [23], microdroplets [24], liquid crystal in Fabry-Perot res-

onators, where the optical bistability and solitons were studied [25–28]. The results presented in this work introduce a new concept of the study of artificial gauge fields and synthetic Hamiltonians in a planar liquid crystal microcavity.

1.5. Spin-orbit interaction of light

1.5.1. Origin of spin-orbit interaction

In general, in non-relativistic quantum mechanics; where the evolution of a system represented by a given Hamiltonian is described by the Schrödinger equation; the spin of the particle and the center-of-mass motion are separated. Thus, these degrees of freedom (internal and external) are independent unless additional terms of interaction are introduced. Indeed, such terms are present in the Dirac equation:

$$\begin{pmatrix} mc^2 - E + V & c\boldsymbol{\sigma} \cdot (\mathbf{p} - e\mathbf{A}) \\ -c\boldsymbol{\sigma} \cdot (\mathbf{p} - e\mathbf{A}) & mc^2 + E - V \end{pmatrix} \begin{pmatrix} \psi_+ \\ \psi_- \end{pmatrix} = \begin{pmatrix} 0 \\ 0 \end{pmatrix} \quad (1.45)$$

which describes the motion of a quantum electron of rest mass m and energy E in an electromagnetic field of vector potential \mathbf{A} and scalar potential V , in accordance with Einstein's special theory of relativity. The Pauli vector is given by $\boldsymbol{\sigma} = (\sigma_x, \sigma_y, \sigma_z)$, where σ_i are the Pauli matrices:

$$\begin{aligned} \sigma_0 &= \begin{pmatrix} 1 & 0 \\ 0 & 1 \end{pmatrix}, \quad \sigma_x = \begin{pmatrix} 0 & 1 \\ 1 & 0 \end{pmatrix}, \\ \sigma_y &= \begin{pmatrix} 0 & -i \\ i & 0 \end{pmatrix}, \quad \sigma_z = \begin{pmatrix} 1 & 0 \\ 0 & -1 \end{pmatrix}. \end{aligned} \quad (1.46)$$

Here, these terms constitute a momentum-dependent coupling between the matter (ψ_+) and antimatter (ψ_-) components of the bispinor. It is often convenient to consider only the non-relativistic limit of the Dirac equation, which describes the matter component. By means of perturbation theory, we arrive at the formula

$$\left[\frac{1}{2m} (\mathbf{p} - e\mathbf{A})^2 + V(\mathbf{r}) + mc^2 + H_Z + H_{SO} + H_T + H_D \right] \psi_+ = E\psi_+ \quad (1.47)$$

which is the Schrödinger equation with the so-called relativistic corrections:

— spin-orbit coupling (SOC)

$$H_{SO} = \frac{\hbar}{4m^2c^2} \boldsymbol{\sigma} \cdot [\nabla V \times (\mathbf{p} - e\mathbf{A})], \quad (1.48)$$

— relativistic correction to the kinetic energy

$$H_T = -\frac{1}{8m^3c^2} (\mathbf{p} - e\mathbf{A})^4, \quad (1.49)$$

— Darwin term

$$H_D = \frac{\hbar^2}{8m^2c^2} \nabla^2 V(\mathbf{r}), \quad (1.50)$$

and the Zeeman term;

$$H_Z = -\frac{e\hbar}{2m} \boldsymbol{\sigma} \cdot \mathbf{B}, \quad (1.51)$$

which describes the effect of magnetic field \mathbf{B} on spin. In the absence of an external magnetic field, the spin-orbit term reduces to

$$H_{SO} = \frac{\hbar}{4m^2c^2} \boldsymbol{\sigma} \cdot (\nabla V \times \mathbf{p}), \quad (1.52)$$

i.e., it involves a coupling between the particle's momentum and spin arising in a nonuniform electric potential.

In spherically symmetric potentials $V(\mathbf{r}) = V(r)$, for example, in the hydrogen atom, H_{SO} assumes an especially simple form. Using the fact that $\nabla V(\mathbf{r}) = \frac{dV(r)}{dr} \frac{\mathbf{r}}{r}$ we get

$$H_{SO} = \frac{\hbar}{4m^2c^2} \frac{1}{r} \frac{dV(r)}{dr} \boldsymbol{\sigma} \cdot (\mathbf{r} \times \mathbf{p}) = \frac{1}{2m^2c^2} \frac{1}{r} \frac{dV(r)}{dr} \mathbf{S} \cdot \mathbf{L}. \quad (1.53)$$

We introduced the operators of spin angular momentum $\mathbf{S} = \frac{\hbar}{2} \boldsymbol{\sigma}$ and orbital angular momentum $\mathbf{L} = \mathbf{r} \times \mathbf{p}$. The name *spin-orbit coupling* originates from the product $\mathbf{S} \cdot \mathbf{L}$ that appears in the above formula. However, the concept of spin-orbit coupling is not limited to spherically symmetrical systems and extends to other phenomena that stem from Eq. (1.52), as is the case in solid-state physics.

The spin-orbit coupling can be explained intuitively by considering that, according to the Lorentz transformation, a static electric field in a laboratory frame (at rest) transforms into a composition of an electric and a magnetic field in the frame of a moving electron. The spin angular momentum of the

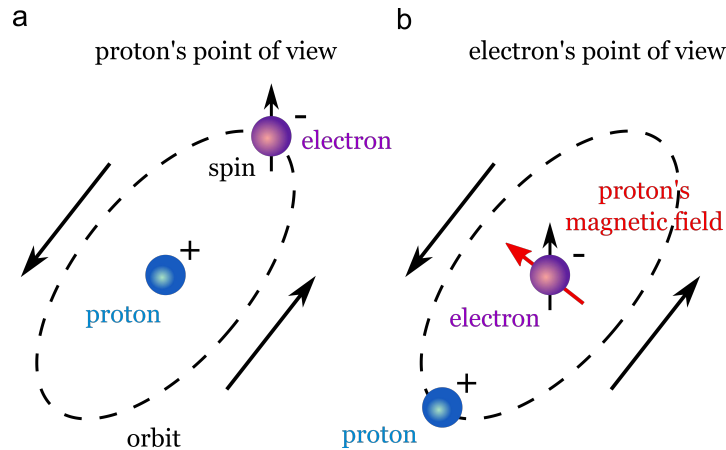


Figure 1.18: Semiclassical depiction of an electron in an atom. **a** In the frame of reference of a stationary proton, the electron moves through the electrostatic field of the protons. **b** In the frame of reference of the electron revolving around the proton, the apparent motion of the proton creates a magnetic field, which affects the electron's spin.

electron gives rise to a magnetic moment that couples with the magnetic field. The simplified scheme is shown in Fig. 1.18.

Rashba and Dresselhaus effects

In semiconductor systems, the center-of-mass motion of the electrons is characterized by Bloch wave functions, and the energy spectrum forms Bloch bands. The structure of the electronic bands is influenced by the spin-orbit interaction, which in condensed matter originates from the movement of electrons in the periodic crystal potential. It is shown schematically in Fig. 1.19.

The electron moves in a periodic potential coming from the positively charged ionic lattice and, in approximation, from the remaining electrons screening the ions. In the most simplified description, it can be said that from the point of view of the electron, the ions are in motion and generate a magnetic field that will couple with the spin of the electron. In fact, the picture of the interaction is much more complicated, and the coupling forms depend on the conditions, e.g. the crystal structure or the symmetry properties.

In 1955 Gene Dresselhaus published an article [29] that focused on III-V compounds with a zinc-blend structure that lacks a center of inversion. He

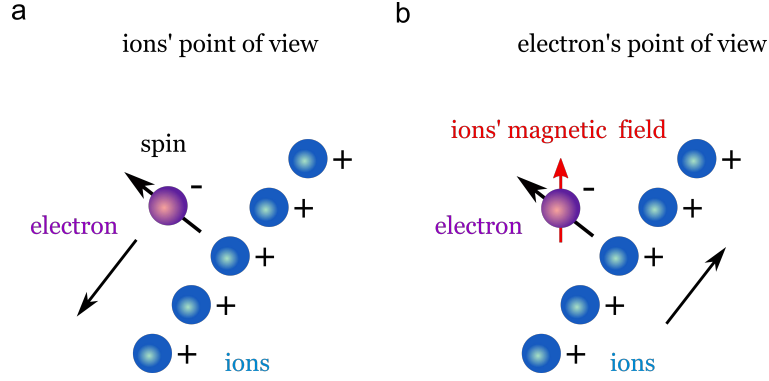


Figure 1.19: Semiclassical depiction of an electron in a group of ions. **a** Ions' point of view. **b** Electron's point of view.

noticed that in such structures the SOC close to the Γ point adopts the form:

$$\hat{H}_D = \gamma \left((k_y^2 - k_z^2) k_x \sigma_x + c.p. \right), \quad (1.54)$$

where *c.p.* notes circular permutations of indices, and k_i are components of the crystal momentum. In two-dimensional nanostructures (with z as the confinement direction), the above formula can be reduced to the linear Dresselhaus SOC:

$$\hat{H}_{D1} = \beta (\sigma_x k_x - \sigma_y k_y), \quad (1.55)$$

where β is the coupling constant, and we omitted terms of third or higher order in k .

Four years later Rashba and Sheka [30,31] proposed the description of SOC in wurtzite-type crystals. Furthermore, quantum wells with broken structural inversion symmetry along the growth direction and respecting symmetry C_{2v} were investigated by Vas'ko [32] and Bychkov and Rashba [33]. The SOC term in the Hamiltonians of these systems takes the form:

$$\hat{H}_R = \alpha (\sigma_x k_y - \sigma_y k_x) \quad (1.56)$$

where α is the Rashba parameter. Both the Dresselhaus and Rashba effects are the momentum-dependent spin splitting of doubly degenerate bands. The corotating (Fig. 1.20 **a** – Rashba SOC) and counterrotating (Fig. 1.20 **b** – Dresselhaus SOC) spin textures emerge from these Hamiltonian terms.

The microscopic origin of the Dresselhaus spin-orbit terms is the bulk

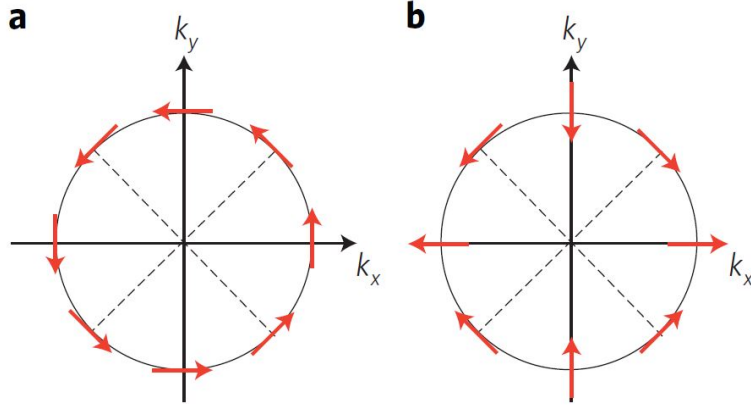


Figure 1.20: Spin texture at the Fermi surface. **a** Spin texture due to Rashba, **b** linear Dresselhaus SO coupling when strain is applied along [001]. Figure after [34]

inversion asymmetry (BIA), which is correlated with the lack of the inversion center in the bulk crystal structure. It can be affected by, e.g. charge carrier density or temperature. Rashba SOC can be referred to as structure inversion asymmetry (SIA) caused by additional symmetry reduction: confining potential, strain, or symmetry reduction introduced during growth process.

Altogether, the general form of the SOC occurring in 2D electron systems is given by the sum of the linear Dresselhaus and Rashba couplings:

$$\hat{H}_{SOC} = \frac{\hbar^2 k^2}{2m} + \beta (\sigma_x k_x - \sigma_y k_y) + \alpha (\sigma_x k_y - \sigma_y k_x). \quad (1.57)$$

The Rashba ($\alpha \neq 0, \beta = 0$) and Dresselhaus ($\alpha = 0, \beta \neq 0$) dispersions are presented schematically in Fig. 1.21 **a** and **b**, respectively.

A special case is the Rashba-Dresselhaus SOC under the conditions of the equal Rashba and Dresselhaus parameters ($\alpha = \beta$). Then the Hamiltonian reduces to:

$$\hat{H}_{RD} = \frac{\hbar^2 k^2}{2m} + 2\alpha \left(\frac{\sigma_x - \sigma_y}{\sqrt{2}} \right) \left(\frac{k_x + k_y}{\sqrt{2}} \right). \quad (1.58)$$

By an appropriate change of the coordinate system such that $k_+ = \frac{k_x + k_y}{\sqrt{2}}$ and $\sigma'_z = \frac{\sigma_x - \sigma_y}{\sqrt{2}}$ we arrive at the simplified expression

$$\hat{H}_{RD} = \frac{\hbar^2 k^2}{2m} + 2\alpha k_+ \sigma'_z. \quad (1.59)$$

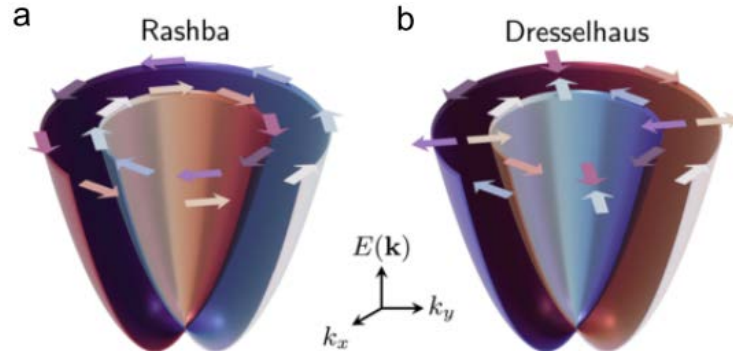


Figure 1.21: **a** Rashba and **b** Dresselhaus dispersion relation with the spin texture represented by the arrows on top. Image after [35]

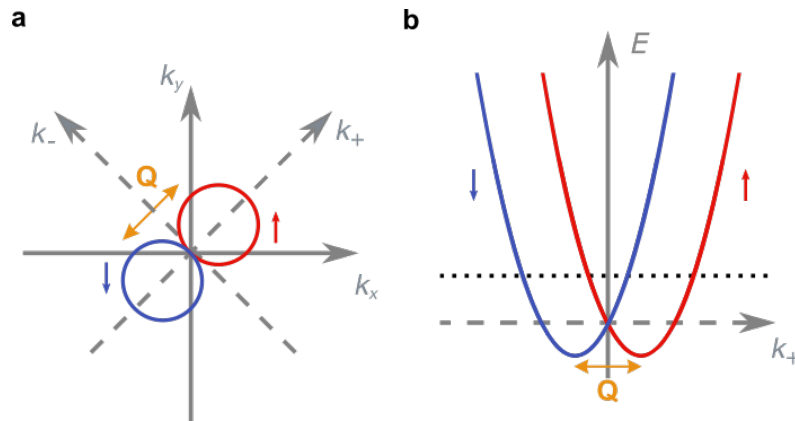


Figure 1.22: Scheme of persistent spin helix in reciprocal space. **a** Constant energy cross-section (black dotted line in **b**) in reciprocal space. Two circles shifted by the wave vector \mathbf{Q} . **b** Parabolic dispersion along k_+ direction.

The dispersion relation calculated for the Hamiltonian H_{RD} is shown in Figure 1.22. It features two oppositely spin-polarized paraboloids separated in reciprocal space by a vector \mathbf{Q} .

Persistent spin helix state

In systems with Rashba and Dresselhaus SOC, when Rashba and Dresselhaus terms have equal strength (Eq. 1.58), the coherent precession of spins can be observed, depending only on the momentum in one direction. This is the so-called persistent spin helix that is protected by a unique $SU(2)$ symmetry, as introduced by Bernevig et al. [36].

First, we recall the basics of the standard SU(2) group of the electron's spin. The rotation matrices of electron spin

$$R_{\hat{\mathbf{n}}}(\theta) = e^{i\frac{\theta}{\hbar}(n_x S_x + n_y S_y + n_z S_z)}, \quad (1.60)$$

where θ is the angle and $\hat{\mathbf{n}} = (n_x, n_y, n_z)$ is the unit vector defining the axis, form the symmetry group SU(2). Importantly, the angular momentum operators S_x, S_y, S_z , which for spin-1/2 are described by Pauli matrices (with an additional factor $\hbar/2$, i.e., $S_i = (\hbar/2)\sigma_i$), are generators of the SU(2) group. Depending on how the physical system is constructed, the rotation of an electron's spin may or may not change its energy. For example, the rotation of the spin of a free electron (in a vacuum) does not change the energy of the electron. In the theoretical description, this means that the Hamiltonian of the system

$$\hat{H} = \sum_{\mathbf{k}} \sum_{\sigma \in \{\uparrow, \downarrow\}} \sum_{\sigma' \in \{\uparrow, \downarrow\}} \frac{\hbar^2 \mathbf{k}^2}{2m} \delta_{\sigma\sigma'} |\sigma, \mathbf{k}\rangle \langle \sigma', \mathbf{k}| \quad (1.61)$$

commutes with spin rotation matrices from the SU(2) symmetry group, and, equivalently, with the generators

$$\hat{\sigma}_i = \sum_{\mathbf{k}} \sum_{\sigma \in \{\uparrow, \downarrow\}} \sum_{\sigma' \in \{\uparrow, \downarrow\}} [\sigma_i]_{\sigma\sigma'} |\sigma, \mathbf{k}\rangle \langle \sigma', \mathbf{k}|, \quad \text{where } i \in \{x, y, z\}, \quad (1.62)$$

where we denoted the elements of the Pauli matrices as $[\sigma_i]_{\sigma\sigma'}$, such that for every Pauli matrix σ_i

$$\sigma_i = \begin{pmatrix} [\sigma_i]_{\uparrow\uparrow} & [\sigma_i]_{\uparrow\downarrow} \\ [\sigma_i]_{\downarrow\uparrow} & [\sigma_i]_{\downarrow\downarrow} \end{pmatrix}. \quad (1.63)$$

Explicitly the generators are

$$\hat{\sigma}_x = \sum_{\mathbf{k}} (|\uparrow, \mathbf{k}\rangle \langle \downarrow, \mathbf{k}| + |\downarrow, \mathbf{k}\rangle \langle \uparrow, \mathbf{k}|), \quad (1.64)$$

$$\hat{\sigma}_y = \sum_{\mathbf{k}} (-i|\uparrow, \mathbf{k}\rangle \langle \downarrow, \mathbf{k}| + i|\downarrow, \mathbf{k}\rangle \langle \uparrow, \mathbf{k}|), \quad (1.65)$$

$$\hat{\sigma}_z = \sum_{\mathbf{k}} (|\uparrow, \mathbf{k}\rangle \langle \uparrow, \mathbf{k}| - |\downarrow, \mathbf{k}\rangle \langle \downarrow, \mathbf{k}|). \quad (1.66)$$

In the above equations, we have explicitly written the basis states in bracket notation, where the state vector $|\sigma, \mathbf{k}\rangle$ denotes a plane wave with wavevector \mathbf{k} and spin state $\sigma = \uparrow$ or $\sigma = \downarrow$ with respect to the z axis. We note that the

spin rotation matrices act only on the internal degree of freedom (spin), while conserving the momentum \mathbf{k} .

In short, the commutation rules are

$$[\hat{H}, \hat{\sigma}_i] = 0. \quad (1.67)$$

As their consequence, in the system described by \hat{H} , the electron's initial spin state remains unchanged and its spin angular momentum is conserved.

Conversely, in systems with a strong spin-orbit interaction, rotating the electron spin can change the energy of the system because the spin is coupled to the momentum of the electron. Generally in systems with SO interaction, there is no SU(2) rotational symmetry – that is, rotation matrices from the SU(2) group do not commute with the spin-orbit Hamiltonian. Taking the Rashba-Dresselhaus Hamiltonian (1.59) (omitting the prime symbols)

$$\hat{H}_{RD} = \sum_{\mathbf{k}} \sum_{\sigma \in \{\uparrow, \downarrow\}} \sum_{\sigma' \in \{\uparrow, \downarrow\}} \left[\frac{\hbar^2 \mathbf{k}^2}{2m} \delta_{\sigma\sigma'} + 2\alpha k_y [\sigma_z]_{\sigma\sigma'} \right] |\sigma, \mathbf{k}\rangle \langle \sigma', \mathbf{k}|, \quad (1.68)$$

we find that

$$[\hat{H}_{RD}, \hat{\sigma}_z] = 0, \quad \text{but} \quad [\hat{H}_{RD}, \hat{\sigma}_x] \neq 0, \quad [\hat{H}_{RD}, \hat{\sigma}_y] \neq 0. \quad (1.69)$$

The result shows that \hat{H}_{RD} has a U(1) spin rotation symmetry around the z axis, but not a SU(2) spin rotation symmetry around an arbitrary axis. In the Rashba-Dresselhaus system, the electron's spin angular momentum is conserved only in the z -axis component.

Bernevig et al. [36] discovered a different kind of SU(2) symmetry of the Rashba-Dresselhaus Hamiltonian. Namely, the interpretation of transformations described with the group SU(2) matrices is not spin rotations, but rotations with an additional shift in momentum space (see Fig. 1.22).

The group generators are

$$\hat{s}_z = \sum_{\mathbf{k}} \sum_{\sigma \in \{\uparrow, \downarrow\}} \sum_{\sigma' \in \{\uparrow, \downarrow\}} [\sigma_z]_{\sigma\sigma'} |\sigma, \mathbf{k}\rangle \langle \sigma', \mathbf{k}|, \quad (1.70)$$

which is equivalent to $\hat{\sigma}_z$, and

$$\hat{s}_x = \hat{s}_+ + \hat{s}_-, \quad \hat{s}_y = -i(\hat{s}_+ - \hat{s}_-), \quad (1.71)$$

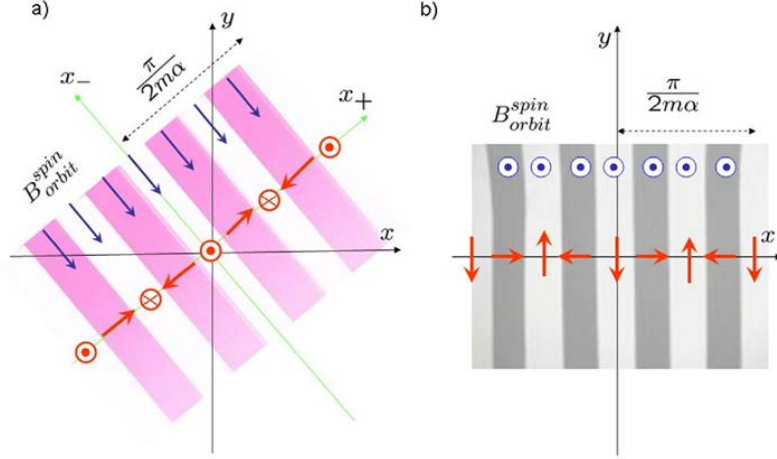


Figure 1.23: Scheme of persistent spin helix formation. Figure after [36].

where

$$\hat{s}_+ = \sum_{\mathbf{k}} \sum_{\sigma \in \{\uparrow, \downarrow\}} \sum_{\sigma' \in \{\uparrow, \downarrow\}} [\sigma_+]_{\sigma\sigma'} |\sigma, \mathbf{k} + \mathbf{Q}\rangle \langle \sigma', \mathbf{k}|, \quad (1.72)$$

$$\hat{s}_- = \sum_{\mathbf{k}} \sum_{\sigma \in \{\uparrow, \downarrow\}} \sum_{\sigma' \in \{\uparrow, \downarrow\}} [\sigma_-]_{\sigma\sigma'} |\sigma, \mathbf{k}\rangle \langle \sigma', \mathbf{k} + \mathbf{Q}|, \quad (1.73)$$

$$\sigma_{\pm} = \frac{\sigma_x \pm i\sigma_y}{2}, \quad (1.74)$$

and

$$\mathbf{Q} = \frac{4m\alpha}{\hbar^2} \mathbf{e}_y \quad (1.75)$$

is the reciprocal space vector that denotes the separation between the spin-split paraboloids shown in Fig. 1.22 **b**. Note that the operators \hat{s}_+ and \hat{s}_- couple states with different crystal momenta.

Because $[\hat{H}_{RD}, \hat{s}_x] = [\hat{H}_{RD}, \hat{s}_y] = 0$, the expectation values of \hat{s}_x and \hat{s}_y are conserved quantities. However, these values do not denote the components of angular momentum, but rather the helicity of a spin density wave. This is evident in position representation, where the operators attain the form

$$\hat{s}_x = \sum_{\mathbf{r}} \sum_{\sigma \in \{\uparrow, \downarrow\}} \sum_{\sigma' \in \{\uparrow, \downarrow\}} [\cos(\mathbf{Q} \cdot \mathbf{r})\sigma_x - \sin(\mathbf{Q} \cdot \mathbf{r})\sigma_y]_{\sigma\sigma'} |\sigma, \mathbf{r}\rangle \langle \sigma', \mathbf{r}|, \quad (1.76)$$

$$\hat{s}_y = \sum_{\mathbf{r}} \sum_{\sigma \in \{\uparrow, \downarrow\}} \sum_{\sigma' \in \{\uparrow, \downarrow\}} [\sin(\mathbf{Q} \cdot \mathbf{r})\sigma_x + \cos(\mathbf{Q} \cdot \mathbf{r})\sigma_y]_{\sigma\sigma'} |\sigma, \mathbf{r}\rangle \langle \sigma', \mathbf{r}|, \quad (1.77)$$

obtained by substituting $|\sigma, \mathbf{k}\rangle = 1/\sqrt{V} \sum_{\mathbf{r}} e^{i\mathbf{k}\cdot\mathbf{r}} |\sigma, \mathbf{r}\rangle$, where V is the system size. It follows immediately that, for instance, the state,

$$|\psi\rangle = \frac{1}{\sqrt{2V}} \sum_{\mathbf{r}} \left(e^{i(\frac{\mathbf{Q}}{2}\cdot\mathbf{r}+\Theta)} |\uparrow, \mathbf{r}\rangle + e^{-i(\frac{\mathbf{Q}}{2}\cdot\mathbf{r}+\Theta)} |\downarrow, \mathbf{r}\rangle \right), \quad (1.78)$$

will satisfy $\langle \hat{s}_x \rangle = 1$ and $\langle \hat{s}_y \rangle = \langle \hat{s}_z \rangle = 0$. By explicitly calculating the spin density, we find that it has a helical structure

$$\begin{aligned} \langle \psi | \hat{\rho}_x(\mathbf{r}) | \psi \rangle &= (1/V) \cos(\mathbf{Q} \cdot \mathbf{r} + 2\Theta), \\ \langle \psi | \hat{\rho}_y(\mathbf{r}) | \psi \rangle &= -(1/V) \sin(\mathbf{Q} \cdot \mathbf{r} + 2\Theta), \\ \langle \psi | \hat{\rho}_z(\mathbf{r}) | \psi \rangle &= 0, \end{aligned} \quad (1.79)$$

where we introduced the spin density operators at point \mathbf{r}

$$\hat{\rho}_i(\mathbf{r}) = \sum_{\sigma \in \{\uparrow, \downarrow\}} \sum_{\sigma' \in \{\uparrow, \downarrow\}} [\sigma_i]_{\sigma\sigma'} |\sigma, \mathbf{r}\rangle \langle \sigma', \mathbf{r}| \quad (1.80)$$

(note no summation over \mathbf{r}).

Therefore, the new SU(2) symmetry leads to the stability of the specific spin polarization pattern called the persistent spin helix state (Figure 1.23). It is characterized by a real-space periodic texture of the spin of particles with the period $L = 2\pi\hbar/Q$. The spin becomes robust against spin-dependent scattering, and the spin lifetime increases. This phenomenon was first observed by Koralek et al. [37]. Performing spin-grating spectroscopy measurements of GaAs quantum wells, they showed an enhancement of the spin coherence time by two orders of magnitude higher than in previous works. Then the direct mapping of the persistent spin helix by Walser et al. [38] in the Kerr rotation experiment was demonstrated. So far, this effect has been experimentally presented in many implementations and has been subject to several reviews [39–41].

1.5.2. Spin-orbit interaction of light

In 1992, Liberman and Zeldovich introduced the concept of spin-orbit interaction of light in the context of the behavior of polarized photons propagating in inhomogeneous media and related them to the geometric Berry phases resulting from the continuous change of the direction of the photon wave vector during propagation [42]. The term is now commonly used to ex-

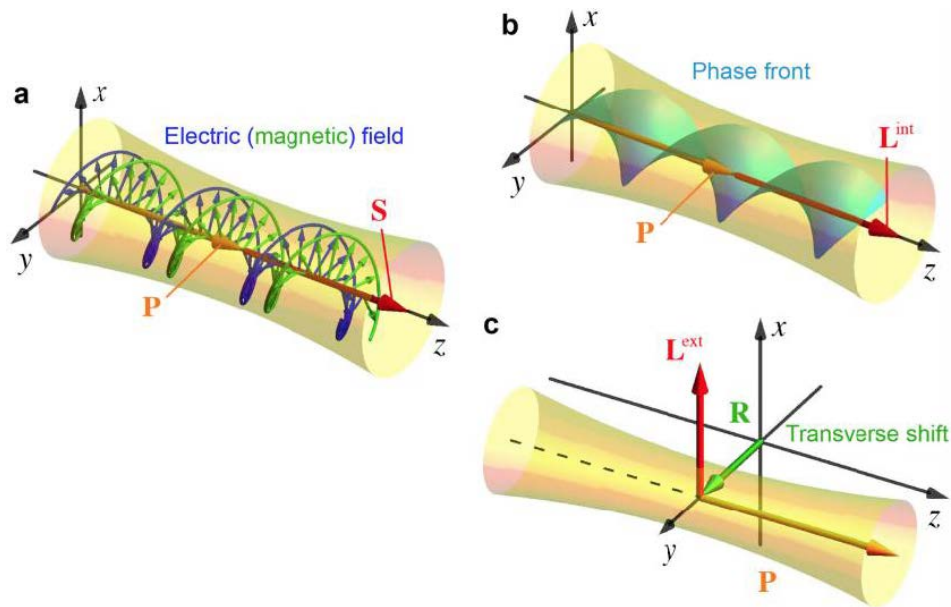


Figure 1.24: Three types of angular momentum of light. **a** Spin angular momentum (SAM) for a right-hand circularly polarized beam with $\sigma = 1$. **b** Intrinsic orbital angular momentum in a vortex beam with $l = 2$. **c** Extrinsic orbital angular momentum. Image taken from [43]

plain various newly investigated optical effects, following the work of Bliokh et al. [43]. We can distinguish three types of angular momentum (AM) of light: spin angular momentum (SAM) and intrinsic and extrinsic orbital angular momentum (OAM). The SAM is determined by the ellipticity of the polarization, the degree of circular polarization that takes a value between -1 for left-hand and $+1$ for right-hand circular polarization (see Figure 1.24a). It is aligned with the momentum of the beam, i.e., the propagation direction. The intrinsic OAM is associated with a helical or twisted wavefront (see Figure 1.24b), and the extrinsic OAM is associated with the optical beam trajectory, and is obtained by a standard cross product of the position and momentum vectors (see Figure 1.24c).

The spin-orbit interaction of light is currently intensively studied due to its fundamental importance and practical implementations. It enables the control and manipulation of optical wave propagation, which gives rise to new designs of optical or optoelectronic systems and devices. [42–45].

In the present work the discussion of the spin-orbit interaction of light

is confined to the SAM case, as the effects observed in the liquid crystal microcavity concern primarily the polarization of light.

Optical spin Hall effect

Spin-orbit coupling in electronic systems leads to the so-called *spin Hall effect* i.e. separation of electrons of different spin during their flow in an electric field, the effect predicted by D'Yakonov and Perel in 1971 [46]. By analogy, the separation of particles with a light component of different polarizations in microcavities is called the *optical spin Hall effect* (OSHE). The effect, originally predicted [47] and observed [48] in semiconductor microcavities in a strong coupling regime, leads to pseudospin⁸ separation of exciton polaritons occurring in both real and reciprocal space caused by longitudinal-transverse splitting, Δ_{LT} (TE–TM splitting), acting as an effective magnetic field Ω according to the equations:

$$\begin{aligned}
 H_{SO} &= \frac{\hbar}{2} \hat{\sigma} \cdot \Omega \\
 \mathbf{H}_{\text{eff}} &= \frac{\hbar}{\mu_B g} \Omega_{\mathbf{k}} \\
 \Omega_x &= \frac{\Delta_{LT}}{\hbar k^2} (k_x^2 - k_y^2) \\
 \Omega_y &= \frac{\Delta_{LT}}{\hbar k^2} k_x k_y \\
 \Omega_z &= 0
 \end{aligned} \tag{1.81}$$

The model describes the dynamics of the polarization of polaritons in microcavities, where the pseudospin $\hat{\sigma}$ is a three-dimensional vector whose components in the plane of the cavity describe both orientations of linear polarization in a given polariton state, while its component normal to the plane of the cavity is proportional to the circular polarization of the polariton state, that is, to the total average spin of the polaritons in a given quantum state (see Figure 1.25).

The polarization of photons that leave the cavity, measured in the experiment [48], directly translates into the pseudospin separation of the polaritons inside the cavity. As shown in the first experimental realization for linearly polarized excitation, the scattered light becomes circularly polarized (Figure

⁸ The difference between *spins* and *pseudospins* is related to their transformation laws. We will refer to this difference when we discuss symmetry operations in Chapter 4.

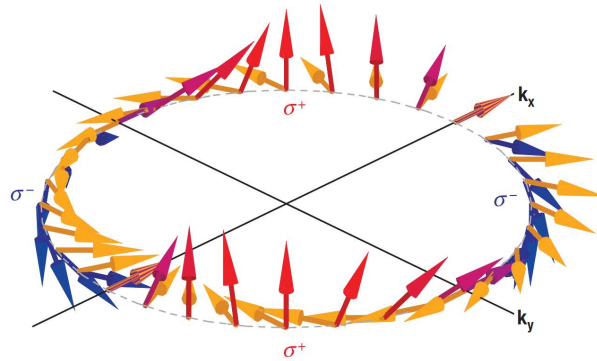


Figure 1.25: Polariton pseudospin vectors in effective magnetic field. The effective magnetic field (yellow arrows) lies in the plane of the cavity, and its direction depends on the wavevector. Figure after [48]

1.26), which translates into nonzero average spin. The reciprocal (momentum) space characteristic of OSHE is the quadrupole pattern of the degree of circular polarization, the orientation of which relative to the center of the pattern depends on the excitation polarization. It is shown in Figure 1.26 **a** for a transverse magnetic (x) polarized pump and **b** for a transverse electric (y) polarized pump. In each quadrant, the sign of the circular polarization switches. The polaritons are distributed around an elastic circle, and different spin currents develop in different quadrants of the circle as a result of the TE-TM polarization energy splitting, as described above.

OSHE, which has been studied extensively in exciton-polariton systems, has later been shown to exist in a purely photonic cavity [8] (see Figure 1.27). As in the case of polaritons, the effective magnetic field is caused by TE-TM splitting, which is characteristic of the structure of optical microcavities. In fact, the purely photonic effect is the underlying cause of OSHE in polaritonic systems.

In the literature, a similar term – *spin Hall effect of light* – is also used referring to the drift of a wave packet of light in a medium with a refractive index gradient [49, 50]. A summary of the spin Hall effect of light is presented in detail in the review by Ling et al. [51]. OSHE is a different but related effect since it also involves an inhomogeneity of the refractive index manifested through the TE–TM splitting.

Many other effects arising from the TE-TM splitting, where the quasi-particles exhibit spin textures or anisotropic spin current, have been dis-

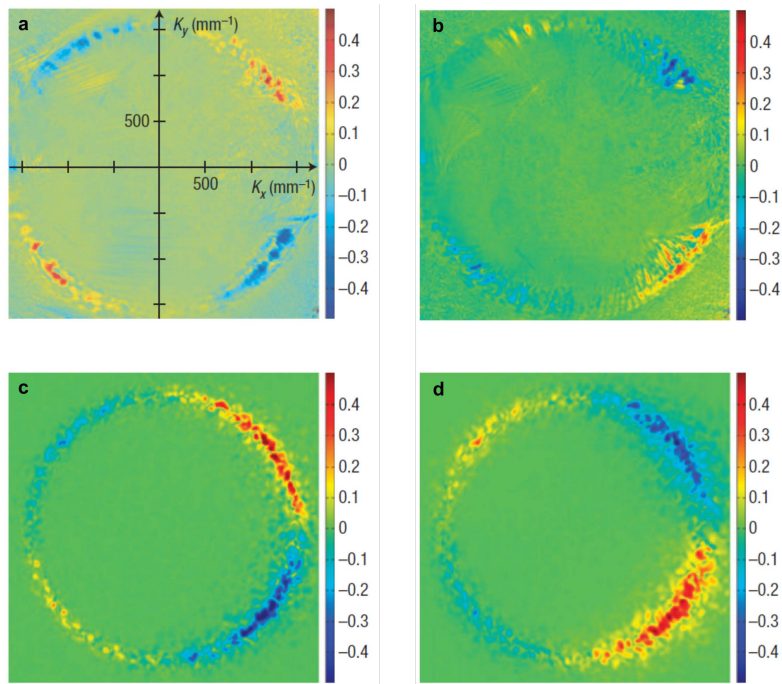


Figure 1.26: First experimental realization of the optical spin Hall effect in exciton-polaritons in semiconductor GaAs/AlGaAs microcavity. **a** Degree of circular polarization (DOCP) obtained in polaritons emission for a transverse magnetic (x) polarized pump. **b** The same as in **a**, but for a transverse electric (y) with the corresponding numerical calculations, respectively **c** and **d**. Figure after [48].

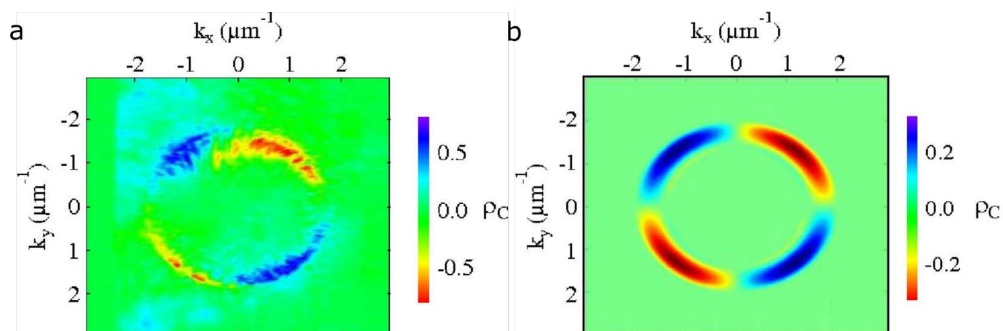


Figure 1.27: Optical analogue of the spin Hall effect. **a** Quadrupole polarization pattern of transmitted light for a transverse magnetic (x) polarized pump. **b** Simulations for the measurement conditions. Degree of circular polarization obtained with the transfer matrix method. Image after [8].

cussed in the literature [48, 52], such as: spin whirls [53], spin currents [54], skyrmions [54, 55], half skyrmions [55], hedgehog vortices [55, 56], hyperspin vortices [56], pairs of halfvortices [57] etc.

Chapter 2

Experimental methods and sample preparation

This chapter presents the experimental methods used in this work. Experimental setups are discussed in which measurements of reflectivity, transmission, and luminescence spectra were made. Both two-dimensional angularly resolved measurements and full tomography results are presented, along with measurements in real space. The processes of preparing individual parts as well as the entire target structures of the LC cavities are described.

2.1. Experimental setup

Measurements were performed on several setups that differ in light sources, lasers, and objectives with various numerical apertures, where their schemes are typical and are presented below. The main types of measurement performed in this work are the measurement of transmission, reflectivity, and photoluminescence spectra. All measurements were made at room temperature on the Andor Shamrock SR-750 spectrometer.

Optical spin Hall effect measurements were conducted in the transmission setup in Fourier space. The setup scheme is presented in Fig. 2.1. For these measurements, two microscope $50\times$ objectives with numerical aperture $NA = 0.55$ were used. The wavelength of the incident laser light was set to 775 nm (1.599 eV). Using different orientation of linear polarization of incident light, it was possible to distinguish the polarization of the cavity modes. The polarization analyzer contains: a quarter-wave plate, a half-wave plate, and a linear polarizer, and allows one to resolve all six main polarizations (tab. 1.1). To tune the liquid crystal in the cavity, an external voltage of up to 100 V (peak-to-peak) of a square waveform of frequency 30 kHz generated by the Rigol DG 2041A function generator was used.

For the excitation and characterization of the samples containing the emitter, mainly the 532 nm Nd:YAG continuous-wave laser was used. On the other

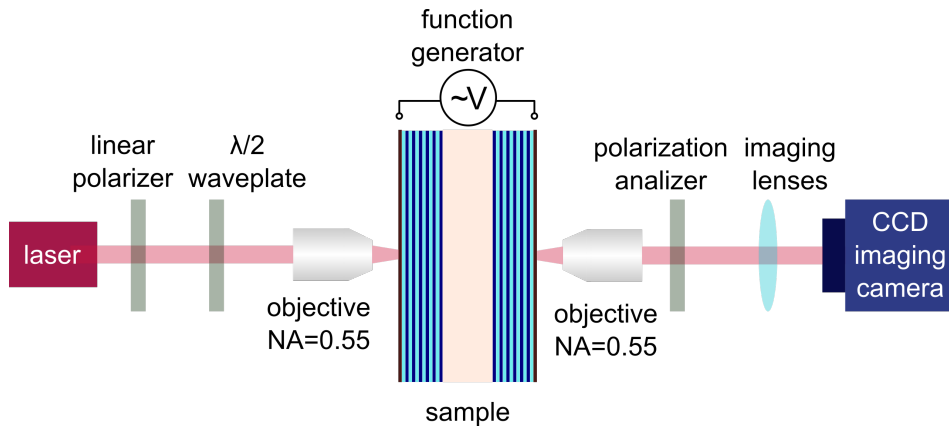


Figure 2.1: Scheme of a transmission measurements setup. In such a scheme, the optical spin Hall effect and persistent spin helix measurements were performed.

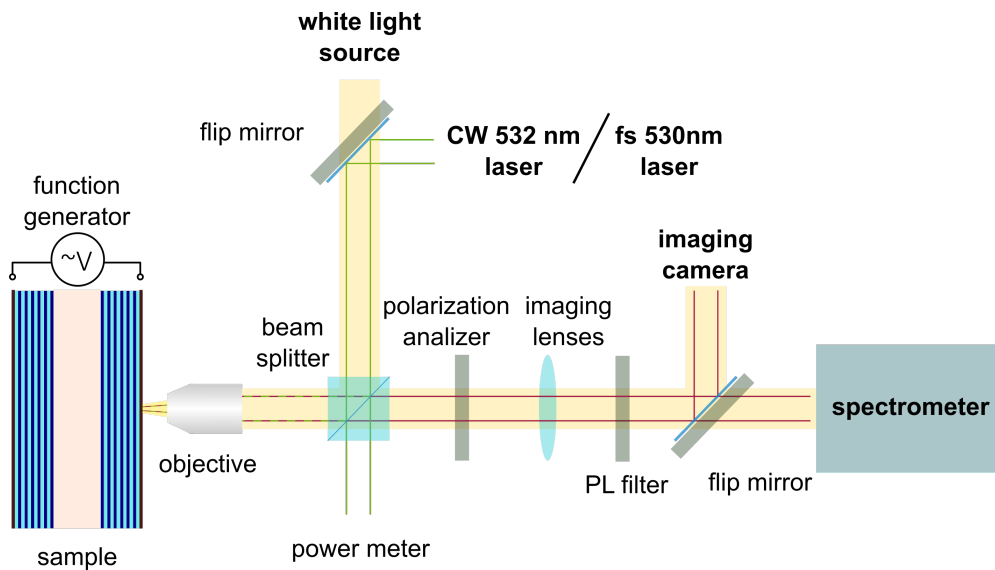


Figure 2.2: Scheme of a photoluminescence and reflectivity measurements setup. The green lines represent the green laser, and the red lines are the emission from the sample. Between the beam splitter and the objective, the dashed green and red lines represent the laser and the emission that occur together on this part of the optical path.

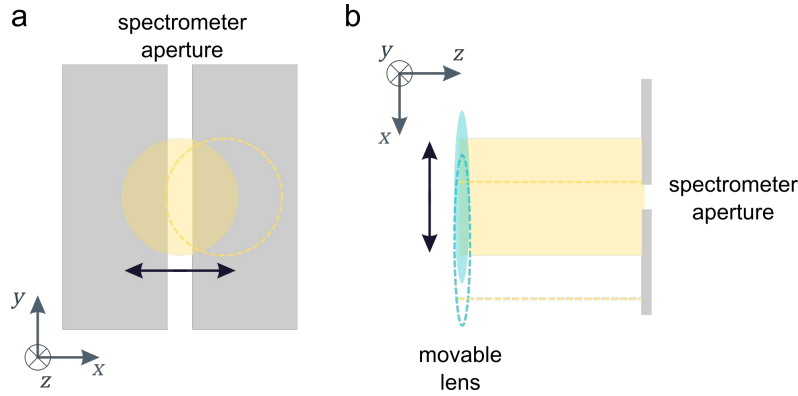


Figure 2.3: Scheme of tomography measurements. (a) Front view of the spectrometer. (b) Spectrometer side view.

hand, when measuring the lasing effects, a pulsed laser tuned to the wavelength of 530 nm was used. The pulse duration was 100 fs and the repetition rate was 1.5 kHz. All measurements with pulse excitation were performed in the Prof. Piotr Fita laboratory at the Faculty of Physics at the University of Warsaw.

A modification of the standard setup for measurements in the reciprocal space was to place the movable lens in front of the spectrometer. This allowed for the scanning of successive wavevectors in the k_x direction by moving the lens in the x direction, while the resolution in the k_y direction is initially set in the standard setup for angularly resolved measurements (see Fig. 2.2). The tomography measurement scheme is shown in Figure 2.3 in two views, in the spectrometer slit plane and perpendicular.

The figure 2.4 shows the cavity mode dispersion, which in the simplest case is a paraboloid (Fig. 2.4 a). A cross-section along k_x (much like along k_y) gives a parabola (Fig. 2.4 b), while the constant energy cross-section will have a circular shape (Fig. 2.4 c).

During the measurements, objectives with different numerical apertures (NA) were used. In Figure 2.5 we show how the working distance and the range of the observed angles change with the change of the NA value. As we can see, the observation angle increases with increasing NA , while the working distance decreases. Below, on the example of converting a given pixel in the camera to an angle, we will show what the relation is between the observation angle and NA .

Let x denote a position on the CCD camera relative to the optical axis

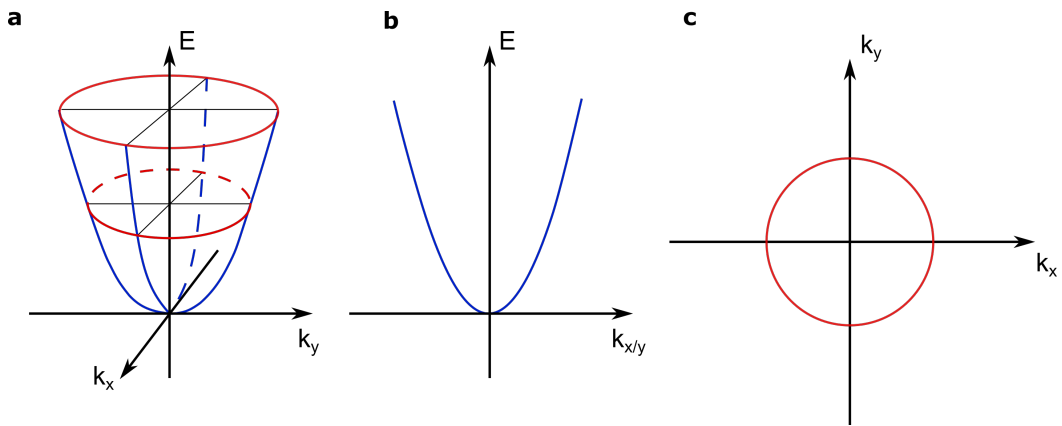


Figure 2.4: Schematic representation of the standard cavity photon dispersion. **a** Three-dimensional paraboloid. **b** The dispersion for the in-plane wave vectors takes a parabolic form. **c** The constant energy cross-section (in the absence of anisotropy of the effective masses in the x and y directions) takes the form of a circle.

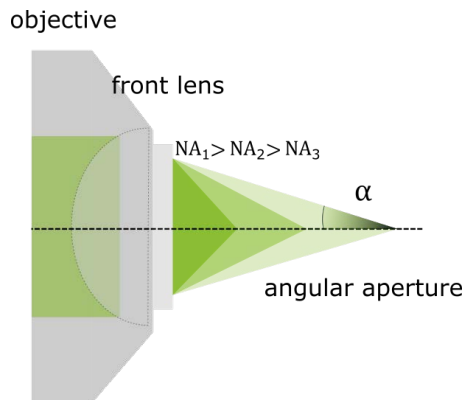


Figure 2.5: Scheme of changing the angular aperture with the change of the numerical aperture. α is one-half the angular aperture.

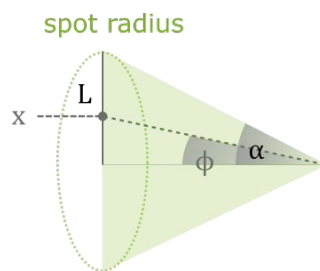


Figure 2.6: Converting pixels on the camera (x) to the corresponding detection angles (ϕ).

and L the radius of the light spot (Fig. 2.6). The numerical aperture is given by

$$\text{NA} = n \sin(\alpha) = \sin(\alpha), \quad (2.1)$$

where α is half the angular diameter of the light spot, and we have used the fact that in air $n \approx 1$. Hence,

$$\alpha = \arcsin(\text{NA}). \quad (2.2)$$

By simple trigonometry (see Fig. 2.6) we may write

$$\frac{x}{L} = \frac{\tan(\phi)}{\tan(\alpha)}, \quad (2.3)$$

from which it follows that

$$\phi = \arctan\left(\frac{x \tan(\arcsin(\text{NA}))}{L}\right) = \arctan\left(\frac{x}{L} \frac{\text{NA}}{\sqrt{1 - \text{NA}^2}}\right). \quad (2.4)$$

If we express L in terms of pixels of the CCD camera, the above formula allows for a direct conversion between the pixel index x (potentially including a constant shift depending on the position of the CCD) and the observation angle ϕ .

2.1.1. Real and reciprocal space measurements

At this point, we will briefly focus on the two types of imaging that we used in our measurements. These are measurements in the so-called *real* and *reciprocal* (Fourier) space. The scheme of the real space measurements is presented in Figure 2.7. In this case, properly positioned lenses allow one to visualize the image of the tested sample on the camera in spatial coordinates. At the same time, we can choose the magnification at which we observe the image by choosing the right ratio of the focal lengths of the lenses and their positions.

Fourier-space imaging is a very important tool in spectroscopy. It gives an insight into an alternative set of information to that obtained in the real-space imaging. In a reciprocal space image, information is given in angular coordinates, unlike the case of real space image, where the resolution is given in spatial coordinates.

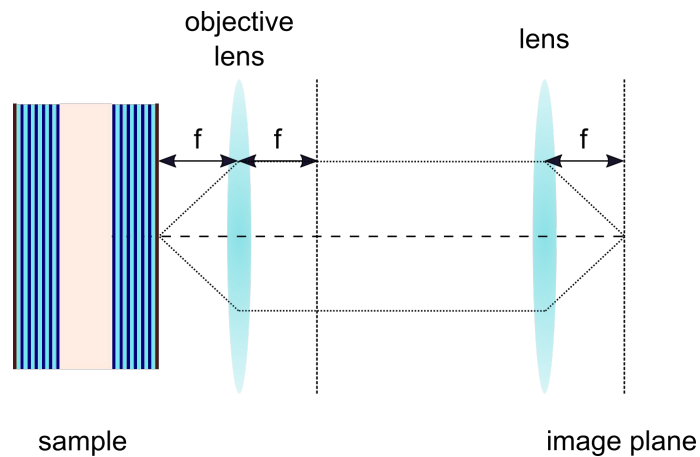


Figure 2.7: Scheme of the setup for measurements in a real space.

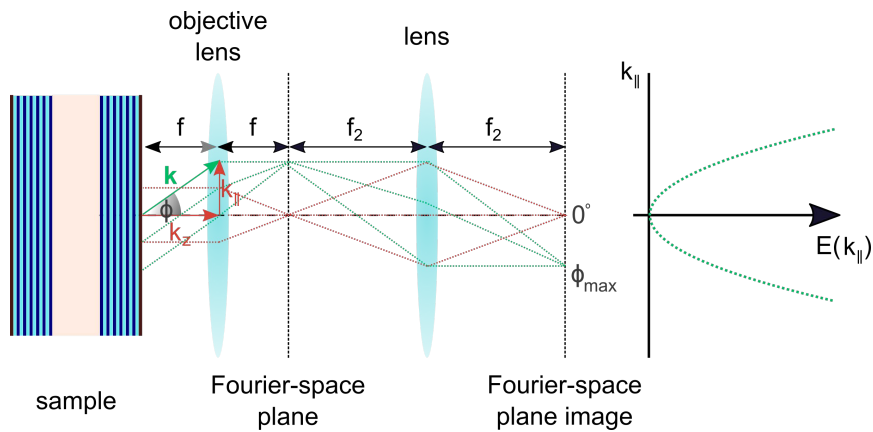


Figure 2.8: Scheme of the setup for measurements in a reciprocal space.

The light coming out from the sample can be divided into waves coming out at different angles (marked red and green in Figure 2.8). As light passes through the lens, the different components of the wave are separated. The Fourier-space plane is imaged at the focal distance f . Each wave coming out from a specific angle is finally imaged at a given point on the CCD matrix. The lens maps each direction to a single point on the camera and thus provides information on the angular distribution of the light emitted from the sample plane. Figure 2.8 shows the scheme with two lenses that was used in this work.

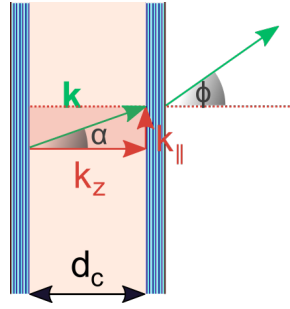


Figure 2.9: Wave vector \mathbf{k} (green arrow) of the photon in the cavity with the components k_z and k_{\parallel} (red arrows).

The k_{\parallel} component is connected to the angle of detection/excitation ϕ (see Fig. 2.9) and can be written as:

$$k_{\parallel} = |\mathbf{k}| \sin \phi = \frac{E_{ph}(k)}{\hbar c} \sin \phi, \quad (2.5)$$

According to the above dependence, we have easy experimental access to the dispersion of cavity photons in angularly resolved reflectivity, luminescence, or transmission measurements.

2.2. Design and preparation of the samples

This chapter contains information on the samples used in the research. The preparation of dielectric mirrors, the mechanical exfoliation of thin layers (including molybdenum diselenide), and the preparation of liquid crystal samples are described.

2.2.1. Dielectric mirrors

The substrates for the mirrors were made of quartz plates of thicknesses 4 mm and 1 mm. The standard size of the substrates was: 27.0×12.6 mm and depending on the experiment, it could be cut to a smaller size, e.g. with open cavities it was most often 6.35×5.40 mm.

At the first stage, transparent conductive indium tin oxide (ITO) electrodes were deposited on the substrate. Then, alternating layers SiO_2 and TiO_2 forming a distributed Bragg reflector (DBR) were applied to the ITO. The growth of the dielectric layers as well as ITO electrodes was carried out

using the electron–beam physical vapor deposition (EBPVD) method with the Telemark 264 electron gun and XIAD ion source at the Military University of Technology (MUT), Warsaw, Poland in the Prof. Wiktor Piecek group by Dr. Rafał Mazur. The mirrors were designed according to the target experiment for the specific wavelength of incident/emitted light.

2.2.2. Liquid crystals

In this thesis, samples with two different liquid crystal compounds are presented. The parameters of the liquid crystals have been summarized in Table 2.1. The dual-frequency nematic mixture [58] 1999C (DFNLC)¹ was custom designed and synthesized at the Military University of Technology in the group of Prof. Przemysław Kula. This mixture exhibits a wide temperature range of the existence of the nematic phase and relatively low birefringence (see Table 2.1). This compound was used to fabricate the sample for an optical spin Hall effect experiment.

The second nematogenic LC, used in optical Rashba-Dresselhaus and persistent spin helix experiments, was a highly birefringent nematic liquid crystal 2091 HBNLC designed and synthesized at the Military University of Technology in Prof. Przemysław Kula group [59, 60]. This compound allowed for a wide range of tunability of the effective refractive index of the cavity.

2.2.3. Emitters

Thin layers of dichalcogenides

There are many methods to prepare single layers of transition metal dichalcogenides (TMD). One of the most commonly used methods is mechanical exfoliation. It was proposed in 1963 by Frindt [61] for the production of thin layers of crystals WSe₂ and MoTe₂, and then, in 2004, Geim and Novoselov successfully adapted it to obtain atomically thin layers of graphite (graphene). It is a method that currently provides the best structures in terms of optical quality.

¹ DFNLCs are characterized by inversion of the sign of dielectric anisotropy at a certain frequency called the *cross-over frequency* f_c , as discussed in Subsection 1.4.2. Recall that $\Delta\varepsilon > 0$ for $f < f_c$ and $\Delta\varepsilon < 0$ for $f > f_c$. It is important from the point of view of display technology, as it allows to switch the director very fast. However, in the research presented in this work, this LC property is not crucial and was not used.

Table 2.1: **Selected materials data of the 1999C DFNLC and 2091 HBNLC** [58,60]. T_{cr} - crystallization temperature obtained by DSC method, T_{Iso} - isotropization temperature obtained DSC method, Δn - refractive index anisotropy, n_o - ordinary refractive index, $\Delta\epsilon$ - dielectric permittivity anisotropy, ϵ_{\perp} - component of the dielectric permittivity tensor perpendicular to the molecular director, ϵ_{\parallel} - component of the dielectric permittivity tensor parallel to the molecular director, f_c - cross-over frequency, $\Delta\epsilon_{low}$ - dielectric permittivity anisotropy at low ($f \ll f_c$) frequency of the external electric field, $\Delta\epsilon_{high}$ - dielectric permittivity anisotropy at high ($f \gg f_c$) frequency of the external electric field.

Liquid crystal	Parameter	Value
2091 HBNLC	T_{cr} (°C)	<- 10.0
	T_{Iso} (°C)	52.1
	Δn (633 nm) at 23 °C	0.43
	n_o	1.539
	$\Delta\epsilon$ (1 kHz) at 23 °C	14.50
	ϵ_{\perp} (1 kHz) at 23 °C	5.45
	ϵ_{\parallel} (1 kHz) at 23 °C	19.95
1999C DFNLC	T_{cr} (°C)	<- 20
	T_{Iso} (°C)	146.4
	n_o	1.504
	n_e	1.801
	$\Delta\epsilon_{low}$ (1 kHz) at 23 °C	3.19
	$\Delta\epsilon_{high}$ (1 MHz) at 23 °C	-2.91
	f_c (kHz) at 23 °C	8.35
	f_c (kHz) at 50 °C	79.4

The second method, which is very often used to obtain monolayers, is the chemical method, e.g. chemical vapor deposition (CVD). The flakes obtained by this method were used in this work. In the current stage of technology development, it still does not provide structures of such good optical quality as mechanical exfoliation, but it has many advantages. In particular, it allows one to obtain relatively large substrate surfaces uniformly covered with a monolayer material. This method makes it possible to stop the crystal growth process in the stage of single monolayers of material. It should be noted that work to obtain transition metal dichalcogen monolayers using the molecular beam epitaxy (MBE) method is currently underway [62, 63].

The incorporation of TMD flakes into microcavities is discussed in Chapter 8.

Fluorescent proteins

The fluorescent protein mCherry was obtained at the Center of New Technologies of the University of Warsaw in the group of Prof. Jacek Jemielity and Prof. Joanna Kowalska by Mr. Tomasz Śpiewała. The bacteria of BL21(DE3)-RIL strains were modified with the plasmid pET28 mCherry and then grown on agarose medium supplemented with kanamycin. The obtained colonies were centrifuged and the bacterial cells were lysed. The protein was purified by affinity chromatography, confirming the purity by electrophoresis. The obtained product was concentrated using centrifugal filters, aliquoted, frozen in liquid nitrogen, and stored at -80°C .

The concentrated solution of proteins was pipetted onto the bottom mirror and dried to form homogeneous solid-state protein films (Fig. 2.10 **a,b**). Then it was capped by an identical top mirror (Fig. 2.10 **c**) – *open-cavity* structure. Mechanical squeezing allows for the formation of a cavity thickness gradient. Unlike other samples used in this work, the cavity with the protein does not include a liquid crystal component.

2.2.4. Liquid crystal cavities

In general the liquid crystal cavity (transducer) consists of two $\text{SiO}_2/\text{TiO}_2$ DBRs with sputtered indium tin oxide (ITO) electrodes. The DBRs are spin coated with polyimide material (SE-130) (rubbing layer) and the entire cavity is filled with nematic LC as shown in Figure 2.11 **a**. Mirrors are glued together with spacers (glass spheres or rods mixed with glue) to the designed thickness. After gluing, an air-filled cavity structure is obtained. Then, the

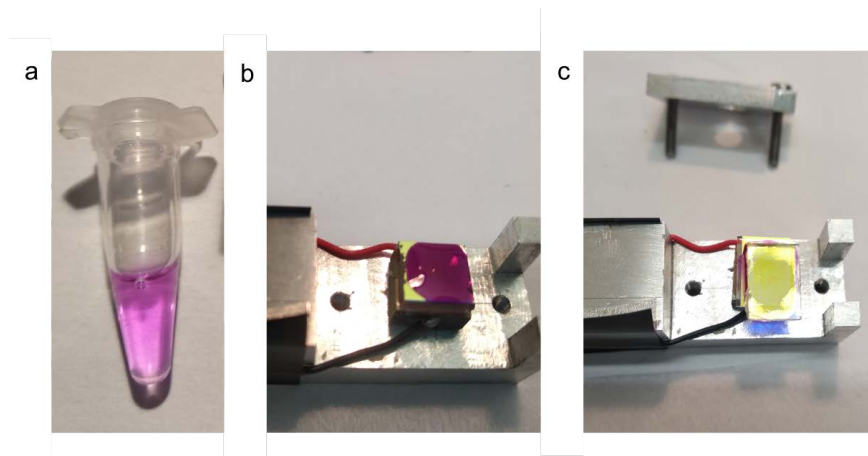


Figure 2.10: mCherry sample preparation. **a** Concentrated solution of mCherry protein. **b** mCherry solution pipetted onto the bottom mirror **c** and capped with the top mirror.

prepared structure is filled with a suitable liquid crystal. The mirrors are not glued along the entire edge; there are small spaces near which liquid crystal material is instilled, filling the space between the mirrors by capillary forces. The process was carried out at a temperature above T_{Iso} (isotropization temperature) and after filling, the cavity was cooled down. For thin cavities, this process was performed in a vacuum chamber. The preparation of the liquid crystal cavities was carried out by Dr. Przemysław Morawiak from the Military University of Technology.

The polymer layer induces a uniform HG or HT orientation of the molecular director in a liquid crystal slab in the cavity (Chapter 1.4.3). The ITO electrodes allow the orientation of the molecular director to be controlled by the applied voltage. After applying a voltage greater than the threshold voltage, the director of the molecules tilts in a specified direction (Figure 2.11 **b**).

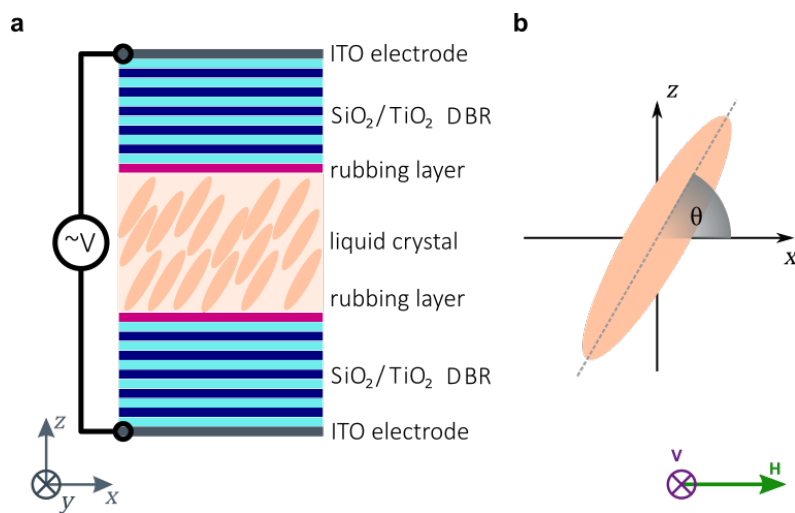


Figure 2.11: The scheme of the **a** liquid crystal microcavity and **b** tilting of the optical indicatrix of the LC medium in the cavity. θ is the molecules director tilt angle. The green H and purple V show how the horizontal and vertical polarizations are oriented with respect to the sample.

Chapter 3

Tunable liquid crystal cavities

In this chapter, we present results concerning the aspect of tunability of the liquid crystal cavities, including:

- changing the energy of the photonic mode with applied voltage
- change of the Q factor with applied voltage
- effect of the frequency of applied voltage on the energy and width of the cavity mode
- polarization of the modes: possibility of tuning the horizontally polarized mode
- observed regimes: crossing of the modes of different parities

For the results presented in this chapter, the measured samples contained either DFNLC or HBNLC. The presented data sets are used to show typical operation of the tunable microcavity. For the specific experiments presented in the subsequent chapters, slightly different systems were used, which are described therein.

3.1. Liquid crystal microcavities – tuning ranges

The energy of the photon mode within the photonic stopband depends directly on the thickness of the cavity (d_c) and the refractive index of the cavity material (n). They are described by the so-called optical cavity thickness, which is expressed by the formula 1.25:

$$d_c n = N \frac{\lambda_0}{2}$$

and is an integer multiple (N) of half the central wavelength (λ_0). If one wishes to vary the central wavelength (λ_0) it is relatively easy to do so by controlling the thickness of the cavity d_c . The most common solution to achieve this in a single sample is to grow wedge-shaped structures (with a certain thickness gradient) or to place one of the mirrors on a piezoelectric element, which can move the entire mirror perpendicular to the cavity plane.

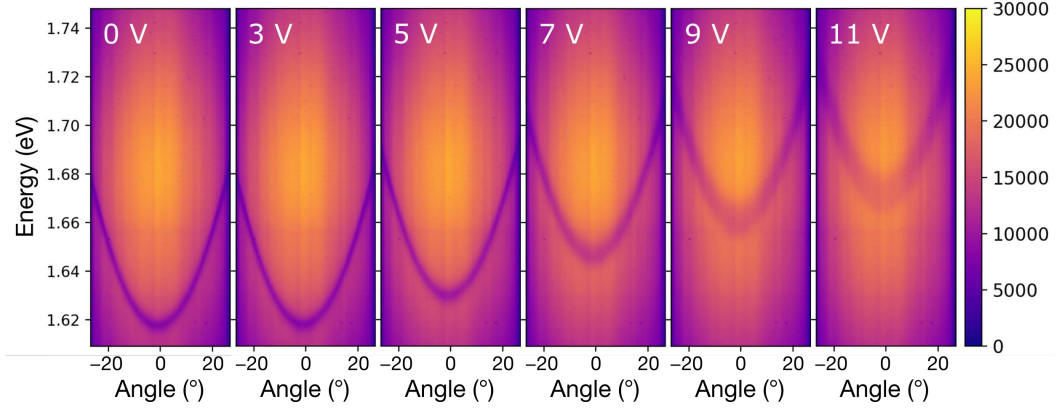


Figure 3.1: Angle-resolved reflectivity maps for the horizontal polarization for different square-wave voltages applied to the cavity filled with 2091 HBNLC.

Another method, which is proposed in this work, is to use the properties of liquid crystals that are sensitive to an external electric field (generated by voltage U), which allows one to change the refractive index of the cavity by turning the molecular director by the angle θ (Fig. 2.11 b). Because of the birefringence of the liquid crystal, the effective refractive index of the cavity depends on the polarization of light. For modes of light polarized linearly along the x -axis (horizontal polarization, H)

$$n_{\text{eff}}(U) = \frac{(n_o n_e)}{\sqrt{n_o^2 \cos^2(\Theta(U)) + n_e^2 \sin^2(\Theta(U))}}, \quad (3.1)$$

while for modes polarized along the y -axis (vertical polarization, V), the effective refractive index is constant and is equal to n_o .

Thus, by applying a square wave alternating voltage, we can tune the energy of the horizontally polarized mode. To characterize the tuning ranges of the cavities, measurements of angularly resolved spectra were made for different voltages applied to the transducer electrodes (Figure 3.1). Applying an external electric field, we observe the shift of the cavity mode in energy. Figure 3.1 shows the measured reflectivity maps of the liquid crystal cavity, depicting the photonic mode tuning range for peak-to-peak voltages ranging from 0.0 to 12.0 V of the square waveform of frequency 1 kHz.

Since the applied voltage can be tuned continuously, the device has the functionality of tuning the photonic mode in a continuous way in a wide range of energies (see Fig. 3.2 **a,b**). Fig. 3.2 **a** shows the cross-sections of

the reflectivity spectra at $k = 0$, and Fig. 3.2 **b** shows the mode energies obtained from the fitting of the Lorentzian line shape to the experimental spectra. Up to a voltage of approx. 3 V, we do not see any line shifting, which determines the threshold voltage. Above 3 V, we observe a shift of the photonic mode towards higher energies. The tunability range in this case is ~ 63.5 meV, for voltages up to 12 V. It can also be observed that apart from the change in the energy of the cavity mode, there is a change of its linewidth (as represented in Fig. 3.2 **c** by the full width at half-maximum, FWHM, of the spectral line). Without the applied voltage, the orientation of the liquid crystal molecules inside the transducer is well defined, which translates into a clearly defined arrangement of the molecular director. This directly translates to the width of the photonic mode, which in this case will mainly depend on the remaining parameters of the cavity (such as the number of pairs of layers in the dielectric mirrors). After a voltage is applied to the structure, we observe a widening of the photonic modes. The arrangement of liquid crystal molecules, kept in an alternating electric field, is no longer homogeneous and leads to a greater dispersion of the molecular director values. The higher the voltage, the greater the dispersion of these values, and thus the greater the widening of the observed cavity mode. This translates into a reduction in the Q factor, where $Q = (\text{mode energy})/(\text{FWHM})$, of the cavity from 378 with no voltage applied to 201 for a voltage of 7V (Fig. 3.2 **d**).

An important parameter that we need to optimize, which depends on the kind of liquid crystal filling the cavity, is the frequency of the alternating square-wave voltage. We will present this relation on the example of HBNLC shown above. Figure 3.3 shows the angle-resolved reflectivity maps for the horizontally polarized mode for 6.0 volts applied to the structure as a function of the frequency of the applied alternating voltage, changing from 100 Hz to 10 kHz.

Figure 3.4 shows cross-sections for angle 0° and parameters obtained from fitting Lorentzian line shape functions to these cross-sections: energy shift, change of the linewidth, and corresponding Q factor. It is clearly visible that, at constant voltage, we can change both the energy position and the shape of the spectrum (cross-sections) depending on the selected frequency. For the low frequency (100 Hz), we observe a significant shift in energy compared to the highest frequency of 10 kHz. However, by looking at the corresponding cross-section at $k = 0$, it can also be seen that the cavity mode has two main components (with two different energies). This indicates that the selected

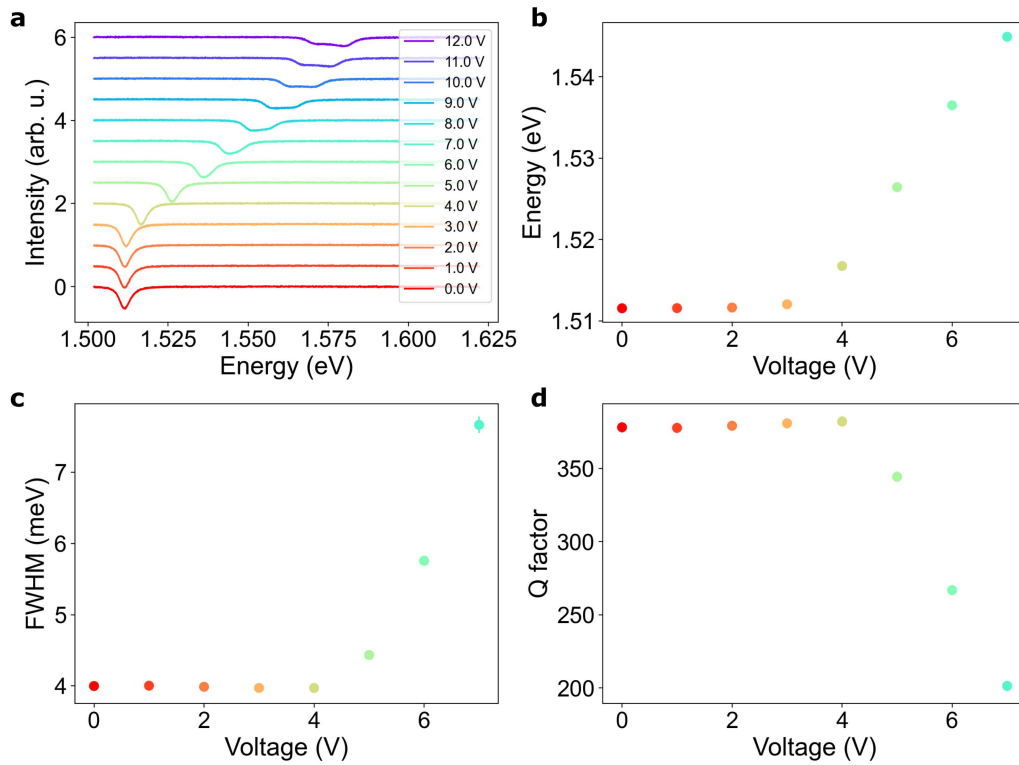


Figure 3.2: Horizontally polarized photonic mode tuning with applied voltage. **a** Cross-sections at $k = 0$ for subsequent voltages applied to the structure (reflectivity measurements). **b** Energy of the cavity modes, **c** FWHM and **d** Q-factor for subsequent voltages obtained from fitting to the cavity modes presented in **a**. The vertical lines in **b-d** denote the measurement uncertainty, unless it extends within the size of the markers.

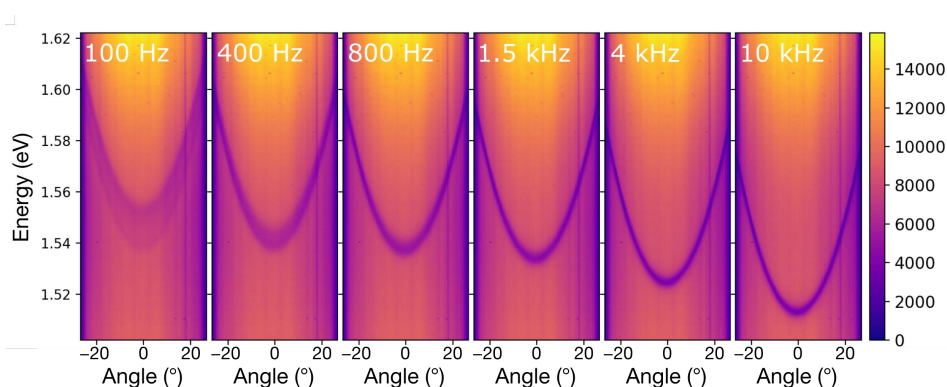


Figure 3.3: Angle-resolved reflectivity maps for the horizontally polarized mode for 6.0 volts applied to the structure as a function of the frequency of the alternating voltage applied to the cavity filled with 2091 HBNLC.

frequency is too low and that there are leftover molecules that have tilted much less than the others. On the other hand, at high frequency (10 kHz), the cavity mode is narrow and well defined in energy. However, in this case, the possibility of tuning the cavity mode by voltage is significantly reduced. We can see that the Q-factor of the cavity increases with increasing frequency of the alternating voltage applied to the sample from 269 (at 1 kHz) to 373 (at 10 kHz) (Figure 3.4 d). The high quality factor of the cavity is useful, i.e., because of the elongation of the lifetime of the photon in the cavity. However, it should be remembered that in the case of the presented structure, we must take into account the possibility of tuning the cavity mode. Hence, the highest frequencies of the electric field for which we note the highest Q-factor will not be optimal. As we can see in the case of frequency of 10 kHz (Fig. 3.4 a), the energy of the cavity mode is the same as in the case of no voltage (Fig. 3.2 a). On the basis of the above considerations, we choose the optimal frequency of external alternating voltage to 1 kHz.

Depending on the type of liquid crystal selected and the rubbing direction, we can obtain a cavity with a different initial orientation of the molecules (as discussed in the case of LC cells in sec. 1.4.3): homogeneous or homeotropic. The schematic structure of the LCMC in the HG and HT configuration is shown in Figure 3.5.

Figure 3.6 presents the reflectivity maps for increasing voltage for LCMC with LC in HG configuration. In contrast to the previous figures, selected maps present both the horizontally and vertically polarized mode. This is

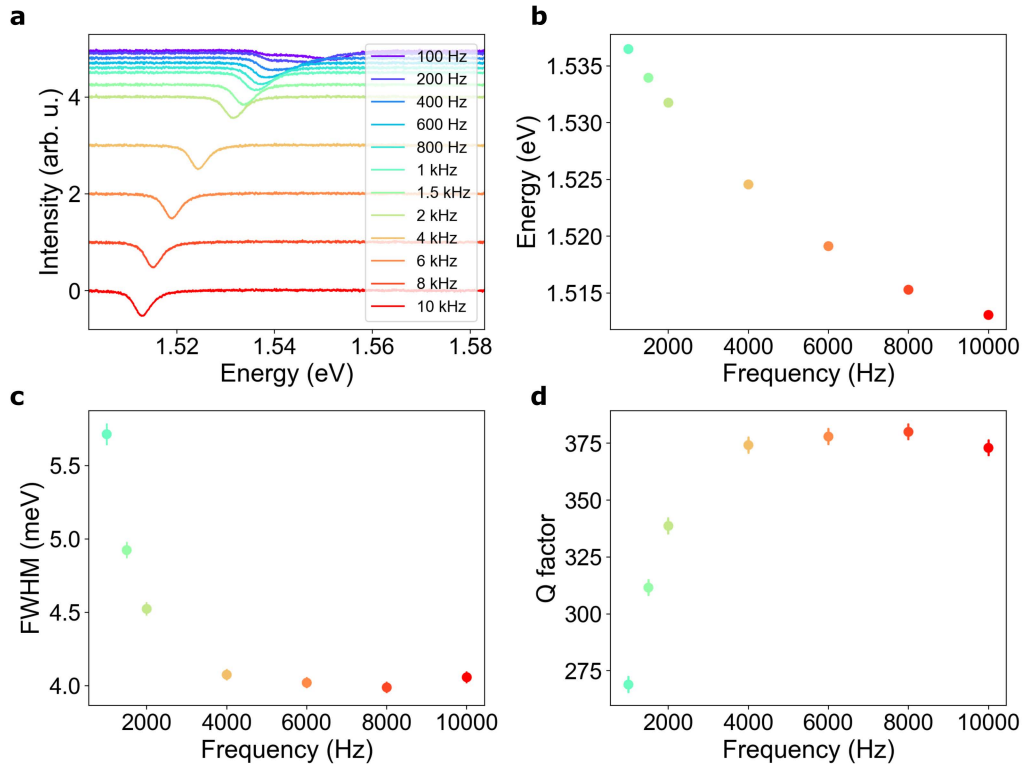


Figure 3.4: Horizontally polarized photonic mode tuning for different frequency of alternating voltage. **a** Cross-sections at $k = 0$ for subsequent frequencies (reflectivity measurements). For better visibility, the intensity curves are shifted vertically by: $-f \times 5 \cdot 10^{-4} \text{s} \cdot (\text{arb.u.})$, with f denoting the frequency of the alternating voltage. **b** Energy of the cavity modes, **c** FWHM and **d** Q-factor for subsequent voltages obtained from fitting to the cavity modes presented in **a**. The vertical lines in scatter plots denote the measurement uncertainty, although in **b** they extend within the size of the markers.

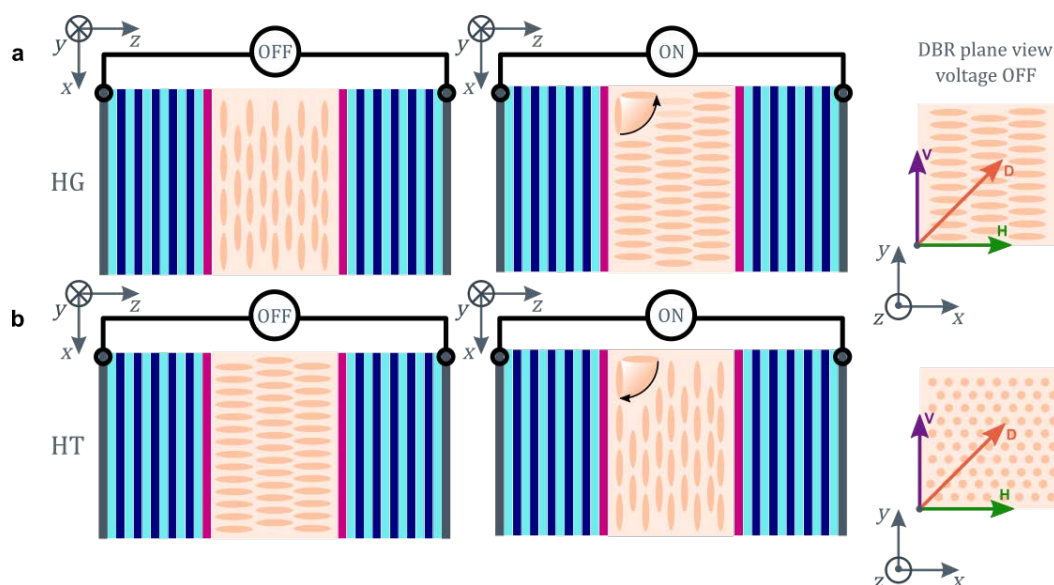


Figure 3.5: Scheme of the liquid crystal microcavity in the **a** homogeneous (HG) and **b** homeotropic (HT) configuration tuning. The scheme shows a simplified view of the DBR (mirror) plane with axes described with main polarizations: H - horizontal, V - vertical, D - diagonal.

achieved by adjusting the polarizer in front of the detector to the diagonal polarization (D). Without applied external voltage, the LC director lies parallel to the cavity plane, which gives the initial splitting of the cavity modes (here of the order of 100 meV). When a voltage is applied, we observe a shift of the horizontally polarized mode toward higher energies, thus reducing the energy splitting between the photonic modes.

In Figure 3.7 the reflectivity maps are presented for increasing voltage for LCMC with second type of LC, the DFNLC, in HT configuration. Initially, the LC director lies perpendicular to the cavity plane, thus the photonic modes are initially unsplit (at $k = 0$). With increasing external voltage (with the frequency of the alternating voltage set to 30 kHz¹), we observe a continuous splitting of the modes. The threshold voltage value in this case is 12.5 V. Above this value, we can see the shift of the horizontally polarized mode towards lower energies.

The possibility of tuning the photonic mode is valuable from the perspec-

¹ In this case, the dependence on the frequency is more complex as mentioned in Chapter 2.2. For more information, see article [58]. For this work, all measurements for the 1999C DFNLC were made at 30 kHz.

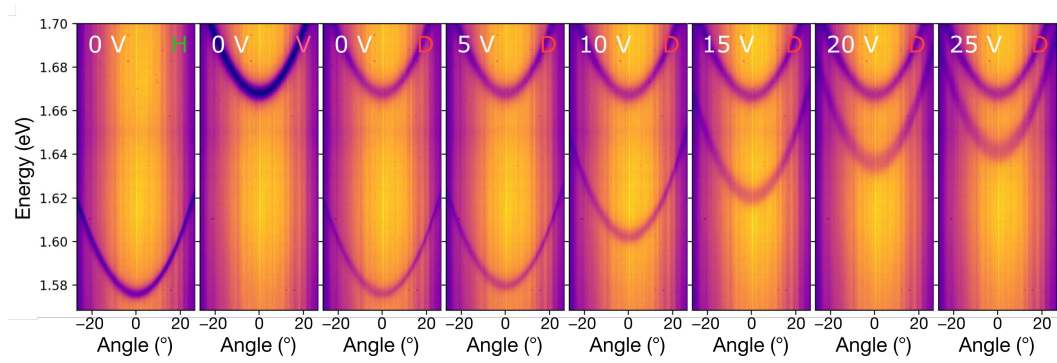


Figure 3.6: Reflectivity maps for increasing voltage applied to the LCMC structure with LC (2091 HBNLC) in HG configuration.

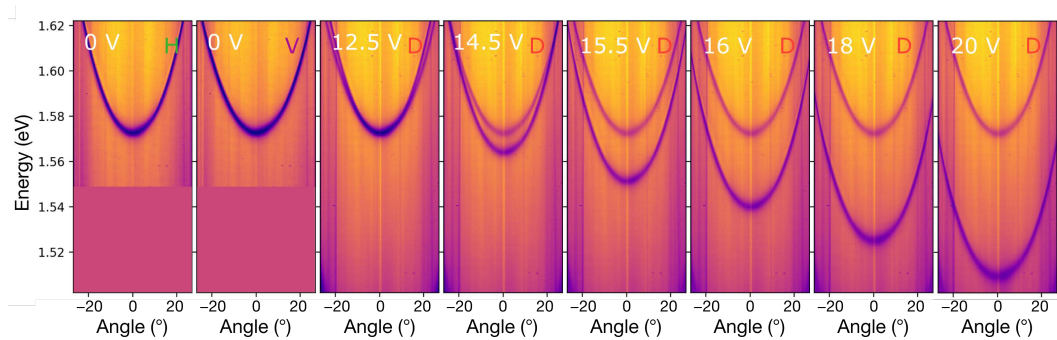


Figure 3.7: Reflectivity maps for increasing voltage applied to the LCMC structure with LC (1999C DFNLC) in HT configuration.

tive of the study of light-matter coupling, as it allows one to obtain any energy match between the photon states in the cavity and the exciton states in the emitter.

3.2. Photonic modes resonances in LCMC

In the case of a multimode LC cavity, by applying the proper voltage to the structure, we can observe subsequent photonic mode resonances. We will call them (N_x, N_y) , with N_x denoting the index of the horizontally polarized mode and N_y denoting the index of the vertically polarized mode. The case of the resonance of modes described with the same N will be referred to as the (N, N) regime in this work and similarly for the following resonances: $(N + 1, N)$, $(N + 2, N)$. Each of the resonances is characterized by a different regime, which means that in each of them we can observe different phenomena in both real and Fourier space.

For subsequent resonance types, we observed the following phenomena:

- (N, N) regime
 - Tunable optical spin Hall effect
 - Second order meron
- $(N + 1, N)$ regime
 - Rashba-Dresselhaus effect
 - Optical persistent spin helix
 - Optical Stern-Gerlach experiment
- $(N + 2, N)$ regime
 - Second-order antimeron

The primary subjects of the experimental part of the thesis are the (N, N) and $(N + 1, N)$ regimes and the observations of the tunable optical spin Hall effect, Rashba-Dresselhaus effect, optical persistent spin helix, and optical Stern-Gerlach experiment. The experimental results for the second order meron ((N, N) regime) and antimeron for $(N + 2, N)$ regime obtained with contributions of the author of the present work are published elsewhere [64].

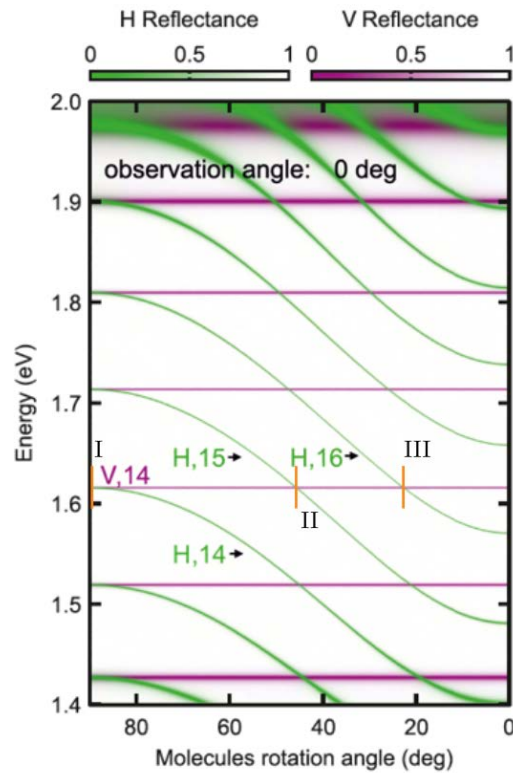


Figure 3.8: Resonances of cavity modes. An example of calculated reflectance with tilting of LC molecules at normal incidence for horizontally (green color) and vertically (violet color) polarized cavity modes for cavity with LC in HT configuration. Results calculated within the Berreman model by Mateusz Król. Labels I, II, and III denote crossings corresponding to (N, N) , $(N + 1, N)$ and $(N + 2, N)$ regimes. Colored curve labels denote polarization and mode index.

Chapter 4

Synthetic Hamiltonians of liquid crystal cavity

This chapter presents the theoretical model developed by Professor Witold Bardyszewski describing the liquid crystal microcavity derived from Maxwell equations for a birefringent medium. The approximation assumes a waveguide imprinting two parallel flat perfect mirrors enclosing an anisotropic optical medium. The final equation is mathematically analogous to the Schrödinger equation for a massive particle with spin $\frac{1}{2}$.

4.1. General information

The propagation of the electromagnetic wave in a thin layer in a linear medium is determined by the Maxwell equations. There are no free charges or currents in the medium, and the permittivity constant is ε_r , and the magnetic permeability is μ_r (where $n = \sqrt{\varepsilon_r \mu_r}$). In that case, we have the following Maxwell equations:

$$\nabla \cdot \mathbf{D} = 0, \nabla \cdot \mathbf{B} = 0, \nabla \times \mathbf{E} = -\frac{\partial \mathbf{B}}{\partial t}, \nabla \times \mathbf{H} = \frac{\partial \mathbf{D}}{\partial t}, \quad (4.1)$$

where $\mathbf{D} = \varepsilon_0 \varepsilon_r \mathbf{E}$, $\mathbf{B} = \mu_0 \mu_r \mathbf{H}$ and μ_0 is the magnetic permeability in vacuum and ε_0 is the electric permittivity in vacuum.

In the case of a birefringent medium (e.g., liquid crystal), due to the anisotropy of the system, the dielectric permittivity must be considered as a tensor, which is a 3×3 matrix denoted as $\hat{\varepsilon}$. In general, in the frame fixed to the LC orientation, this matrix takes the form:

$$\hat{\varepsilon}_{\text{LC}} = \begin{bmatrix} n_e^2 & 0 & 0 \\ 0 & n_o^2 & 0 \\ 0 & 0 & n_o^2 \end{bmatrix}, \quad (4.2)$$

assuming the x -axis is along the long axis of the optical indicatrix. Magnetic permeability is assumed to be isotropic.

4.2. Approximate model for an anisotropic cavity

To describe the optical properties of the cavity when the LC molecules are tilted with respect to the plane of the mirrors, the matrix (4.2) must be transformed into a laboratory frame. In the following considerations, the convention was adopted, where LC molecules rotate around the y axis by the θ angle measured with respect to the x axis in the laboratory frame (2.11). Therefore, for any tilt angle θ , the matrix takes the form:

$$\hat{\varepsilon} = \hat{R}\hat{\varepsilon}_{\text{LC}}\hat{R}^{-1} = \begin{bmatrix} n_o^2 \sin^2 \theta + n_e^2 \cos^2 \theta & 0 & (n_e^2 - n_o^2) \sin \theta \cos \theta \\ 0 & n_o^2 & 0 \\ (n_e^2 - n_o^2) \sin \theta \cos \theta & 0 & n_o^2 \cos^2 \theta + n_e^2 \sin^2 \theta \end{bmatrix}, \quad (4.3)$$

where the rotation matrix \hat{R} is:

$$\hat{R} = \begin{bmatrix} \cos \theta & 0 & -\sin \theta \\ 0 & 1 & 0 \\ \sin \theta & 0 & \cos \theta \end{bmatrix}.$$

The Maxwell's rotational equations take the form:

$$\nabla \times \mathbf{E} = -\mu_0 \frac{\partial \mathbf{H}}{\partial t} \quad (4.4)$$

$$\nabla \times \mathbf{H} = -\varepsilon_0 \hat{\varepsilon} \frac{\partial \mathbf{E}}{\partial t} \quad (4.5)$$

To solve the equations, we assume the following forms of the electric-field vector and magnetic-field strength:

$$\mathbf{E}(x, y, z) = \mathbf{E}_{\mathbf{k}}(z) e^{i(k_0 \boldsymbol{\kappa} \mathbf{r} - \omega t)}, \quad (4.6)$$

$$\mathbf{H}(x, y, z) = \mathbf{H}_{\mathbf{k}}(z) e^{i(k_0 \boldsymbol{\kappa} \mathbf{r} - \omega t)}, \quad (4.7)$$

where $\mathbf{k} = [k_x, k_y] = k_0 \boldsymbol{\kappa} = [k_0 \kappa_x, k_0 \kappa_y]$ and $\omega = k_0 c$, while $\mathbf{E}_{\mathbf{k}}(z)$ and $\mathbf{H}_{\mathbf{k}}(z)$ are unknown vector-valued functions of z . Therefore, we will focus on solutions for a single wave vector \mathbf{k} in the plane of the sample. In order

to improve legibility, the subscript \mathbf{k} is omitted from most of the following formulas.

After plugging (4.6) and (4.7) into the equations (4.4) and (4.5), the z components of the electric field and magnetic field vectors can be eliminated, which allows to reduce the problem to a system of four equations.

$$\partial_z \begin{bmatrix} E_x \\ E_y \\ H_x \\ H_y \end{bmatrix} = \hat{M} \begin{bmatrix} E_x \\ E_y \\ H_x \\ H_y \end{bmatrix}, \quad (4.8)$$

where the matrix \hat{M} is:

$$\hat{M} = ik_0 \begin{bmatrix} -\frac{\varepsilon_{zx}\kappa_x}{\varepsilon_{zz}} & -\frac{\varepsilon_{zy}\kappa_x}{\varepsilon_{zz}} & \frac{\kappa_x\kappa_y R}{\varepsilon_{zz}} & \frac{(\varepsilon_{zz}-\kappa_x^2)R}{\varepsilon_{zz}} \\ -\frac{\varepsilon_{zx}\kappa_y}{\varepsilon_{zz}} & -\frac{\varepsilon_{zy}\kappa_y}{\varepsilon_{zz}} & \frac{(\kappa_y^2-\varepsilon_{zz})R}{\varepsilon_{zz}} & -\frac{\kappa_x\kappa_y R}{\varepsilon_{zz}} \\ -\frac{\varepsilon_{yx}-\kappa_x\kappa_y+\frac{\varepsilon_{yz}\varepsilon_{zx}}{\varepsilon_{zz}}}{R} & \frac{\kappa_x^2-\varepsilon_{yy}+\frac{\varepsilon_{yz}\varepsilon_{zy}}{\varepsilon_{zz}}}{R} & -\frac{\varepsilon_{yz}\kappa_y}{\varepsilon_{zz}} & \frac{\varepsilon_{yz}\kappa_x}{\varepsilon_{zz}} \\ -\frac{\kappa_y^2+\varepsilon_{xx}-\frac{\varepsilon_{xz}\varepsilon_{zx}}{\varepsilon_{zz}}}{R} & \frac{\varepsilon_{xy}+\kappa_x\kappa_y-\frac{\varepsilon_{xz}\varepsilon_{zy}}{\varepsilon_{zz}}}{R} & \frac{\varepsilon_{xz}\kappa_y}{\varepsilon_{zz}} & -\frac{\varepsilon_{xz}\kappa_x}{\varepsilon_{zz}} \end{bmatrix}. \quad (4.9)$$

ε_{ij} denotes the components of the relative dielectric tensor, while $R = \sqrt{\frac{\mu_0}{\varepsilon_0}}$ is the impedance of free space.

Substituting expression (4.3) into matrix \hat{M} , we get a simplified form:

$$\hat{M} = ik_0 \begin{bmatrix} -\frac{\varepsilon_{zx}\kappa_x}{\varepsilon_{zz}} & 0 & \frac{\kappa_x\kappa_y R}{\varepsilon_{zz}} & \frac{(\varepsilon_{zz}-\kappa_x^2)R}{\varepsilon_{zz}} \\ -\frac{\varepsilon_{zx}\kappa_y}{\varepsilon_{zz}} & 0 & \frac{(\kappa_y^2-\varepsilon_{zz})R}{\varepsilon_{zz}} & -\frac{\kappa_x\kappa_y R}{\varepsilon_{zz}} \\ -\frac{\kappa_x\kappa_y}{R} & \frac{\kappa_x^2-\varepsilon_{yy}}{R} & 0 & 0 \\ -\frac{\kappa_y^2+\varepsilon_{xx}-\frac{\varepsilon_{xz}\varepsilon_{zx}}{\varepsilon_{zz}}}{R} & \frac{\kappa_x\kappa_y}{R} & \frac{\varepsilon_{xz}\kappa_y}{\varepsilon_{zz}} & -\frac{\varepsilon_{xz}\kappa_x}{\varepsilon_{zz}} \end{bmatrix} \quad (4.10)$$

Eliminating further from (4.8) the magnetic field components and expanding to the second order in k_x, k_y we get the approximate equation for electric field only:

$$-\partial_z^2 \mathbf{E} + \hat{A} \partial_z \mathbf{E} + \hat{B}_1 \mathbf{E} = k_0^2 \hat{B}_0 \mathbf{E}, \quad (4.11)$$

with

$$\hat{A} = \frac{-i}{\varepsilon_{zz}} \begin{bmatrix} (\varepsilon_{xz} + \varepsilon_{zx})k_x & \varepsilon_{xz}k_y \\ \varepsilon_{zx}k_y & 0 \end{bmatrix}, \quad (4.12)$$

which acts on the electric field derivatives, and

$$\hat{B}_1 = \frac{1}{\varepsilon_{zz}} \begin{bmatrix} \varepsilon_{xx}k_x^2 + \tilde{\varepsilon}_{zz}k_y^2 & (\varepsilon_{yy} - \varepsilon_{zz})k_yk_x \\ (\varepsilon_{xx} - \tilde{\varepsilon}_{zz})k_yk_x & \varepsilon_{zz}k_x^2 + \varepsilon_{yy}k_y^2 \end{bmatrix} \quad (4.13)$$

$$\hat{B}_0 = \begin{bmatrix} \tilde{\varepsilon}_{xx} & 0 \\ 0 & \varepsilon_{yy} \end{bmatrix}, \quad (4.14)$$

which act on the electric field. For brevity of notation, we introduced $\tilde{\varepsilon}_{zz} = \varepsilon_{zz} + \varepsilon_{xz}\varepsilon_{zx}/\varepsilon_{zz}$ and $\tilde{\varepsilon}_{xx} = \varepsilon_{xx} - \varepsilon_{xz}\varepsilon_{zx}/\varepsilon_{zz} = n_{\text{eff}}^2$.

Equation (4.11) can be solved by representing the electric field as a series of standing waves in a microcavity according to the equation:

$$\mathbf{E}_{\mathbf{k}}(z) = \sum_{s=1}^2 \sum_{n=1}^N f_{sn} |s, n\rangle, \quad (4.15)$$

where the orthonormal basis functions are given by:

$$|1, m\rangle = \sqrt{\frac{2}{L}} \sin\left(\frac{m\pi}{L}z\right) \begin{bmatrix} 1 \\ 0 \end{bmatrix}, \quad (4.16)$$

$$|2, n\rangle = \sqrt{\frac{2}{L}} \sin\left(\frac{n\pi}{L}z\right) \begin{bmatrix} 0 \\ 1 \end{bmatrix}. \quad (4.17)$$

They correspond to the polarization parallel to the x and y axis, respectively, i.e. horizontally and vertically polarized cavity modes. f_{sm} denotes the individual amplitudes of the polarized sine waves in (4.16 and 4.17). The parameters m and n represent the index of the photonic mode, i.e. the number of minima (or maxima) of the electric field between two ideal mirrors, which are separated by a distance L .

Let us represent individual terms of the equation (4.11) in the newly introduced basis. For the first term, i.e., the second derivative of the electric field, we find

$$\langle s'n | \partial_z^2 | sm \rangle = -\frac{\pi^2}{L^2} m^2 \delta_{mn} \delta_{s's}. \quad (4.18)$$

The only contribution comes from the diagonal elements. The second component of equation (4.11) is the first derivative of the electric field multiplied

by the matrix \hat{A} , which gives:

$$\langle s'n|\hat{A}\partial_z|sm\rangle = A_{s's} \begin{cases} \frac{4nm}{L(n^2-m^2)} & \text{when } m \text{ and } n \text{ are of different parity,} \\ 0 & \text{when } m \text{ and } n \text{ are of the same parity.} \end{cases} \quad (4.19)$$

The remaining terms of the equation involve two matrices $\hat{B}_{1,0}$. Their form in the new basis is trivially

$$\langle s'n|\hat{B}_{1,0}\partial_z|sm\rangle = (\hat{B}_{1,0})_{s,s'}\delta_{nm}. \quad (4.20)$$

Equation (4.11) is now transformed into a generalized eigenvalue problem with respect to the frequency $k_0^2 = \omega^2/c^2$. For $k_x = k_y = 0$ it has simple solutions $\mathbf{E}_{x,m} = |1, m\rangle$ and $\mathbf{E}_{y,n} = |2, n\rangle$. They correspond to modes polarized along the x -axis and y -axis, respectively. Their respective frequencies are $\omega_{1m} = ck_{1m} = c\pi m/(Ln_{\text{eff}})$ and $\omega_{2n} = ck_{2n} = c\pi n/(Ln_o)$, where n_{eff} is given by (3.1).

Then considering the dispersion in k_x and k_y , we will focus only on the relevant regime where two cavity modes (characterized by m and n mode indices) are in resonance ($\omega_{1m} \approx \omega_{2n}$). There are three distinct possibilities for such coupling.

- $m = n$, i.e, the (N, N) **regime**,
- $m = n \pm 1$, that is, the $(N + 1, N)$ **regime**,
- $m = n \pm 2$, that is, the $(N + 2, N)$ **regime**.

In each case, the electric field near the degeneracy point is approximated by:

$$\mathbf{E}_k(z) = f_{1m}|1, m\rangle + f_{2n}|2, n\rangle, \quad (4.21)$$

where we neglected contributions of modes lying further away in energy.

- (N, N) **regime**: For $m = n$ we have to solve the equation:

$$\begin{bmatrix} (k_0^2 - k_{1m}^2)\tilde{\epsilon}_{xx} & 0 \\ 0 & (k_0^2 - k_{2n}^2)\epsilon_{yy} \end{bmatrix} \vec{F} = \frac{1}{\epsilon_{zz}} \begin{bmatrix} \epsilon_{xx}k_x^2 + \tilde{\epsilon}_{zz}k_y^2 & (\epsilon_{yy} - \epsilon_{zz})k_yk_x \\ (\epsilon_{xx} - \tilde{\epsilon}_{zz})k_yk_x & \epsilon_{zz}k_x^2 + \epsilon_{yy}k_y^2 \end{bmatrix} \vec{F}, \quad (4.22)$$

where $\vec{F} = [f_{1m}, f_{2n}]^T$.

- $(N + 2, N)$ **regime**: For $m \neq n$ and both m and n are of the same parity, then the two modes do not couple directly and we have:

$$\begin{bmatrix} (k_0^2 - k_{1m}^2)\tilde{\epsilon}_{xx} & 0 \\ 0 & (k_0^2 - k_{2n}^2)\epsilon_{yy} \end{bmatrix} \vec{F} = \frac{1}{\epsilon_{zz}} \begin{bmatrix} \epsilon_{xx}k_x^2 + \tilde{\epsilon}_{zz}k_y^2 & 0 \\ 0 & \epsilon_{zz}k_x^2 + \epsilon_{yy}k_y^2 \end{bmatrix} \vec{F}. \quad (4.23)$$

- $(N + 1, N)$ **regime**: For m and n of different parity:

$$\begin{bmatrix} (k_0^2 - k_{1m}^2)\tilde{\epsilon}_{xx} & 0 \\ 0 & (k_0^2 - k_{2n}^2)\epsilon_{yy} \end{bmatrix} \vec{F} = \frac{1}{\epsilon_{zz}} \begin{bmatrix} \epsilon_{xx}k_x^2 + \tilde{\epsilon}_{zz}k_y^2 & -i\frac{4mn}{L(m^2-n^2)}\epsilon_{xz}k_y \\ i\frac{4mn}{L(m^2-n^2)}\epsilon_{xz}k_y & \epsilon_{zz}k_x^2 + \epsilon_{yy}k_y^2 \end{bmatrix} \vec{F}. \quad (4.24)$$

We have thus derived the structure of coupling between the horizontally and vertically polarized LCMC modes depending on the modes' parities and the tilt of the permittivity tensor. Solving the above equations for $k_0 = \omega/c$ yields the desired dispersion relations $\omega(k_x, k_y)$. It is possible to further transform the equations into eigenvalue problems for energy $\hbar\omega$. This is in general possible only for energies near $\omega' = \sqrt{(\omega_{1n}^2 + \omega_{2m}^2)}/2$, after formally expanding the terms to linear order in $\Delta\omega = \omega - \omega'$. With certain other careful approximations, as outlined in the supplementary material of Ref. [65], one can formulate in this way the effective Hamiltonians presented in section 4.4. Nonetheless, in the following section, we will derive the same Hamiltonians by considering only the symmetries of the LCMC system.

4.3. Symmetry of the liquid crystal cavity

To work out the structure of the effective Hamiltonian operators describing the resonance of modes H and V inside the liquid-crystal microcavity, the symmetry group of the system must be determined first. By analyzing symmetry invariants, we can find the form of all non-zero terms, including terms of higher order in k_x, k_y neglected in the previous section. Still, we will confine the analysis to terms at most second order (quadratic) in k_x, k_y , as these are sufficient to capture all the phenomena discussed in this work.

Table 4.1: The character table of the symmetry group C_{2h} [66]. The axes labels were changed compared to the source material, to match to the coordinate system used in this work.

C_{2h}	e	$\hat{c}_2(y)$	\hat{i}	$\hat{\sigma}_{xz}$	basis
A_g	1	1	1	1	x^2, y^2, z^2, xz
A_u	1	1	-1	-1	y
B_g	1	-1	1	-1	yz, xy
B_u	1	-1	-1	1	x, z

In this section we assume that the basis modes of the cavity are polarized horizontally (H) or vertically (V). They are indicated by $E_H^\pm(z)$ and $E_V^\pm(z)$ and have a well-defined parity with respect to the inversion: $\hat{i}E^\pm = \pm E^\pm$. Compared to the notation in the previous section, for example, the mode $E_H^-(z)$ corresponds to a vector $|1, 2n\rangle$ for some n , that is, a standing wave polarized along x , with odd parity.

— $(N + 1, N)$ **and** $(N + 2, N)$ **regimes**

To achieve resonance in the $(N + 1, N)$ and $(N + 2, N)$ regimes the LC molecules must be tilted with respect to the cavity plane at $\theta > 0$. As a result, the considered system has C_{2h} symmetry with the two-fold rotation about the y -axis. The symmetry transformations of the cavity are shown schematically in Figure 4.1. The character table of C_{2h} is presented as Table 4.1, where we denoted by \hat{c}_2 the rotation by angle π around the y axis, and by $\hat{\sigma}_{xz}$ the mirror reflection about the xz plane.

— (N, N) **regime**

A special case is the (N, N) regime, for which the molecules inside the cavity are perpendicular to the cavity plane. Then the symmetry group describing the system changes to $D_{\infty h}$. The symmetry transformations of the cavity are shown schematically in Figure 4.2. The irreducible representations of the symmetry group $D_{\infty h}$ for LCMC are listed in Table 4.2. We note that C_{2h} is a subgroup of $D_{\infty h}$.

In the following theoretical treatment of the (N, N) regime we focus on the case of exact resonance. A slight tilt of the molecules reduces the symmetry group to C_{2h} . Under this perturbation, the effective Hamiltonian should be extended by correction terms analogous to the terms of the Hamiltonian of the $(N + 2, N)$ regime.

Table 4.3: Two-dimensional representations of C_{2h} symmetry group for the modes of mixed parity. $(N + 1, N)$ regime.

C_{2h}	e	\hat{c}_2	\hat{i}	$\hat{\sigma}_{xz}$	basis
D^{-+}	$\begin{pmatrix} 1 & 0 \\ 0 & 1 \end{pmatrix}$	$\begin{pmatrix} -1 & 0 \\ 0 & -1 \end{pmatrix}$	$\begin{pmatrix} -1 & 0 \\ 0 & 1 \end{pmatrix}$	$\begin{pmatrix} 1 & 0 \\ 0 & -1 \end{pmatrix}$	(E_H^-, E_V^+)
D^{+-}	$\begin{pmatrix} 1 & 0 \\ 0 & 1 \end{pmatrix}$	$\begin{pmatrix} 1 & 0 \\ 0 & 1 \end{pmatrix}$	$\begin{pmatrix} 1 & 0 \\ 0 & -1 \end{pmatrix}$	$\begin{pmatrix} 1 & 0 \\ 0 & -1 \end{pmatrix}$	(E_H^+, E_V^-)

Table 4.4: The symmetry of $\sigma_{0,x,y,z}$ matrices under the C_{2h} symmetry group operations for the modes of the opposite parity. $(N + 1, N)$ regime.

	e	\hat{c}_2	\hat{i}	$\hat{\sigma}_{xz}$	Representation
$D\sigma_0D^{-1}$	σ_0	σ_0	σ_0	σ_0	A_g
$D\sigma_xD^{-1}$	σ_x	σ_x	$-\sigma_x$	$-\sigma_x$	A_u
$D\sigma_yD^{-1}$	σ_y	σ_y	$-\sigma_y$	$-\sigma_y$	A_u
$D\sigma_zD^{-1}$	σ_z	σ_z	σ_z	σ_z	A_g

(E_H^+, E_V^-) , respectively. They are listed in Table 4.3. All transformation operators in these bases can be expressed with the third Pauli matrix σ_z and the zeroth Pauli matrix (identity matrix) σ_0 , multiplied by ± 1 .

The 2×2 Hamiltonian matrix, due to its hermiticity, is expressible as

$$H(k_x, k_y) = h_0(k_x, k_y)\sigma_0 + h_x(k_x, k_y)\sigma_x + h_y(k_x, k_y)\sigma_y + h_z(k_x, k_y)\sigma_z, \quad (4.25)$$

where functions h_0, h_x, h_y, h_z are real-valued. This motivates us to analyze the transformation rules of the Pauli matrices, which are summarized in Table 4.4. It is important to note that these transformation rules are identical for both the representations D^{-+} and D^{+-} , so in Table 4.3 a shorthand notation D is used for both cases. This analysis allows us to assign the Pauli matrices to their irreducible representations, as shown in Table 4.5.

As the Hamiltonian is a symmetry invariant, it can be composed only of terms belonging to the trival representation A_g . It follows from the character table (Table 4.1), that a product of a function $f(k_x, k_y)$ and Pauli matrix σ_μ belongs to A_g if and only if both $f(k_x, k_y)$ and σ_μ belong to a common representation. The terms that satisfy this condition, up to second order in k , are

$$\sigma_0, \sigma_0 k_x^2, \sigma_0 k_y^2, \sigma_x k_y, \sigma_y k_x, \sigma_z, \sigma_z k_x^2, \sigma_z k_y^2, \quad (4.26)$$

Table 4.5: Assignment of the cavity modes, the wavevector components, and their quadratic forms, as well as Pauli matrices expressed in the basis of cavity modes in the $(N + 1, N)$ regime to the irreducible representations of C_{2h} .

	cavity modes	functions of k_x, k_y	Pauli matrices
A_g	E_H^+	k_x^2, k_y^2	σ_0, σ_z
A_u	E_V^-	k_y	σ_x, σ_y
B_g	E_V^+	$k_x k_y$	none
B_u	E_H^-	k_x	none

where each of them can be multiplied by an independent real-valued constant.

Apart from the spatial symmetry, the system also conserves time-reversal symmetry. As the basis states are bosonic, the time-reversal operator T acts according to

$$TH(k_x, k_y)T^{-1} = H^*(-k_x, -k_y), \quad (4.27)$$

where the star denotes complex conjugation. It is straightforward to check that of the terms (4.26), the ones compatible with time-reversal symmetry are:

$$\sigma_0, \sigma_0 k_x^2, \sigma_0 k_y^2, \sigma_y k_y, \sigma_z, \sigma_z k_x^2, \sigma_z k_y^2, \quad (4.28)$$

which are all the allowed Hamiltonian terms for the $(N + 1, N)$ regime.

4.3.2. $(N + 2, N)$ regime

In this regime, the symmetry group is also C_{2h} , therefore the analysis is largely the same as in the previous section. In this case, the basis modes are either (E_H^-, E_V^-) or (E_H^+, E_V^+) .

The groups of 2×2 transformation matrices D^{--} and D^{++} that transform the pairs of basis modes (E_H^-, E_V^-) or (E_H^+, E_V^+) , respectively, are shown in Table 4.6. The consequent transformation rules for Pauli matrices are shown in Table 4.7.

The assignment of possible components of the effective Hamiltonian to their respective irreducible representations is shown in Table 4.8. By analogous arguments as in the previous section, we find that the terms that are invariant with respect to the C_{2h} group, up to the second order in k , are

$$\sigma_0, \sigma_0 k_x^2, \sigma_0 k_y^2, \sigma_x k_x k_y, \sigma_y k_x k_y, \sigma_z, \sigma_z k_x^2, \sigma_z k_y^2. \quad (4.29)$$

Table 4.6: Two dimensional representations of C_{2h} symmetry group for the modes of the same parity. $(N + 2, N)$ regime.

C_{2h}	e	\hat{c}_2	\hat{i}	$\hat{\sigma}_{xz}$	basis
D^{--}	$\begin{pmatrix} 1 & 0 \\ 0 & 1 \end{pmatrix}$	$\begin{pmatrix} -1 & 0 \\ 0 & 1 \end{pmatrix}$	$\begin{pmatrix} -1 & 0 \\ 0 & -1 \end{pmatrix}$	$\begin{pmatrix} 1 & 0 \\ 0 & -1 \end{pmatrix}$	(E_H^-, E_V^-)
D^{++}	$\begin{pmatrix} 1 & 0 \\ 0 & 1 \end{pmatrix}$	$\begin{pmatrix} 1 & 0 \\ 0 & -1 \end{pmatrix}$	$\begin{pmatrix} 1 & 0 \\ 0 & 1 \end{pmatrix}$	$\begin{pmatrix} 1 & 0 \\ 0 & -1 \end{pmatrix}$	(E_H^+, E_V^+)

Table 4.7: The symmetry of $\sigma_{0,x,y,z}$ matrices under the C_{2h} symmetry group operations for the modes of the same parity. $(N + 2, N)$ regime.

	e	\hat{c}_2	\hat{i}	$\hat{\sigma}_{xz}$	Representation
$D\sigma_0D^{-1}$	σ_0	σ_0	σ_0	σ_0	A_g
$D\sigma_xD^{-1}$	σ_x	$-\sigma_x$	σ_x	$-\sigma_x$	B_g
$D\sigma_yD^{-1}$	σ_y	$-\sigma_y$	σ_y	$-\sigma_y$	B_g
$D\sigma_zD^{-1}$	σ_z	σ_z	σ_z	σ_z	A_g

Accordingly, the requirement of conservation of time-reversal symmetry (4.27), reduces the list of Hamiltonian terms allowed in the $(N + 2, N)$ regime to

$$\sigma_0, \sigma_0 k_x^2, \sigma_0 k_y^2, \sigma_x k_x k_y, \sigma_z, \sigma_z k_x^2, \sigma_z k_y^2. \quad (4.30)$$

4.3.3. (N, N) regime

In this regime, the symmetry group is $D_{\infty h}$. Much like in the $(N + 2, N)$ regime, the basis modes are either (E_H^-, E_V^-) or (E_H^+, E_V^+) . However, now these

Table 4.8: Assignment of the cavity modes, the wavevector components, and their quadratic forms, as well as Pauli matrices expressed in the basis of cavity modes in the $(N + 2, N)$ regime to the irreducible representations of C_{2h} .

	cavity modes	functions of k_x, k_y	Pauli matrices
A_g	E_H^+	k_x^2, k_y^2	σ_0, σ_z
A_u	E_V^-	k_y	none
B_g	E_V^+	$k_x k_y$	σ_x, σ_y
B_u	E_H^-	k_x	none

Table 4.9: Assignment of the cavity modes, the wavevector components, and their quadratic forms, as well as Pauli matrices expressed in the basis of cavity modes in the (N, N) regime to the irreducible representations of $D_{\infty h}$.

	cavity modes	functions of k_x, k_y	Pauli matrices
A_{1g}	none	$k_x^2 + k_y^2$	σ_0
A_{2g}	none	none	σ_y
E_{1g}	(E_H^+, E_V^+)	none	none
E_{2g}	none	$(k_x^2 - k_y^2, k_x k_y)$	(σ_x, σ_z)
E_{2u}	(E_H^-, E_V^-)	(k_x, k_y)	none

modes have identical indices and are hence related by a $\pi/2$ rotation around the z -axis. The representations corresponding to the basis cavity modes can be found with the method presented in previous subsections. They are shown in Table 4.9.

In analogy to the above sections, it is necessary to determine the irreducible representations describing transformations of the Pauli matrices. The appropriate transformation matrices describing arbitrary rotations around z are, for both pairs of basis states,

$$D^{++(--)}(\phi) = \begin{pmatrix} \cos \phi & -\sin \phi \\ \sin \phi & \cos \phi \end{pmatrix} \quad (4.31)$$

for any angle ϕ . The matrices describing the identity transformation, mirror reflection about xz (σ_{xz}), and inversion (\hat{i}) are identical to those already listed in Table 4.6. The transformations of the Pauli matrices under the matrices D^{++} and D^{--} turn out to have identical results for the two cases. Table 4.10 shows the results of the analysis. We note that the matrices σ_x and σ_z transform together according to the representation E_{2g} , while σ_y transforms according to A_{2g} , and σ_0 transforms trivially according to A_{1g} . The irreducible representations corresponding to the Pauli matrices are listed in Table 4.9 together with the representations corresponding to the wave vector components k_x and k_y and their quadratic forms read from the character table.

The product terms of the form $h_\mu(k_x, k_y)\sigma_\mu$ will transform according to an appropriate product of representations. The only products that can form symmetry-invariant terms have A_{1g} in their decomposition. These are

$$A_{1g} \otimes A_{1g} = A_{1g}, \quad (4.32)$$

Table 4.10: The symmetry of $\sigma_{0,x,y,z}$ matrices under the $D_{\text{inf}h}$ symmetry group operations for the modes of the same index.

	e	$\hat{c}(\phi)$	\hat{i}	$\hat{\sigma}_{xz}$	Representation
$D\sigma_0D^{-1}$	σ_0	σ_0	σ_0	σ_0	A_{1g}
$D\sigma_xD^{-1}$	σ_x	$\cos(2\phi)\sigma_x - \sin(2\phi)\sigma_z$	σ_x	$-\sigma_x$	E_{2g} , together with σ_z
$D\sigma_yD^{-1}$	σ_y	σ_y	σ_y	$-\sigma_y$	A_{2g}
$D\sigma_zD^{-1}$	σ_z	$\sin(2\phi)\sigma_x + \cos(2\phi)\sigma_z$	σ_z	σ_z	E_{2g} , together with σ_x

$$E_{2g} \otimes E_{2g} = A_{1g} \oplus A_{2g} \oplus E_{4g}. \quad (4.33)$$

For completeness, we verify the other relevant products:

$$E_{1u} \otimes E_{2g} = E_{1u} \oplus E_{3u}, \quad (4.34)$$

also for any irreducible representation V

$$A_{1g} \otimes V = V, \quad (4.35)$$

and for all two-dimensional irreducible representations E_α

$$E_\alpha \otimes A_{2g} = E_\alpha. \quad (4.36)$$

The product $A_{1g} \otimes A_{1g}$ is clearly compatible with terms

$$\sigma_0, (k_x^2 + k_y^2)\sigma_0. \quad (4.37)$$

The product $E_{2g} \otimes E_{2g}$ in general involves terms of the form

$$H_{E_{2g} \otimes E_{2g}} = h_1(k_x^2 - k_y^2)\sigma_x + h_2(k_x^2 - k_y^2)\sigma_z + h_3k_xk_y\sigma_x + h_4k_xk_y\sigma_z. \quad (4.38)$$

By explicitly demanding invariance $H_{E_{2g} \otimes E_{2g}} = DH_{E_{2g} \otimes E_{2g}}D^{-1}$ for all transformation matrices D , we arrive at

$$H_{E_{2g} \otimes E_{2g}} \propto (k_x^2 - k_y^2)\sigma_z + 2k_xk_y\sigma_x, \quad (4.39)$$

which leaves only the composite term

$$(k_x^2 - k_y^2)\sigma_z + 2k_xk_y\sigma_x. \quad (4.40)$$

The requirement of time-reversal invariance (4.27) turns out to be satisfied by all terms found already. Thus, we arrive at the final list of Hamiltonian terms in the (N, N) regime

$$\sigma_0, (k_x^2 + k_y^2)\sigma_0, (k_x^2 - k_y^2)\sigma_z + 2k_x k_y \sigma_x. \quad (4.41)$$

4.4. Synthetic Hamiltonians

The symmetry analysis presented above allows the description of liquid crystal cavity work regimes in the language of synthetic Hamiltonians expressed in the basis of the orthonormal eigenmodes (4.16) and (4.17). The Pauli matrices that appear in the formulas can be interpreted as analogous to spin 1/2 operators. Therefore, we may represent the terms of the Hamiltonians as components of a k -dependent synthetic magnetic field, i.e.,

$$H(k_x, k_y) = h_0(k_x, k_y)\sigma_0 + \mu_B \mathbf{B} \cdot \boldsymbol{\sigma}. \quad (4.42)$$

In all the Hamiltonians below, a trivial term $E_0\sigma_0$ is neglected. Its only function is to shift the entire spectrum in energy.

In the three regimes, the Hamiltonians and the associated synthetic magnetic fields are:

— (N, N) :

$$\hat{H} \sim \frac{\hbar^2}{2m} (k_x^2 + k_y^2) \hat{\sigma}_0 + \delta [(k_x^2 - k_y^2) \hat{\sigma}_z + 2k_x k_y \hat{\sigma}_x], \quad (4.43)$$

$$\vec{B}_{(N,N)} = \frac{1}{\mu_B} (2\delta k_x k_y, 0, \delta(k_x^2 - k_y^2)), \quad (4.44)$$

— $(N + 1, N)$:

$$\hat{H} \sim \left(\frac{\hbar^2 k_x^2}{2m_x} + \frac{\hbar^2 k_y^2}{2m_y} \right) \hat{\sigma}_0 + (\Delta E + \delta_x k_x^2 + \delta_y k_y^2) \hat{\sigma}_z - 2\alpha k_y \hat{\sigma}_y, \quad (4.45)$$

$$\vec{B}_{(N+1,N)} = \frac{1}{\mu_B} (0, 2\alpha k_y, (\Delta E + \delta_x k_x^2 + \delta_y k_y^2)), \quad (4.46)$$

— $(N + 2, N)$:

$$\hat{H} \sim \left(\frac{\hbar^2 k_x^2}{2m_x} + \frac{\hbar^2 k_y^2}{2m_y} \right) \hat{\sigma}_0 + (\Delta E + \delta_x k_x^2 + \delta_y k_y^2) \hat{\sigma}_z + \delta_{xy} k_x k_y \hat{\sigma}_x, \quad (4.47)$$

$$\vec{B}_{(N+2,N)} = \frac{1}{\mu_B} (\delta_{xy} k_x k_y, 0, (\Delta E + \delta_x k_x^2 + \delta_y k_y^2)). \quad (4.48)$$

It is sometimes useful to express the Hamiltonians in an alternative basis $(E_{\sigma_+}, E_{\sigma_-})$

$$E_{\sigma_+} = \frac{1}{\sqrt{2}} (E_H - iE_V), \quad E_{\sigma_-} = \frac{1}{\sqrt{2}} (E_H + iE_V). \quad (4.49)$$

The basis transformation is chosen the same for all possible parity configurations of E_H and E_V . It is equivalent to substitution $(\sigma_x, \sigma_y, \sigma_z) \rightarrow (-\sigma_y, -\sigma_z, \sigma_x)$. Assuming phase coherence of the linearly polarized old basis vectors, the new basis vectors correspond to cavity modes that have circular polarization locally near the mirrors. This basis is better suited to interpret the experimental results presented in the subsequent chapters, as it corresponds to the Stokes parameters of the light reflected from or transmitted through the LCMC.

The effective Hamiltonian for the (N, N) regime has the following form and resembles the optical spin Hall effect Hamiltonian [47]:

$$\hat{H} \sim \frac{\hbar^2}{2m} (k_x^2 + k_y^2) \hat{\sigma}_0 - (\delta k_x^2 - \delta k_y^2) \hat{\sigma}_x - 2\delta k_x k_y \hat{\sigma}_y. \quad (4.50)$$

The schematic dispersion arising from the Hamiltonian (4.50), colored according to the linear polarization of the wave functions, is shown in Fig. 4.3

In the $(N + 1, N)$ regime the Hamiltonian becomes

$$\hat{H} \sim \frac{\hbar^2 k_x^2}{2m_x} \hat{\sigma}_0 + \frac{\hbar^2 k_y^2}{2m_y} \hat{\sigma}_0 + 2\alpha k_y \hat{\sigma}_z + (\Delta E + \delta_x k_x^2 + \delta_y k_y^2) \hat{\sigma}_x, \quad (4.51)$$

which is analogous to the Rashba-Dresselhaus Hamiltonian with a Zeeman-like splitting term ΔE with quadratic corrections δ_x, δ_y . The schematic dispersion for $\Delta E = 0$ and $\delta_x = \delta_y = 0$ is shown in Fig. 4.4

For this regime, we show the values of the parameters derived from the Maxwell's equations in the procedure described in Section 4.2:

$$\frac{1}{m_x} = \frac{1}{2m'_0} \left(\frac{n_o^2 \sin^2 \theta + n_e^2 \cos^2 \theta + n_e^2}{n_e^2 n_o^2} \right), \quad (4.52)$$

$$\frac{1}{m_y} = \frac{1}{2m'_0} \left(\frac{n_o^2 + n_e^2}{n_e^2 n_o^2} \right), \quad (4.53)$$

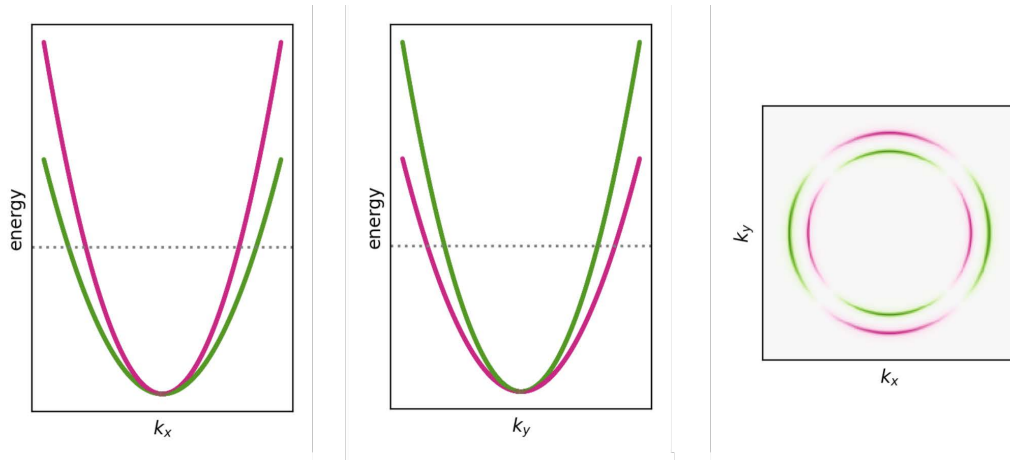


Figure 4.3: (N, N) **regime**. Photonic modes dispersions along k_x and k_y direction, and constant energy cross-section (for the energy marked by black dotted line on both k_x and k_y dispersions) obtained from eq. 4.50. The colors correspond to the polarization direction, where green is polarized in x direction and purple in y direction.

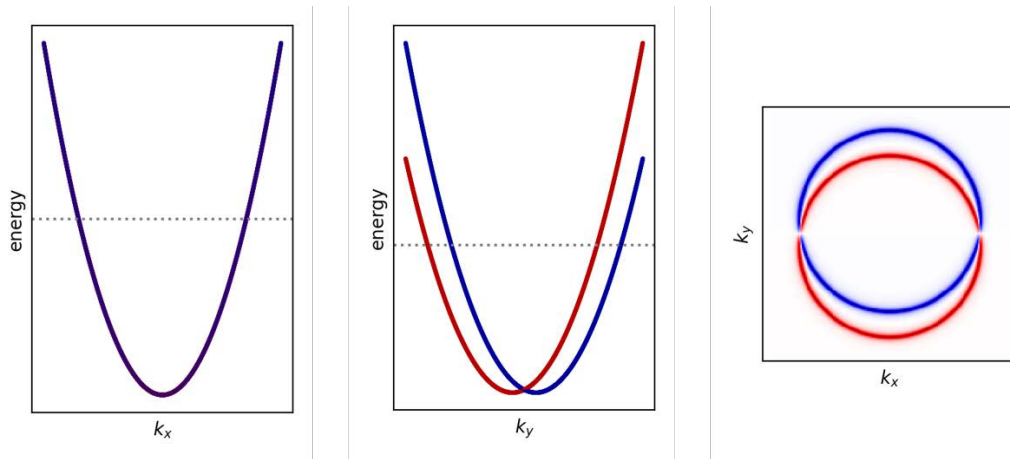


Figure 4.4: $(N+1, N)$ **regime**. Photonic modes dispersions in k_x and k_y direction, and constant energy cross-section (for the energy marked by black dotted line on both k_x and k_y dispersions) obtained from eq. 4.51 for $\Delta E = 0$. The red color corresponds to σ_+ polarization and blue σ_- .

$$\alpha = -\frac{\hbar^2}{m'_0 L} \frac{mn}{m^2 - n^2} \left(\frac{n_e^2 - n_o^2}{n_e^2 n_o^2} \right) \frac{\sin \theta \cos \theta}{\sqrt{n_o^2 \sin^2 \theta + n_e^2 \cos^2 \theta}}, \quad (4.54)$$

$$\delta_x = \frac{\hbar^2}{4m'_0} \left(\frac{n_o^2 - n_e^2}{n_e^2 n_o^2} \right) \sin^2 \theta, \quad (4.55)$$

$$\delta_y = \frac{\hbar^2}{4m'_0} \left(\frac{n_e^2 - n_o^2}{n_e^2 n_o^2} \right) \frac{n_e^2 \sin^2 \theta - n_o^2 \cos^2 \theta}{n_e^2 \sin^2 \theta + n_o^2 \cos^2 \theta}, \quad (4.56)$$

and $\Delta E = \frac{1}{2}(E_{1m} - E_{2n})$. In the above formulas we introduced $m'_0 = \sqrt{(E_{1m}^2 + E_{2n}^2)/(2c^4)}$. The Rashba-Dresselhaus coupling strength α increases for:

- decreasing the difference between the mode indices m and n , the lowest possible being 1,
- increasing birefringence $n_e^2 - n_o^2$,
- changing the angle θ of the tilt of the molecules' director towards the optimal value (in our case 47.2°),
- decreasing cavity width L .

In the $(N+2, N)$ regime the synthetic Hamiltonian can also be expressed in the new basis to yield

$$\hat{H} \sim \frac{\hbar^2 k_x^2}{2m_x} \hat{\sigma}_0 + \frac{\hbar^2 k_y^2}{2m_y} \hat{\sigma}_0 - (\delta_x k_x^2 + \delta_y k_y^2 + \Delta E) \hat{\sigma}_x - \delta_{xy} k_x k_y \hat{\sigma}_y. \quad (4.57)$$

An example of a schematic dispersion obtained from the Hamiltonian, colored according to the linear polarization of the wave functions, is shown in Fig. 4.5. Much like for the case of the $(N+1, N)$ regime, the values of all Hamiltonian parameters in (N, N) and $(N+2, N)$ regimes can be derived from the Maxwell equations, according to the procedure shown in Section 4.2.

The results of this section show that the final Hamiltonians consist of terms $\frac{\hbar^2 k^2}{2m}$ corresponding to *massive* photons and terms $k_x^p k_y^q \sigma_j$ (where p, q are non-negative integers) which couple momentum of light (k_x, k_y) and its polarization (encoded in σ_j). In these equations photons in the microcavity resemble massive particles with spin, that are subjected to spin-orbit interaction (for $p+q > 0$) and magnetic fields (for $p=q=0$). Therefore, we find it justified to refer to the effective Hamiltonians as *synthetic Hamiltonians* with spin-orbit coupling of light and artificial magnetic field.

As a final remark it is worth noting that formulas (4.52)–(4.56) are derived in a model that assumes perfect mirrors, i.e., it neglects TE-TM splitting

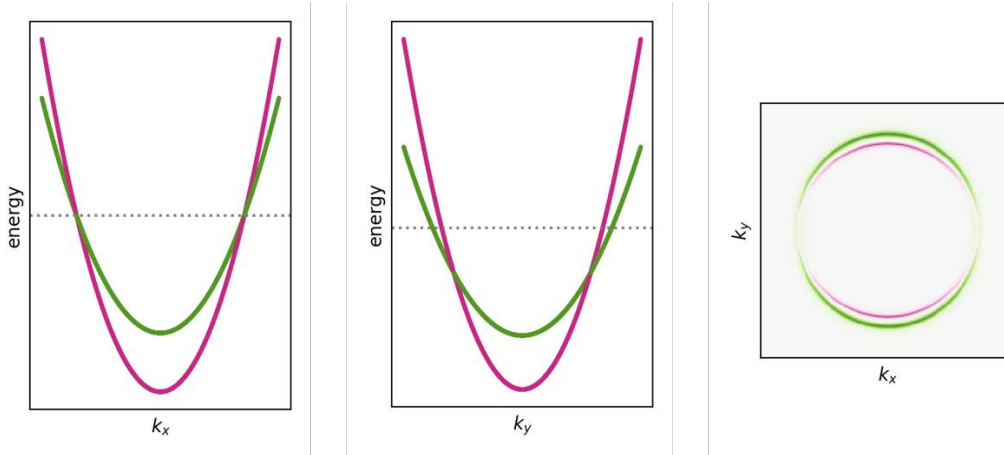


Figure 4.5: $(N+2, N)$ **regime**. Photonic modes dispersions in k_x and k_y direction, and constant energy cross-section (for the energy marked by black dotted line on both k_x and k_y dispersions) obtained from eq. 4.57. The colors correspond to the polarization direction, where green is polarized in the x direction and purple in the y direction.

occurring in the actual structure of the mirrors. Taking into account finite width of DBRs and the TE-TM splitting would lead to slight modifications of these equations. However, it would not change the symmetry of the system and, consequently, the structure of the Hamiltonians (4.50), (4.51), and (4.57). Thus, in the following chapters, the Hamiltonian parameters will be treated as fitting parameters.

Chapter 5

Tunable optical spin Hall effect

In this chapter, we focus on research devoted to the tunable optical spin Hall effect in dielectric microcavity containing a liquid crystal. In this part, we show that, thanks to the possibility to tune the H–V splitting, we were able to observe quadrupole spin textures typical for normal cavities as patterns well as never reported before resembling: dipoles, spin whirls, and spin doughnuts. The paper [67] K. Lekenta et al. 'Tunable optical spin Hall effect in a liquid crystal microcavity', *Light Sci Appl.*, **7**, 74, 2018 is the basis for the results presented in this chapter.

5.1. Sample

For this experiment the sample consisting of two dielectric mirrors made of 6 pairs of alternating SiO₂/TiO₂ dielectric layers, which were deposited on a 30 nm transparent electrode made of ITO grown directly on 4 mm thick quartz substrates, was used (Figure 5.1 **a**). On top of the DBR surface, 60 nm of polyimide SE1211 (with refractive index $n_{PI} = 1.54$) was spin-coated to ensure the homeotropic (HT) orientation of the mean direction of the liquid crystal molecules. The mirrors were mounted to a cavity by thermopolymerizing glue with 0.9 μm glass spacers. The cell was filled with a 1999C dual frequency nematic liquid crystal (DFNLC) ¹ (with $n_o = 1.504$, $n_e = 1.801$) in a vacuum chamber by capillary forces. The parameters of the 1999C LC are presented in Table 2.1 and details about the sample are summarized in the Table. 5.1. The sample was measured in transmission configuration (Figure 5.1 **b**), where the size of the pump spot has a diameter of 1 μm .

¹ DFNLC 1999C was custom designed and synthesized at the Military University of Technology

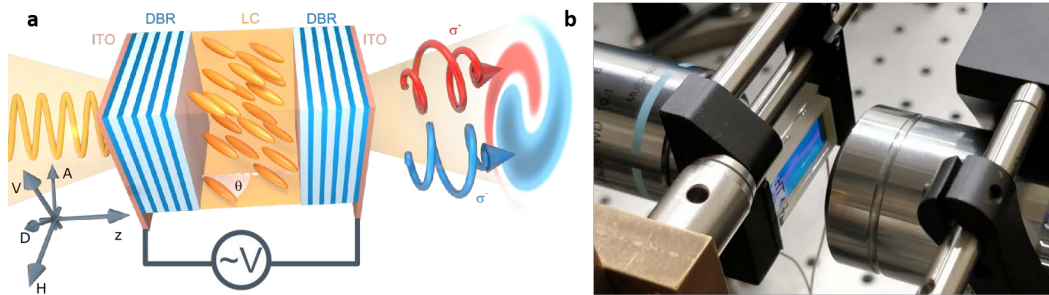


Figure 5.1: **a** Scheme of the sample used in the experiment showing the (N, N) regime [67]. **b** Photo of the sample used in the experiment. The liquid crystal cavity on 4 mm quartz substrates.

Table 5.1: Optical spin Hall effect – parameters of the sample.

Layer	Thickness, d	Refractive index, n
ITO	30 nm	1.89
SiO ₂	133 nm	1.456
TiO ₂	79.5 nm	2.436
PI SE1211	60 nm	1.54
LC 1999C	1.7 μ m	$n_o = 1.504, n_e = 1.801$

5.2. Dispersion relation: Tunability and H–V splitting

Due to the interaction of DFNLC with the inner surfaces of the cell covered with SE1211 polyimide at zero voltage, the director adopts the homeotropic orientation. This means that for light passing through the cell at normal incidence ($k = 0$, zero observation angle), the DFNLC medium is perceived as an optical medium of refractive index n_{eff} equal to the ordinary refractive index n_o of the DFNLC. The molecular director is aligned parallel to the z axis, resulting in a lack of polarization-dependent splitting at normal incidence. In Figure 5.2 **a**, we show the dispersion of cavity photons without voltage applied to the sample on the white-light reflectivity map performed for circular polarization σ_+ .

To avoid confusion with the nomenclature normally used to describe the TE–TM splitting, we will call it the H–V splitting (Δ_{HV}). Due to the fact that our medium is birefringent and tunable, the value of the splitting will change and will be related to the shift of horizontally polarized modes (along the x axis) versus vertically polarized ones (along the y axis) – Figure 2.11. In our case, the polarizations TE and TM are the same as H and V only if the angle ϕ is in the plane yz (see Fig. 1.11). That is, for each point (k_x, k_y) , the polarizations TE and TM are defined differently, while the polarizations H and V are globally fixed. In contrast to the standard understanding of TE–TM splitting, H–V separation of the modes can also occur for normal incidence (e.g. in HG arrangement of LC molecular director when no voltage is applied or in HT arrangement upon applying an external voltage).

By applying an external electric field, we control the tilt of the molecular director in the xz plane (plane perpendicular to the cavity plane) and thus shift the horizontally polarized mode (H). Figures 5.2 **b–d** present the dispersions of cavity photons for 8.2V, 8.6 V and 9.6 V. Based on the fitting to the dispersion relations, the values of Δ_{HV} were obtained, which were successively: 0 meV, 0.9 meV, 11.4 meV and 26.6 meV. In the presented measurements to tune the photonic modes, we used an external voltage of square waveform with frequency 30 kHz.

The cross-sections for $k = 0$ from the reflectivity maps shown in Fig. 5.2 allow for easy tracking of the energy changes of the cavity modes (Fig. 5.3 **a**). Without applied voltage, only one minimum is observed. The splitting becomes visible for voltages above 8.2 V. Based on the fitting to the measurements of reflectivity in the H and V polarizations, we can check how exactly

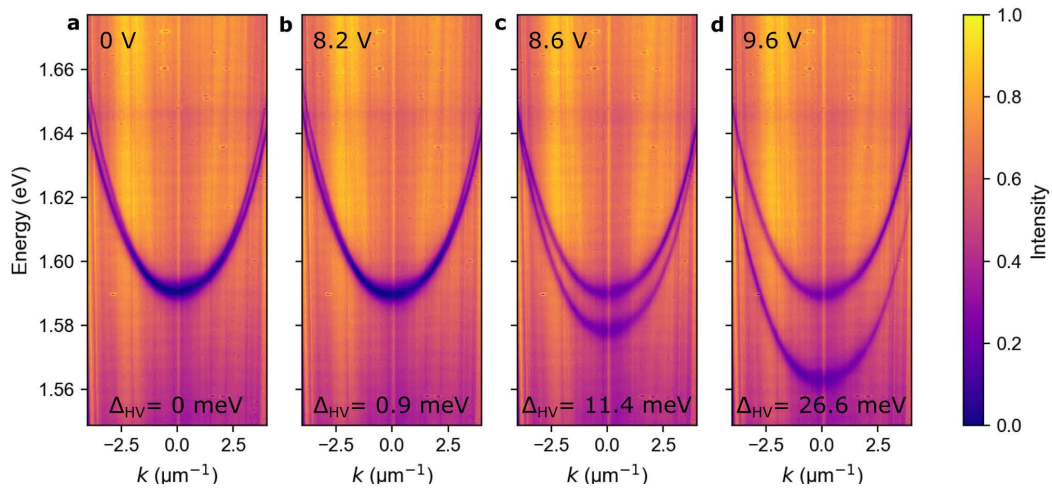


Figure 5.2: Tunability of the cavity modes with applied voltage. Dispersion of the cavity photons for successive voltages performed in circular polarization σ_+ . **a** 0 V, **b** 8.2 V, **c** 8.6 V and **d** 9.6 V. The values of Δ_{HV} obtained from the fitting to the dispersions are: 0 meV, 0.9 meV, 11.4 meV and 26.6 meV, respectively.

the energy of both photonic modes changes (see Figure 5.3 **b**). As described before, the horizontal polarized mode shifts toward red with respect to the zero-voltage case, and the vertical polarization mode remains unchanged. The Δ_{HV} splitting is tunable between 0 and 27.6 meV as presented in figure 5.3 **c**². Figure 5.3 **d** shows how the Q-factor changes with the applied voltage. The mean value of the Q-factor for the studied sample was 260.

Figure 5.4 shows the reflectivity map corresponding to the (N, N) regime, presented as a function of wavenector k_y , calculated according to Eq. (2.5). By fitting the Hamiltonian spectrum 4.50 to the experimental dispersion, including an additional $\sim k_y^4$ term to improve the conformity of theory and experiment, we determine that in our system $m = (6.55 \pm 0.12) \times 10^{-6} m_e$, $\delta = (6.4 \pm 1.1) \text{ eV } \mu\text{m}^2$. The fitted spectra are shown as dotted lines in the Figure 5.4.

5.3. Polarization patterns

Without applied voltage, the light transmitted through the liquid crystal microcavity shows similar polarization properties as shown and discussed in

² A similar analysis is presented in Fig. 3.2. In this chapter, another sample is used that contains liquid crystal 1999C.

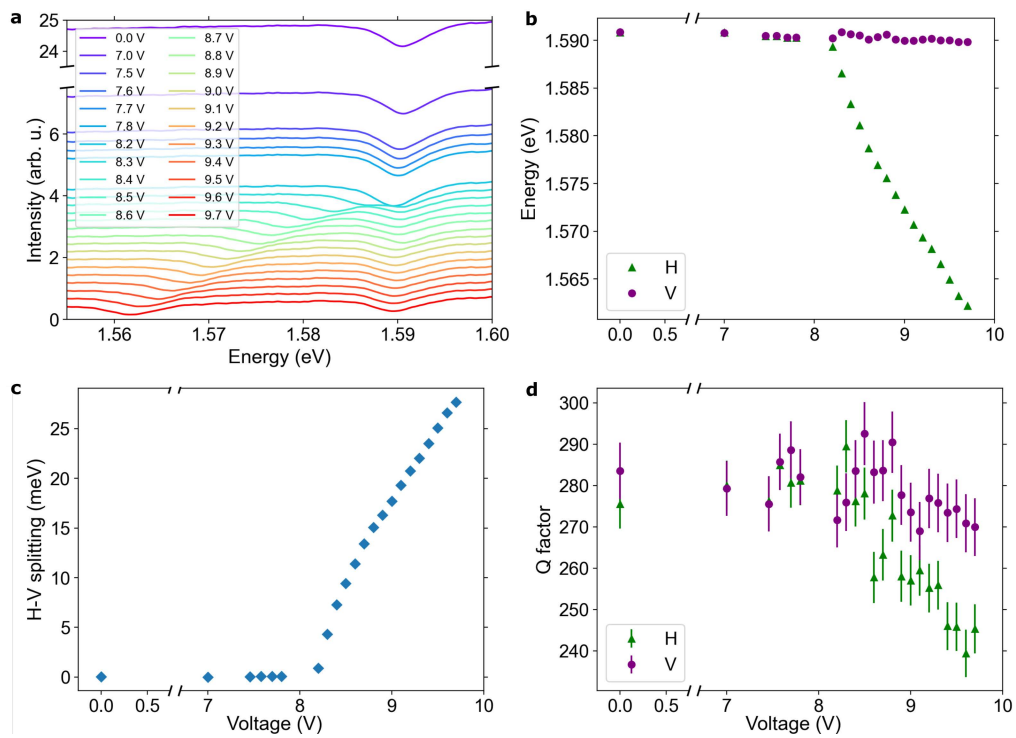


Figure 5.3: Tunability of the cavity modes with applied voltage. **a** Cross-sections of reflectance maps for normal incidence for subsequent applied voltages showing tunability. **b** Energy of the cavity modes polarized horizontally (green triangles) and vertically (purple dots). **c** Dependence on the applied voltage of the H-V splitting for normal incidence and **d** corresponding Q-factor of horizontally (green triangles) and vertically (purple dots) polarized cavity modes. The vertical lines in **b–d** denote the measurement uncertainty, although in **b** and **c** they extend within the size of the markers.

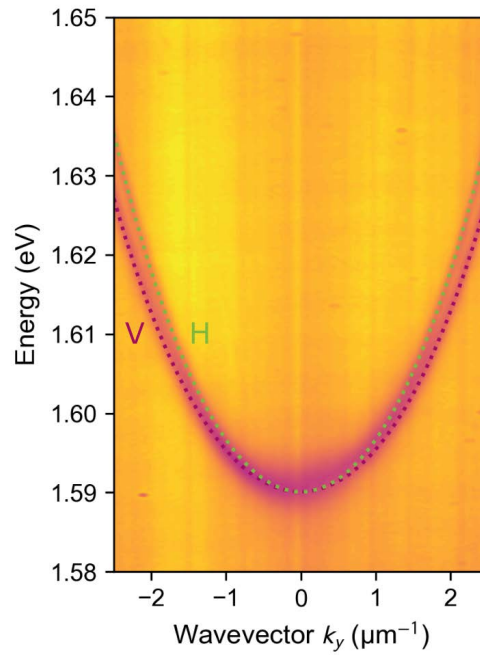


Figure 5.4: Reflectivity map at voltage 0V, as a function of wavevector k_y in the cavity plane. The dotted lines denote spectra calculated with the Hamiltonian (4.50), with parameters fitted to the experimental dispersion with the least squares method, including an additional k_y^4 term. The color of the lines denote the polarization of light: green – horizontal, purple – vertical.

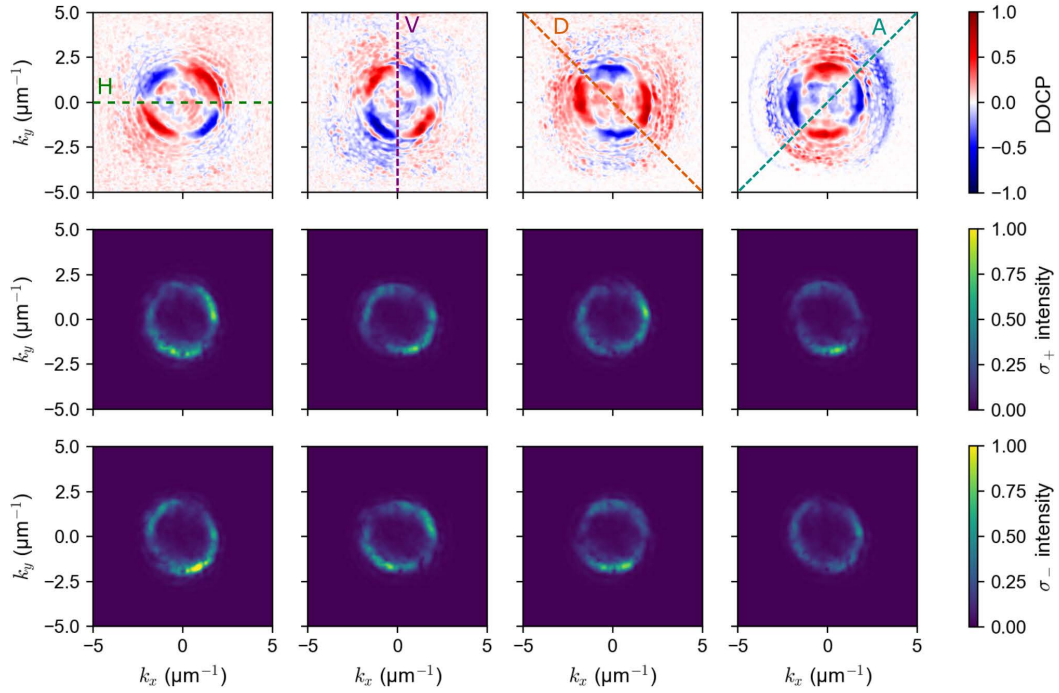


Figure 5.5: Degree of circular polarization (DOCP) for different polarizations of incident light in 0.0 V with corresponding transmission maps for σ_+ and σ_- polarization on detection. From the left: horizontal, vertical, diagonal, anti-diagonal. The dashed lines show the polarization axes of the excitation light.

the section 1.5.2 in the Introduction (Chapter 1). The wavelength of the incident laser light was set at 775 nm (1.599 eV). In reciprocal space (k_x, k_y) we observe the quadrupole polarization pattern of degree of circular polarization (DOCP, i.e., S_3 Stokes parameter) for transmitted light as presented in Figure 5.5 for horizontal, vertical, diagonal and anti-diagonal polarization of incident light, similar to the pattern presented in Fig. 1.26 and Fig. 1.27.

Depending on the polarization of the incident light, the profile of the quadrupole pattern is different. In each case, the DOCP is observed along an ellipse whose axes lie parallel and perpendicular to the axis of the polarization of the incident light.

For the H polarization, zero DOCP is observed along the x and y axes. The maxima corresponding to the σ_+ polarization lie in the second and fourth quadrants of the coordinate system. The minima denoting the σ_- polarization are located in the first and third quadrants. The patterns for the V, D, and A polarizations are rotated around the origin relative to H by angles: $\pi/2$,

$\pi/4$, and $-\pi/4$, respectively. These rotations are consistent with the angles between the polarization axis H and the axes V, D, and A.

The polarization patterns change drastically when voltage is applied to the LCMC. Figure 5.6 displays the reciprocal space maps of light transmitted through the sample for several magnitudes of voltage, obtained with horizontally polarized incident light. For the 8.2 V bias, corresponding to H–V splitting 0.9 meV, the pattern remains similar to the result for an unbiased sample. However, at voltages 8.6 V and 9.6 V, which induce H–V splittings 11.4 meV, and 26.6 meV, respectively, the polarization pattern acquires a dipolar profile. At 9.6 V the maximum of circular polarization, defined as the difference between the transmission intensities σ_+ and σ_- , lies on the positive y axis, while the minimum is on the negative y axis. The x axis, which is parallel to the H polarization axis, has zero circular polarization. In the DOCP pictures for voltages 8.6 V and 9.6 V the dipolar profile is not as evident.

Moreover, with increasing voltage, we observe an increase in the radius of the transmitted light cone for the component of horizontal polarization, because this mode is tunable and the parabola (H in Fig. 5.4) lowers its energy. For the polarization pattern of circular polarization (S_3), we do not notice a significant change in diameter regardless of the value of the applied voltage. In the case of excitation with vertically polarized light (Fig. 5.7), the radius of the transmitted light cone remains unchanged with increasing voltage, while the diameter of the DOCP pattern increases.

Figure 5.8 shows the DOCP for the diagonal polarization of the incident laser. For a zero applied voltage, as described above, we observe the rotation of the DOCP quadrupole pattern by $\pi/4$ with respect to that observed for the horizontal laser polarization. In the presence of an externally applied field, we observe quenching of the quadrupole texture in favor of a homogeneously σ_+ circularly polarized ring-like pattern (8.6 V), which then transforms into a whirl pattern for 9.6 V.

Analogous measurements were made for the antidiagonally polarized laser, as shown in Figure 5.9. In this case, the initial quadrupole polarization pattern is rotated relative to the horizontal polarization by $-\pi/4$, which then transforms into a σ_- polarized doughnut pattern for 8.6 V. At a higher voltage (9.6 V), we again observe a vortex texture with opposite chirality and opposite circular polarization (σ_-) with respect to that shown for diagonal excitation.

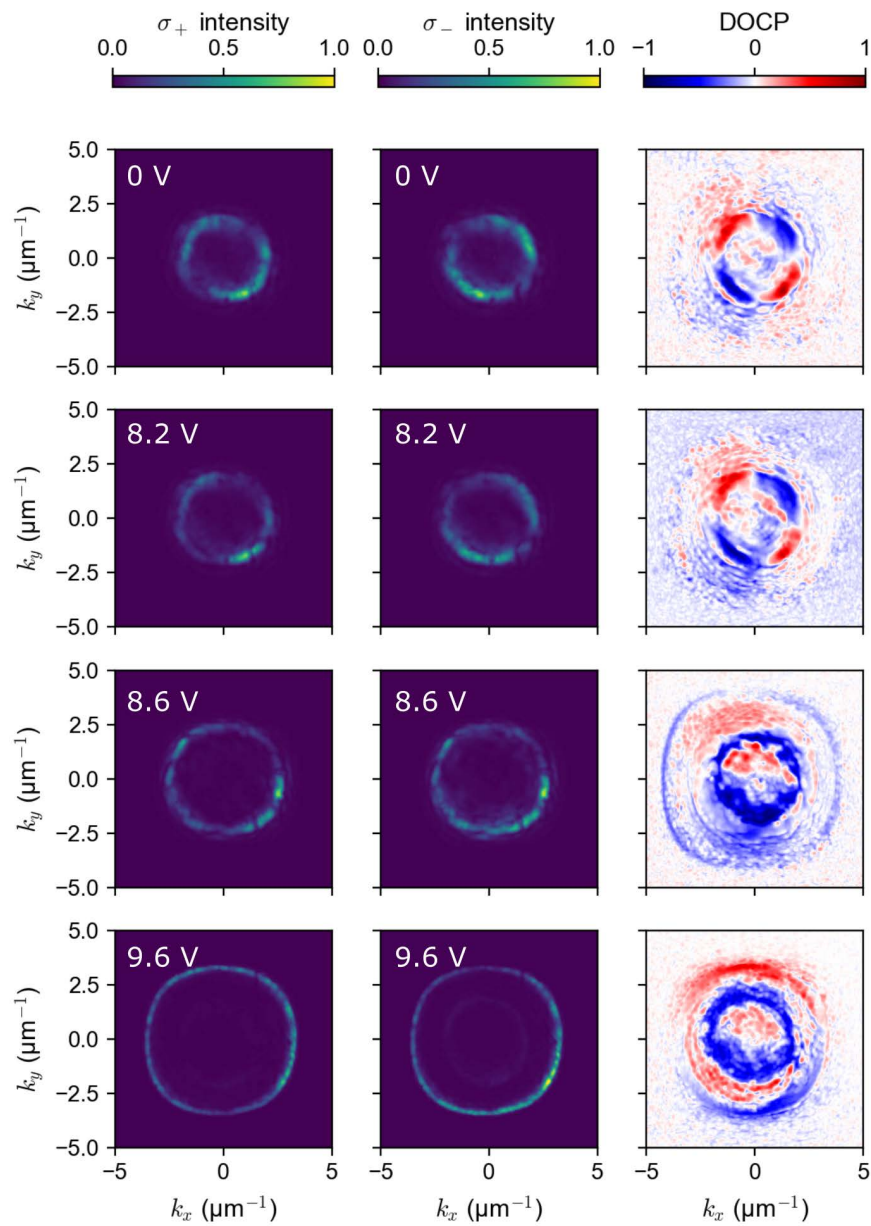


Figure 5.6: **Tunable optical spin Hall effect in horizontal (H) polarization of the incident light for different voltages applied to the structure.** Two left columns presents transmission of the laser light for circular (σ_+/σ_-) polarization on the detection line. Third column presents the degree of circular polarization (S_3 parameter).

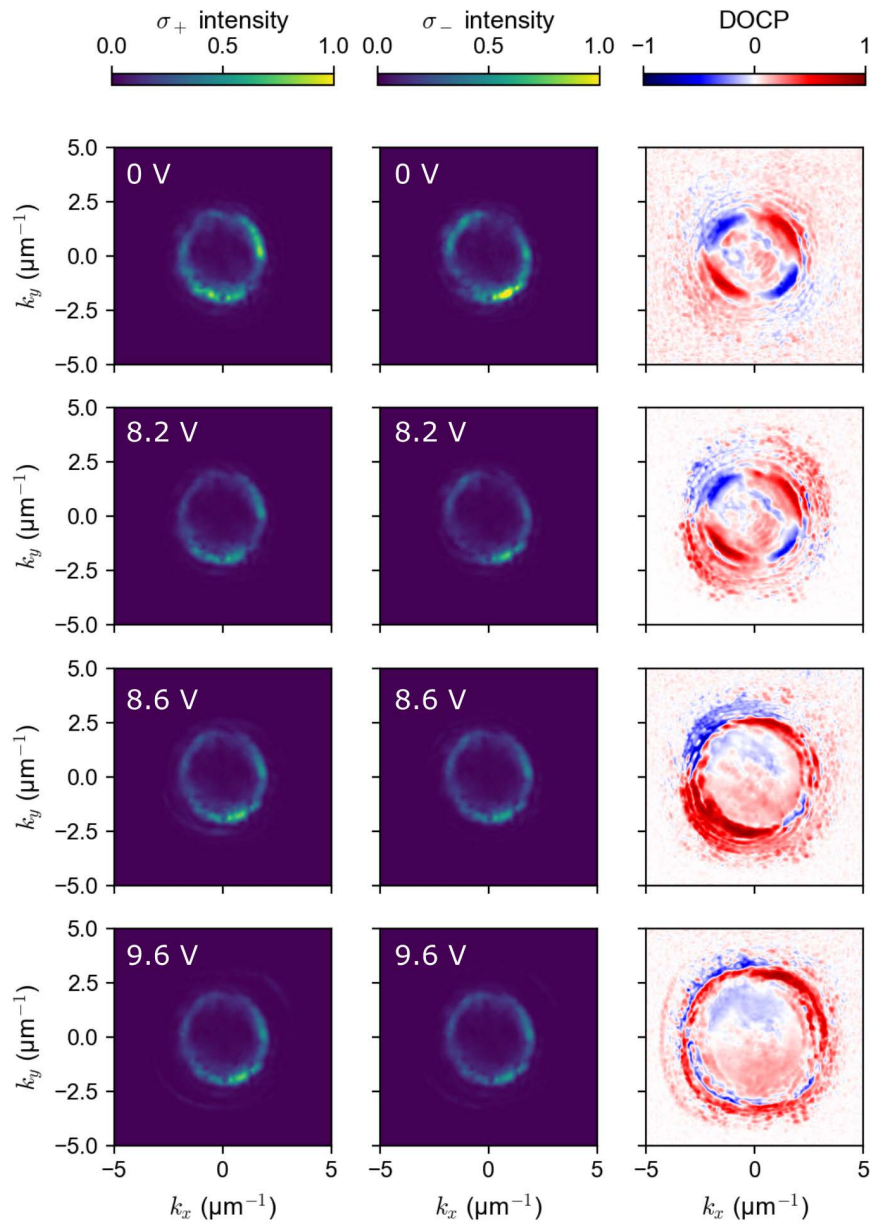


Figure 5.7: **Tunable optical spin Hall effect in vertical (V) polarization of the incident light for different voltages applied to the structure.** The two left columns present transmission of the laser light for circular (σ_+/σ_-) polarization on the detection line. The third column presents the degree of circular polarization (S_3 parameter).

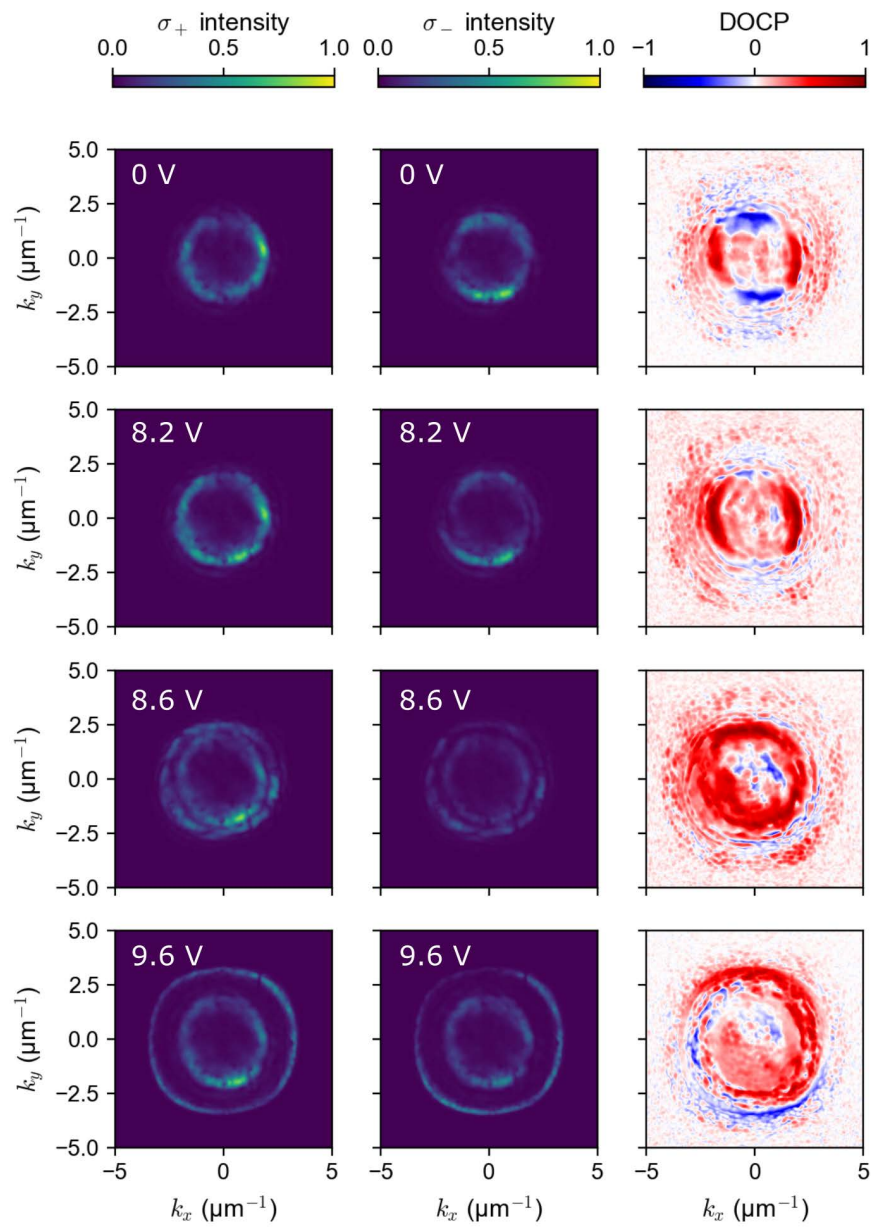


Figure 5.8: **Tunable optical spin Hall effect in diagonal (D) polarization of the incident light for different voltages applied to the structure.** The two left columns present transmission of the laser light for circular (σ_+/σ_-) polarization on the detection line. The third column presents the degree of circular polarization (S_3 parameter).

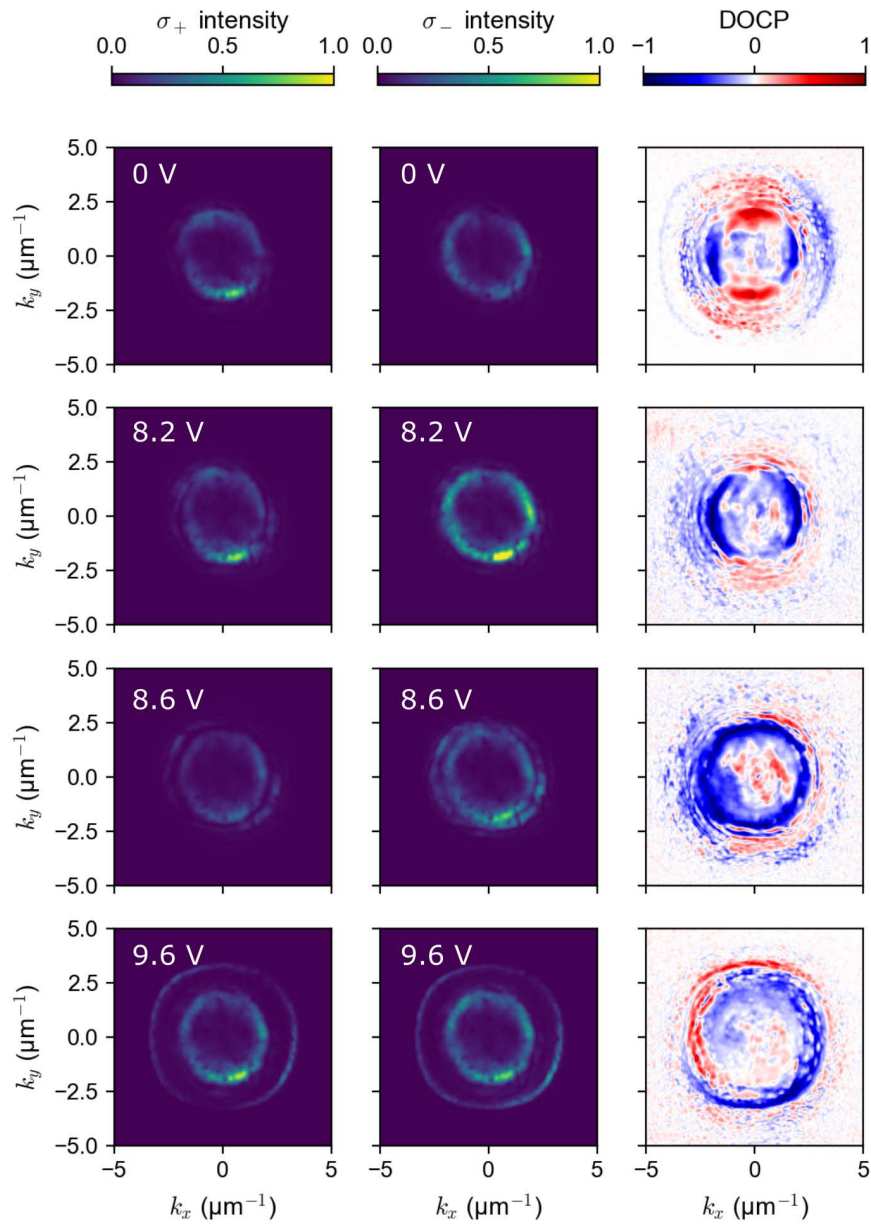


Figure 5.9: **Tunable optical spin Hall effect in anti-diagonal (A) polarization of the incident light for different voltages applied to the structure.** The two left columns present transmission of the laser light for circular (σ_+/σ_-) polarization on the detection line. The third column presents the degree of circular polarization (S_3 parameter).

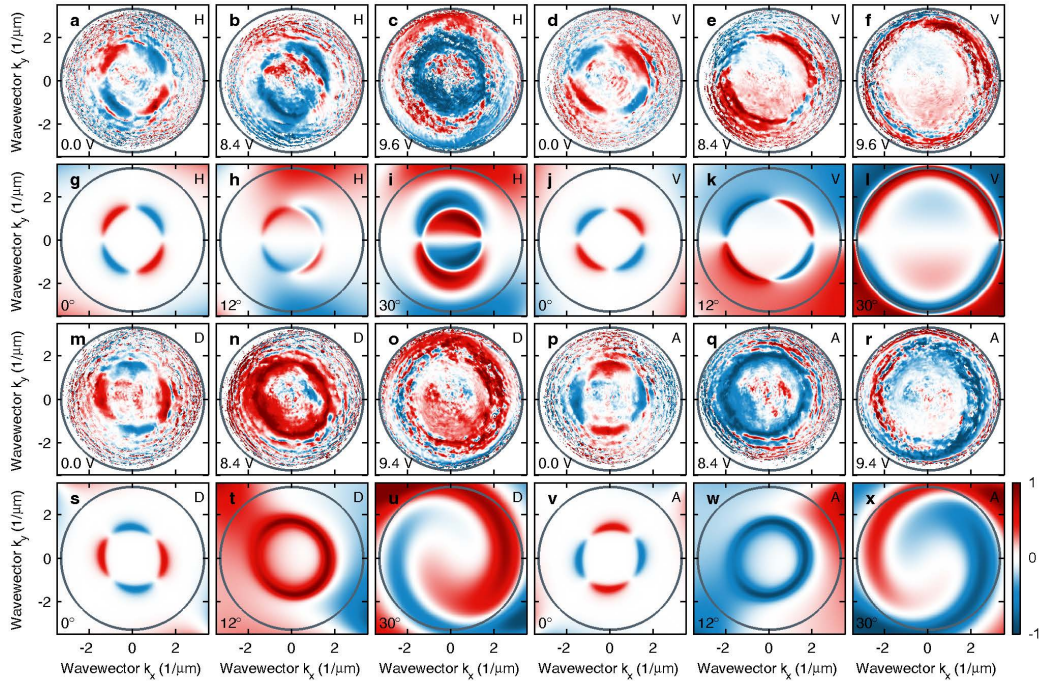


Figure 5.10: **Tunable optical spin Hall effect: experiment vs model.** [67]

These results can be fully understood and modeled by numerical simulation of light transmission using the Berreman method [67]. Numerical simulations were performed using a Mathematica code written by Mateusz Król. The comparison is shown in Figure 5.10.

By using LCMC we were able to observe an optical analogue of the spin Hall effect for parameters range far beyond those previously considered experimentally and theoretically. The H–V splitting (except in the case of no applied voltage) corresponds to the term $\frac{1}{2}(E_H - E_V)\sigma_x$ which is analogous to the Zeeman term of an electron in a magnetic field. Although this term is absent in the (N, N) Hamiltonian, it is present in the $(N+2, N)$ Hamiltonian. As mentioned in the section 4.3 concerning symmetry of the LCMC, it can be applied to the case of (N, N) regime with slightly tilted molecules. Then the symmetry group of the system is reduced to C_{2h} . This energy difference, $E_H - E_V$, is proportional to the artificial magnetic field that acts on the spin degree of freedom of photons.

5.4. Summary

One of the most interesting phenomena directly dependent on the TE–TM splitting in a cavity is so-called optical spin Hall effect. Originally predicted and observed in microcavities in strong coupling regime leads to spin separation occurring in both: real and reciprocal space caused by TE–TM splitting acting as effective magnetic field. This effect which was studied extensively in exciton-polariton systems only recently was shown to exist also in an empty cavity. In the research presented in this chapter, we show that thanks to novel design and unique possibility to tune the H–V splitting for any given observation angle, we are able to observe typical for normal cavities quadrupole spin patterns as well as never reported before patterns resembling: dipole, spin whirls and spin doughnuts. We underline that this is the first demonstration of electrically tunable polarization-dependent splitting in microcavities [67], which are the basic components for devices employed strong light-matter coupling and lasing [14]. Our work shows the effectiveness of integration and control of spin-polarized light with room-temperature devices.

Chapter 6

Rashba-Dresselhaus interaction

In this chapter we concentrate on the results obtained for the multimode liquid crystal cavity in the $(N + 1, N)$ regime. We show that the system in this regime is described by a Hamiltonian with Rashba-Dresselhaus term, originally used to describe fermions. The results presented in this chapter are the subject of the article [65] Katarzyna Rechcińska et al., "Engineering spin-orbit synthetic Hamiltonians in liquid-crystal optical cavities" *Science*, **366**, 727-730 (2019)

6.1. Sample

For the experiment showing the $(N + 1, N)$ regime the liquid crystal microcavity was assembled in plane-parallel quartz plates of 4 mm thick each. Then, the transparent, conductive ITO layer and the distributed Bragg reflector (DBR) were deposited. The thickness of the ITO layer (with refractive index $n_{ITO} = 1.89$) obtained was $d_{ITO} = 30nm$. DBR consists of 6 pairs of alternating TiO_2 (refractive index $n_{TiO_2} = 2.436$ at $\lambda = 632.8nm$) and SiO_2 (refractive index $n_{SiO_2} = 1.456$ at $\lambda = 632.8nm$) layers. In the DBR mirrors, a polymer aligning layer of SE130 polyimide (PI) solution was spin-coated and dried. The final polymer layer was subjected to the rubbing procedure to induce a planar (homogeneous) orientation of the molecular director of a liquid crystalline layer in the cavity. The thickness of the polyimide layer (refractive index $n_{PI} = 1.63$) has been estimated at 60 nm using ellipsometry measurements. The final cell was assembled using glass spacers with a nominal diameter of $0.9 \mu m$ with thermally polymerized adhesive. To fill the sample, the high birefringence nematogenic mixture 2091¹ was used. The parameters of the liquid crystal are presented in Table 2.1 and details about the sample

¹ 2091 LC was designed and synthesized at the Military University of Technology.

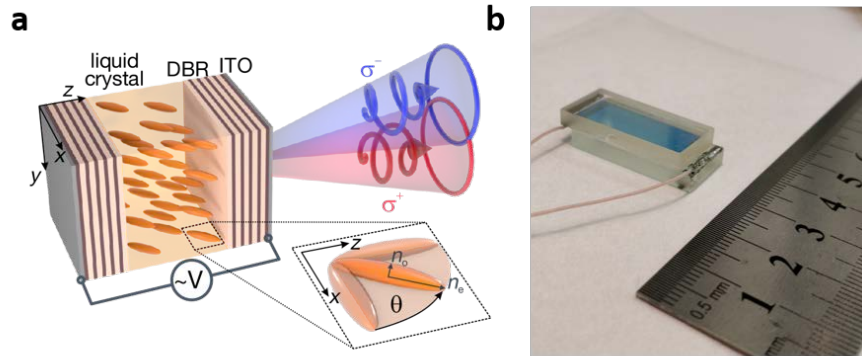


Figure 6.1: **a** Scheme of the sample used in the experiment showing the $(N + 1, N)$ regime [65]. **b** Real sample used in the experiment.

Table 6.1: Rashba-Dresselhaus effect – parameters of the sample.

Layer	Thickness, d	Refractive index, n
ITO	30 nm	1.89
SiO ₂	128.8 nm	1.456
TiO ₂	77 nm	2.436
PI	60 nm	1.63
LC	3.5 μ m	$n_o = 1.539, n_e = 1.951$

are summarized in the Table. 6.1. The sample is schematically shown in Figure 6.1 **a** and the photo is shown in Figure 6.1 **b**.

6.2. $(N + 1, N)$ regime – the Rashba-Dresselhaus dispersion relation

The cavity used in the experiment is characterized by a planar (homogeneous) arrangement of the liquid crystal (compare Figure 3.5 **a**). The preferential arrangement of the molecular director, without applied external voltage, is along the x axis. Therefore, the photonic modes originally observed in the reflectivity spectrum are energetically separated along the entire dispersion (see Figure 6.2)². Figure 6.2 presents reflectivity maps for six main polarizations. The cavity is multimode, and three modes can be seen within one

² All the dispersions presented in this section are along $k_x = 0$. Compare with Fig. 2.4

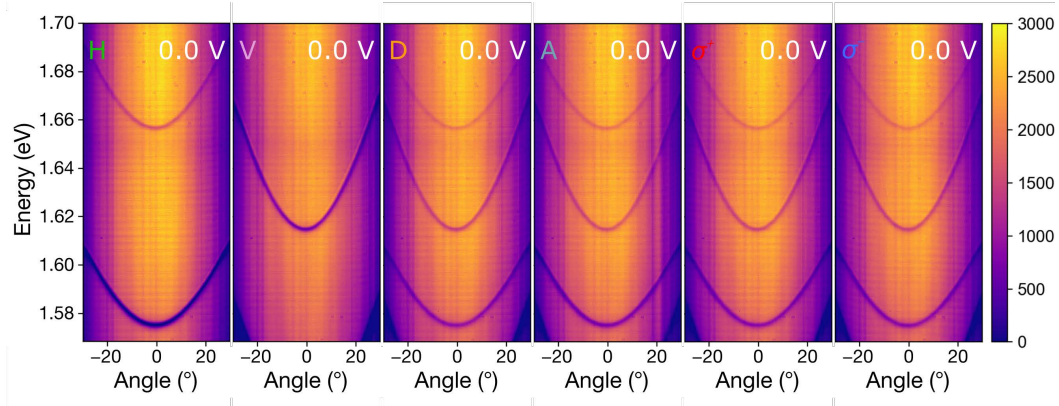


Figure 6.2: Reflectivity maps in Fourier space without applied voltage for six polarizations on detection for $k_x = 0$. From left: horizontal (H), vertical (V), diagonal (D), antidiagonal (A), right circular (σ_+), left circular (σ_-).

spectral window – two polarized horizontally and one polarized vertically. The modes observed in the H and V polarizations are energetically separated. As shown in Figure 6.3, the observed photonic modes are fully linearly polarized H and V, and virtually no contribution from the other polarization states can be seen. The low-energy photonic modes observed for high angles, especially visible on the polarization degree maps, come from the stopband. Note that in the case of analysis of the reflectivity maps, the light transmitted through the cavity corresponds to a decrease in the intensity of the detected signal. Thus, the reflected light acquires a certain polarization through a decrease in the intensity of the opposite polarization component, which is transmitted into the cavity. It follows that the polarization of the reflected light, measured by the Stokes parameters, is opposite to the polarization of the light transmitted into the cavity. Thus, the green color in the maps of the Stokes parameter S_1 corresponds to the modes with V polarization and the purple color corresponds to the H polarized modes (inversely to the case of analyzing the transmission maps). We note here that in the case of H and V polarized modes in our device, the polarization of light entering the cavity is preserved inside the cavity and in the light leaving the cavity.

When two successive cavity modes with opposite parity are brought into resonance, the nature of the eigenstates deeply modifies. This can be seen by further increasing the voltage, which leads to another resonance, i.e. $(N + 1, N)$. Experimentally we observe this resonance for a voltage of 2.46 V. The reflectivity maps for the different polarizations of the detected light are

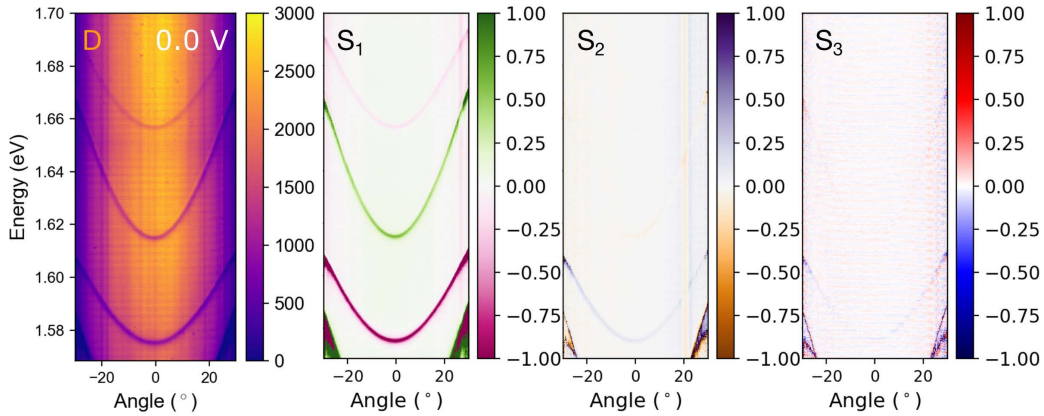


Figure 6.3: Degree of polarization maps obtained from reflectance maps without applied voltage. From left: reflectivity dispersion for diagonal polarization, S_1 Stokes parameter map, S_2 Stokes parameter map, S_3 Stokes parameter map.

shown in Figure 6.4. The shape of the dispersion of cavity photons changes significantly. It demonstrates two minima of opposite circular polarization. For linear polarizations of detected light we observe two separated parabolas. On the other hand, in the case of circular polarizations σ_+ and σ_- , we can see individual parabolic dispersions symmetrically shifted with respect to the $k_y = 0$ line.

The maps of the degree of polarization, presented in Figure 6.5, clearly show that the cavity modes become fully circularly polarized and the contribution from linear polarizations is zero. The observed dispersion, with its shape and polarization, realizes the Rashba-Dresselhaus Hamiltonian.

While the H and V polarized modes have uniform polarization in the cavity, this is not the case for the circularly polarized modes. As discussed in chapter 4.4 the Hamiltonian of the $(N + 1, N)$ regime can be defined in the basis of circular polarizations of out-coupled light σ_{\pm} at the mirror interface. In this regime, the LC layer acts as a half-wave plate, and the polarization near the mirrors is not conserved deeper inside the cavity. As shown in Figure 6.6 **b**, the handedness of light changes after crossing the width of the cavity and after internal reflection from the mirror. As a result, the light leaving the cavity has the same σ_{\pm} polarization on both sides of the cavity (see Figure 6.6 **a**), as long as it originates from a single mode. In this sense, we refer to these cavity modes as σ_{\pm} polarized.

Figure 6.7 shows the reflectivity map with the Rashba-Dresselhaus dis-

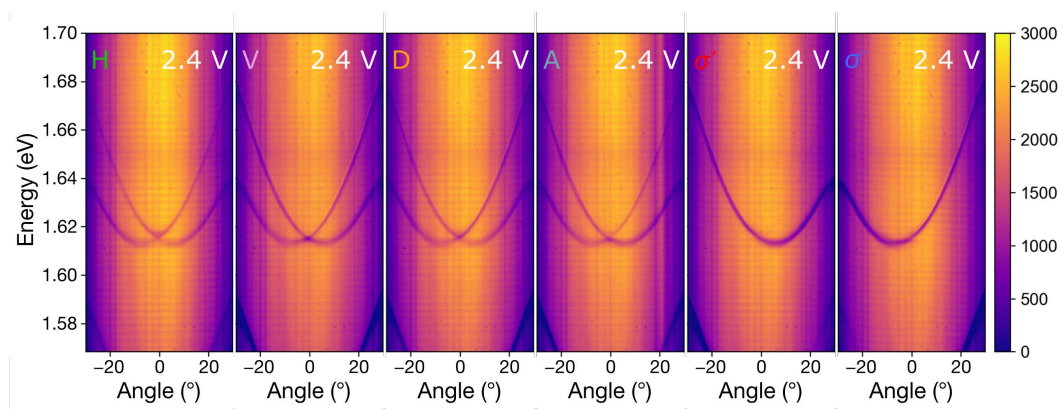


Figure 6.4: **Rashba-Dresselhaus dispersion.** Reflectivity maps in Fourier space for 2.46 V applied for six polarizations. From left to right: horizontal (H), vertical (V), diagonal (D), antidiagonal (A), right circular (σ_+), left circular (σ_-).

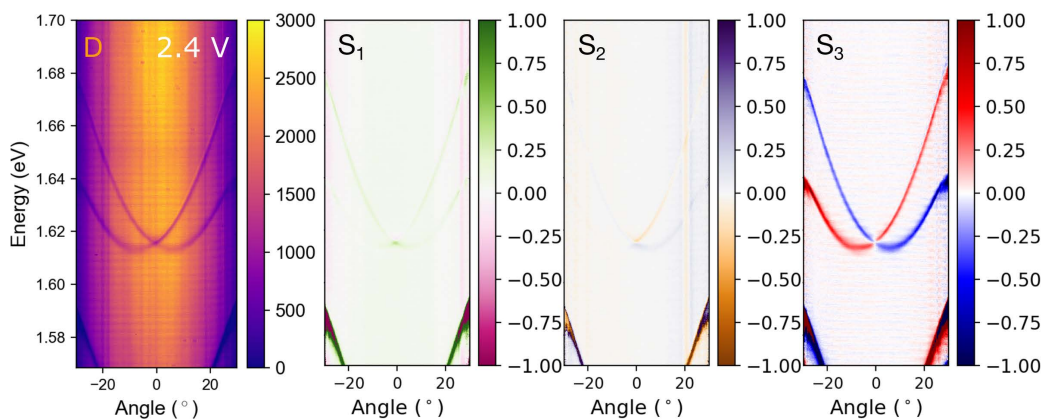


Figure 6.5: **The dispersions of the degree of polarization realising Rashba-Dresselhaus Hamiltonian.** From left to right: reflectivity dispersion for diagonal polarization, S_1 , S_2 and S_3 Stokes parameters obtained from reflectance maps for 2.46 V applied.

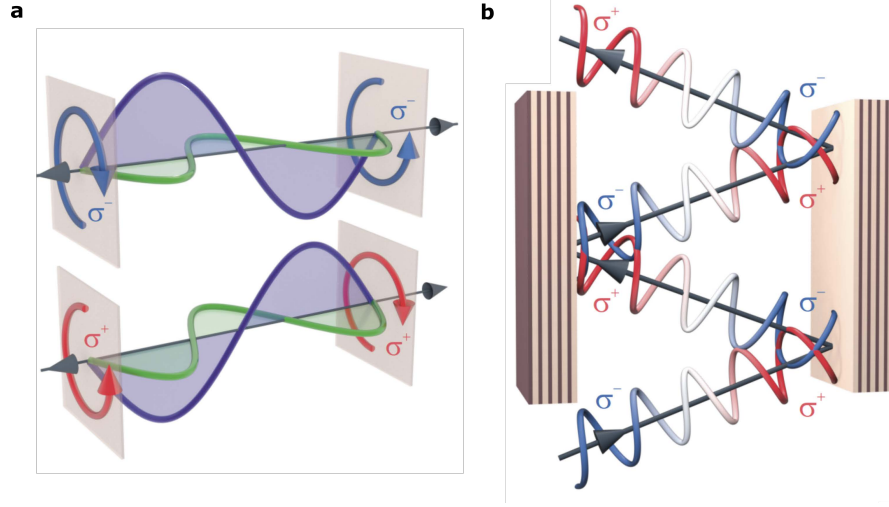


Figure 6.6: **Polarization of photonic modes in the $(N + 1, N)$ regime [65].** **a** Schematic representation of the modes of opposite parity in LCMC with polarization of the light at the mirror interfaces. **b** Polarization of the cavity modes inside the LCMC.

persion, presented as a function of the wavevector k_y , which was calculated according to Eq. (2.5). By fitting the Hamiltonian spectrum (4.51) to the experimental reflectivity map, we determine $m_y = (6.81 \pm 0.05) \times 10^{-6} m_e$, $\alpha = (34.0 \pm 0.4) \text{ eV \AA}$. We assumed $\Delta E = 0$ and $\delta_y = 0$. The fitted spectra are shown as dotted lines in the Figure 6.7.

6.2.1. (N, N) and $(N + 2, N)$ regimes

Importantly, for the multimode cavity described in this chapter, it is possible to observe the other regimes: (N, N) and $(N + 2, N)$. Here we briefly demonstrate them.

By applying to the structure a voltage of 1.3 V, we can bring the H- and V-polarized modes to the resonance which belongs to the $(N + 2, N)$ regime. The modes are degenerate at $k_y = 0$. In Fig. 6.8 showing the reflectivity maps obtained by detecting different polarizations of light, we can clearly see two photonic modes. For H and V polarizations of the detected light, we observe one mode on each map. Looking at the Stokes parameter maps in Fig. 6.9), we can see that this is related to the fact that these modes are purely linearly polarized. It can be seen that the H-polarized mode has a greater effective

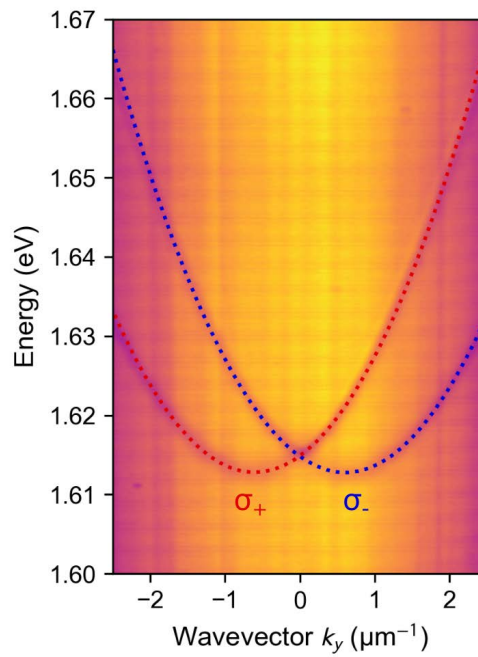


Figure 6.7: **Rashba-Dresselhaus dispersion.** Reflectivity map as a function of wavevector k_y in the cavity plane. The dotted lines denote spectra calculated with the Hamiltonian (4.51), with parameters fitted to the experimental dispersion with the least squares method. The color of the lines denote the polarization of light: red – σ_+ , blue – σ_- .

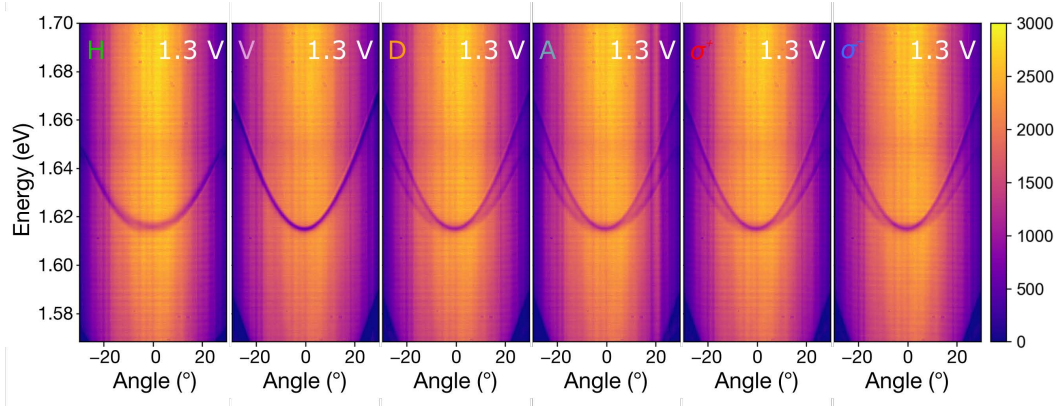


Figure 6.8: Reflectivity maps in Fourier space for 1.3 V applied voltage for six polarizations. From left to right: horizontal (H), vertical (V), diagonal (D), antidiagonal (A), right circular (σ_+), left circular (σ_-).

mass than the V-polarized mode, which is consistent with a non-zero value of the parameter δ_y in the Hamiltonian (4.57).

Increasing the voltage to 100 V leads to another resonance, as shown in Figure 6.10. With this voltage, we are able to tilt the molecular director to the HT arrangement, i.e., rotate it by 90° from the initial planar arrangement. In this case, we induce the resonance of modes with the same indices, i.e., the (N, N) regime. We can see that the observed modes are practically completely degenerate for $k_y = 0$ ³.

Again, the cavity modes become purely linearly polarized (Figure 6.11). In this case, the H-polarized mode has a lower effective mass than the V-polarized mode due to TE-TM splitting accounted for by the parameter δ in the Hamiltonian (4.50). We can see that there is an anisotropy of the effective masses depending on the director orientation.

6.3. Tomography

In order to provide a complete view of the regimes discussed above, we present here the tomography measurements, which provide an insight into the

³ The minor splitting observed experimentally for $k_y = 0$ results from the high voltage that has to be applied to the sample. Under such conditions, the photonic modes broaden, and the image becomes unstable. Over time, we observe modes shifting. This problem can be minimized, for example, by using another liquid crystal or increasing the thickness of the cavity.

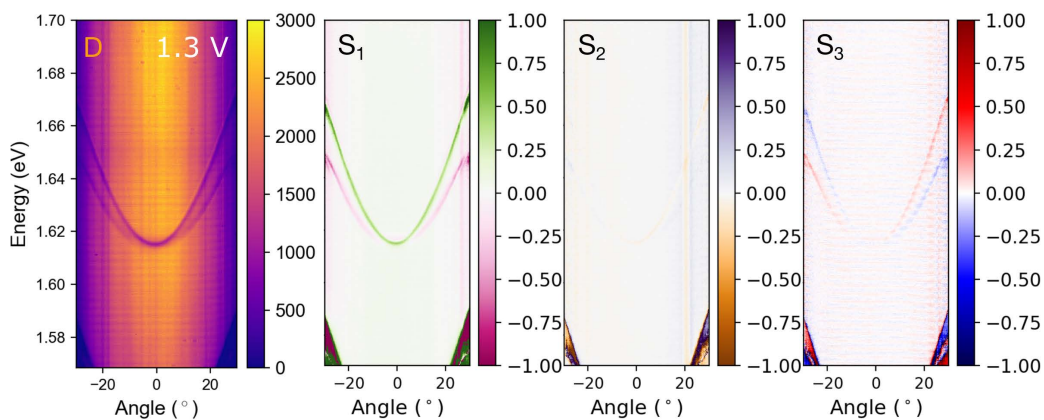


Figure 6.9: Degree of polarization maps obtained from reflectance maps for 1.3 V applied voltage. From left to right: reflectivity dispersion for diagonal polarization, S_1 Stokes parameter map, S_2 Stokes parameter map, S_3 Stokes parameter map.

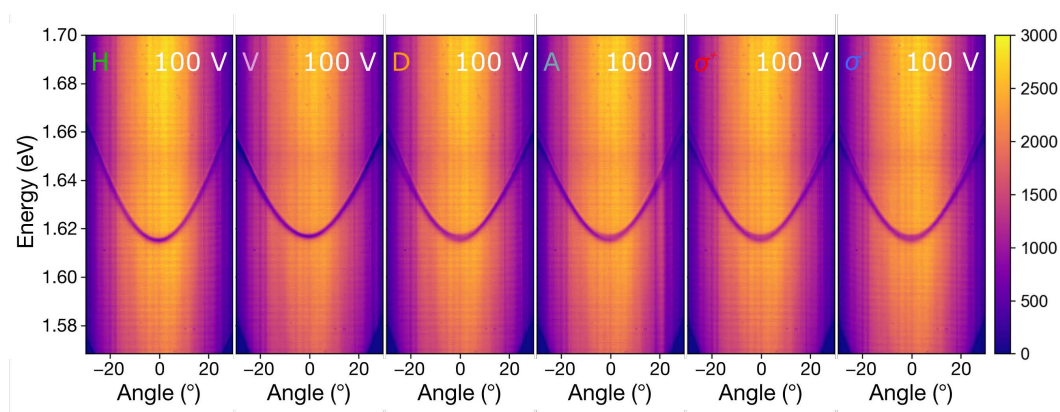


Figure 6.10: Reflectivity maps in Fourier space for 100 V applied for six polarizations. From left to right: horizontal (H), vertical (V), diagonal (D), antidiagonal (A), right circular (σ_+), left circular (σ_-).

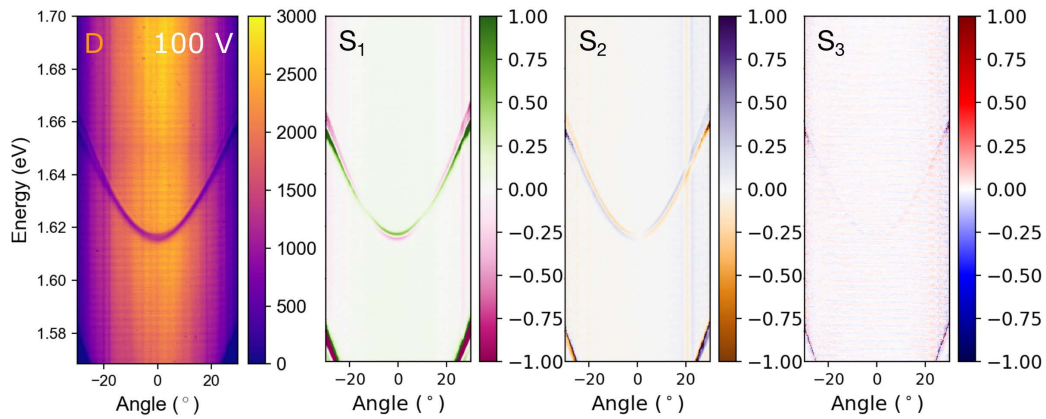


Figure 6.11: Degree of polarization maps obtained from reflectance maps for 100 V applied. From left to right: reflectivity dispersion for diagonal polarization, S_1 Stokes parameter map, S_2 Stokes parameter map, S_3 Stokes parameter map.

full dispersion of photonic modes. Figure 6.12 shows reflectivity tomography measured in the reciprocal space with the corresponding Stokes parameters S_1 and S_3 for 0.00 V and 1.38 V. In the Figure we denoted the angular coordinates as a and b , corresponding to reciprocal axes k_x and k_y , respectively. The figure shows selected cross-sections at constant energy, constant a and constant b . With no voltage applied, the dispersion of the cavity modes comprises two coaxial paraboloids that are separated and linearly polarized. Applying a voltage of 1.38 V corresponds to the mode resonance ($N+2, N$), for which the photonic modes are fully linearly polarized. Figure 6.13 **a** shows a three-dimensional view of the experimental reciprocal space tomography. The data points defining the presented dispersion surfaces denote minima of the reflectivity spectra at consecutive a and b values. The green surface is obtained from the spectrum of H polarized light, while the purple surface pertains to the spectrum of V polarized reflected light.

In Figure 6.14 we present the Rashba-Dresselhaus regime observed at 2.48 V and two sets of results, one at a slightly lower voltage of 2.42 V and one at a slightly higher voltage of 2.60 V. As we can clearly see in the Stokes parameter S_1 maps, some linear polarization is preserved for 2.42 V applied to the sample (Fig. 6.14 **b**) and similarly for 2.60 V (Fig. 6.14 **h**). The main contribution is from the circular polarization, as can be seen in S_3 Stokes parameter tomography (Fig. 6.14 **c, i**). For exact Rashba-Dresselhaus regime at 2.48 V (Fig. 6.14 **e**) there is no contribution from linear polarization and

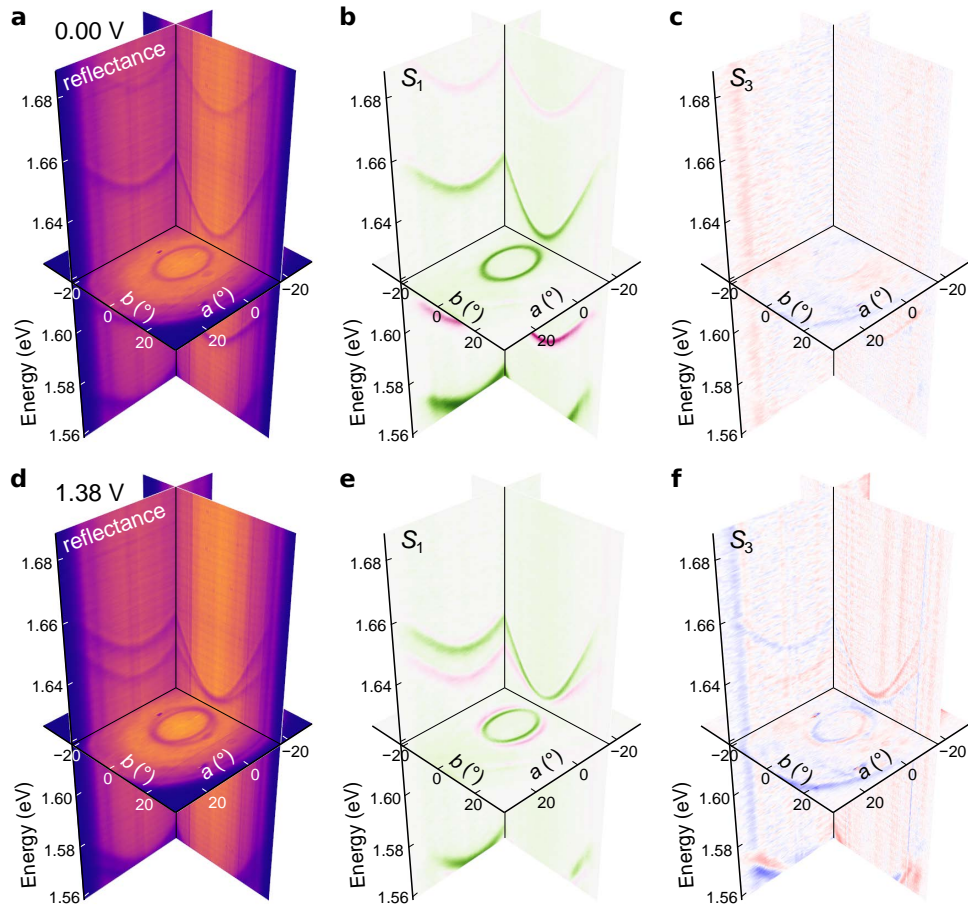


Figure 6.12: **No voltage and $(N + 2, N)$ regime.** Experimental reciprocal space tomography of reflectance at **a** 0.0 V and **d** 1.38 V. **b**, **c** Corresponding reciprocal space tomography of S_1 and S_3 Stokes parameters for 0.0 V and **e**, **f** corresponding reciprocal space tomography of S_1 and S_3 Stokes parameters for 1.38 V, respectively.

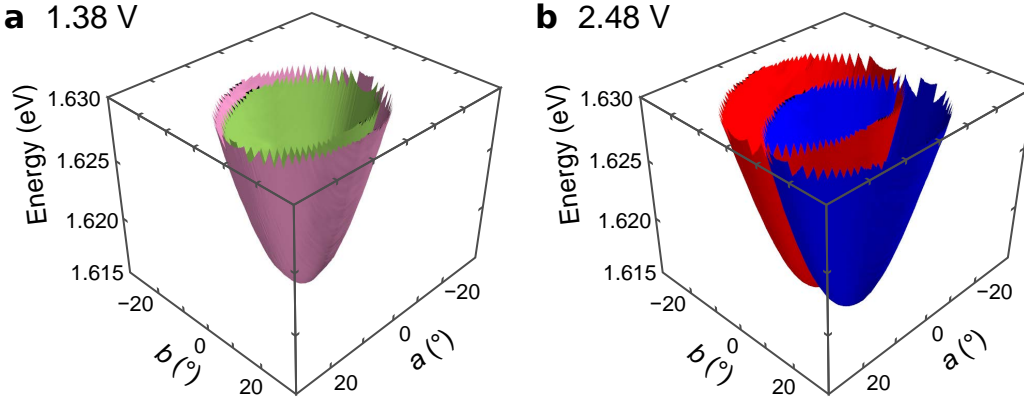


Figure 6.13: $(N + 2, N)$ and $(N + 1, N)$ regimes. Three-dimensional view of the experimental reciprocal space tomography of the cavity modes in resonance in the **a** $(N + 2, N)$ regime and the **b** $(N + 1, N)$ regime. The surfaces represent the dispersion of the cavity modes. The colors denote the predominant polarization of reflected light (green – H, violet – V, red – σ_+ , blue – σ_-).

photonic modes are circularly polarized (Fig. 6.14 **f**), which indicates tuning to the $(N + 1, N)$ resonance. For the Rashba-Dresselhaus regime, we observe a splitting of the paraboloids along the b axis which corresponds to the k_y direction in the wavevector space. Figure 6.13 **b** shows a three-dimensional view of the experimental reciprocal space tomography. Red and blue surfaces correspond to reflectivity minima in maps of σ_+ and σ_- -polarized light, respectively.

6.4. Rashba-Dresselhaus parameter

In order to obtain the Rashba-Dresselhaus parameter, measurements were made for different voltages. Figure 6.15 **a** shows the Rashba-Dresselhaus dispersion measured at 2.46 V with diagonal polarization detection. The Lorentz line shape functions were fitted to the modes observed on the presented reflectivity map. Then the observation angle was converted to the wave vector component k_{\parallel} . The mode energies as functions of k_{\parallel} are shown in Figure 6.15 **b**). The measured dispersion parabolas were approximated by quadratic polynomials in k_{\parallel} by a least-squares approximation. The difference between the two polynomials gave the k_{\parallel} -dependent energy difference between the σ_+ and σ_- polarized modes, which is shown in Figure 6.15 **c**. It is evident that the

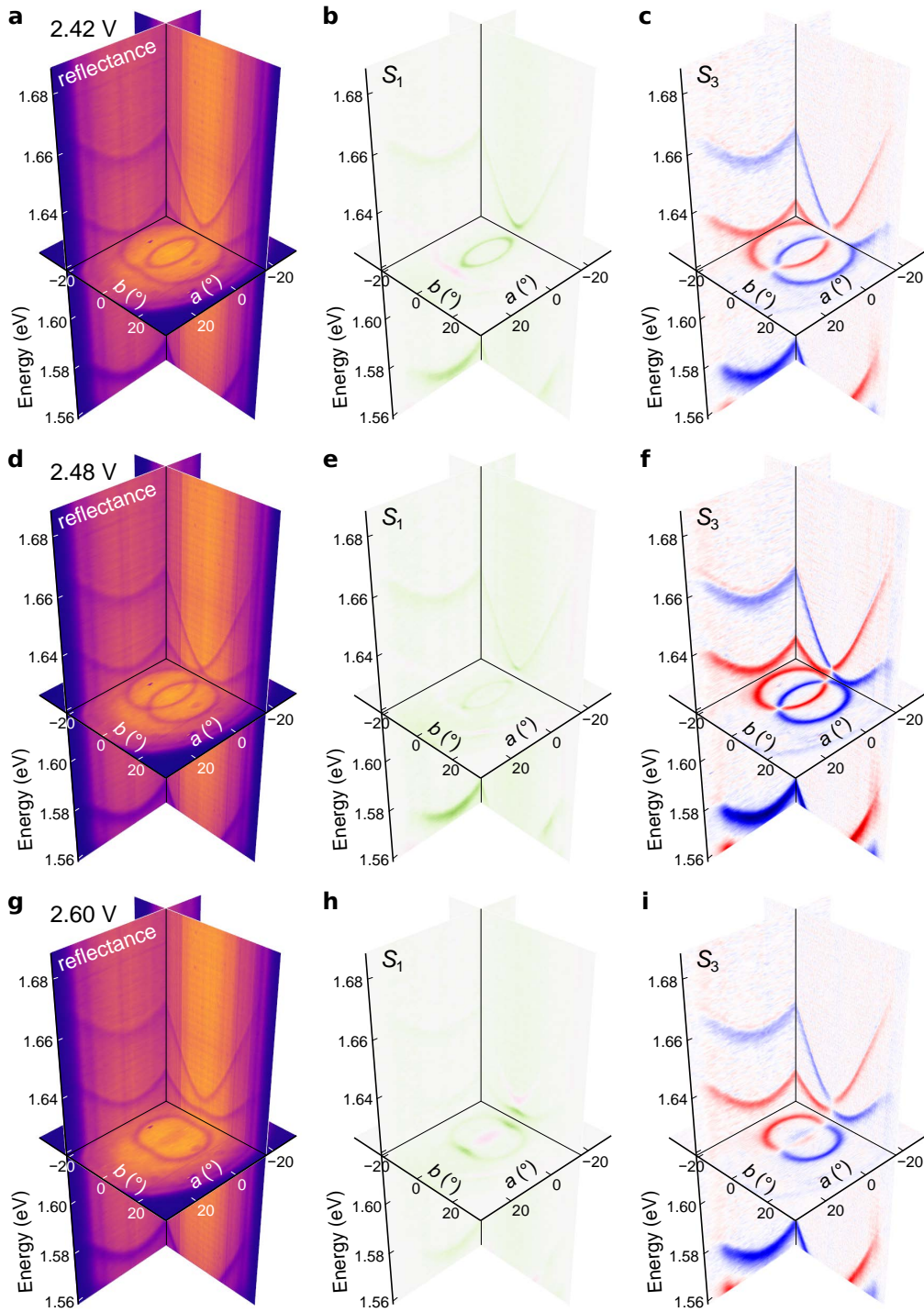


Figure 6.14: $(N + 1, N)$ regime. Experimental reciprocal space tomography of **a** reflectance, **b** S_1 Stokes parameter and **c** S_3 Stokes parameter at 2.42 V. Experimental reciprocal space tomography of **d** reflectance, **e** S_1 Stokes parameter and **f** S_3 Stokes parameter at 2.48 V. Experimental reciprocal space tomography of **g** reflectance, **h** S_1 Stokes parameter and **i** S_3 Stokes parameter at 2.60 V.

dependence is linear, which is in agreement with the theoretical dependence of the energy splitting on the wave vector for the Rashba-Dresselhaus Hamiltonian. The value of the Rashba-Dresselhaus parameter obtained from the fitting procedure is equal to $\alpha = 31.9 \text{ eV}\cdot\text{\AA}$.

To better illustrate how the coupling between the modes changes, we traced the reflectivity spectrum as a function of the applied voltage, at certain fixed observation angles. Figures 6.15 **d-i** show the reflection spectra as a function of the voltage applied to the sample for the following observation angle: 0, 5, 10, 15, 20 and 25 degrees (the angles are marked with dashed lines on the dispersion shown in Fig. 6.15 **a**). These maps clearly show the increasing anti-crossing between the cavity modes with the increasing observation angle.

We can also trace how the modes' polarization changes depending on the applied voltage for different observation angles. Below, in Figure 6.16, maps of the degree of polarization (S_1 , S_2 and S_3) for successive observation angles: 0, 5, 10 and 15 degrees are shown. The first row shows the polarization maps for an angle of 0 degrees. We can see that, regardless of the applied voltage, the polarization is linear. We observe a V-polarized mode (green) that does not change its energy and a H-polarized mode (purple) whose energy increases with increasing voltage. We can see that, also for the voltage of 2.46 V, corresponding to the Rashba-Dresselhaus dispersion, the polarization of the photonic modes remains linear. For this angle, in the case of R-D coupling, we have a superposition of circularly polarized modes, resulting in linear polarization. For the next row, i.e. for the 5-degree observation angle, we can see that the modes' polarization clearly changes. Around the voltage corresponding to the R-D coupling, the cavity modes are purely circularly polarized. While for voltages increasingly distant from 2.46 V, the contribution from the primary linear polarizations of H and V is stronger. The trend is even more pronounced for higher observation angles. The transition between the circular and linear polarization modes is smoother and takes place for voltages that are increasingly far from 2.46 V.

6.5. Summary and discussion

In this chapter, we demonstrate the control of the refractive index anisotropy in a multimode LCMC that allows us to change the coupling between subsequent photonic modes in a form corresponding to a Hamiltonian with Zeeman,

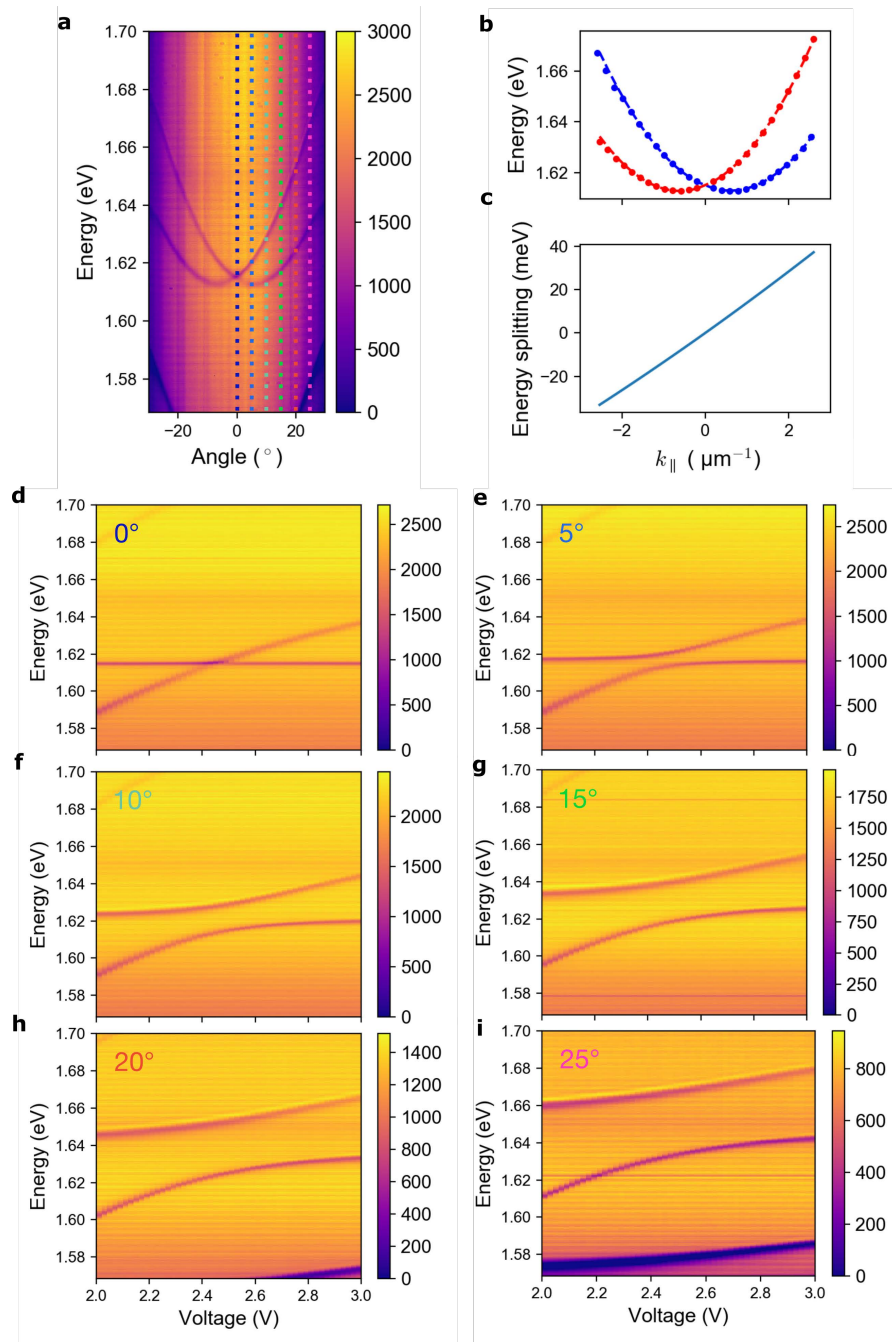


Figure 6.15: **Coupling between the cavity modes.** **a** Angle-resolved reflectance map for diagonal polarization. **b** Parabolic dispersion (dashed lines) fitted to the experimental data (dots) with the angle converted to the wave vector. **c** The energy difference for successive wave vectors. Rashba-Dresselhaus parameter obtained from the fitting is equal $\alpha = 31.9 \text{ eV}\cdot\text{\AA}$. **d-i** Energy resolved reflectance maps in a function of the voltage applied to the structure for different observation angles ranging from 0° to 25° marked with dashed lines in **a**.

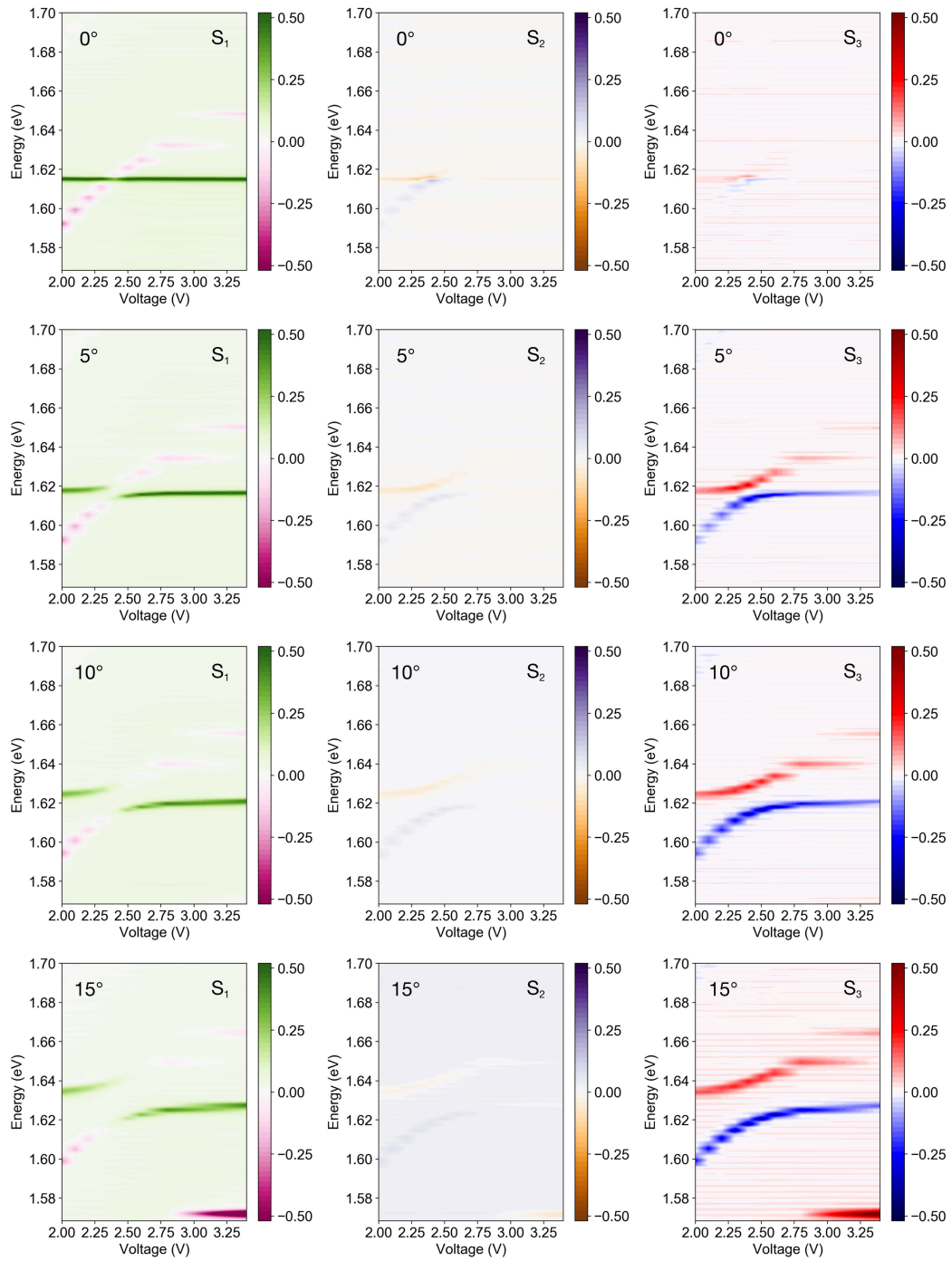


Figure 6.16: Energy resolved Stokes parameters maps in a function of the voltage applied to the structure for different observation angles ranging from 0° to 15° .

Dresselhaus, and Bychkov-Rashba, terms derived for fermions. In the study of condensed matter, they are of particular interest, as they allow manipulation and detection of electron spin [34]. Moreover, similarly to the spin Hall effect of light [49–51, 68] and the quantum spin Hall effect of light [43] in the Rashba-Dresselhaus regime, the electromagnetic wave in a uniaxial anisotropic medium possesses two distinct spin-polarized modes that can be controlled through the refractive index anisotropy in the photonic structure. With the control of the Rashba-Dresselhaus spin-orbit interaction, one can suppress spin relaxation [36,39] and create new topological states in solid-state systems [69]. Our study presents significant advances with respect to previous systems in which the spin-orbit interaction of light was demonstrated:

- We can tune the cavity modes to realize the Hamiltonian, in which Rashba-Dresselhaus and Zeeman (effective magnetic field) terms are present.
- We observe a giant value of the spin-orbit Rashba coupling coefficient $\alpha = 31.9 \text{ eV}\cdot\text{\AA}$, which is about 100 larger than in semiconductors and metals.
- The consequence of the Rashba effect is the observation of persistent spin helix (discussed in the Chapter 7), which is due to an emergent SU(2) symmetry.

Furthermore, the structure is tunable. This tunability, achieved by applying a voltage to the device, offers unprecedented control over the different terms of the synthetic Hamiltonian that describe our system. By tuning the splitting of the photon eigenmodes in the cavity, we can match the conditions of different regimes.

Our realization of Rashba-Dresselhaus Hamiltonian in a pure bosonic field can be used as a new platform for quantum simulators with synthetic magnetic field and micrometer control over light (pseudo)spin states (e.g. persistent spin helix) and suppression of spin relaxation [39].

Chapter 7

Persistent spin helix

Rashba and Dresselhaus fields of equal strengths acting on spin of electrons propagating in semiconductor quantum wells, lead to the emergence of the persistent spin helix (PSH) [36]. We use the same Hamiltonian to describe photons confined in an optically anisotropic cavity. Following these similarities [39,41] we observe, in a real space experiment, spatial oscillations of the polarization state of photons propagating in the plane of the birefringent cavity with strong spin-orbit interactions that recreate the PSH polarization texture in a purely optical system. In this chapter, we focus on the presentation of the results and the description of the optical analog of PSH in the liquid crystal microcavity system. The results presented in this chapter are the subject of article M. Król, K. Rechcińska et al., "Realizing Optical Persistent Spin Helix and Stern-Gerlach Deflection in an Anisotropic Liquid Crystal Microcavity", *Phys. Rev. Lett.* **127**, 190401 (2021).

7.1. Theory

We start the theoretical analysis from the simplest case – let us cut the Rashba-Dresselhaus dispersion at the minimum energy, that is, at the bottom of the valleys, where the centers of the valleys are separated by a vector \mathbf{Q} . This is presented schematically in the Figure 7.1.

This cross-section is defined by two spots in reciprocal space, separated by \mathbf{Q} , where each of these spots denotes the source of a plane wave of the wave vector $\mathbf{Q}/2$. The light emitted from the valleys is circularly polarized. We denote the Jones vectors corresponding to circular polarization, as defined in Table 1.1, as $\mathbf{J}_{\sigma_{\pm}}$. The expression for the electric field of the transmitted wave is the combination of plane waves in the form:

$$\mathbf{E}_{\text{out}}(\Theta) \sim e^{i(\frac{\mathbf{Q}}{2}\mathbf{r}+\Theta)}\mathbf{J}_{\sigma_+} + e^{-i(\frac{\mathbf{Q}}{2}\mathbf{r}+\Theta)}\mathbf{J}_{\sigma_-} =: E_+(\mathbf{r})\mathbf{J}_{\sigma_+} + E_-(\mathbf{r})\mathbf{J}_{\sigma_-}, \quad (7.1)$$

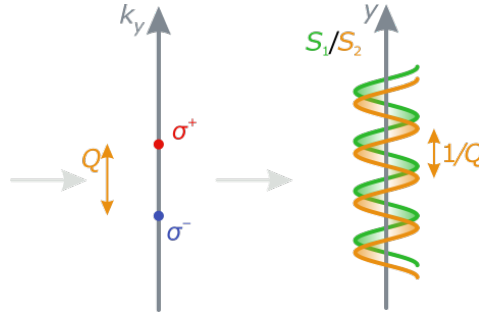


Figure 7.1: Persistent spin helix state creation as reciprocal spin-valley experiment for minimum energy cross-section.

where Θ denotes the angle of polarization of the incident light linearly polarized (Fig. 7.1). We assume here that the two plane waves are coherent in time, which is the case when they both originate from the same laser beam.

The two waves have opposite circular polarization (σ_+/σ_-) and opposite wave vectors. If we consider their interference at the surface of the cavity, we get a standing wave pattern in two linear polarizations.

The Stokes parameters can be expressed in terms of circularly polarized electric field components with the formulas:

$$\begin{aligned}
 S_1 &= \frac{2\text{Re}(E_-^* E_+)}{|E_+|^2 + |E_-|^2}, \\
 S_2 &= \frac{-2\text{Im}(E_-^* E_+)}{|E_+|^2 + |E_-|^2}, \\
 S_3 &= \frac{|E_+|^2 - |E_-|^2}{|E_+|^2 + |E_-|^2}
 \end{aligned} \tag{7.2}$$

Then we can easily see that:

$$\begin{aligned}
 S_1 &= \cos(\mathbf{Q} \cdot \mathbf{r} + 2\Theta), \\
 S_2 &= -\sin(\mathbf{Q} \cdot \mathbf{r} + 2\Theta), \\
 S_3 &= 0.
 \end{aligned} \tag{7.3}$$

The vanishing of the parameter S_3 means that the circular polarization component is absent in outgoing light in the near-field (close to the surface). Note that the electric field described by Eqs. (7.1) and (7.3) is analogous to the electronic state presented in Eqs. (1.78) and (1.79) in the Introduction. The

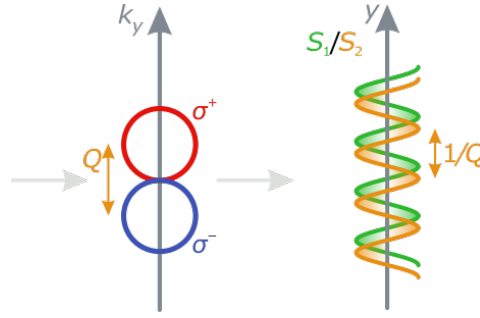


Figure 7.2: Persistent spin helix state creation as reciprocal spin-valley experiment for given energy cross-section.

upper row of Figure 7.3 shows maps of the parameter S_1 calculated according to (7.3), at fixed Θ (Fig. 7.3 a) and fixed x (Fig. 7.3 b).

In general, the paraboloids (Fig. 6.13 b) of the Rashba-Dresselhaus dispersion can be excited for any chosen energy (E) and the states that form the outgoing light can be represented by circles in reciprocal space, as presented in the scheme in Fig. 7.2. Then, the spatial distribution of the electric field at the surface of the cavity under Rashba-Dresselhaus conditions can be obtained by integrating the appropriately polarized plane waves over these circles and written as:

$$\mathbf{E}_{\text{out}}(\Theta) \sim e^{i(\frac{Q}{2}\mathbf{r}+\Theta)}\psi_{+}(\mathbf{r})\mathbf{J}_{\sigma_{+}} + e^{-i(\frac{Q}{2}\mathbf{r}+\Theta)}\psi_{-}(\mathbf{r})\mathbf{J}_{\sigma_{-}}, \quad (7.4)$$

where:

$$\psi_{\pm} = J_0 \left(\sqrt{\frac{2m}{\hbar^2} \left(E + \frac{2m\alpha^2}{\hbar^2} \right)} |\mathbf{r} \pm R^2\mathbf{Q}| \right) \quad (7.5)$$

and

$$R = \sqrt{\frac{F}{2k_0}}. \quad (7.6)$$

J_0 is the zeroth order Bessel function, m is the effective mass, E is the chosen energy, α the Rashba-Dresselhaus parameter and R depends on the distance between the focal point of the incident beam and the illuminated surface – F and the light wavenumber in the vacuum – k_0 .

The final interference pattern (the Stokes parameters) is given by:

$$\begin{aligned}
 S_1 &= \frac{2\psi_+(\mathbf{r})\psi_-(\mathbf{r})}{\psi_+(\mathbf{r})^2 + \psi_-(\mathbf{r})^2} \cos(\mathbf{Q} \cdot \mathbf{r} + 2\Theta), \\
 S_2 &= -\frac{2\psi_+(\mathbf{r})\psi_-(\mathbf{r})}{\psi_+(\mathbf{r})^2 + \psi_-(\mathbf{r})^2} \sin(\mathbf{Q} \cdot \mathbf{r} + 2\Theta), \\
 S_3 &= \frac{\psi_-(\mathbf{r})^2 - \psi_+(\mathbf{r})^2}{\psi_+(\mathbf{r})^2 + \psi_-(\mathbf{r})^2}.
 \end{aligned} \tag{7.7}$$

This simplifies to (7.3) when $E = -\frac{2m\alpha^2}{\hbar^2}$, which is exactly at the minimum of the dispersion. The bottom row of Figure 7.3 shows maps of the parameter S_1 calculated according to (7.7), at fixed Θ (Fig. 7.3 c) and fixed x (Fig. 7.3 d).

The situation described above applies to the case where the points of polarization σ_+ and σ_- shifted by the vector \mathbf{Q} are simultaneously excited and the phase Θ is the same at each point on the circles. In particular, we consider a homogeneous excitation of two valleys. However, if we consider the case of nonhomogeneous population of both valleys (as in Figure 7.4), i.e., a situation in which not every point in the k -space with polarization σ_+ has an equivalent σ_- polarized photon shifted by the vector \mathbf{Q} , it turns out that the image in the real space transforms into a separation of circular polarization along the y direction. After passing through the partially illuminated valleys, the photons will in effect give the image of two oppositely polarized areas that we refer to as the optical Stern-Gerlach experiment. In the far-field, i.e. far from the cavity, the σ_+ and σ_- polarized waves propagates at different wave vectors Q , thus the $S_3 \neq 0$ and achieve ± 1 at wave vectors $\pm \frac{Q}{2}$.

7.2. All-optical persistent spin helix

Experimental spatial distribution of light polarization in the cavity

As we showed earlier, in the liquid crystal cavity tuned to the resonance of modes with opposite parities, light is subjected to an effective Rashba–Dresselhaus field. This means that analogously to electronic systems, we can observe the effect of a persistent spin helix in this regime.

The sample used in the experiment is described in Section 6.1. The incident laser beam (polarized linearly) was tightly focused with a microscope objective (magnification 100 \times , NA= 0.55) in the cavity. The laser energy was set to be resonant with the cavity modes at normal incidence ($E = 1.705$

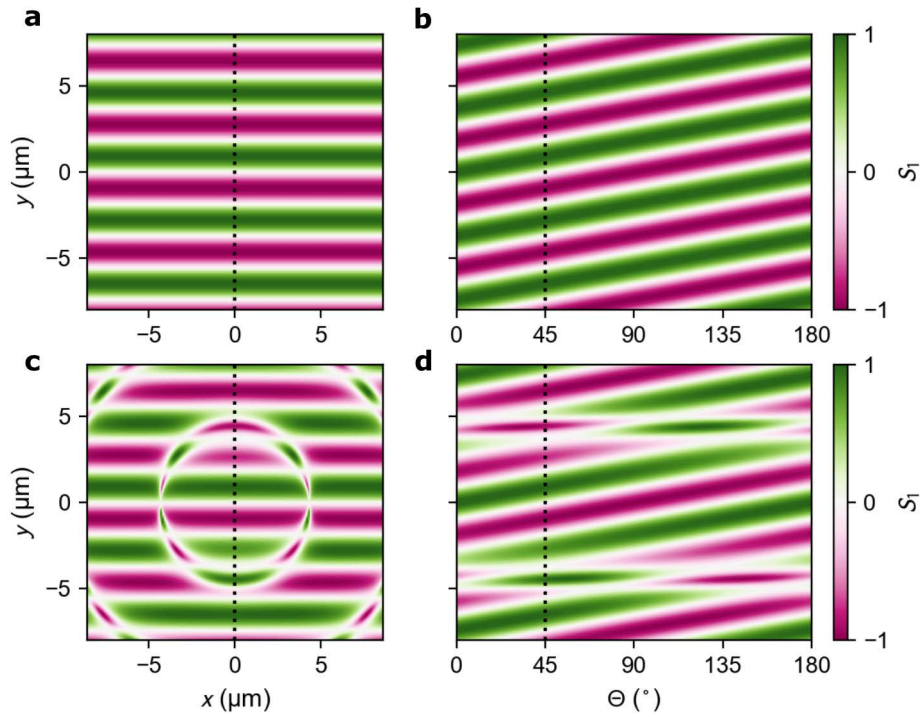


Figure 7.3: Theoretical S_1 Stokes parameter maps, calculated from **a**, **b**, Eq. (7.3) and **c**, **d**, Eq. (7.7). **a**, **c** maps in two spatial dimensions x and y at fixed $\Theta = \pi/4$. **b**, **d** maps at fixed $x = 0$, for successive polarization angles Θ . Vertical dotted lines denote the value of x or Θ which is fixed in the other calculation. Parameters used for the calculations: $Q_x = 0, Q_y = -1.7 \mu\text{m}^{-1}$, $\sqrt{\frac{2m}{\hbar^2} \left(E + \frac{2m\alpha^2}{\hbar^2} \right)} = 0.55 \mu\text{m}^{-1}$, $R^2 = 0.35 \mu\text{m}^2$.

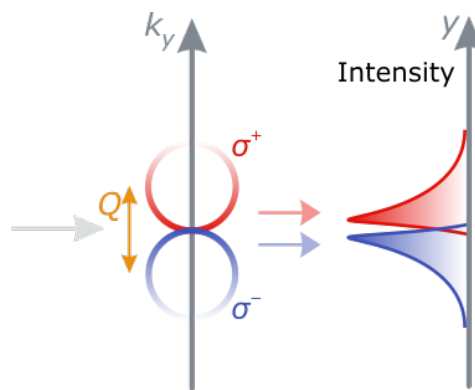


Figure 7.4: Photonic Stern-Gerlach experiment.

eV). The transmitted light was collected with a second microscope objective (magnification $50\times$, NA= 0.55), the polarization was resolved and imaged on a CCD camera. The resulting real-space transmission images and the corresponding spatial distribution of the Stokes parameters S_1 , S_2 , and S_3 are shown in Fig. 7.5 (no external voltage) and Fig. 7.6 (voltage tuned to Rashba-Dresselhaus SOC).

Figure 7.5 presents the polarization-resolved maps of light transmitted through the cavity. Three sets of basis polarizations are presented: horizontal and vertical, diagonal and antidiagonal, and both circular, as well as the corresponding Stokes parameters¹ in the situation without voltage applied to the sample. Under these conditions, the photonic modes are energetically separated (see Fig. 7.7a). It can be seen that in the presented case the transmitted light is fully vertically polarized. There is no light intensity for the H polarization on the transmission map (Fig. 7.5 a), while for the V polarization, the intensity is the highest (Fig. 7.5 b). For the polarizations D, A, $\sigma+$ and $\sigma-$, the transmitted light intensities are comparable, which translates into a zero degree of polarization for the parameters S_2 and S_3 .

After applying the voltage (2.12 V) to tune the resonance of the photonic modes with different parities ($N + 1, N$), that is, the Rashba-Dresselhaus regime (see Fig. 7.7b), we obtain as expected an image of a characteristic stripe pattern in real space (Fig. 7.6).

Figure 7.7 compares two regimes: with no voltage (panels **a**, **c**, **e**) applied to the structure and the PSH regime (panels **b**, **d**, **f**). Figures 7.7 **a**, **b** show the dispersions of the cavity modes with the energy of the laser used for resonance transmission measurements (marked with horizontal purple lines). The maps of the parameter S_1 are then shown in Figures 7.7 **c**, **d** with the corresponding measured Stokes vectors projected onto a linear polarization plane (Figures 7.7 **e**, **f**). As can be clearly seen, in the case of no voltage applied, the arrows are all arranged in one direction, which corresponds to linear polarization. However, in the case of the applied voltage of 2.12 V, we can see that the spin texture of light polarization is characteristic for persistent spin helix.

According to the theoretical predictions presented in section 7.1, in the cross-section along the y axis for the experimental maps of the Stokes parameters S_1 and S_2 , we observe an oscillation – the spatial variation of linear polarization. The mean value of the parameters S_1 , S_2 and S_3 , averaged over

¹ Incident light polarization is diagonal (D) for all presented maps.

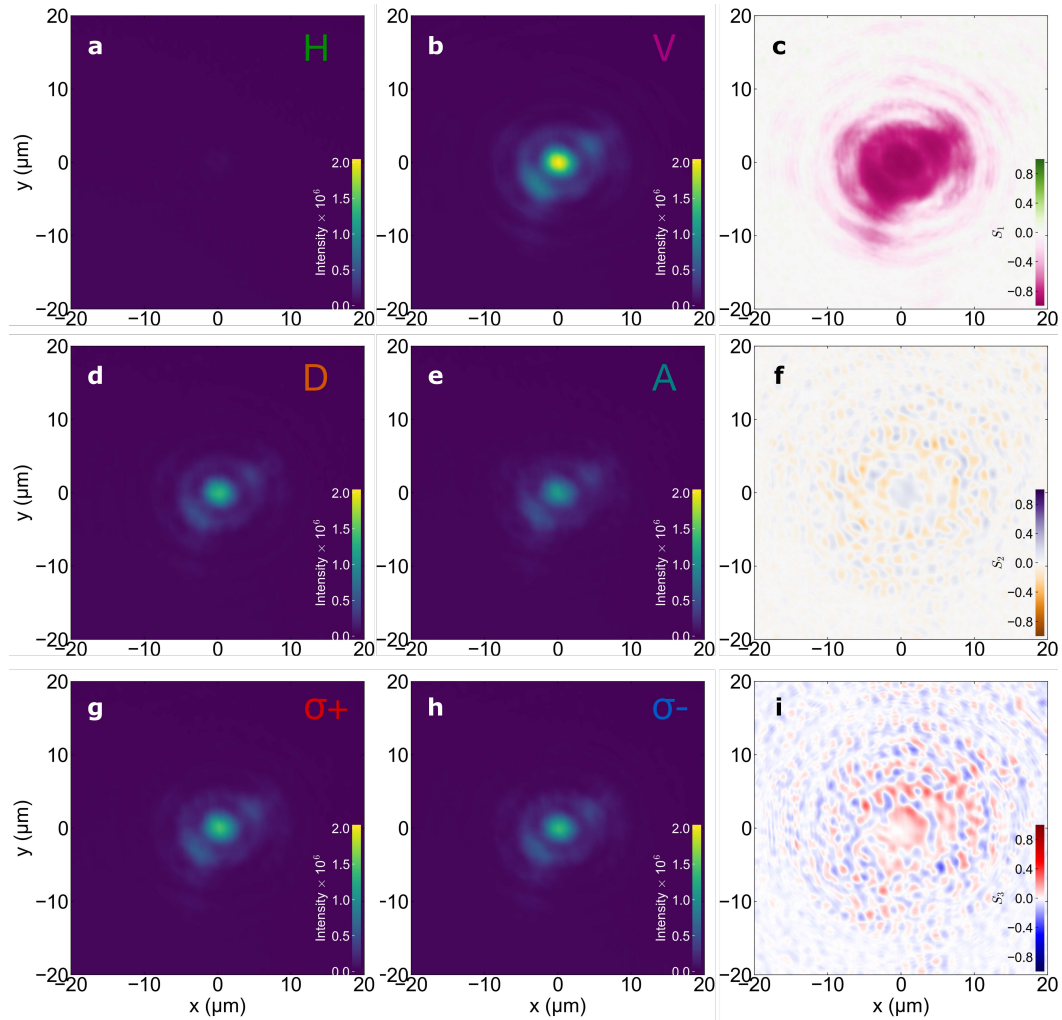


Figure 7.5: Polarization-resolved transmission maps in real space for diagonal polarization of incident light, without applied voltage. Transmission maps for successive polarizations of detected light: **a** diagonal, **b** vertical, **d** diagonal, **e** antidiagonal, **g** $\sigma+$ and **h** $\sigma-$. Stokes parameter maps: **c** S_1 , **f** S_2 , **i** S_3 .

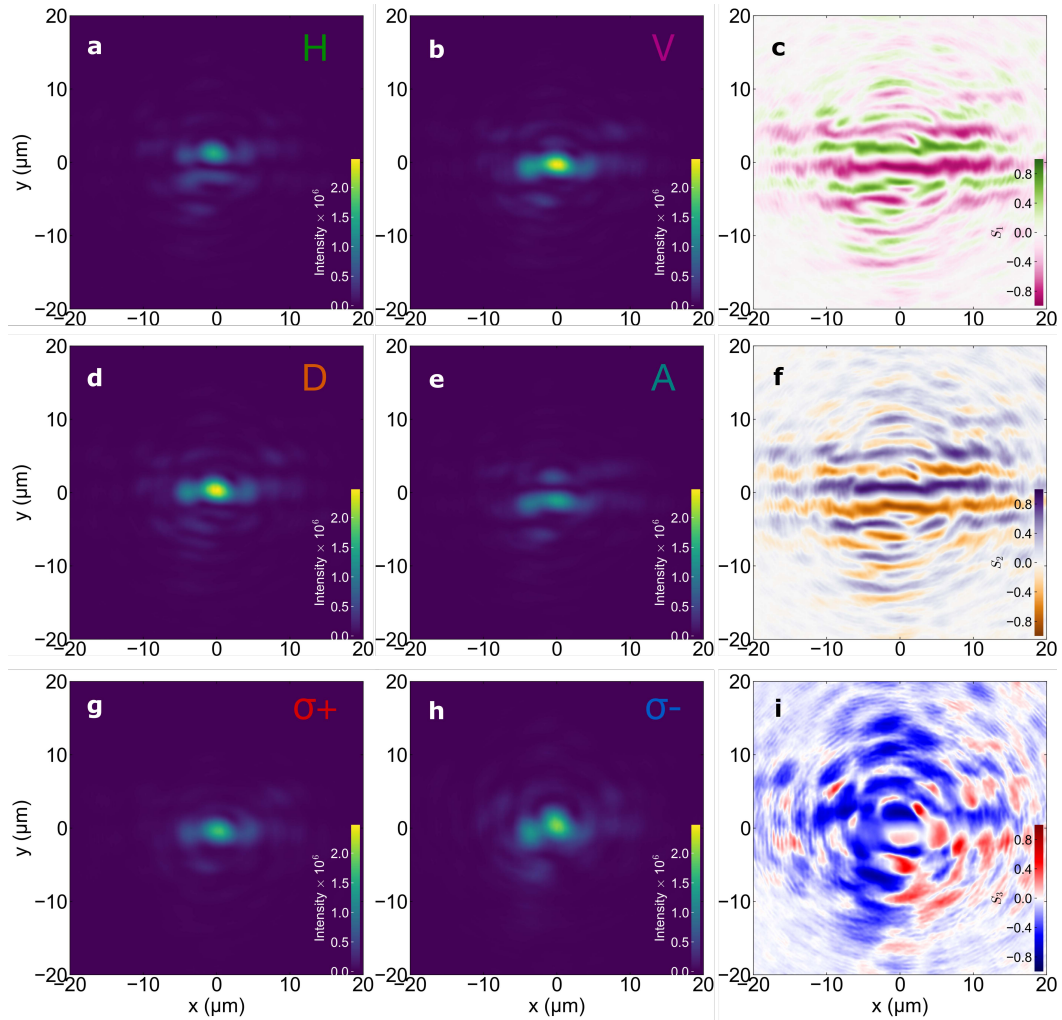


Figure 7.6: **Optical persistent spin helix** Polarization-resolved transmission maps in real space for diagonal polarization of incident light, for applied voltage corresponding to the Rashba-Dresselhaus resonance (2.12 V). Transmission maps for successive polarizations of detected light: **a** diagonal, **b** vertical, **d** diagonal, **e** antidiagonal, **g** $\sigma+$ and **h** $\sigma-$. Stokes parameter maps: **c** S_1 , **f** S_2 , **i** S_3 .

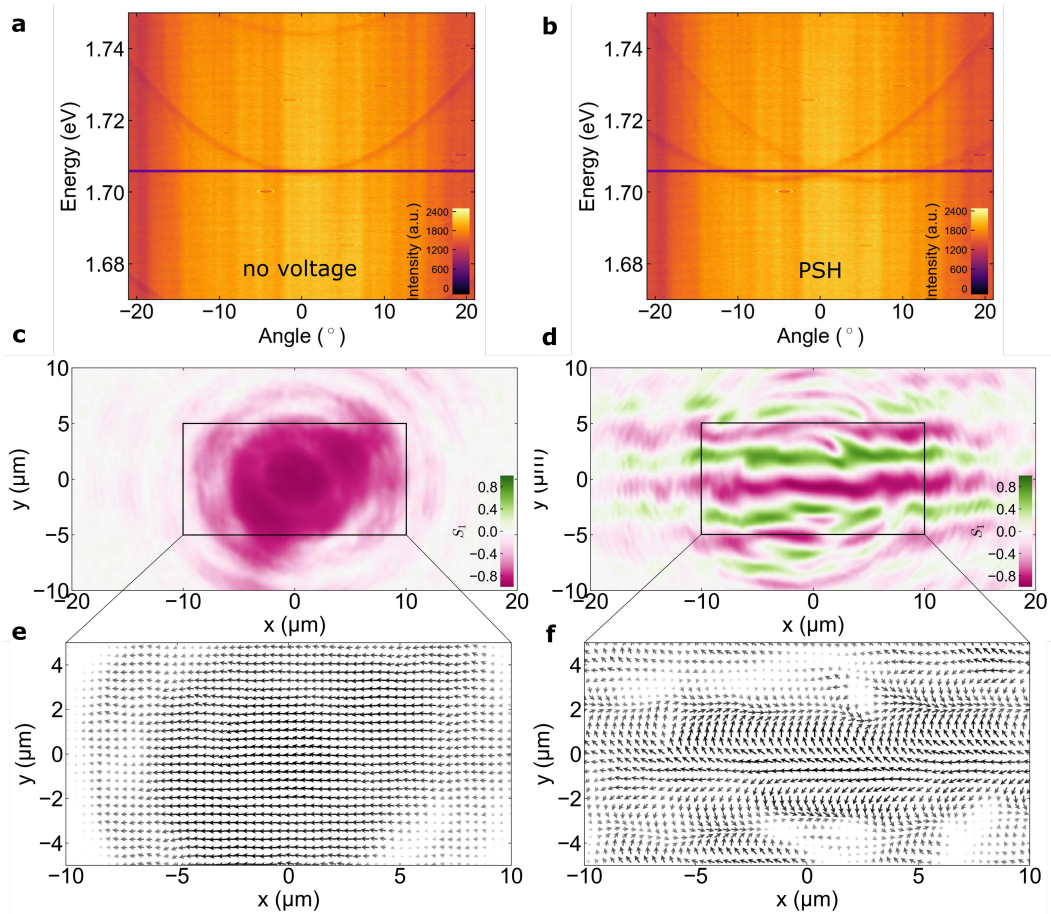


Figure 7.7: No voltage regime **a, c, e** vs. PSH regime **b, d, f**. **a, b** Dispersion of the cavity modes for diagonal polarization on detection for **a** no voltage applied to the structure, **b** with voltage corresponding PSH formation (2.12 V). The horizontal purple lines show the energy of the incident laser used for resonance transmission measurements. **c, d** S_1 Stokes parameter maps. **e, f** Measured Stokes vectors projected onto linear polarization plane (S_1, S_2).

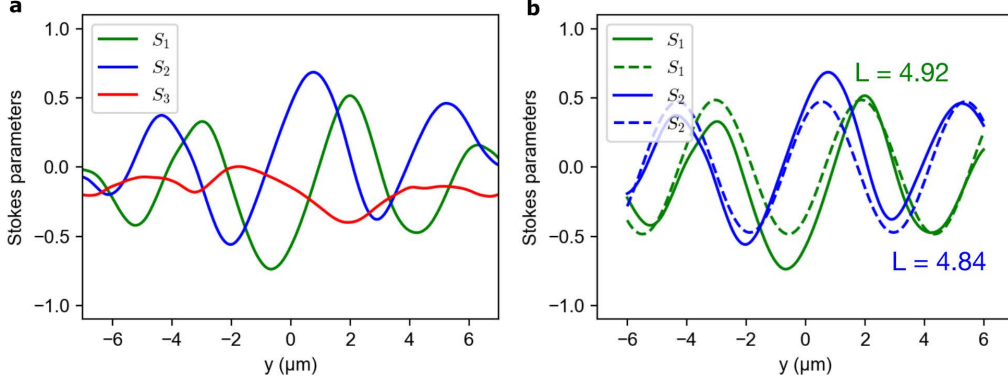


Figure 7.8: **a** Mean value of Stokes parameters in Fig. 7.6 **c**, **f** and **i** along the y direction. **b** Mean value of S_1 and S_2 Stokes parameters from Fig. 7.6 **c** and **f** along y direction with sin fitted. Averaging range $\pm 15 \mu\text{m}$.

the x direction, is plotted in Fig. 7.8 **a**. It clearly shows periodic oscillations with $\pi/2$ phase shift between the Stokes parameters S_1 and S_2 , while S_3 is less significant and shows no regular oscillations. The period of the helix is proportional to $L = \frac{2\pi}{Q}$, where $Q = |\mathbf{Q}|$. By fitting a sine function to the experimentally observed oscillations, we estimated L to $4.88 \mu\text{m}$ (Fig. 7.8 **b**).

7.2.1. Persistent spin helix for different incidence linear polarizations

As was described in Section 7.1 the observation of PSH requires an equal population of both circularly polarized valleys in the photon dispersion relation. This means that the incident light has to be linearly polarized. The angle of orientation of polarization Θ defines the common phase shift of σ_+/σ_- components of linearly polarized light and can be calculated from the Stokes parameters at the surface of the cavity at the arbitrarily chosen origin of the coordinate system $\mathbf{r} = 0$:

$$\Theta = \frac{1}{2} \arctan \left. \frac{S_2}{S_1} \right|_{\mathbf{r}=0}. \quad (7.8)$$

Figure 7.9 presents S_1 and S_2 parameter maps of the transmitted light for linearly polarized incident light with Θ equal to 0° , 45° , 90° and 135° , respectively. As can be seen, each linearly polarized excitation leads to creation of a PSH spatial polarization texture of transmitted light with different phases

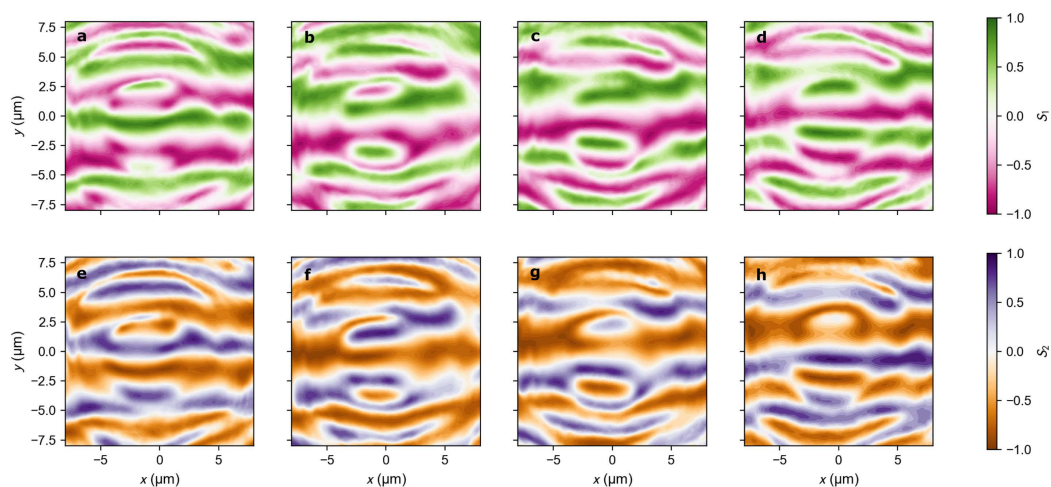


Figure 7.9: S_1 Stokes parameter maps (top panel) and S_2 Stokes parameter maps (bottom panel) for transmitted light for four different linear polarization of incident light: **a**, **e** 0° , **b**, **f** 45° , **c**, **g** 90° , **d**, **h** 135° .

of the helix, that is, with turning of the polarization of incident light, the PSH pattern moves along the y -axis. We trace this dependence by checking the polarization-resolved maps of the transmitted light in real space, as a function of the polarization orientation of the incident light (Figure 7.10). The experiment confirms that the helix moves along the y axis with rotating of the polarization plane, and that a rotation by 180° corresponds to a shift of the helix by its pitch (a single period). We note that at $y \approx -5 \mu\text{m}$ and $y \approx +3 \mu\text{m}$ the maps in Fig. 7.10 seem to break the pattern and not follow Eqs. (7.3) derived from a simple model (compare Fig. 7.3 **b**). However, the behavior at these points can be attributed to the zero-crossing points of the Bessel functions featured in Eqs. (7.7) obtained in the full model (compare Fig. 7.3 **d**).

7.3. Photonic Stern-Gerlach experiment

By looking at the S_3 parameter, we can demonstrate the separation of right- and left-handed circularly polarized light as an optical analogy of the Stern-Gerlach experiment. Currently, we can find interesting works that discuss the optical equivalent of the Stern-Gerlach experiment in nonlinear optics [70, 71]. Our system operates in the classical optics regime, where

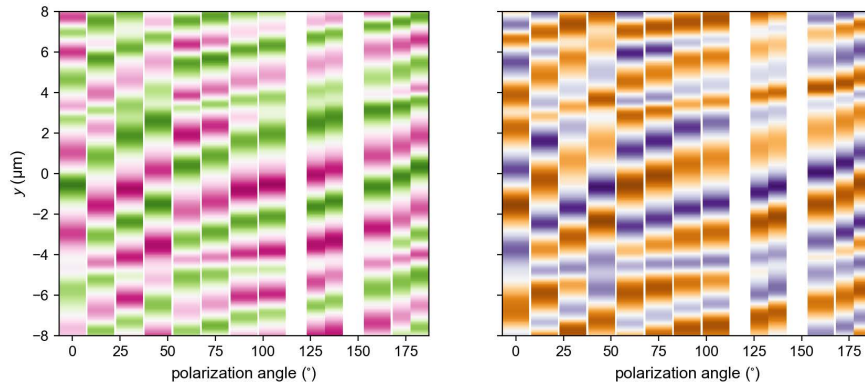


Figure 7.10: Stokes parameter maps **a** S_1 and **b** S_2 in a function of successive polarization angles.

the effective magnetic field appearing in the Rasha-Dresselhaus SOC causes the spin-selective deflection of the cavity photons in two opposite directions in the cavity plane (which are defined by the position of the valleys $\pm \frac{Q}{2}$). This should not be confused with chiral-selective displacement of chiral liquid crystal microspheres [72] or circular birefringence in chiral materials like the Fresnel triprism [73], because our system is achiral (i.e., the xz plane is a plane of symmetry). A similar separation is also observed in the spin Hall effect of light, resulting from refractive index gradients [74]. However, these gradients are negligible in comparison with the birefringence of LCs in our system.

As discussed in Section 7.1, the spin-selective deflection of the cavity photons can be obtained by nonhomogeneous occupancy of the two valleys of the Rashba-Dresselhaus dispersion. Experimentally, it was achieved by the use of the broad-bandwidth incoherent light (a broadband halogen lamp) transmitted through the cavity. This allowed for local stimulation of valleys around $k = 0$ in the reciprocal space. Figure 7.11 presents the photonic Stern-Gerlach experiment comprising measurements of the circular polarization of light transmitted through the cavity. The transmission maps are taken from real space tomography for σ_+ (Fig. 7.11 **a**) and σ_- polarization of the detected light (Fig. 7.11 **b**). In Figure 7.11 **c** the difference of the intensities of the two polarizations is shown and Figure 7.11 **c** contains corresponding S_3 Stokes parameter map. We can clearly see the real-space separation of the light polarized σ_+ and σ_- .

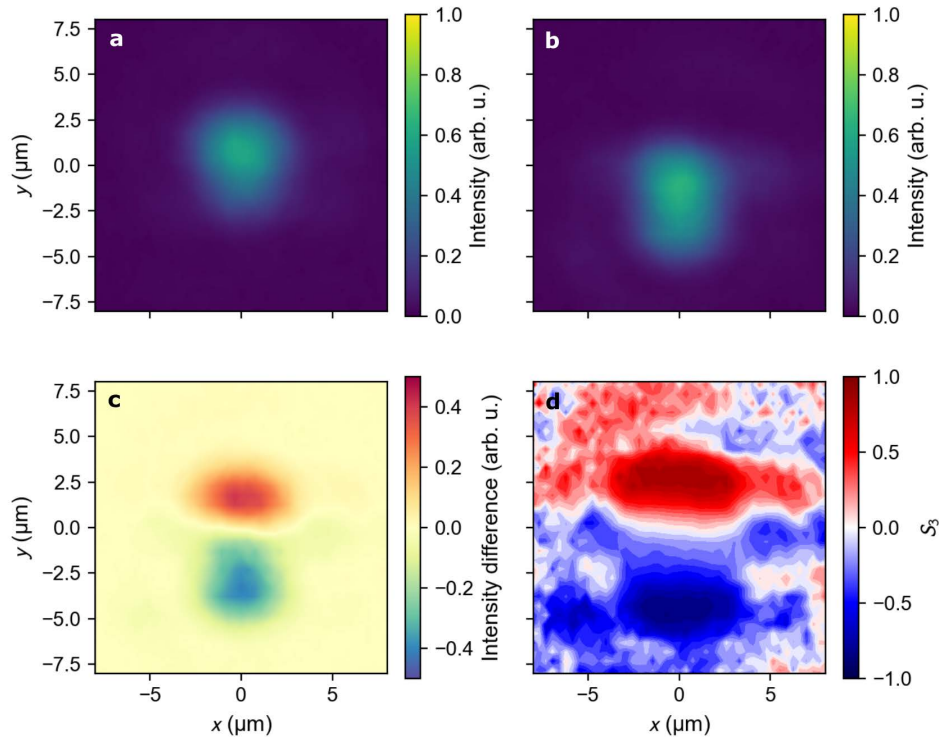


Figure 7.11: Photonic Stern-Gerlach experiment. Measurements of incoherent light transmission for a wide Gaussian beam. **a** Transmission map from real space tomography detected in σ_+ polarization and **b** σ_- polarization. **c** The difference between the light intensities in the polarizations σ_+ and σ_- **d** Map of the S_3 Stokes parameter. The incident light polarization was set to diagonal.

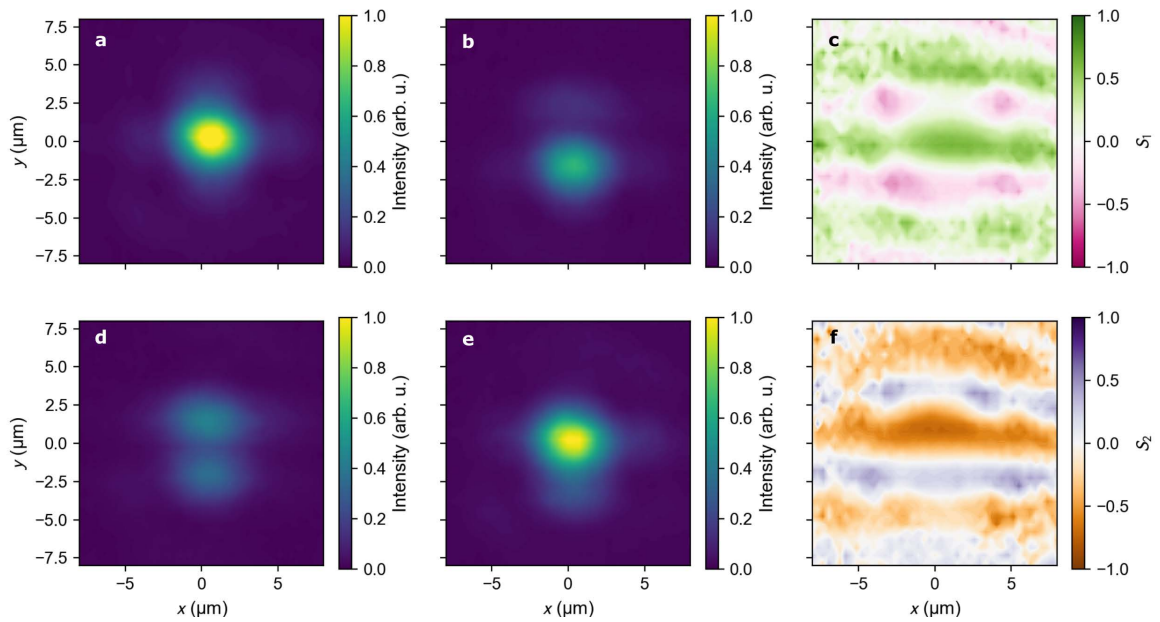


Figure 7.12: Measurements of incoherent light transmission for a wide Gaussian beam. **a** Transmission map from real space tomography detected in H polarization and **b** V polarization with **c** corresponding S_1 Stokes parameter map. **d**, **e** Real space transmission maps for D and A polarization respectively with **f** corresponding map of the S_2 Stokes parameter. The incident light polarization was set to diagonal.

For completeness, we present complementary measurements for the linear polarizations of the detected light (Figure 7.12). Figures 7.12 **a,b,d,e** show transmission maps detected in the H, V, D, and A polarizations successively, while Figures 7.12 **c,f** present corresponding S_1 and S_2 parameter maps, where we see the characteristic PSH pattern, demonstrating the partial coherence of the source of the white light².

7.4. Summary

SU(2) symmetry of the Rashba-Dresselhaus Hamiltonian leads to an interesting phenomenon of the persistent spin helix, known from semiconductor physics. In this chapter we discussed the direct observation of an analogous phenomenon in an optical cavity filled with liquid crystal. We optically determined the formation of a persistent spin helix polarization texture of cavity

² To obtain homogeneous illumination we used a pinhole of diameter 50 μm . The light passing through the pinhole is partially spatially coherent.

photons. Our system allows for full determination of the pseudospin, which is preserved in polarization of photons transmitted through the microcavity. We observe periodic in space precession of spin for photons moving in plane of the cavity. We also discussed the experimental conditions that allow us to observe the photonic equivalent of the Stern-Gerlach experiment.

Chapter 8

Cavities with an emitter

This part of the thesis focuses on investigating the light-and-matter interaction, including lasing in liquid crystal microcavities. The emitters presented in this part of the work were selected according to their properties, to allow the observation of interesting phenomena: weak or strong light-matter coupling or lasing. Due to technical reasons (laboratory capabilities), the most convenient range for system operation is the range of visible light 500-900 nm (1.4-2.5 eV). In the following sections, the tested emitters and investigated structures are described.

8.1. Exciton types and emitter selection criteria

In 1931, Yakov Frenkel proposed a model of neutral excitation in a crystal induced by light absorption. The bound state resulting from the interaction of an electron and a hole (an empty electronic state) is called an exciton. Excitons represent a broad class of electronic excitations in a variety of materials. The two basic types of excitons are Frenkel excitons (Fig. 8.1 **a**) and Wannier-Mott excitons (Fig. 8.1 **b**).

The Frenkel variation describes excitons with a high binding energy localized at one molecule. They are typically found in alkali halide crystals and organic molecular crystals. Electron excitations in organic molecules that involve the transfer of an electron from the highest occupied molecular orbital (HOMO) to the lowest unoccupied molecular orbital (LUMO) are also usually classified as Frenkel excitons. Their characteristic binding energy is of the order of 0.1 up to 1 eV.

In the Wannier-Mott model, the exciton is considered as an electron-hole pair bound by the Coulomb interaction. It is found in inorganic semiconductor crystals, where the dielectric constants are large and the effective masses are small. Then, the electron-hole interaction is strongly reduced by the crystal lattice, which causes the Bohr radius of this type of exciton to be much larger

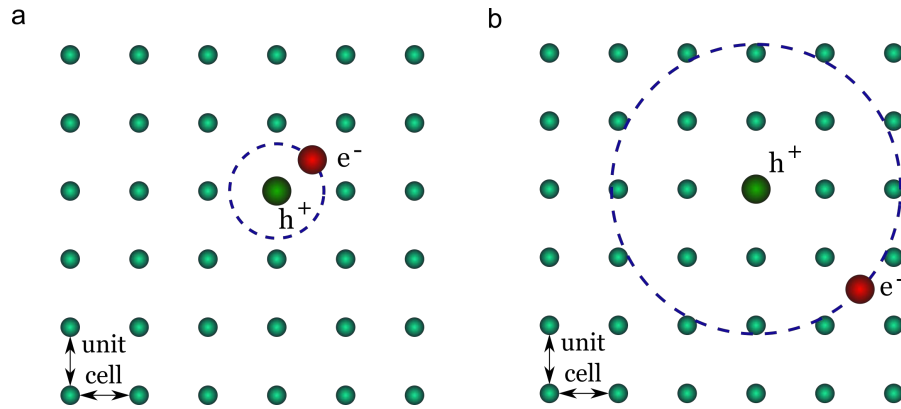


Figure 8.1: Types of excitons. **a** Frenkel and **b** Wannier–Mott excitons.

than the crystal lattice constant of the material and is characterized by a small binding energy (a few microelectronvolts). Low binding energies most often make the exciton unstable at room temperature.

To explain the selection of the emitters we used, the properties which we identified as the most important should be discussed. First of all, due to future applications, of particular interest are those active materials that have an exciton that is stable at room temperature. As mentioned previously, a cavity structure with an emitter is needed to obtain polariton states. In such a structure, as a result of the interaction of a cavity photon with an exciton, we obtain these quasiparticles. To observe strong coupling, the emitter must meet certain conditions, which we paid particular attention to when selecting active materials for our cavities.

- The Stokes shift between the absorption spectrum and the emission spectrum of a given material must be small. Both spectra must overlap as much as possible, so that the photon emitted into the cavity can be reabsorbed after reflection from the mirror. In the ideal case, the energy spectrum of the emitter can be described as a two-level system.
- The oscillator strength (i.e. transition dipole moment) of the exciton should be large enough to observe anticrossing between photonic and excitonic modes. The parameter describing this anticrossing is the so-called Rabi frequency.
- The lifetime of the photon should be comparable with the lifetime of the exciton, which basically means that their linewidths should match.

In Table 8.1 a wide selection of materials are presented that can play the

Table 8.1: Room temperature polariton systems – based on Guillet and Brimont article [75].

Active layer	Cavity geometry	Strong coupling	Polariton laser	Other demonstrations
Inorganic				
GaN bulk	Planar MC	[76–78]	[18]	spatial coherence [18], spontaneous polarization buildup [79], electrically injected polariton laser [80]
	Nanowire WGMs	[81]		
GaN QWs	Planar MC	[82]	[83]	electrically injected polariton diode [84]
ZnO bulk	Planar MC	[85–88]	[89, 90]	condensate propagation [91, 92], condensate localization [93]
	Nanowire FP	[94, 95]		parametric scattering [102], 97% excitonic condensates,
	Nanowire WGMs	[96–99] up to 550 K	[100, 101] up to 450 K	spatial coherence [103]; parametric relaxation [104], 1D polariton superlattice [105]
ZnO QWs	Planar MC	[106]		
ZnSe QWs	Planar MC	[107] (175 K) [109, 110] (300 K)		polariton refrigerator [108]
CuCl bulk	Planar MC	[111] (300 K)		
CuBr	Planar MC	[112]	[113]	
Organic				
Perovskites	Planar MC	[114, 115]	[116]	in-plane confinement, $Q = 750$ [117]
J-Aggregates	Planar MC	[118, 119]		
Anthracene	Planar MC	[120]	[16]	
TDPAF	Planar MC	[121]	[121]	spatial coherence [122]
Conjugated polymer	Planar MC		[19]	spatial coherence [19]

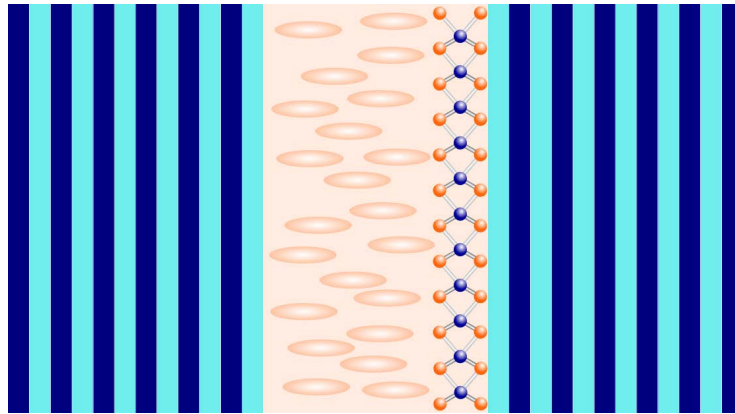


Figure 8.2: Scheme of the LCMC with an emitter on top of the DBR.

role of an active layer in cavities for room-temperature applications. Among them, we examined several groups: Pyrromethene laser dye, transition-metal dichalcogenide monolayers, and luminescent proteins. The selected materials differ in many aspects, including the structure that forces the location of a given emitter in the cavity. Therefore, the presented results were divided into:

- Section 8.2: emitter placed on the mirror surface.
- Section 8.3: emitter inside the liquid crystal.

8.2. Emitter on top of the DBR

In recent years, a lot of research has been devoted to two-dimensional layered materials [123–125]. It is a broad class of compounds that contains materials with different electronic and optical properties [126], and due to its diversity, it is an ideal basis for the construction of nanophotonic devices [126]. One of the classes of such compounds is semiconductor transition metal dichalcogenides. Transition metal dichalcogenides, which tend to form layered structures (Fig. 8.3), are a combination of a chalcogen and a metal of group IV (d^2 electron configuration), V (d^3), VI (d^4) or VII (d^5) [127].

They are characterized by unusual properties, such as the enhanced direct bandgap photoluminescence quantum yield, which are related to the atomically thin structures. The occurrence of a direct band gap in monolayers (ML) of this type of materials opens up the possibility of their application in optoelectronic devices. These materials are characterized by high exciton binding energies and small effective exciton Bohr radius, enabling the observer

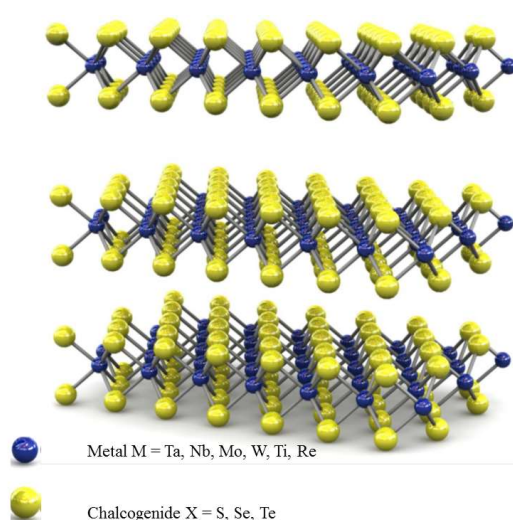


Figure 8.3: Transition metal dichalcogenide crystal structure [128].

to detect excitonic phenomena even at room temperatures. In addition, they are characterized by valley degeneracy, which endows excitons with an additional degree of freedom, the valley pseudospin [129–133]. Recent investigations have demonstrated that transition metal dichalcogenides, for example molybdenum diselenide monolayers (MoSe_2), are suitable materials to use as emitters in exciton-polaritons studies in microcavities [134].

In this section, we will describe an experiment carried out for a microcavity filled with a liquid crystal, where MoSe_2 monolayers, exfoliated or grown by CVD, were deposited onto one of the dielectric mirrors.

In the current state of technology, the mechanical exfoliation technique provides monolayers with the best optical properties. An example of a luminescence spectrum at room temperature for an exfoliated MoSe_2 monolayer excited with a continuous wave laser of 532 nm for several excitation powers is shown in Figure 8.4. The inset shows a photo of the monolayer at $50\times$ magnification. The MoSe_2 monolayers were transferred one by one to the target substrate (mirror), which allows one to control the number of flakes and their location in the sample. However, still monolayers obtained in such a way are local emitters, which requires that the LC alignment is proper in the vicinity of the flake. In the case of the structure of the liquid crystal cavity discussed here, one of the key parameters was the lack of three-dimensional impurities such as thicker MoSe_2 layers, because they make it very difficult to control the homogeneity of the arrangement of LC molecules (as shown in Fig. 8.5),

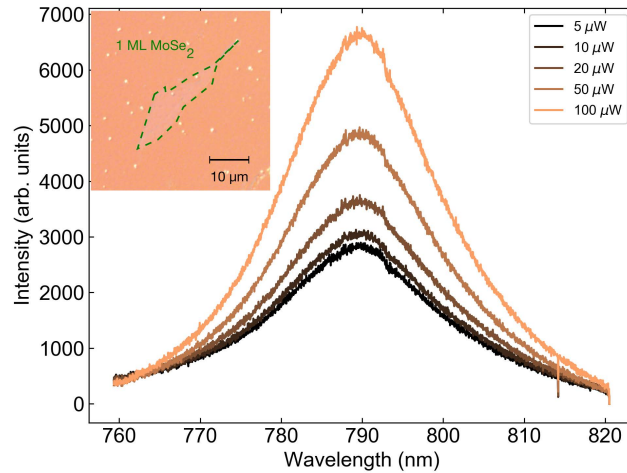


Figure 8.4: Photoluminescence spectra from MoSe₂ monolayer for several excitation powers. Inset contains optical microscope image of monolayer at 50× magnification.

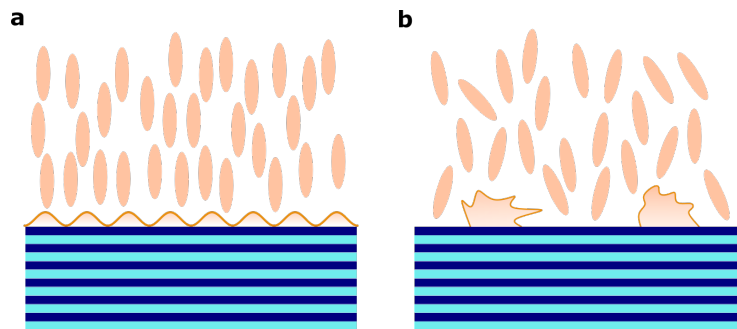


Figure 8.5: Arranging the liquid crystal at the surface. **a** No flakes, orientating layer on surface. **b** with flakes/dust, rough surface.

and thus to control the energy of the cavity modes. The CVD-grown flakes are distributed evenly across the whole mirror, therefore, even with sparsely distributed defects present, one is able to find an area with a proper LC alignment.

In Fig. 8.6 we present the comparison of the photoluminescence spectra for two different samples: exfoliated MoSe₂ ML and CVD-grown MLs. Photographs of MLs at the same magnification for both samples are shown in the insets. The emission from the exfoliated flake is visibly narrower and more intense than that from the CVD-grown one. In this case, the broadening of the emission line for CVD ML may be related to the size of the excitation spot that covered the area of several different flakes (around 4 μm).

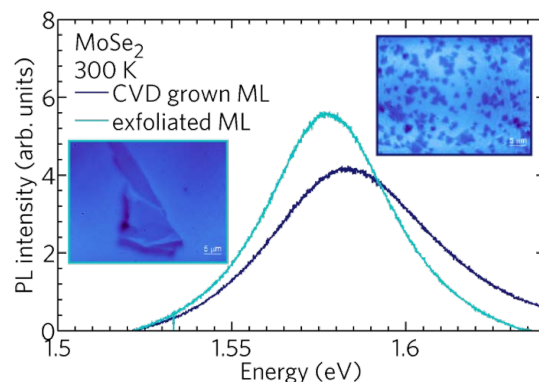


Figure 8.6: Photoluminescence spectra from MoSe₂ monolayers. Comparison of emission from exfoliated and chemically grown monolayers. Insets contain optical microscope images of both types monolayers. Presence of flakes adds disorder to the LC. With many flakes we can look for best local conditions.

Figure 8.7 shows angle-resolved luminescence maps as a function of the voltage applied to the sample. The emission from MoSe₂ monolayers is presented for horizontal polarization. With no voltage applied, the emission is narrow, and we observe a single optical cavity mode. As the voltage increases, the change in the emission intensity along the dispersion curve and the mode broadening with the applied voltage is observed. The photon mode broadening effect in the liquid crystal cavity is expected and was discussed in the subsection 3.1. The most important observation is the increase in emission intensity observed for a voltage of 8 V. In this case, the photonic mode energy is in resonance with the exciton energy in the MoSe₂ monolayer (the exciton energy at room temperature is equal to 1.58 eV). We can also trace this enhancement in cross-sections for zero angle shown in Fig. 8.8. Importantly, the emission enhancement effect may be related to the weak photon-exciton coupling (Purcell effect) in the cavity. However, it needs further experimental confirmation. For instance, the PL decay kinetics could be checked, as the Purcell effect is associated with a shortening of the radiative lifetime. Nevertheless, the observation of tunable emission and amplification of the emission intensity for such a structure is very interesting and promising for future experiments with LCMCs with an emitter.

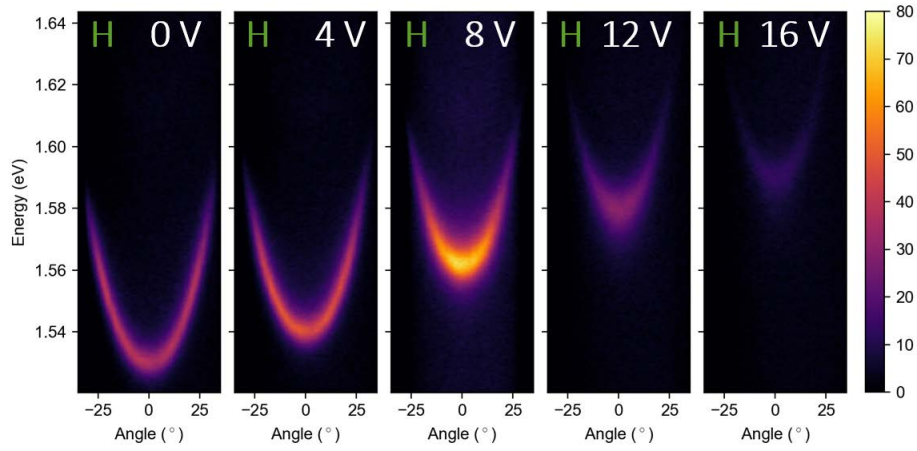


Figure 8.7: Photoluminescence maps for LCMC with MoSe₂ MLs in horizontal polarization. Experiment was performed with a continuous wave excitation of laser 532 nm (laser power 3 mW) for successive voltages applied to the sample. The color scale has been set the same for all PL maps shown.

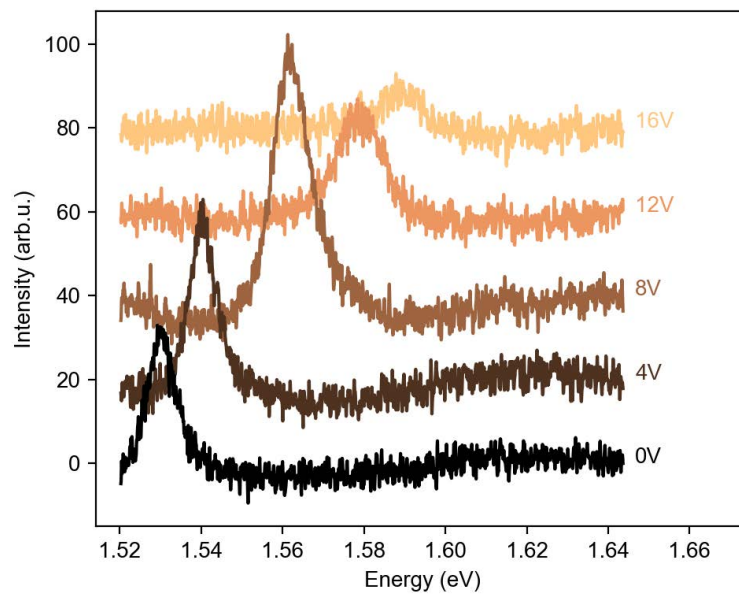


Figure 8.8: Cross-sections at normal incidence for the successive panels of figure 8.7, corresponding to successive voltage values applied to the sample.

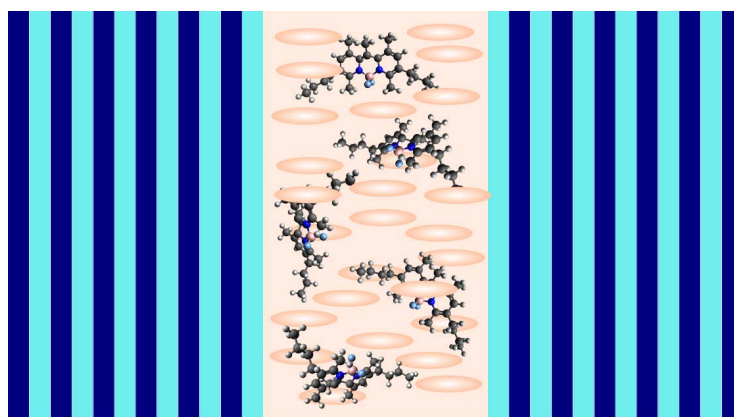


Figure 8.9: Scheme of the LCMC with an emitter inside the liquid crystal

8.3. Emitter inside the liquid crystal

8.3.1. Fluorescent proteins

Fluorescent proteins are a broad class of proteins that are self-sufficient in forming a visible wavelength chromophore within their own polypeptide sequence.¹ The first protein discovered in this family was green fluorescent protein (GFP). It was discovered in the tissues of *Aequorea victoria* jellyfish by Davenport and Nicol in 1955 [135], but the nature of the chromophore was correctly interpreted and described in 1979 by Osamu Shimomura [136]. Many years of research have allowed the synthesis, discovery, and description of a whole class of luminescent proteins, including mFruits (Fig. 8.11). They come from a variety of marine organisms, from chordate to cnidarians, with many obtained by specific gene mutations (mCherry was derived from mRFP1.5, dTomato was derived from dimer2). The structure of all proteins belonging to this group is similar (shown in Fig. 8.10) and two main elements can be distinguished. The cylindrical shell of the polypeptide chains is called a β barrel and the central part is called a chromophore, which is an organic moiety with an extensive π -electron system, which is responsible for the fluorescent properties of these substances.

Because of its fluorescent properties, the main application of fluorescent proteins has become molecular imaging in medicine, genetics, chemistry, and

¹ This means that such a protein does not need to be modified, e.g. to visualize the location or dynamics of a gene product using fluorescence microscopy.

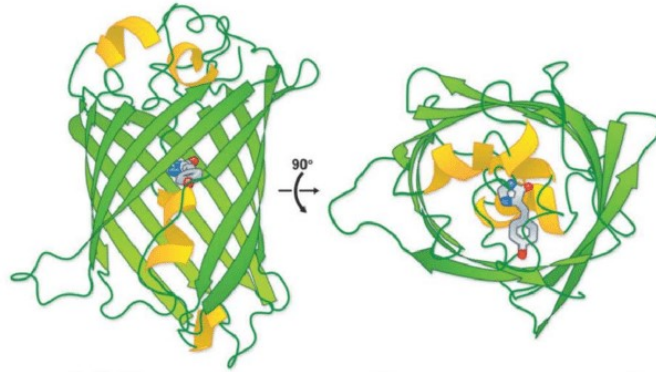


Figure 8.10: Schematic structure of Green Fluorescent Protein GFP showing a side view and a top down view. Figure after [137].

biology. Other applications are optogenetics (for light activation of individual neurons) or mapping the neural circuits of the brain [138,139]. However, from the perspective of this work, the most important application is basic research in solid-state physics of the light–matter interaction. Due to their strong and stable luminescence at room temperature, these proteins have been shown to be ideal candidates for an emitter in the optical cavity [140].

Among the entire set of luminescent proteins, only some of them have found use in polaritonic systems. During the last few years, there has been a lot of work on the use of luminescent proteins in the physics of polaritons. The promising materials turned out to be proteins of the aforementioned group of mFruits: eGFP (Fig. 8.12 a), tdTomato (Fig. 8.12 b) and mCherry (Fig. 8.12 c).

Among the published research devoted to polaritonics in fluorescent proteins, one can single out the exciton-polariton laser [145] obtained in laminated eGFP-filled high-Q microcavity, mixed system with two different proteins – eGFP and tdTomato [146], nonlinear response and polariton condensate observed in hemispheric optical cavity filled with the fluorescent protein mCherry [147], more sophisticated works devoted to direct laser writing in the structure with thin film of tdTomato [148] or topological polariton laser in an organic lattice in a one-dimensional Su-Schrieffer-Heeger chain of microcavities containing a thin film of mCherry [149].

In our research, we focused on two proteins from the described group: tdTomato and mCherry. However, in the following, we will focus on the mCherry protein, for which promising results were obtained. The proteins were pro-

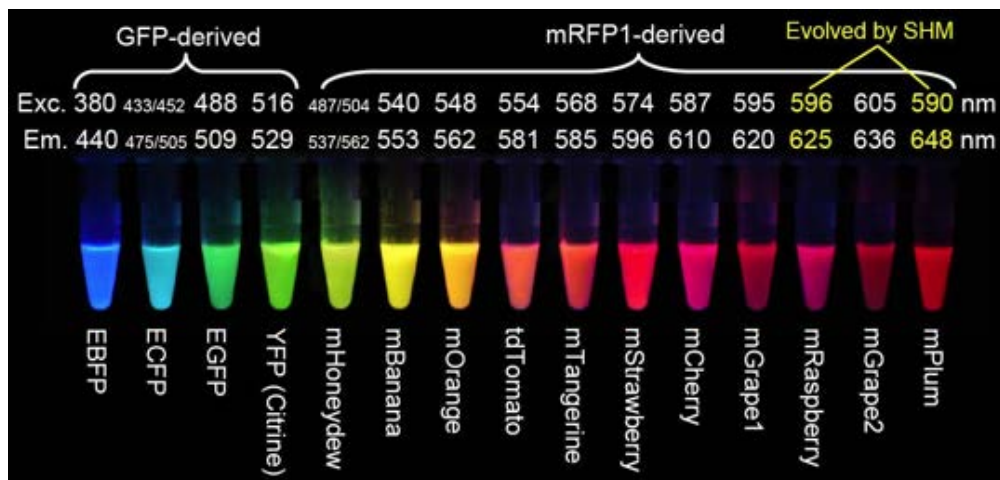


Figure 8.11: Fluorescent proteins discussed in this chapter, and the mFruit fluorescent proteins derived by Roger Tsien from mRFP1 (Red Fluorescent Protein) (Shaner et al., 2004) and by somatic hypermutation (SHM) (Wang et al., 2004). *E* stands for enhanced versions of GFP, *m* are monomeric proteins, and tdTomato is a head-to-tail dimer. Monomeric or tandem dimeric fluorescent proteins derived from *Aequorea* GFP or *Discosoma* RFP, expressed in bacteria, and purified. This photo is a time-exposure of fluorescences excited at different wavelengths and viewed through different cutoff filters. Figure after [141].

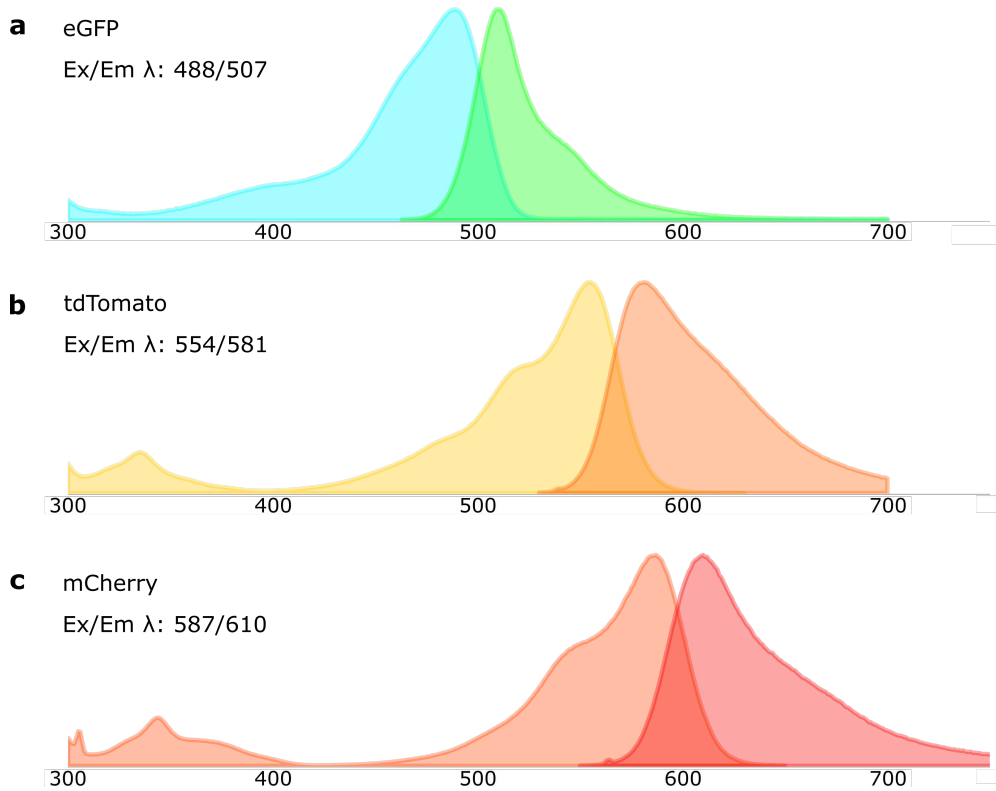


Figure 8.12: **a** eGFP fluorescent protein absorption and emission spectrum [142]. **b** tdTomato fluorescent protein absorption and emission spectrum. tdTomato is a basic (constitutively fluorescent) orange fluorescent protein published in 2004, derived from *Discosoma* sp. It has been reported to be a somewhat slow maturing tandem dimer with low acid sensitivity [143]. **c** mCherry fluorescent protein absorption and emission spectrum. mCherry is a basic (constitutively fluorescent) red fluorescent protein published in 2004, derived from *Discosoma* sp. It is reported to be a monomer that develops very rapidly with low acid sensitivity [144].

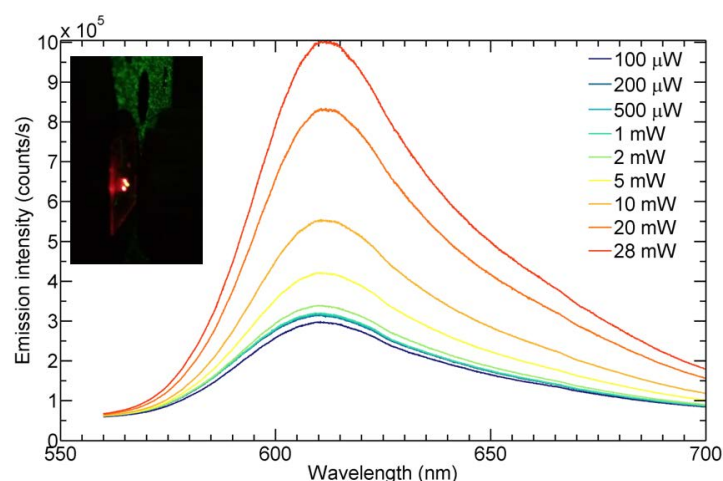


Figure 8.13: mCherry (drop on glass) emission spectra in function of excitation power. The cw green laser was used (532 nm).

vided by the group of Prof. Jacek Jemielity and Prof. Joanna Kowalska at the Centre of New Technologies and the Division of Biophysics, Faculty of Physics, University of Warsaw. In this work, we show preliminary results regarding the use of fluorescent proteins as emitters. In this section, we focus on open-cavity without a liquid crystal (see Section 2.2.3). Creating the final structure with the liquid crystal and protein requires further work, because of the differences in the chemical structure of both materials.

The mCherry protein is characterized by optical properties similar to those of the tdTomato protein, but the emission and absorption spectra are slightly shifted toward longer wavelengths. The process of culturing bacteria modified with the pET28_mCherry plasmid was carried out by Mr. Tomasz Śpiewła (see the subsection 2.2.3). In the first stage, the frozen protein solution in water (Fig. 2.10 a) was thawed. The first step of characterization was the luminescence measurements as a function of the excitation power (cw 532 nm laser). The results are presented in Fig. 8.13. The shape of the spectra is in good agreement with data found in the literature for this protein. It is worth noting that the obtained results indicate a surprisingly high photostability of mCherry. Even with excitation beam powers as high as a few milliwatts, the shape of the spectrum remains practically unchanged. This shows that there is no light-induced degradation of the fluorophore leading to photobleaching.

Next, preliminary measurements of the open-cavity, composed of two dielectric mirrors designed for the wavelength corresponding to the maximum emission of the protein, and a drop of an mCherry water solution were carried out. The emission was observed to be modified by the cavity modes; however, there was no noticeable gain or strong coupling. In the second stage, a concentrated protein solution of 127 mg/ml was prepared. For such a solution, an open-cavity structure (photography of the preparation of the open-cavity structure is in Fig. 2.10 **a**, **b**) with thickness $8.5 \mu\text{m}$ (value obtained from photoluminescence spectra) was prepared and luminescence studies were performed under pulse excitation of fs laser with kHz repetition rate and the wavelength set at 530 nm. Figure 8.14 shows the luminescence maps for successive excitation powers. In the measured energy range, two cavity modes (1.89 eV and 1.96 eV) are observed. Already for small excitation powers, instead of homogeneously occupied cavity modes, the highest occupancy is observed in the minima of modes at $k_{\parallel} = 0$. The higher-energy mode is less visible because of the absorption by the protein. The emission at $k_{\parallel} = 0$ (Figs. 8.15 **a**, **b**) can be traced and the increase of the intensity, shifting, and narrowing of the lines is observed. By fitting the Lorentz curve to the successive spectra, the change of each parameter with the excitation power: intensity (Fig. 8.15 **c**, **d**), energy change (Fig. 8.15 **e**, **f**), and linewidth change (Fig. 8.15 **g**, **h**) can be determined for both cavity modes (left panels – lower energy mode and right panels – higher energy mode). For both modes, the emission intensity increases, the energy of the minimum is blue-shifted, and the linewidth is decreasing. Such changes may suggest that the observed regime is consistent with polariton lasing, where the polariton–polariton interaction causes an energetic shift. However, confirmation of such lasing would require additional measurements, e.g. spatial coherence.

The second observed regime (different place on the sample) is shown in Fig. 8.16. Similarly, changes in occupation can be followed along the dispersion of the mode. It can be seen that the dispersion is not smooth and symmetric, which may occur due to the presence of a local defect. However, an intense emission close to normal incidence, even for small excitation powers, is observed. For the highest excitation power (333 nJ/pulse), a transition to a very strong and spectrally narrow lasing is observed. The maps are presented on a logarithmic scale to show signatures that remain from the originally observed cavity modes. The broadened modes are the background for the lasing appearing higher in the energy. When analyzing the cross-sections for

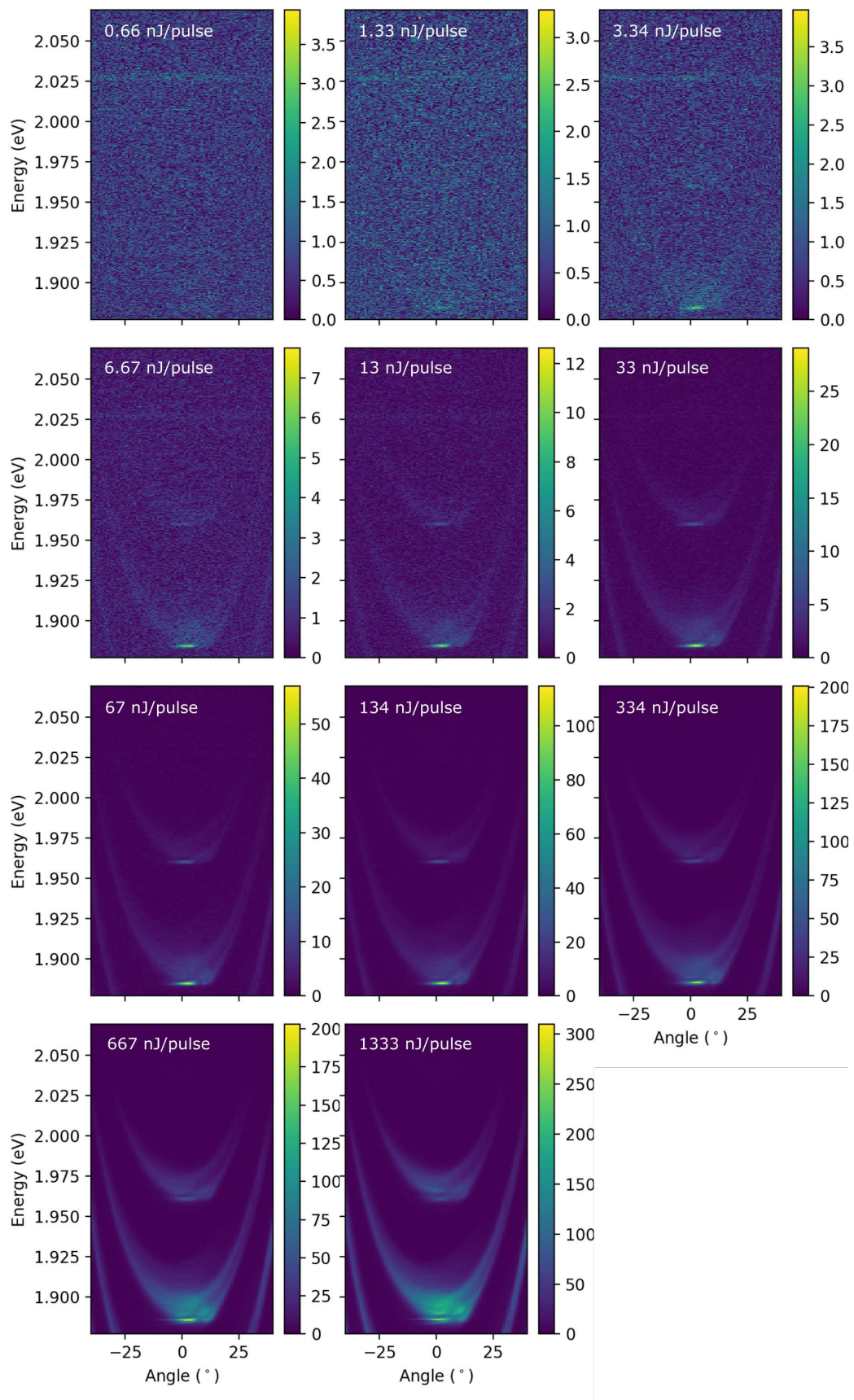


Figure 8.14: **mCherry first lasing regime.** Angle-resolved photoluminescence maps of mCherry open-cavity under non-resonant pulsed excitation as a function of excitation power. Objective with NA = 0.75.

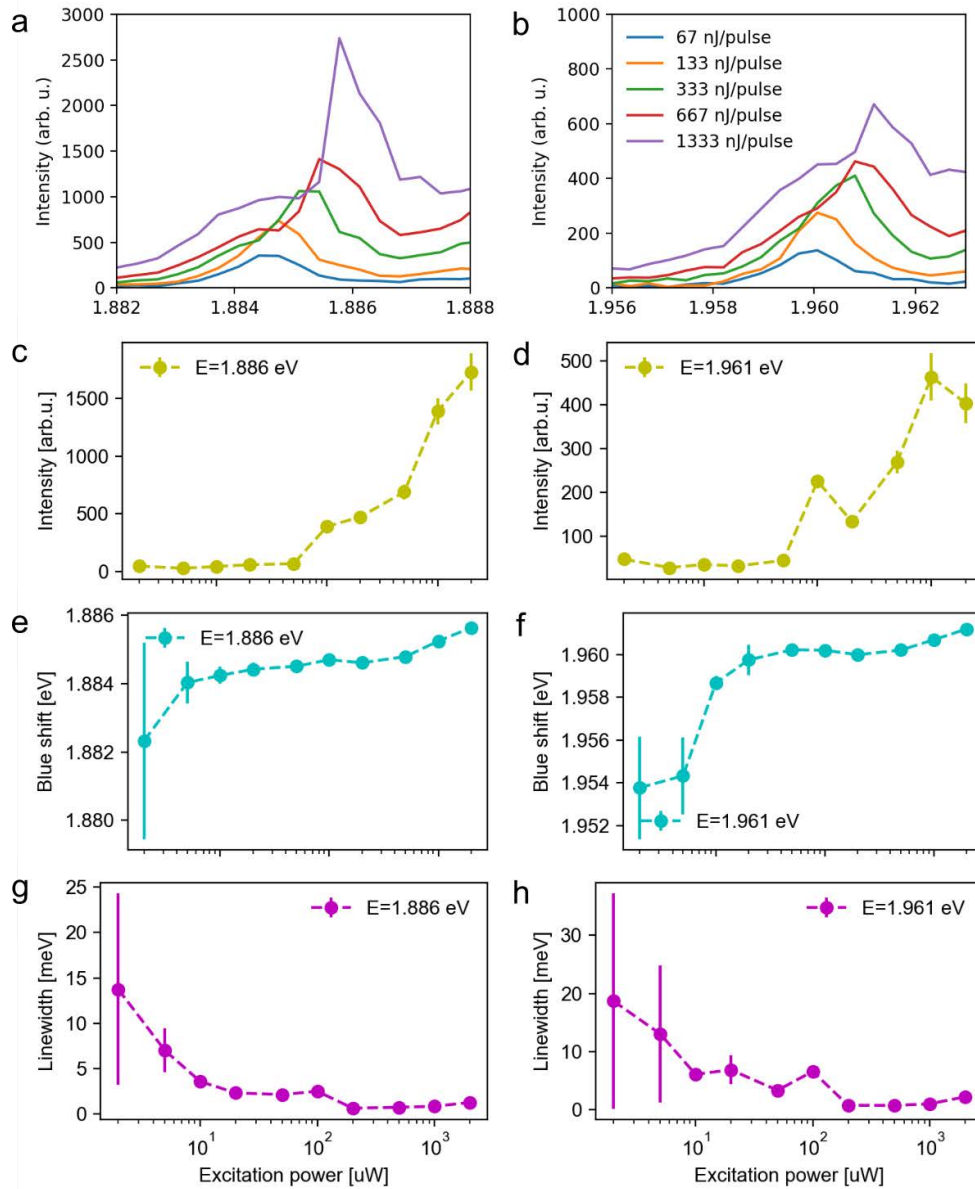


Figure 8.15: **a** Photoluminescence spectra of mCherry open-cavity at normal incidence. Intensity of **b** cavity mode, **c** its energy blue shift and **d** linewidth versus the excitation power. Lines connecting experimental points are guide for the eye.

the minimum of the dispersion in Fig. 8.17, one can notice nonlinear dependencies of both the change in emission intensity and the energy shift and the narrowing of the emission line. This may indicate the transition to the lasing regime. The sharp and significant shift in energy is especially noticeable.

8.3.2. Pyrromethene 580

The last of the material classes discussed here are laser dyes [150]. This class is very broad and includes many compounds that differ in chemical structure and optical properties. We will focus only on one subclass – the pyrromethenes (boron-dipyrromethene dyes also known as BODIPY) – fluorescent dyes used in solid-state dye lasers [150]. They cover the green-yellow part of the visible region of the electromagnetic spectrum. For BODIPY-Br (bromine-substituted boron dipyrromethene) incorporated in an optical cavity, exciton-polariton condensation has been reported [151].

The laser dye used in this work is Pyrromethene 580 (known as P580), which lases at a wavelength of 580 nm². Its structure is shown in Fig. 8.18 **a** and the absorption and emission spectra are presented in Fig. 8.18 **b**. P580 is a convenient choice for our purposes, because of easy mixing with LCs and commercial availability at low cost. It was used, i.a., in the work on the band-edge liquid crystal laser [152], concerning the emission characteristics of a series of chiral nematic liquid crystal lasers doped with different laser dyes (DCM, pyrromethene 580, and pyrromethene 597).

Figure 8.19 presents the experimental reflectance maps for successive voltages applied to the cavity in the HG configuration filled with 2091 HBLC mixed with the P580 dye. Measurements were made with polarization resolution. The upper panels of Figure 8.19 show dispersion relations for horizontal detection, and the middle panels for vertical polarization. The bottom panels are S_1 Stokes parameter maps for the corresponding voltages.

The typical spectra for the liquid crystal cavity are observed. For 0.0 V applied to the cavity, the horizontal and vertical modes are degenerate at angles other than 0°. As we can see, the horizontally polarized mode is characterized with higher effective mass and higher minimum energy, when the vertically polarized mode has lower effective mass and lower minimum energy. The green color on S_1 Stokes parameter maps presents the lines that are reflected from the cavity detected with horizontal polarization and the

² Under specific excitation conditions and in a specific solvent (solvent effect).

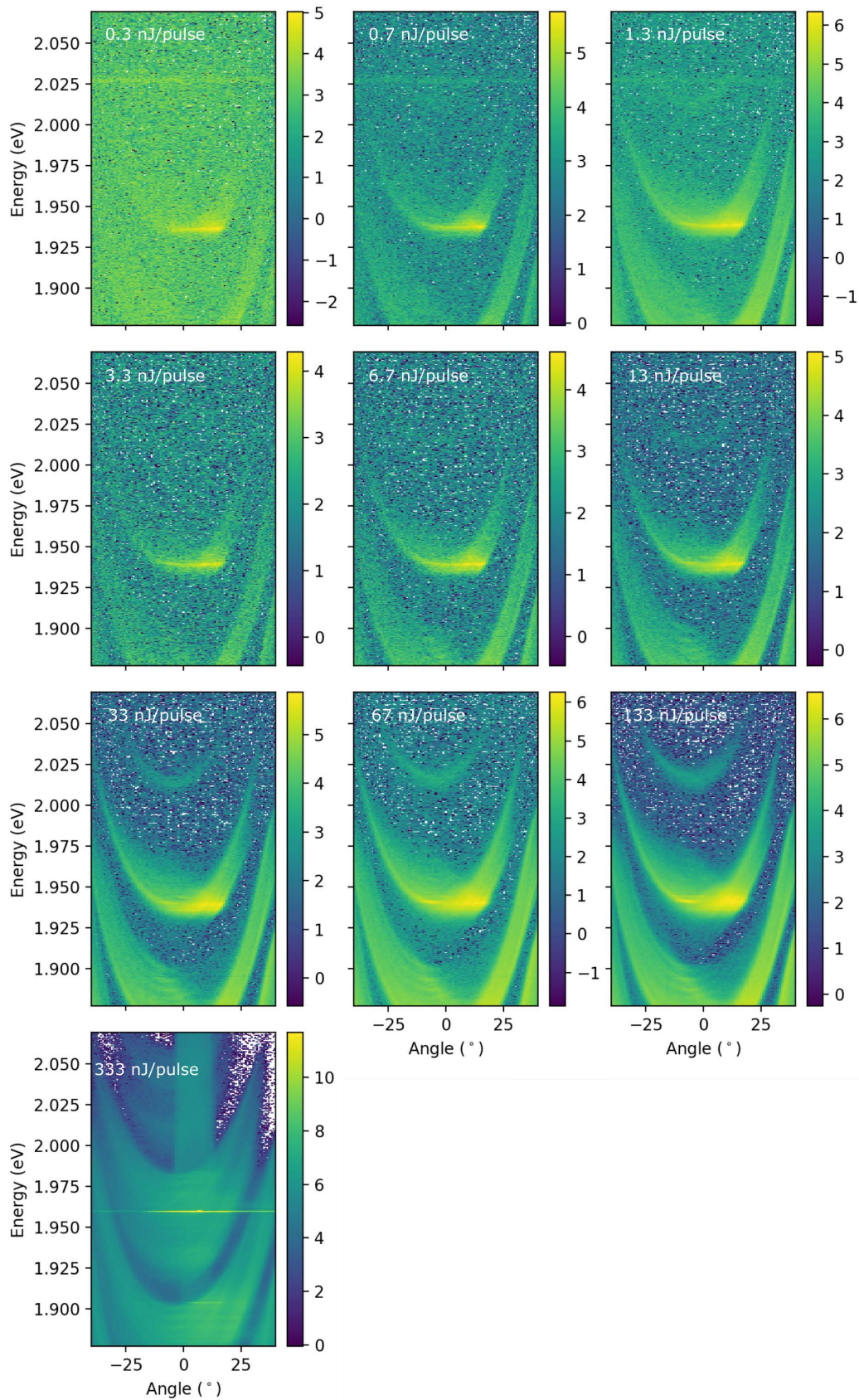


Figure 8.16: **mCherry second lasing regime.** Angle-resolved photoluminescence maps of mCherry open-cavity under non-resonant pulsed excitation as a function of excitation power. Maps in logarithmic scale. Objective with $NA = 0.75$.

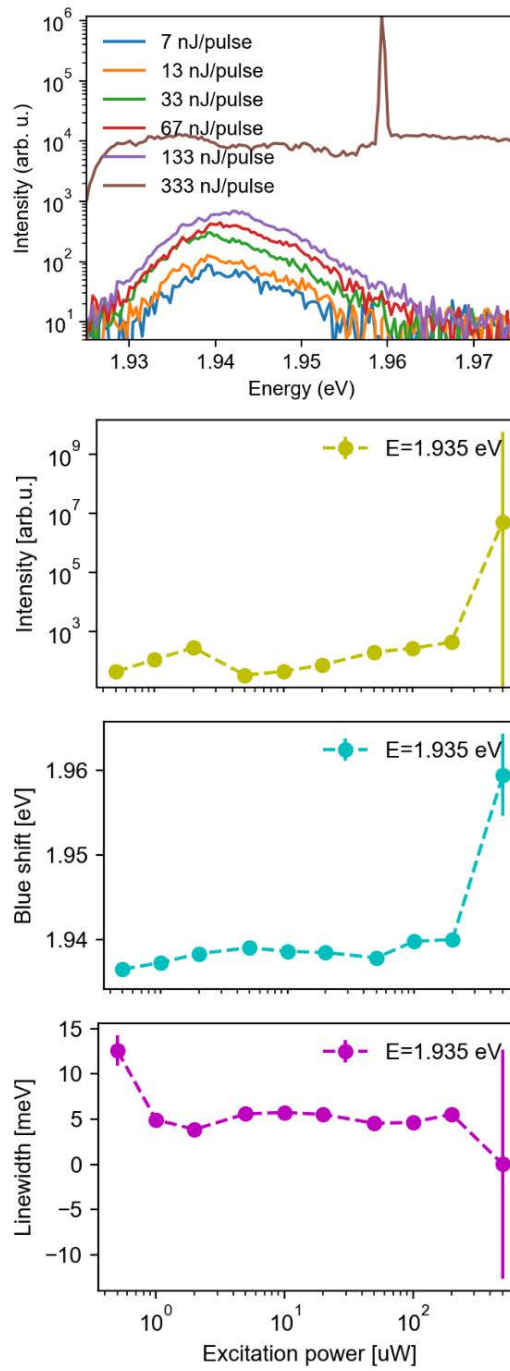


Figure 8.17: (a,b) Cross-section at $k_{\parallel} = 0$ of low energy (a) and high energy (b) mode (compare 8.14). Intensity of the lower (c) and upper (d) cavity mode, (e,f) its energy blueshift, and (g,h) linewidth versus the excitation power. Lines connecting experimental points are guide for the eye.

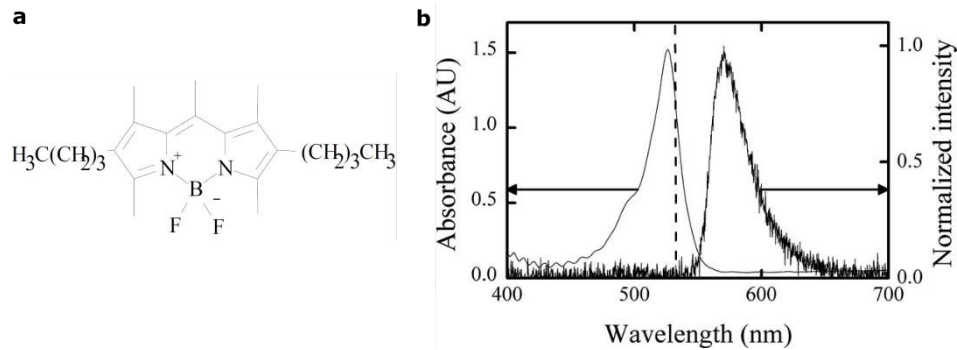


Figure 8.18: **a** P580 dye chemical structure. **b** Example of an absorbance (left) and fluorescence (right) spectra parallel to the director for the P580-doped nematic sample. Image after [152].

purple lines represent the reflected light detected with vertical polarization. When the voltage is applied, the horizontally polarized mode starts to shift to higher energies. At an applied voltage of 1.82 V, we observe characteristic Rashba-Dresselhaus coupling. This regime is shown in more detail in Fig. 8.20 for six main polarizations of detected light and the corresponding Stokes parameter maps. We clearly see that, as expected, in the Rashba-Dresselhaus regime the cavity modes become circularly polarized and no contribution from linear polarizations is observed.

For the discussed sample, we observed emission tunable with applied voltage. This is the first observation of fully tunable emission including the Rashba-Dresselhaus regime from the LCMC structure. In Figure 8.21 we present photoluminescence maps and Stokes parameters maps for 0 V and 1.82 V. The experiment was carried out for excitation with a continuous wave green laser (532 nm) with power $5 \mu\text{W}$. In the upper panels, we see photoluminescence maps for H, V, and D polarization of the detected light with the corresponding S_1 parameter map at 0 V, while panels in the bottom row present the Rashba-Dresselhaus regime (at 1.82 V). The photoluminescence maps for the σ_+ , σ_- and D polarization of the detected light, as well as the S_3 parameter map, are presented.

For the Rashba-Dresselhaus regime, we performed measurements as a function of the excitation power of continuous wave laser. This is shown in Fig. 8.22 on photoluminescence maps for σ_+ polarization of detected light. We note that the cavity modes are shifting while the voltage applied to the cavity is constant. The resulting detuning is persistent, i.e., it remains present even

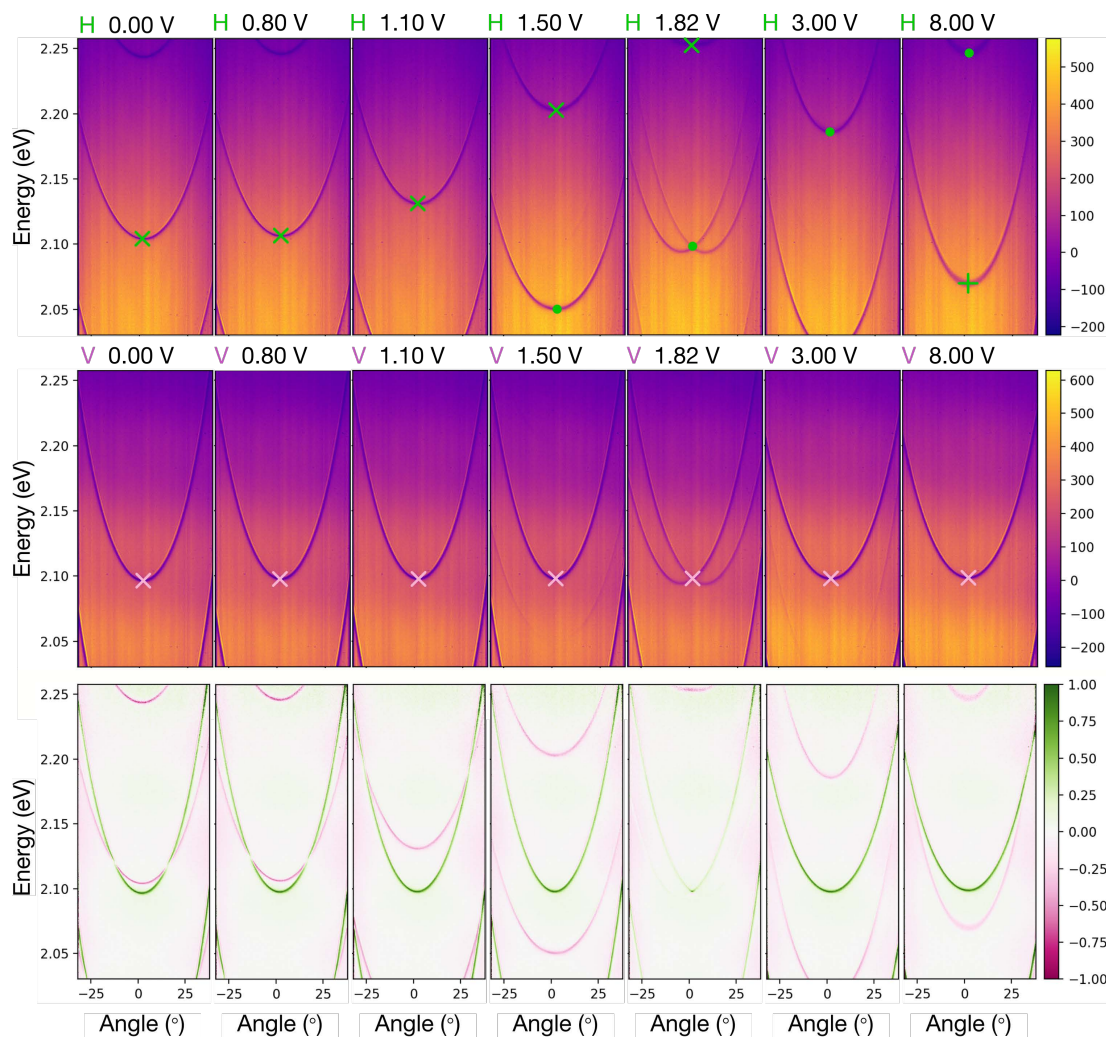


Figure 8.19: Angle-resolved reflectivity maps for successive voltages applied to the LCMC with P580 dye. Top panel: H polarization on detection. Middle panel: V polarization on detection. Bottom panel: S_1 Stokes parameters maps for corresponding reflectivity maps. The crosses and dots follow successive cavity modes to guide the eye.

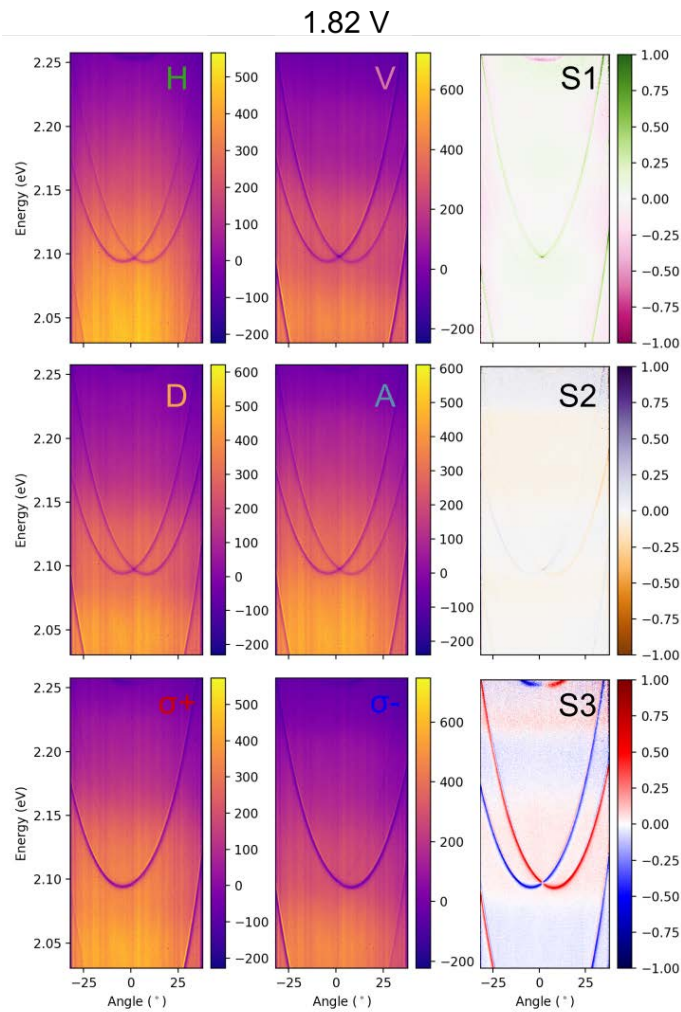


Figure 8.20: Rashba-Dresselhaus regime. Angle-resolved reflectivity maps for six main polarizations (H, V, D, A, σ_+ , σ_-) with corresponding Stokes parameter maps S_1 , S_2 and S_3 .

after lowering the excitation power. The origin of the observed effect requires further investigation. It may emerge due to local heating of the sample. This changes the ordering of the LC at that location, thus changing $\Delta\varepsilon$.

After a series of measurements presented in Fig. 8.22, we adjusted the voltage applied to the sample to revert the system to the Rashba-Dresselhaus regime (see Fig. 8.23). The effect caused by the laser light corresponds to the voltage change by -105meV (at the beginning of the measurements it was 2.015V , and 1.91V afterwards).

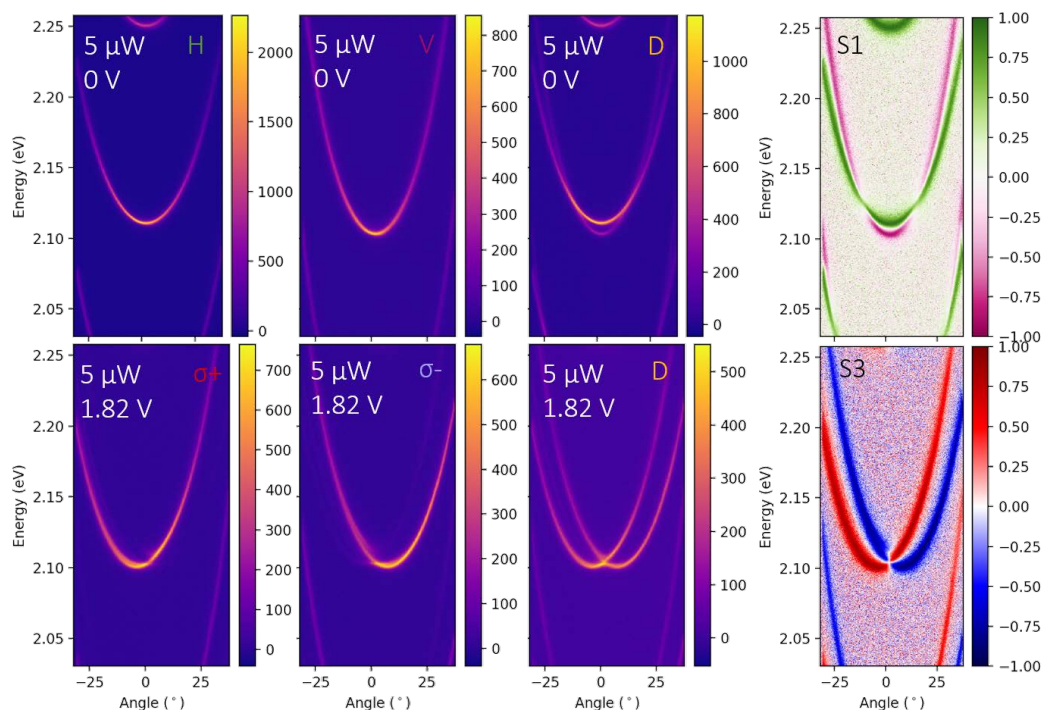


Figure 8.21: Photoluminescence maps for different polarization detection (H, V, D) with S1 (at 0.00 V) and S3 (at 1.82 V) Stokes parameter maps. Polarized emission observed in a liquid crystal cavity with P580 dye with continuous wave excitation.

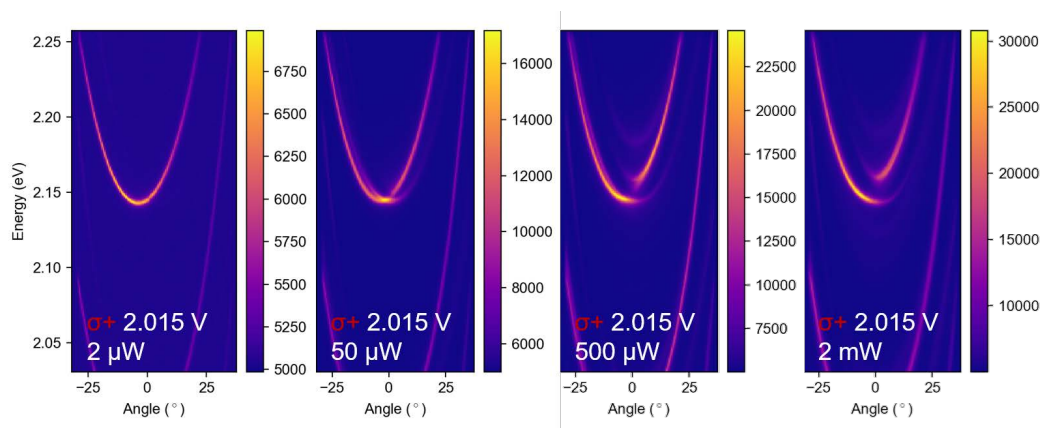


Figure 8.22: Photoluminescence maps for σ_+ polarization of detected light as a function of excitation power: $2 \mu W$, $50 \mu W$, $500 \mu W$ and $2 mW$. Voltage applied to the sample corresponds to the Rashba-Dresselhaus regime. Here the position on the sample was different from previously presented maps, consequently the Rashba-Dresselhaus regime is observed at a different voltage (2.015 V).

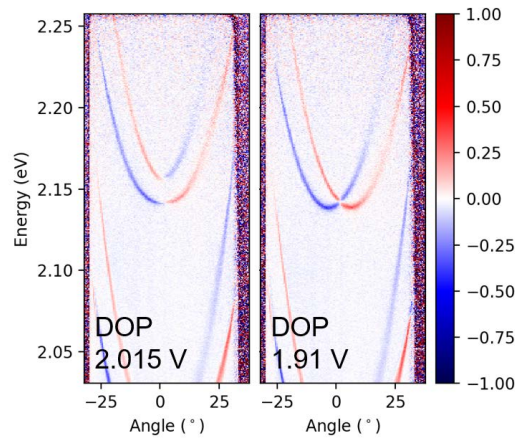


Figure 8.23: S_3 Stokes parameter maps for LCMC with P580 dye after measurements in function of excitation power. Left: DOCP map for 2.015 V voltage applied to the sample (the voltage corresponding to the RD coupling before the series of measurements). Right: DOCP map for 1.91 V (the voltage corresponding to the RD coupling after the series of measurements).

We also performed preliminary measurements for pulsed excitation (fs laser with kHz repetition rate and the wavelength set at 530 nm). Typical results are shown in Fig. 8.24. Both photoluminescence maps are obtained for the same conditions (D polarization of the detected light and power $0.13 \mu\text{J}/\text{pulse}$) for two different spots in the sample. At that stage, the experimental setup allows only for observation of the lasing, but not for systematic measurements. We observed an immediate degradation of the illuminated spot.

The measurements presented in this section contributed to the observation of lasing in a structure containing a liquid crystal and a P580 dye under the Rashba-Dresselhaus regime. The results were published by Marcin Muszyński et al. [153].

8.4. Summary

This chapter presents the first stage of the work that focuses on placing the emitter inside the LCMC structure. We propose two different methods of introducing the emitter: on top of the DBR or inside the LC, depending on the type of the emitter (its chemical structure). The presented results are only a part of the investigations carried out. These preliminary results

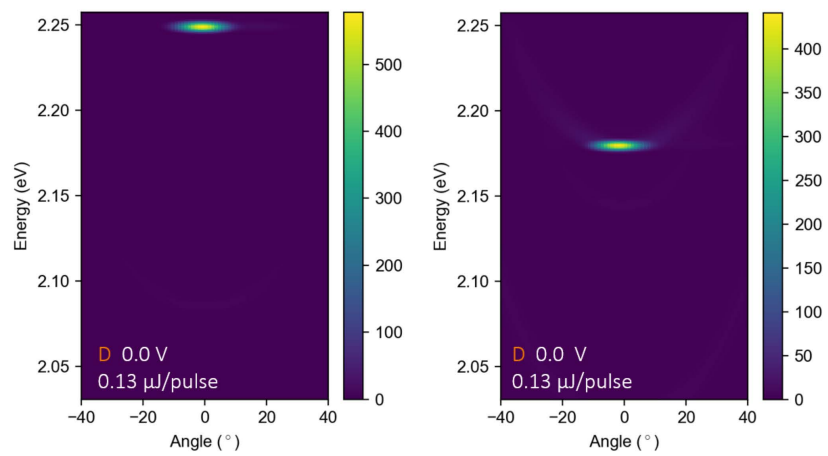


Figure 8.24: Lasing from the LCMC with P580 dye. Photoluminescence maps for two different places on the sample. Pulsed fs laser 530 nm. Time of the of spectrometer shutter set to 0.1 s. Objective with $NA = 0.75$.

show the potential application of the new type of a microcavity. They are also important from the perspective of other ongoing research [64, 153–156]. The concept of a tunable liquid crystal cavity was also used in the group of Prof. Tingge Gao in research on exciton polariton condensates at room temperature [157, 158].

Chapter 9

Conclusions

The work involved the creation and investigation of optical microcavities filled with liquid crystal. The characteristic regimes observed in this type of multimode cavity were shown. We presented and described previously unobserved effects known from other systems, in particular from solid-state physics: the tunable optical spin Hall effect, the optical Rashba-Dresselhaus effect, and the state of the persistent spin helix. In the final part, we focused on the possibility of using a liquid-crystalline microcavity system to study the light-matter interaction. The technological challenges resulting from the system with a liquid crystal cavity have been presented. We carried out preliminary measurements for several groups of emitters, the parameters of which enables them to be placed in the liquid crystal environment, while their emission properties allow for the observation of strong coupling or lasing. We proposed several technological solutions for placing the emitter in the cavity depending on its structure and properties.

The system presented in the present dissertation can be interpreted as a simulation platform that allows one to investigate artificial gauge fields. The LCMC device presented in this work, in fact, involves a synthetic electromagnetic field, an Abelian gauge field, which manifests itself through the effective spin-orbit interaction. Gauge theories descend from the classical theory of electromagnetism, and nowadays encompass general relativity or quantum electrodynamics, and they are useful in condensed matter, nuclear, and high-energy physics among other subfields [159]. Research of artificial gauge fields has been conducted in many systems, including semiconductor devices, but also photonic crystals, ultracold gases, or mechanical systems.

As we have shown in this work, thanks to the fact that our structure is tunable, we have the ability to switch between different regimes described by characteristic effective Hamiltonians and associated synthetic magnetic fields. This will allow such a structure to become a widely used platform

for basic research and further applications. On the basis of the presented research, potential topics that can be continued are research on skyrmions [64], conical intersections [156], and strong coupling and lasing with various materials [153–155, 157, 158]. Each of these topics is a separate field with a broad literature. However, in each of them, the presented system can make an interesting contribution.

Our approach combines the advantages of previous solutions – different methods of the tunability of optical spin Hall effect, including the ease of tunability through the application of an external voltage, and a broad tunability range, which enables adiabatic control of different spin textures in reciprocal and real space.

From the application point of view, the reported transducer technology can be easily integrated with light emitters (such as different dopants: quantum dots, dyes, exfoliated layers of transition-metal dichalcogenides) for room temperature strong light-matter coupling [154], condensation [157, 158] and lasing [153].

	Spin-orbit coupling	Effective magnetic field (Zeeman term)	Operating temperatures	SOI and effective magnetic field tunability	Integration with photonic systems	Applicability for strong light-matter coupling	Rashba parameter
Our work	Rashba-Dressel-hauss, OSHE	yes	room	yes	yes	yes	31.9 eV·Å
Semiconductors [160]	Rashba, Dressel-hauss	yes	cryogenic	no	yes	no	0.034 eV·Å
Semiconductor micro-cavities [48, 52–57, 161]	SOI, OSHE	yes	cryogenic	no	yes	yes	-
Metals and other solid state systems [162–166]	Rashba-Dressel-hauss	yes	room	no	no	no	1.6 eV·Å 1.9 eV·Å 0.7 eV·Å 0.8 eV·Å
Cold atoms [167–169]	Rashba-Dressel-hauss	yes	nano K, micro K	yes	no	no	not provided
Antennas [170], meta-materials and photonic structures [171, 172]	Rashba	no	room	no	depends	no	not provided

List of publications

Publications directly related to this thesis

1. M. Król*, K. Rechcińska*, H. Sigurdsson, P. Oliwa, R. Mazur, P. Morawiak, W. Piecek, P. Kula, P. G. Lagoudakis, M. Matuszewski, W. Bardyszewski, B. Piętka, J. Szczytko, "Realizing Optical Persistent Spin Helix and Stern-Gerlach Deflection in an Anisotropic Liquid Crystal Microcavity", *Physical Review Letters* **127**, 190401 (2021)
2. K. Rechcińska, M. Król, R. Mazur, P. Morawiak, R. Mirek, K. Łempicka, W. Bardyszewski, M. Matuszewski, P. Kula, W. Piecek, P. G. Lagoudakis, B. Piętka, J. Szczytko, "Engineering spin-orbit synthetic Hamiltonians in liquid-crystal optical cavities" *Science*, **366**, 727-730 (2019)
3. K. Lekenta, M. Król, R. Mirek, K. Łempicka, D. Stephan, R. Mazur, P. Morawiak, P. Kula, W. Piecek, P. G. Lagoudakis, B. Piętka, J. Szczytko "Tunable optical spin Hall effect in a liquid crystal microcavity", *Light: Science & Applications*, **7**, 74 (2018)

Publications related to this thesis

1. M. Muszyński, M. Król, K. Rechcińska, P. Oliwa, M. Kędziora, K. Łempicka-Mirek, R. Mazur, P. Morawiak, W. Piecek, P. Kula, P. G. Lagoudakis, B. Piętka, J. Szczytko "Realizing Persistent-Spin-Helix Lasing in the Regime of Rashba-Dresselhaus Spin-Orbit Coupling in a Dye-Filled Liquid-Crystal Optical Microcavity." *Physical Review Applied* **17** 014041 (2022)
2. M. Król, H. Sigurdsson, K. Rechcińska, P. Oliwa, K. Tyszka, W. Bardyszewski, A. Opala, M. Matuszewski, P. Morawiak, R. Mazur, W. Piecek, P. Kula, P. G. Lagoudakis, B. Piętka, J. Szczytko "Observation of second-order meron polarization textures in optical microcavities" *Optica*, **8**, 255-261 (2021)

3. K. Łempicka, M. Furman, M. Muszyński, M. Król, A. Wincukiewicz, K. Rechcińska, R. Mazur, W. Piecek, M. Kamińska, J. Szczytko, B. Piętka "Exciton-polaritons in a tunable microcavity with 2D-perovskite" *Terahertz Science and Applications JW4A*. 66 (2019)

Publications not directly related to this thesis

1. M. Król, K. Rechcińska, K. Nogajewski, M. J. Grzeszczyk, K. Łempicka, R. Mirek, S. Piotrowska, K. Watanabe, T. Taniguchi, M. Molas, M. Potemski, J. Szczytko, B. Piętka "Exciton-polaritons in multilayer WSe₂ in a planar microcavity", *2D Materials*, **7**, 015006 (2019)
2. M. Król, R. Mirek, D. Stephan, K. Lekenta, J-G. Rousset, W. Pacuski, A. V. Kavokin, M. Matuszewski, J. Szczytko, B. Piętka "Giant spin Meissner effect in a nonequilibrium exciton-polariton gas" *Physical Review B*, **99** 115318 (2019)
3. M. Król, K. Lekenta, R. Mirek, K. Łempicka, D. Stephan, K. Nogajewski, M. R. Molas, A. Babiński, M. Potemski, J. Szczytko, B. Piętka "Valley polarization of exciton-polaritons in monolayer WSe₂ in a tunable microcavity", *Nanoscale*, **11**, 9574-9579 (2019)
4. M. Król, R. Mirek, K. Lekenta, J-G. Rousset, D. Stephan, M. Nawrocki, M. Matuszewski, J. Szczytko, W. Pacuski, B. Piętka "Spin polarized semimagnetic exciton-polariton condensate in magnetic field" *8*, 1-7 (2018)
5. J-G. Rousset, B. Piętka, M. Król, R. Mirek, K. Lekenta, J. Szczytko, W. Pacuski, M. Nawrocki "Magnetic field effect on the lasing threshold of a semimagnetic polariton condensate", *Physical Review B*, **96**, 125403 (2017)
6. B. Piętka, N. Bobrovska, D. Stephan, M. Teich, M. Król, S. Winnerl, A. Pashkin, R. Mirek, K. Lekenta, F. Morier-Genoud, H. Schneider, B. Deveaud, M. Helm, M. Matuszewski, J. Szczytko "Doubly dressed bosons: exciton polaritons in a strong terahertz field" *Physical Review Letters*, **7**, 077403 (2017)
7. B. Piętka, M. R. Molas, N. Bobrovska, M. Król, R. Mirek, K. Lekenta, P. Stepnicki, F. Morier-Genoud, J. Szczytko, B. Deveaud, M. Matuszewski, M. Potemski "2s exciton-polariton revealed in an external magnetic field" *Physical Review B* **96**, 081402 (2017)
8. K. Łempicka, K. Norowski, M. Grzeszczyk, M. Król, K. Lekenta, A. Babiński, B. Piętka, J. Szczytko "Relative Reflection Difference as a Method for

- Measuring the Thickness of the Exfoliated MoSe₂ Layers" *Acta Physica Polonica A* **132**, 2 (2017)
9. R. Mirek, M. Król, K. Lekenta, J-G. Rousset, M. Nawrocki, M. Kulczykowski, M. Matuszewski, J. Szczytko, W. Pacuski, B. Piętka "Angular dependence of giant Zeeman effect for semimagnetic cavity polaritons", *Physical Review B*, **95**, 085429 (2017)
 10. J-G. Rousset, B. Piętka, M. Król, R. Mirek, K. Lekenta, J. Szczytko, J. Borysiuk, J. Suffczyński, T. Kazimierzczuk, M. Goryca, T. Smoleński, P. Kossacki, M. Nawrocki, W. Pacuski "Strong coupling and polariton lasing in Te based microcavities embedding (Cd, Zn) Te quantum wells", *Applied Physics Letters*, **107**, 201109 (2015)

Other achievements

1. The results discussed in the thesis were presented at international conferences as oral presentations:
 - 49th "Jaszowiec" International School and Conference on the Physics of Semiconductors, online, September 2021. "Optical persistent spin helix phenomenon in liquid crystal microcavities"
 - META2021 the 11th International Conference on Metamaterials, Photonic Crystals and Plasmonics, online, July 2021. "Photonic simulation of Rashba-Dresselhaus spin-orbit coupling in a tunable birefringent cavity"
 - The 2020 MRS Spring/Fall Meeting & Exhibit, online, December 2020. "Liquid Crystal Cavities as a Platform for Engineering of Spin-Orbit Optical Interaction"
 - International Workshop on the Optical Properties of Nanostructures OPON 2020, Warsaw, Poland, February 2020. "Rashba-Dresselhaus spin-orbit coupling orbit in tunable birefringent microcavity"
 - International Conference on Terahertz Emission, Metamaterials and Nanophotonics 4, Lecce, Italy, May 2019. "Liquid crystal microcavity as a new building block for the next-generation of spin Hall based devices"
 - Conference on Liquid Crystals - Chemistry, Physics and Applications XXII CLC'2018, Jastrzębia Góra, September 2018. "Optical spin Hall effect in a liquid crystal microcavity with tunable TE-TM splitting"

2. Short term internships
 - Internship in the „Hybrid Photonics” Laboratory, Department of Physics & Astronomy, University of Southampton. Research group led by Prof. Pavlos Lagoudakis; (September 2019)
 - Internship at the Faculty of New Technologies and Chemistry of the Military University of Technology, Warsaw. Research group led by Prof. Wiktor Piecek (March-June 2017)
 - Internship at Laboratoire National des Champs Magnétiques Intenses, Grenoble, France. Research group led by Prof. Marek Potemski (July 2016)
3. Awards and scholarships
 - Prof. Leonard Sosnowski Prize (2021)
 - Joanna and Jerzy Glazer prize for the best master’s thesis done at the Faculty of Physics of the University of Warsaw (2017)
 - Scholarship from Ministry of Science and Higher Education for outstanding achievements (2016)
4. Project leader "Organic-inorganic hybrid tuned microcavities for strong light-matter coupling" *Diamentowy Grant*, grant from the Ministry of Science and Higher Education realized at the Faculty of Physics of the University of Warsaw
5. Patent Application: "Tunable optical microcavity for modulation and generation of specific radiation", J. Szczytko, K. Lekenta, B. Pietka, M. Krol, R. Mirek, D. Stephan, W. Piecek, R. Mazur, P. Morawiak, US 2022/0026777 A1 (2022)
6. Popular science project promoting scientific research entitled "When photons pretend to be electrons" on liquid crystal optical microcavities under the Action III.3.2 "Promotion of scientific research" program at University of Warsaw (2021) <https://www.youtube.com/watch?v=-qmCU7iTaHs&t=31s>

Bibliography

- [1] D. W. Berreman, “Optics in stratified and anisotropic media: 4×4 -matrix formulation,” *J. Opt. Soc. Am.*, vol. 62, pp. 502–510, Apr 1972.
- [2] M. Schubert, “Polarization-dependent optical parameters of arbitrarily anisotropic homogeneous layered systems,” *Phys. Rev. B*, vol. 53, pp. 4265–4274, Feb 1996.
- [3] A. Kavokin, J. J. Baumberg, G. Malpuech, and F. P. Laussy, *Microcavities*, vol. 21 of *Series on Semicond. Sci. Technol.* Oxford University Press, 2017.
- [4] R. Hivet, H. Flayac, and D. e. a. Solnyshkov, “Half-solitons in a polariton quantum fluid behave like magnetic monopoles,” *Nature Physics*, no. 8, pp. 724–728, 2012.
- [5] G. Liu, D. W. Snoke, A. Daley, L. N. Pfeiffer, and K. West, “A new type of half-quantum circulation in a macroscopic polariton spinor ring condensate,” *Proceedings of the National Academy of Sciences*, vol. 112, no. 9, pp. 2676–2681, 2015.
- [6] L. Lu, J. D. Joannopoulos, and M. Soljacic, “Topological photonics,” *Nat. Photonics*, vol. 8, p. 821, Oct 2014.
- [7] G. Panzarini, L. C. Andreani, A. Armitage, D. Baxter, M. S. Skolnick, V. N. Astratov, J. S. Roberts, A. V. Kavokin, M. R. Vladimirova, and M. A. Kaliteevski, “Exciton-light coupling in single and coupled semiconductor microcavities: Polariton dispersion and polarization splitting,” *Phys. Rev. B*, vol. 59, pp. 5082–5089, Feb 1999.
- [8] M. Maragkou, C. E. Richards, T. Ostatnický, A. J. D. Grundy, J. Zajac, M. Hugues, W. Langbein, and P. G. Lagoudakis, “Optical analogue of the spin Hall effect in a photonic cavity,” *Optics Letters*, vol. 36, p. 1095, apr 2011.
- [9] C. Weisbuch, M. Nishioka, A. Ishikawa, and Y. Arakawa, “Observation of the coupled exciton-photon mode splitting in a semiconductor quantum microcavity,” *Phys. Rev. Lett.*, vol. 69, pp. 3314–3317, Dec 1992.
- [10] V. Shahnazaryan, S. Morina, S. A. Tarasenko, and I. A. Shelykh, “Spin

- currents of exciton polaritons in microcavities with (110)-oriented quantum wells,” *Phys. Rev. B*, vol. 92, p. 155305, Oct 2015.
- [11] M. A. Sentef, M. Ruggenthaler, and A. Rubio, “Cavity quantum-electrodynamical polaritonically enhanced electron-phonon coupling and its influence on superconductivity,” *Sci. Adv.*, vol. 4, no. 11, 2018.
- [12] G. Nardin, R. Cerna, T. K. Paraíso, B. Pietka, Y. Léger, O. E. Daif, F. Morier-Genoud, and B. Deveaud-Plédran, “Probability density tomography of microcavity polaritons confined in cylindrical traps of various sizes,” *Superlattices and Microstructures*, vol. 47, no. 1, pp. 207 – 212, 2010. Proceedings of the 9th International Conference on Physics of Light-Matter Coupling in Nanostructures, PLMCN 2009 (Lecce - Italy).
- [13] P. Wölfle, “Quasiparticles in condensed matter systems,” *Rep. Prog. Phys.*, vol. 81, p. 032501, jan 2018.
- [14] D. Sanvitto and S. Kéna-Cohen, “The road towards polaritonic devices,” *Nat. Mater.*, vol. 15, p. 1061, Jul 2016. Review Article.
- [15] S. Klembt, T. H. Harder, O. A. Egorov, K. Winkler, R. Ge, M. A. Bandres, M. Emmerling, L. Worschech, T. C. H. Liew, M. Segev, C. Schneider, and S. Höfling, “Exciton-polariton topological insulator,” *Nature*, vol. 562, no. 7728, pp. 552–556, 2018.
- [16] S. Kéna-Cohen and S. Forrest, “Room-temperature polariton lasing in an organic single-crystal microcavity,” *Nature Photonics*, vol. 4, no. 6, pp. 371–375, 2010.
- [17] A. V. Zasedatelev, A. V. Baranikov, D. Urbonas, F. Scafirimuto, U. Scherf, T. Stöferle, R. F. Mahrt, and P. G. Lagoudakis, “A room-temperature organic polariton transistor,” *Nature Photonics*, vol. 13, no. 6, pp. 378–383, 2019.
- [18] S. Christopoulos, G. B. H. Von Högersthal, A. Grundy, P. Lagoudakis, A. Kavokin, J. Baumberg, G. Christmann, R. Butté, E. Feltn, J.-F. Carlin, *et al.*, “Room-temperature polariton lasing in semiconductor microcavities,” *Physical Review Letters*, vol. 98, no. 12, p. 126405, 2007.
- [19] J. D. Plumhof, T. Stöferle, L. Mai, U. Scherf, and R. F. Mahrt, “Room-temperature Bose–Einstein condensation of cavity exciton–polaritons in a polymer,” *Nature Materials*, vol. 13, no. 3, pp. 247–252, 2014.
- [20] J. Kasprzak, M. Richard, S. Kundermann, A. Baas, P. Jeambrun, J. M. J. Keeling, F. Marchetti, M. Szymańska, R. André, J. Staehli, *et al.*, “Bose–Einstein condensation of exciton polaritons,” *Nature*, vol. 443, no. 7110, pp. 409–414, 2006.
- [21] R. Balili, V. Hartwell, D. Snoke, L. Pfeiffer, and K. West, “Bose-Einstein

- condensation of microcavity polaritons in a trap,” *Science*, vol. 316, no. 5827, pp. 1007–1010, 2007.
- [22] D.-K. Yang and S.-T. Wu, *Fundamentals of liquid crystal devices*. John Wiley & Sons, 2014.
- [23] G. V. Prakash, M. Kaczmarek, A. Dyadyusha, J. Baumberg, and G. D’Alessandro, “Control of topological defects in microstructured liquid crystal cells,” *Optics Express*, vol. 13, no. 6, pp. 2201–2209, 2005.
- [24] M. Humar, M. Ravnik, S. Pajk, and I. Mušević, “Electrically tunable liquid crystal optical microresonators,” *Nature photonics*, vol. 3, no. 10, pp. 595–600, 2009.
- [25] I. Khoo, R. Normandin, and V. So, “Optical bistability using a nematic liquid crystal film in a fabry-perot cavity,” *Journal of Applied Physics*, vol. 53, no. 11, pp. 7599–7601, 1982.
- [26] M.-M. Cheung, S. Durbin, and Y. Shen, “Optical bistability and self-oscillation of a nonlinear Fabry–Perot interferometer filled with a nematic-liquid-crystal film,” *Optics letters*, vol. 8, no. 1, pp. 39–41, 1983.
- [27] S. Hoogland, J. Baumberg, S. Coyle, J. Baggett, M. Coles, and H. Coles, “Self-organized patterns and spatial solitons in liquid-crystal microcavities,” *Physical Review A*, vol. 66, no. 5, p. 055801, 2002.
- [28] G. D’Alessandro and A. A. Wheeler, “Bistability of liquid crystal microcavities,” *Physical Review A*, vol. 67, no. 2, p. 023816, 2003.
- [29] G. Dresselhaus, “Spin-orbit coupling effects in zinc blende structures,” *Phys. Rev.*, vol. 100, pp. 580–586, Oct 1955.
- [30] E. Rashba, “Symmetry of energy bands in crystals of wurtzite type. 1. symmetry of bands disregarding spin-orbit interaction,” *Soviet Physics-Solid State*, vol. 1, no. 3, pp. 368–380, 1959.
- [31] E. I. Rashba and V. I. Sheka, “Simmetriya energeticheskikh zon v kristallakh tipa vyurtsita. II. Simmetriya zon s uchyotom spinovykh vzaimodeistvii,” *Fiz. Tverd. Tela: Collected Papers*, vol. 2, pp. 162–176, 1959. [English translation: Supplemental Material to the paper by G. Bihlmayer, O. Rader, and R. Winkler, Focus on the Rashba effect, *New J. Phys.* 17, 050202 (2015)].
- [32] F. Vas’ko, “Spin splitting in the spectrum of two-dimensional electrons due to the surface potential,” *Soviet Journal of Experimental and Theoretical Physics Letters*, vol. 30, p. 541, 1979.
- [33] Y. A. Bychkov and E. Rashba, “Properties of a 2D electron gas with lifted spectral degeneracy,” *JETP Lett.*, vol. 39, p. 78, 1984. [Pis’ma Zh. Eksp. Teor. Fiz. **39**, 66 (1984)].
- [34] A. Manchon, H. C. Koo, J. Nitta, S. M. Frolov, and R. A. Duine, “New

- perspectives for Rashba spin-orbit coupling,” *Nat. Mater.*, vol. 14, p. 871, Aug 2015. Review Article.
- [35] M. Schlipf and F. Giustino, “Dynamic Rashba-Dresselhaus effect,” *Physical Review Letters*, vol. 127, no. 23, p. 237601, 2021.
- [36] B. A. Bernevig, J. Orenstein, and S.-C. Zhang, “Exact SU(2) symmetry and persistent spin helix in a spin-orbit coupled system,” *Phys. Rev. Lett.*, vol. 97, p. 236601, Dec 2006.
- [37] J. D. Koralek, C. P. Weber, J. Orenstein, B. A. Bernevig, S.-C. Zhang, S. Mack, and D. D. Awschalom, “Emergence of the persistent spin helix in semiconductor quantum wells,” *Nature*, vol. 458, p. 610, Apr 2009.
- [38] M. P. Walser, C. Reichl, W. Wegscheider, and G. Salis, “Direct mapping of the formation of a persistent spin helix,” *Nature Physics*, vol. 8, pp. 757–762, oct 2012.
- [39] M. Kohda and G. Salis, “Physics and application of persistent spin helix state in semiconductor heterostructures,” *Semicond. Sci. Technol.*, vol. 32, p. 073002, jun 2017.
- [40] J. Schliemann, “Colloquium: Persistent spin textures in semiconductor nanostructures,” *Rev. Mod. Phys.*, vol. 89, p. 011001, Jan 2017.
- [41] F. Passmann, S. Anghel, C. Ruppert, A. D. Bristow, A. V. Poshakinskiy, S. A. Tarasenko, and M. Betz, “Dynamical formation and active control of persistent spin helices in III-V and II-VI quantum wells,” *Semiconductor Science and Technology*, vol. 34, p. 093002, aug 2019.
- [42] V. S. Liberman and B. Y. Zel’dovich, “Spin-orbit interaction of a photon in an inhomogeneous medium,” *Phys. Rev. A*, vol. 46, pp. 5199–5207, Oct 1992.
- [43] K. Y. Bliokh, F. J. Rodríguez-Fortuño, F. Nori, and A. V. Zayats, “Spin-orbit interactions of light,” *Nat. Photonics*, vol. 9, p. 796, Nov 2015.
- [44] K. Y. Bliokh, “Geometrodynamics of polarized light: Berry phase and spin Hall effect in a gradient-index medium,” *Journal of Optics A: Pure and Applied Optics*, vol. 11, p. 094009, aug 2009.
- [45] F. Cardano and L. Marrucci, “Spin-orbit photonics,” *Nat. Photonics*, vol. 9, p. 776, Nov 2015.
- [46] M. I. Dyakonov and V. Perel, “Current-induced spin orientation of electrons in semiconductors,” *Physics Letters A*, vol. 35, no. 6, pp. 459–460, 1971.
- [47] A. Kavokin, G. Malpuech, and M. Glazov, “Optical spin Hall effect,” *Phys. Rev. Lett.*, vol. 95, p. 136601, Sep 2005.
- [48] C. Leyder, M. Romanelli, J. P. Karr, E. Giacobino, T. C. H. Liew, M. M. Glazov, A. V. Kavokin, G. Malpuech, and A. Bramati, “Observation of the optical spin Hall effect,” *Nat. Phys.*, vol. 3, p. 628, Jul 2007.

- [49] M. Onoda, S. Murakami, and N. Nagaosa, “Hall effect of light,” *Phys. Rev. Lett.*, vol. 93, p. 083901, Aug 2004.
- [50] A. Aiello, N. Lindlein, C. Marquardt, and G. Leuchs, “Transverse angular momentum and geometric spin Hall effect of light,” *Phys. Rev. Lett.*, vol. 103, p. 100401, Aug 2009.
- [51] X. Ling, X. Zhou, K. Huang, Y. Liu, C.-W. Qiu, H. Luo, and S. Wen, “Recent advances in the spin Hall effect of light,” *Rep. Prog. Phys.*, vol. 80, p. 066401, mar 2017.
- [52] A. Amo, T. C. H. Liew, C. Adrados, E. Giacobino, A. V. Kavokin, and A. Bramati, “Anisotropic optical spin Hall effect in semiconductor microcavities,” *Phys. Rev. B*, vol. 80, p. 165325, Oct 2009.
- [53] P. Cilibrizzi, H. Sigurdsson, T. C. H. Liew, H. Ohadi, S. Wilkinson, A. Askitopoulos, I. A. Shelykh, and P. G. Lagoudakis, “Polariton spin whirls,” *Phys. Rev. B*, vol. 92, p. 155308, Oct 2015.
- [54] E. Kammann, T. C. H. Liew, H. Ohadi, P. Cilibrizzi, P. Tsotsis, Z. Hatzopoulos, P. G. Savvidis, A. V. Kavokin, and P. G. Lagoudakis, “Nonlinear optical spin Hall effect and long-range spin transport in polariton lasers,” *Phys. Rev. Lett.*, vol. 109, p. 036404, Jul 2012.
- [55] P. Cilibrizzi, H. Sigurdsson, T. C. H. Liew, H. Ohadi, A. Askitopoulos, S. Brodbeck, C. Schneider, I. A. Shelykh, S. Höfling, J. Ruostekoski, and P. Lagoudakis, “Half-skyrmion spin textures in polariton microcavities,” *Phys. Rev. B*, vol. 94, p. 045315, Jul 2016.
- [56] S. Donati, L. Dominici, G. Dagvadorj, D. Ballarini, M. De Giorgi, A. Bramati, G. Gigli, Y. G. Rubo, M. H. Szymańska, and D. Sanvitto, “Twist of generalized skyrmions and spin vortices in a polariton superfluid,” *Proc. Natl. Acad. Sci. U.S.A.*, vol. 113, no. 52, pp. 14926–14931, 2016.
- [57] F. Manni, Y. Léger, Y. G. Rubo, R. André, and B. Deveaud, “Hyperbolic spin vortices and textures in exciton-polariton condensates,” *Nat. Commun.*, vol. 4, p. 2590, Oct 2013. Article.
- [58] R. Mazur, W. Piecek, Z. Raszewski, P. Morawiak, K. Garbat, O. Chojnowska, M. Mrukiewicz, M. Olifierczuk, J. Kedzierski, R. Dabrowski, *et al.*, “Nematic liquid crystal mixtures for 3D active glasses application,” *Liquid Crystals*, vol. 44, no. 2, pp. 417–426, 2017.
- [59] R. Dąbrowski, P. Kula, and J. Herman, “High birefringence liquid crystals,” *Crystals*, vol. 3, no. 3, pp. 443–482, 2013.
- [60] E. Miszczyk, R. Mazur, P. Morawiak, M. Mrukiewicz, W. Piecek, Z. Raszewski, P. Kula, K. Kowiorski, J. Kędzierski, and J. Zieliński, “Refractive index matched liquid crystal cell for laser metrology application,” *Liquid Crystals*, vol. 45, no. 11, pp. 1690–1698, 2018.

- [61] R. Frindt, “The optical properties of single crystals of WSe₂ and MoTe₂,” *Journal of Physics and Chemistry of Solids*, vol. 24, pp. 1107–1108, sep 1963.
- [62] K. Ludwiczak, A. K. Dąbrowska, J. Binder, M. Tokarczyk, J. Iwański, B. Kurowska, J. Turczyński, G. Kowalski, R. Bożek, R. Stepniewski, *et al.*, “Heteroepitaxial growth of high optical quality, wafer-scale van der Waals heterostructures,” *ACS applied materials & interfaces*, vol. 13, no. 40, pp. 47904–47911, 2021.
- [63] W. Pacuski, M. Grzeszczyk, K. Nogajewski, A. Bogucki, K. Oreszczuk, J. Kucharek, K. E. Połczyńska, B. Seredyński, A. Rodek, R. Bożek, T. Taniguchi, K. Watanabe, S. Kret, J. Sadowski, T. Kazimierzuk, M. Potemski, and P. Kossacki, “Narrow Excitonic Lines and Large-Scale Homogeneity of Transition-Metal Dichalcogenide Monolayers Grown by Molecular Beam Epitaxy on Hexagonal Boron Nitride,” *Nano Letters*, vol. 20, pp. 3058–3066, may 2020.
- [64] M. Król, H. Sigurdsson, K. Rechcińska, P. Oliwa, K. Tyszka, W. Bardyszewski, A. Opala, M. Matuszewski, P. Morawiak, R. Mazur, *et al.*, “Observation of second-order meron polarization textures in optical microcavities,” *Optica*, vol. 8, no. 2, pp. 255–261, 2021.
- [65] K. Rechcińska, M. Król, R. Mazur, P. Morawiak, R. Mirek, K. Łempicka, W. Bardyszewski, M. Matuszewski, P. Kula, W. Piecek, P. G. Lagoudakis, B. Piętka, and J. Szczytko, “Engineering spin-orbit synthetic Hamiltonians in liquid-crystal optical cavities,” *Science*, vol. 366, no. 6466, pp. 727–730, 2019.
- [66] F. A. Cotton, *Chemical Applications of Group Theory*. New York: John Wiley & Sons, 1990.
- [67] K. Lekenta, M. Król, R. Mirek, K. Łempicka, D. Stephan, R. Mazur, P. Morawiak, P. Kula, W. Piecek, P. G. Lagoudakis, B. Pietka, and J. Szczytko, “Tunable optical spin Hall effect in a liquid crystal microcavity,” *Light Sci. Appl.*, vol. 7, no. 1, p. 74, 2018.
- [68] K. Y. Bliokh, Y. Gorodetski, V. Kleiner, and E. Hasman, “Coriolis effect in optics: Unified geometric phase and spin-Hall effect,” *Phys. Rev. Lett.*, vol. 101, p. 030404, Jul 2008.
- [69] D. Leykam, K. Y. Bliokh, C. Huang, Y. D. Chong, and F. Nori, “Edge modes, degeneracies, and topological numbers in non-Hermitian systems,” *Phys. Rev. Lett.*, vol. 118, p. 040401, Jan 2017.
- [70] A. Karnieli and A. Arie, “All-optical Stern-Gerlach effect,” *Physical Review Letters*, vol. 120, no. 5, p. 053901, 2018.
- [71] O. Yesharim, A. Karnieli, S. Jackel, G. Di Domenico, S. Trajtenberg-Mills,

- and A. Arie, “Observation of the all-optical Stern–Gerlach effect in nonlinear optics,” *Nature Photonics*, vol. 16, no. 8, pp. 582–587, 2022.
- [72] N. Kravets, A. Aleksanyan, and E. Brasselet, “Chiral optical Stern-Gerlach newtonian experiment,” *Physical Review Letters*, vol. 122, no. 2, p. 024301, 2019.
- [73] O. Arteaga, E. Garcia-Caurel, and R. Ossikovski, “Stern-Gerlach experiment with light: separating photons by spin with the method of A. Fresnel,” *Optics express*, vol. 27, no. 4, pp. 4758–4768, 2019.
- [74] O. Hosten and P. Kwiat, “Observation of the spin Hall effect of light via weak measurements,” *Science*, vol. 319, no. 5864, pp. 787–790, 2008.
- [75] T. Guillet and C. Brimont, “Polariton condensates at room temperature,” *Comptes Rendus Physique*, vol. 17, pp. 946–956, oct 2016.
- [76] N. Antoine-Vincent, F. Natali, D. Byrne, A. Vasson, P. Disseix, J. Leymarie, M. Leroux, F. Semond, and J. Massies, “Observation of Rabi splitting in a bulk GaN microcavity grown on silicon,” *Physical Review B*, vol. 68, no. 15, p. 153313, 2003.
- [77] F. Semond, I. Sellers, F. Natali, D. Byrne, M. Leroux, J. Massies, N. Ollier, J. Leymarie, P. Disseix, and A. Vasson, “Strong light-matter coupling at room temperature in simple geometry GaN microcavities grown on silicon,” *Applied Physics Letters*, vol. 87, no. 2, p. 021102, 2005.
- [78] R. Butté, G. Christmann, E. Feltin, J.-F. Carlin, M. Mosca, M. Ilegems, and N. Grandjean, “Room-temperature polariton luminescence from a bulk GaN microcavity,” *Physical Review B*, vol. 73, no. 3, p. 033315, 2006.
- [79] J. Baumberg, A. Kavokin, S. Christopoulos, A. Grundy, R. Butté, G. Christmann, D. Solnyshkov, G. Malpuech, G. B. H. von Högersthal, E. Feltin, *et al.*, “Spontaneous polarization buildup in a room-temperature polariton laser,” *Physical Review Letters*, vol. 101, no. 13, p. 136409, 2008.
- [80] P. Bhattacharya, T. Frost, S. Deshpande, M. Z. Baten, A. Hazari, and A. Das, “Room temperature electrically injected polariton laser,” *Physical Review Letters*, vol. 112, no. 23, p. 236802, 2014.
- [81] A. Trichet, F. Médard, J. Zúñiga-Pérez, B. Alloing, and M. Richard, “From strong to weak coupling regime in a single GaN microwire up to room temperature,” *New Journal of Physics*, vol. 14, no. 7, p. 073004, 2012.
- [82] T. Tawara, H. Gotoh, T. Akasaka, N. Kobayashi, and T. Saitoh, “Cavity polaritons in InGaN microcavities at room temperature,” *Physical Review Letters*, vol. 92, no. 25, p. 256402, 2004.
- [83] G. Christmann, R. Butté, E. Feltin, J.-F. Carlin, and N. Grandjean, “Room temperature polariton lasing in a GaN/ AlGaN multiple quantum well microcavity,” *Applied Physics Letters*, vol. 93, no. 5, p. 051102, 2008.

- [84] T.-C. Lu, J.-R. Chen, S.-C. Lin, S.-W. Huang, S.-C. Wang, and Y. Yamamoto, “Room temperature current injection polariton light emitting diode with a hybrid microcavity,” *Nano Letters*, vol. 11, no. 7, pp. 2791–2795, 2011.
- [85] R. Shimada, J. Xie, V. Avrutin, Ü. Özgür, and H. Morkoç, “Cavity polaritons in ZnO-based hybrid microcavities,” *Applied Physics Letters*, vol. 92, no. 1, p. 011127, 2008.
- [86] M. Nakayama, S. Komura, T. Kawase, and D. Kim, “Observation of exciton polaritons in a ZnO microcavity with HfO₂/SiO₂ distributed bragg reflectors,” *Journal of the Physical Society of Japan*, vol. 77, no. 9, p. 093705, 2008.
- [87] R. Schmidt-Grund, B. Rheinländer, C. Czekalla, G. Benndorf, H. Hochmuth, M. Lorenz, and M. Grundmann, “Exciton–polariton formation at room temperature in a planar ZnO resonator structure,” *Applied Physics B*, vol. 93, no. 2, pp. 331–337, 2008.
- [88] F. Médard, J. Zúñiga-Pérez, P. Disseix, M. Mihailovic, J. Leymarie, A. Vasson, F. Semond, E. Frayssinet, J.-C. Moreno, M. Leroux, *et al.*, “Experimental observation of strong light-matter coupling in ZnO microcavities: Influence of large excitonic absorption,” *Physical Review B*, vol. 79, no. 12, p. 125302, 2009.
- [89] T. Guillet, M. Mexis, J. Levrat, G. Rossbach, C. Brimont, T. Bretagnon, B. Gil, R. Butté, N. Grandjean, L. Orosz, *et al.*, “Polariton lasing in a hybrid bulk ZnO microcavity,” *Applied Physics Letters*, vol. 99, no. 16, p. 161104, 2011.
- [90] T.-C. Lu, Y.-Y. Lai, Y.-P. Lan, S.-W. Huang, J.-R. Chen, Y.-C. Wu, W.-F. Hsieh, and H. Deng, “Room temperature polariton lasing vs. photon lasing in a ZnO-based hybrid microcavity,” *Optics express*, vol. 20, no. 5, pp. 5530–5537, 2012.
- [91] H. Franke, C. Sturm, R. Schmidt-Grund, G. Wagner, and M. Grundmann, “Ballistic propagation of exciton–polariton condensates in a ZnO-based microcavity,” *New Journal of Physics*, vol. 14, no. 1, p. 013037, 2012.
- [92] R. Hahe, C. Brimont, P. Valvin, T. Guillet, F. Li, M. Leroux, J. Zuniga-Perez, X. Lafosse, G. Patriarche, and S. Bouchoule, “Interplay between tightly focused excitation and ballistic propagation of polariton condensates in a ZnO microcavity,” *Physical Review B*, vol. 92, no. 23, p. 235308, 2015.
- [93] M. Thunert, A. Janot, H. Franke, C. Sturm, T. Michalsky, M. D. Martín, L. Vina, B. Rosenow, M. Grundmann, and R. Schmidt-Grund, “Cavity polariton condensate in a disordered environment,” *Physical Review B*, vol. 93, no. 6, p. 064203, 2016.
- [94] L. K. van Vugt, S. Rühle, P. Ravindran, H. C. Gerritsen, L. Kuipers, and

- D. Vanmaekelbergh, "Exciton polaritons confined in a ZnO nanowire cavity," *Physical Review Letters*, vol. 97, no. 14, p. 147401, 2006.
- [95] M. A. Zimmler, F. Capasso, S. Müller, and C. Ronning, "Optically pumped nanowire lasers: invited review," *Semiconductor Science and Technology*, vol. 25, no. 2, p. 024001, 2010.
- [96] C. Sturm, H. Hilmer, R. Schmidt-Grund, and M. Grundmann, "Observation of strong exciton–photon coupling at temperatures up to 410 k," *New Journal of Physics*, vol. 11, no. 7, p. 073044, 2009.
- [97] S. Zhang, W. Xie, H. Dong, L. Sun, Y. Ling, J. Lu, Y. Duan, W. Shen, X. Shen, and Z. Chen, "Robust exciton-polariton effect in a ZnO whispering gallery microcavity at high temperature," *Applied Physics Letters*, vol. 100, no. 10, p. 101912, 2012.
- [98] L. Sun, Z. Chen, Q. Ren, K. Yu, L. Bai, W. Zhou, H. Xiong, Z. Zhu, and X. Shen, "Direct observation of whispering gallery mode polaritons and their dispersion in a ZnO tapered microcavity," *Physical Review Letters*, vol. 100, no. 15, p. 156403, 2008.
- [99] A. Trichet, L. Sun, G. Pavlovic, N. A. Gippius, G. Malpuech, W. Xie, Z. Chen, M. Richard, and L. S. Dang, "One-dimensional ZnO exciton polaritons with negligible thermal broadening at room temperature," *Physical Review B*, vol. 83, no. 4, p. 041302, 2011.
- [100] J. Dai, C. Xu, X. Sun, and X. Zhang, "Exciton-polariton microphotoluminescence and lasing from ZnO whispering-gallery mode microcavities," *Applied physics letters*, vol. 98, no. 16, p. 161110, 2011.
- [101] D. Xu, W. Xie, W. Liu, J. Wang, L. Zhang, Y. Wang, S. Zhang, L. Sun, X. Shen, and Z. Chen, "Polariton lasing in a ZnO microwire above 450 K," *Applied Physics Letters*, vol. 104, no. 8, p. 082101, 2014.
- [102] W. Xie, H. Dong, S. Zhang, L. Sun, W. Zhou, Y. Ling, J. Lu, X. Shen, and Z. Chen, "Room-temperature polariton parametric scattering driven by a one-dimensional polariton condensate," *Physical Review Letters*, vol. 108, no. 16, p. 166401, 2012.
- [103] A. Trichet, E. Durupt, F. Médard, S. Datta, A. Minguzzi, and M. Richard, "Long-range correlations in a 97% excitonic one-dimensional polariton condensate," *Physical Review B*, vol. 88, no. 12, p. 121407, 2013.
- [104] C. Dietrich, R. Johne, T. Michalsky, C. Sturm, P. Eastham, H. Franke, M. Lange, M. Grundmann, and R. Schmidt-Grund, "Parametric relaxation in whispering gallery mode exciton-polariton condensates," *Physical Review B*, vol. 91, no. 4, p. 041202, 2015.
- [105] L. Zhang, W. Xie, J. Wang, A. Poddubny, J. Lu, Y. Wang, J. Gu, W. Liu, D. Xu, X. Shen, *et al.*, "Weak lasing in one-dimensional polariton superlat-

- tices,” *Proceedings of the National Academy of Sciences*, vol. 112, no. 13, pp. E1516–E1519, 2015.
- [106] S. Halm, S. Kalusniak, S. Sadofev, H.-J. Wünsche, and F. Henneberger, “Strong exciton-photon coupling in a monolithic ZnO/(Zn, Mg) o multiple quantum well microcavity,” *Applied Physics Letters*, vol. 99, no. 18, p. 181121, 2011.
- [107] P. Kelkar, V. Kozlov, H. Jeon, A. Nurmikko, C.-C. Chu, D. Grillo, J. Han, C. G. Hua, and R. Gunshor, “Excitons in a II-VI semiconductor microcavity in the strong-coupling regime,” *Physical Review B*, vol. 52, no. 8, p. R5491, 1995.
- [108] S. Klemmt, E. Durupt, S. Datta, T. Klein, A. Baas, Y. Léger, C. Kruse, D. Hommel, A. Minguzzi, and M. Richard, “Exciton-polariton gas as a nonequilibrium coolant,” *Physical Review Letters*, vol. 114, no. 18, p. 186403, 2015.
- [109] A. Pawlis, A. Khartchenko, O. Husberg, D. As, K. Lischka, and D. Schikora, “Large room temperature Rabi-splitting in a ZnSe/(Zn,Cd)Se semiconductor microcavity structure,” *Solid state communications*, vol. 123, no. 5, pp. 235–238, 2002.
- [110] K. Sebald, A. Trichet, M. Richard, L. Dang, M. Seyfried, S. Klemmt, C. Kruse, and D. Hommel, “Optical polariton properties in ZnSe-based planar and pillar structured microcavities,” *The European Physical Journal B*, vol. 84, no. 3, pp. 381–384, 2011.
- [111] M. Nakayama, K. Miyazaki, T. Kawase, and D. Kim, “Control of exciton-photon interactions in CuCl microcavities,” *Physical Review B*, vol. 83, no. 7, p. 075318, 2011.
- [112] Y. Katakani, T. Kawase, D. Kim, and M. Nakayama, “Characteristics of cavity polaritons in a CuBr microcavity,” *The European Physical Journal B*, vol. 85, no. 11, pp. 1–6, 2012.
- [113] M. Nakayama, K. Murakami, Y. Furukawa, and D. Kim, “Photoluminescence characteristics of polariton condensation in a CuBr microcavity,” *Applied Physics Letters*, vol. 105, no. 2, p. 021903, 2014.
- [114] A. Brehier, R. Parashkov, J.-S. Lauret, and E. Deleporte, “Strong exciton-photon coupling in a microcavity containing layered perovskite semiconductors,” *Applied physics letters*, vol. 89, no. 17, p. 171110, 2006.
- [115] Z. Han, H.-S. Nguyen, F. Réveret, K. Abdel-Baki, J.-S. Lauret, J. Bloch, S. Bouchoule, and E. Deleporte, “Top-mirror migration for the fabrication of high-Q planar microcavities containing fragile active materials,” *Applied Physics Express*, vol. 6, no. 10, p. 106701, 2013.
- [116] R. Su, C. Diederichs, J. Wang, T. C. Liew, J. Zhao, S. Liu, W. Xu, Z. Chen,

- and Q. Xiong, "Room-temperature polariton lasing in all-inorganic perovskite nanoplatelets," *Nano Letters*, vol. 17, no. 6, pp. 3982–3988, 2017.
- [117] H. S. Nguyen, Z. Han, K. Abdel-Baki, X. Lafosse, A. Amo, J.-S. Lauret, E. Deleporte, S. Bouchoule, and J. Bloch, "Quantum confinement of zero-dimensional hybrid organic-inorganic polaritons at room temperature," *Applied Physics Letters*, vol. 104, no. 8, p. 081103, 2014.
- [118] D. G. Lidzey, D. Bradley, M. Skolnick, T. Virgili, S. Walker, and D. Whittaker, "Strong exciton–photon coupling in an organic semiconductor microcavity," *Nature*, vol. 395, no. 6697, pp. 53–55, 1998.
- [119] D. Lidzey, D. Bradley, T. Virgili, A. Armitage, M. Skolnick, and S. Walker, "Room temperature polariton emission from strongly coupled organic semiconductor microcavities," *Physical Review Letters*, vol. 82, no. 16, p. 3316, 1999.
- [120] S. Kéna-Cohen, M. Davanço, and S. Forrest, "Strong exciton-photon coupling in an organic single crystal microcavity," *Physical Review Letters*, vol. 101, no. 11, p. 116401, 2008.
- [121] K. Daskalakis, S. Maier, R. Murray, and S. Kéna-Cohen, "Nonlinear interactions in an organic polariton condensate," *Nature Materials*, vol. 13, no. 3, pp. 271–278, 2014.
- [122] K. S. Daskalakis, S. A. Maier, and S. Kéna-Cohen, "Spatial coherence and stability in a disordered organic polariton condensate," *Physical Review Letters*, vol. 115, no. 3, p. 035301, 2015.
- [123] Q. H. Wang, K. Kalantar-Zadeh, A. Kis, J. N. Coleman, and M. S. Strano, "Electronics and optoelectronics of two-dimensional transition metal dichalcogenides," *Nature Nanotechnology*, vol. 7, pp. 699–712, nov 2012.
- [124] D. Jariwala, V. K. Sangwan, L. J. Lauhon, T. J. Marks, and M. C. Hersam, "Emerging Device Applications for Semiconducting Two-Dimensional Transition Metal Dichalcogenides," *ACS Nano*, vol. 8, pp. 1102–1120, feb 2014.
- [125] A. K. Geim and I. V. Grigorieva, "Van der Waals heterostructures," *Nature*, pp. 0–6, 2013.
- [126] F. Xia, H. Wang, D. Xiao, M. Dubey, and A. Ramasubramaniam, "Two-dimensional material nanophotonics," *Nature Photonics*, vol. 8, no. 12, pp. 899–907, 2014.
- [127] M. Chhowalla, H. S. Shin, G. Eda, L.-J. Li, K. P. Loh, and H. Zhang, "The chemistry of two-dimensional layered transition metal dichalcogenide nanosheets," *Nature Chemistry*, vol. 5, no. 4, pp. 263–275, 2013.
- [128] D. J. Late, C. S. Rout, D. Chakravarty, and S. Ratha, "Emerging energy ap-

- plications of two-dimensional layered materials,” *Can. Chem. Trans.*, vol. 3, no. 118–157, pp. 118–157, 2015.
- [129] H. Zeng, J. Dai, W. Yao, D. Xiao, and X. Cui, “Valley polarization in MoS₂ monolayers by optical pumping,” *Nature Nanotechnology*, vol. 7, pp. 490–493, aug 2012.
- [130] K. F. Mak, K. He, J. Shan, and T. F. Heinz, “Control of valley polarization in monolayer MoS₂ by optical helicity,” *Nature Nanotechnology*, vol. 7, pp. 494–498, aug 2012.
- [131] K. F. Mak, K. L. McGill, J. Park, and P. L. McEuen, “The valley Hall effect in MoS₂ transistors,” *Science*, vol. 344, pp. 1489–1492, jun 2014.
- [132] T. Cao, G. Wang, W. Han, H. Ye, C. Zhu, J. Shi, Q. Niu, P. Tan, E. Wang, B. Liu, and J. Feng, “Valley-selective circular dichroism of monolayer molybdenum disulphide,” *Nature Communications*, vol. 3, p. 887, jan 2012.
- [133] D. Xiao, G.-B. Liu, W. Feng, X. Xu, and W. Yao, “Coupled Spin and Valley Physics in Monolayers of MoS₂ and Other Group-VI Dichalcogenides,” *Physical Review Letters*, vol. 108, p. 196802, may 2012.
- [134] S. Dufferwiel, T. P. Lyons, D. D. Solnyshkov, A. A. P. Trichet, F. Withers, S. Schwarz, G. Malpuech, J. M. Smith, K. S. Novoselov, M. S. Skolnick, D. N. Krizhanovskii, and A. I. Tartakovskii, “Valley-addressable polaritons in atomically thin semiconductors,” *Nature Photonics*, vol. 11, pp. 497–501, aug 2017.
- [135] D. Davenport and J. C. Nicol, “Luminescence in hydromedusae,” *Proceedings of the Royal Society of London. Series B-Biological Sciences*, vol. 144, no. 916, pp. 399–411, 1955.
- [136] O. Shimomura, “Structure of the chromophore of Aequorea green fluorescent protein,” *FEBS letters*, vol. 104, no. 2, pp. 220–222, 1979.
- [137] W. B. Frommer, M. W. Davidson, and R. E. Campbell, “Genetically encoded biosensors based on engineered fluorescent proteins,” *Chemical Society Reviews*, vol. 38, no. 10, pp. 2833–2841, 2009.
- [138] J. Wiedenmann, F. Oswald, and G. U. Nienhaus, “Fluorescent proteins for live cell imaging: opportunities, limitations, and challenges,” *IUBMB life*, vol. 61, no. 11, pp. 1029–1042, 2009.
- [139] A. S. Mishin, V. V. Belousov, K. M. Solntsev, and K. A. Lukyanov, “Novel uses of fluorescent proteins,” *Current opinion in chemical biology*, vol. 27, pp. 1–9, 2015.
- [140] S. Bär, A. Chizhik, R. Gutbrod, F. Schleifenbaum, A. Chizhik, and A. J. Meixner, “Microcavities: Tailoring the optical properties of single quantum emitters,” *Analytical and Bioanalytical Chemistry*, vol. 396, no. 1, pp. 3–14, 2010.

- [141] R. Y. Tsien, “Nobel lecture: constructing and exploiting the fluorescent protein paintbox,” *Integrative Biology*, vol. 2, no. 2-3, pp. 77–93, 2010.
- [142] A. fluorescent protein database, “eGFP spectrum.” <https://www.fpbse.org/protein/egfp/>. [Online; accessed 6-May-2022].
- [143] A. fluorescent protein database, “tdTomato spectrum.” <https://www.fpbse.org/protein/tdtomato/>. [Online; accessed 6-May-2022].
- [144] A. fluorescent protein database, “mCherry spectrum.” <https://www.fpbse.org/protein/mcherry/>. [Online; accessed 6-May-2022].
- [145] C. P. Dietrich, A. Steude, L. Tropic, M. Schubert, N. M. Kronenberg, K. Ostermann, S. Höfling, and M. C. Gather, “An exciton-polariton laser based on biologically produced fluorescent protein,” *Science Advances*, vol. 2, no. 8, p. e1600666, 2016.
- [146] C. P. Dietrich, A. Steude, M. Schubert, J. Ohmer, U. Fischer, S. Höfling, and M. C. Gather, “Strong coupling in fully tunable microcavities filled with biologically produced fluorescent proteins,” *Advanced Optical Materials*, vol. 5, no. 1, p. 1600659, 2017.
- [147] S. Betzold, M. Dusel, O. Kyriienko, C. P. Dietrich, S. Klemmt, J. Ohmer, U. Fischer, I. A. Shelykh, C. Schneider, and S. Höfling, “Coherence and interaction in confined room-temperature polariton condensates with frenkel excitons,” *ACS Photonics*, vol. 7, no. 2, pp. 384–392, 2019.
- [148] C. P. Dietrich, M. Karl, J. Ohmer, U. Fischer, M. C. Gather, and S. Höfling, “Molding photonic boxes into fluorescent emitters by direct laser writing,” *Advanced Materials*, vol. 29, no. 16, p. 1605236, 2017.
- [149] M. Dusel, S. Betzold, T. H. Harder, M. Emmerling, J. Beierlein, J. Ohmer, U. Fischer, R. Thomale, C. Schneider, S. Hofling, *et al.*, “Room-temperature topological polariton laser in an organic lattice,” *Nano Letters*, vol. 21, no. 15, pp. 6398–6405, 2021.
- [150] G. Shankarling and K. Jarag, “Laser dyes,” *Resonance*, vol. 15, no. 9, pp. 804–818, 2010.
- [151] T. Cookson, K. Georgiou, A. Zasedatelev, R. T. Grant, T. Virgili, M. Cavazzini, F. Galeotti, C. Clark, N. G. Berloff, D. G. Lidzey, and P. G. Lagoudakis, “A Yellow Polariton Condensate in a Dye Filled Microcavity,” *Advanced Optical Materials*, vol. 5, p. 1700203, sep 2017.
- [152] C. Mowatt, S. M. Morris, M. H. Song, T. D. Wilkinson, R. H. Friend, and H. J. Coles, “Comparison of the performance of photonic band-edge liquid crystal lasers using different dyes as the gain medium,” *Journal of Applied Physics*, vol. 107, p. 043101, feb 2010.
- [153] M. Muszyński, M. Król, K. Rechcińska, P. Oliwa, M. Kędziora, R. Mazur, P. Morawiak, W. Piecek, P. Kula, P. Lagoudakis, *et al.*, “Lasing in the

- Rashba-Dresselhaus spin-orbit coupling regime in a dye-filled liquid crystal optical microcavity,” *arXiv preprint arXiv:2109.07338*, 2021.
- [154] K. Łempicka-Mirek, M. Król, L. De Marco, A. Coriolano, L. Polimeno, I. Viola, M. Kędziora, M. Muszyński, P. Morawiak, R. Mazur, *et al.*, “Electrical switching of a chiral lasing from polariton condensate in a Rashba-Dresselhaus regime,” *arXiv preprint arXiv:2211.11852*, 2022.
- [155] K. Łempicka-Mirek, M. Król, H. Sigurdsson, A. Wincukiewicz, P. Morawiak, R. Mazur, M. Muszyński, W. Piecek, P. Kula, T. Stefaniuk, *et al.*, “Electrically tunable berry curvature and strong light-matter coupling in liquid crystal microcavities with 2d perovskite,” *Science Advances*, vol. 8, no. 40, p. eabq7533, 2022.
- [156] M. Król, I. Septembre, P. Oliwa, M. Kędziora, K. Łempicka-Mirek, M. Muszyński, R. Mazur, P. Morawiak, W. Piecek, P. Kula, *et al.*, “Annihilation of exceptional points from different dirac valleys in a 2d photonic system,” *arXiv preprint arXiv:2112.06621*, 2021.
- [157] Y. Li, X. Ma, X. Zhai, M. Gao, H. Dai, S. Schumacher, and T. Gao, “Manipulating polariton condensates by Rashba-Dresselhaus coupling at room temperature,” *Nature Communications*, vol. 13, no. 1, pp. 1–6, 2022.
- [158] X. Zhai, X. Ma, Y. Gao, C. Xing, M. Gao, H. Dai, X. Wang, A. Pan, S. Schumacher, and T. Gao, “Electrically controlling vortices in a neutral exciton polariton condensate at room temperature,” *arXiv preprint arXiv:2211.01680*, 2022.
- [159] M. Aidelsburger, S. Nascimbene, and N. Goldman, “Artificial gauge fields in materials and engineered systems,” *C. R. Physique*, vol. 19, no. 6, pp. 394 – 432, 2018. Quantum simulation / Simulation quantique.
- [160] Y. Ho Park, H.-j. Kim, J. Chang, S. Hee Han, J. Eom, H.-J. Choi, and H. Cheol Koo, “Separation of Rashba and Dresselhaus spin-orbit interactions using crystal direction dependent transport measurements,” *Applied Physics Letters*, vol. 103, no. 25, p. 252407, 2013.
- [161] V. G. Sala, D. D. Solnyshkov, I. Carusotto, T. Jacqmin, A. Lemaître, H. Terças, A. Nalitov, M. Abbarchi, E. Galopin, I. Sagnes, J. Bloch, G. Malpuech, and A. Amo, “Spin-orbit coupling for photons and polaritons in microstructures,” *Phys. Rev. X*, vol. 5, p. 011034, Mar 2015.
- [162] C. R. Ast, J. Henk, A. Ernst, L. Moreschini, M. C. Falub, D. Pacilé, P. Bruno, K. Kern, and M. Grioni, “Giant spin splitting through surface alloying,” *Phys. Rev. Lett.*, vol. 98, p. 186807, May 2007.
- [163] K. Ishizaka, M. S. Bahramy, H. Murakawa, M. Sakano, T. Shimojima, T. Sonobe, K. Koizumi, S. Shin, H. Miyahara, A. Kimura, K. Miyamoto, T. Okuda, H. Namatame, M. Taniguchi, R. Arita, N. Nagaosa, K. Kobayashi,

- Y. Murakami, R. Kumai, Y. Kaneko, Y. Onose, and Y. Tokura, “Giant Rashba-type spin splitting in bulk BiTeI,” *Nat. Mater.*, vol. 10, p. 521, Jun 2011. Article.
- [164] P. D. C. King, R. C. Hatch, M. Bianchi, R. Ovsyannikov, C. Lupulescu, G. Landolt, B. Slomski, J. H. Dil, D. Guan, J. L. Mi, E. D. L. Rienks, J. Fink, A. Lindblad, S. Svensson, S. Bao, G. Balakrishnan, B. B. Iversen, J. Osterwalder, W. Eberhardt, F. Baumberger, and P. Hofmann, “Large tunable Rashba spin splitting of a two-dimensional electron gas in Bi₂Se₃,” *Phys. Rev. Lett.*, vol. 107, p. 096802, Aug 2011.
- [165] Y. Zhai, S. Baniya, C. Zhang, J. Li, P. Haney, C.-X. Sheng, E. Ehrenfreund, and Z. V. Vardeny, “Giant Rashba splitting in 2D organic-inorganic halide perovskites measured by transient spectroscopies,” *Sci. Adv.*, vol. 3, no. 7, 2017.
- [166] J. Moser, A. Matos-Abiague, D. Schuh, W. Wegscheider, J. Fabian, and D. Weiss, “Tunneling anisotropic magnetoresistance and spin-orbit coupling in Fe/GaAs/Au tunnel junctions,” *Phys. Rev. Lett.*, vol. 99, p. 056601, Aug 2007.
- [167] Y.-J. Lin, K. Jiménez-García, and I. B. Spielman, “Spin-orbit-coupled Bose-Einstein condensates,” *Nature*, vol. 471, p. 83, Mar 2011.
- [168] V. Galitski and I. B. Spielman, “Spin-orbit coupling in quantum gases,” *Nature*, vol. 494, p. 49, Feb 2013.
- [169] N. R. Cooper, J. Dalibard, and I. B. Spielman, “Topological bands for ultracold atoms,” *Rev. Mod. Phys.*, vol. 91, p. 015005, Mar 2019.
- [170] K. Frischwasser, I. Yulevich, V. Kleiner, and E. Hasman, “Rashba-like spin degeneracy breaking in coupled thermal antenna lattices,” *Opt. Express*, vol. 19, pp. 23475–23482, Nov 2011.
- [171] N. Shitrit, S. Maayani, D. Veksler, V. Kleiner, and E. Hasman, “Rashba-type plasmonic metasurface,” *Opt. Lett.*, vol. 38, pp. 4358–4361, Nov 2013.
- [172] N. Shitrit, I. Yulevich, E. Maguid, D. Ozeri, D. Veksler, V. Kleiner, and E. Hasman, “Spin-optical metamaterial route to spin-controlled photonics,” *Science*, vol. 340, no. 6133, pp. 724–726, 2013.